SRI International

(2)

Final Technical Report • June 1992

MODELING OF MICROSTRUCTURAL EFFECTS ON FRACTURE PROCESSES AT HIGH LOADING RATES

J. H. Giovanola, Program Manager
R. W. Klopp, Research Engineer
D. A. Shockey, Associate Director
Poulter Laboratory

With contributions from: T. Kobayashi, P. Touzé, S. W. Kirkpatrick, D. C. Erlich, C. Kanazawa, J. E. Crocker, and C. G. Schmidt

SRI Project 7294
Contract No. F49620-89-K-0003

Prepared for:

Air Force Office of Scientific Research
AFOSR/NE, Bldg. 410
Bolling Air Force Base
Washington, DC 20332

Attn: Dr. Alan Rosenstein

Approved:

James D. Colton, Director
Poulter Laboratory

David M. Golden
Vice President
Physical Sciences Division

40281

210 pg

. SPONSORING/MONITORING AGENCY NAME(S) AND ADDRESS(ES) Air Force Office of Scientific Research AFOSR/NE, Bldg. 410 Bolling Air Force Base Washington, DC 20332	**10. SPONSORING/MONITORING AGENCY REPORT NUMBER**
1. SUPPLEMENTARY NOTES	
2a. DISTRIBUTION/AVAILABILITY STATEMENT unlimited	**12b. DISTRIBUTION CODE**

3. ABSTRACT ***(Maximum 200 words)***

We extended classical dynamic fracture mechanics to a class of new commercially useful titanium nicrostructures and demonstrated that their dynamic fracture behavior differs significantly from that of reviously studied model materials. By combining continuum measurements (obtained using the torsion plit Hopkinson bar and one-point-bend fracture test methods) and fractographic measurements (obtained sing fracture surface topography analysis, FRASTA), we generated a complete data base on static and ynamic strength and fracture toughness for various microstructures of the alloy Ti-10V-2Fe-3Al. We etermined effects of microstructural features on microfailure behavior and we modeled some of the bserved microfailure processes using finite element analysis.

Whereas the dynamic initiation toughness was only moderately higher than the static initiation ughness (at most 20%), a very strong rise was found in the crack propagation toughness with crack xtension (as much as a 100% increase) for velocities as low as 100 m/s. This rate dependent resistance urve effect is an intrinsic material property (in contrast to a structural effect) and a strong function of icrostructure. We demonstrated that the formation of shear lips is also a strongly rate dependent

CLASSIFIED BY:
DECLASSIFY ON:

13. ABSTRACT (Continued)

phenomenon and that shear lips, when they develop, make only a modest contribution to the propagation toughness (on the order of 20% for the case studied here). Our results also showed that, in general, there is not a direct correlation between the dynamic initiation and propagation toughnesses.

We independently verified the continuum results with fractographic measurements of crack tip opening displacements and angles and obtained, to our knowledge for the first time, a crack opening displacement resistance curve directly from fracture surface topography measurements. We demonstrated in several independent ways that it is possible to extract from fractographic measurements parameters useable in continuum fracture mechanics analyses.

For a given strength level, the microstructure of the alloy (primary alpha content and morphology, grain size, grain boundary alpha film) influenced the fracture mode and the fracture properties in a complex way. Void nucleation and growth at primary alpha particles or in grain boundary alpha films was always the dominant microfailure mode, but decreasing the grain size by two orders of magnitude changed the fracture path from intergranular to transgranular. We identified rate dependent and microstructure dependent mechanisms (such as interactions of the main crack tip with secondary transverse cracks or with unfavorably oriented grains or grain boundaries) which provide partial explanations for the observed dynamic toughness behavior.

Several experimental observations, such as the long crack extension needed for achieving a steady state value of the dynamic propagation toughness, remain without conclusive detailed micromechanical explanation and will require additional research.

On the basis of our fractographic observations, we developed a finite element model of the interaction between heterogeneous grain core and grain boundary material under conditions of highly triaxial stress and quasi-uniaxial strain extension. We used a porous material model for the grain boundary and a strain-hardening plasticity model for the cores. With this relatively simple microstructural model, we were able to reproduce some microfailure features observed in the Ti-10V-2FE-3Al (such as grain boundary cracks and strain localization in the grain cores), and to rationalize the effect of the relative grain boundary/grain core strength on the fracture behavior of this alloy and of titanium alloys more generally.

This study has made a significant contribution to dynamic fracture mechanics by establishing a strong link between microscopic observations and continuum measurements, and by successfully demonstrating an approach for modeling the effects of microstructural constituents on microfailure processes. Thus, the research program has improved our ability to design multiphase materials with engineered mechanical properties.

CONTENTS

CONTENTS

(Concluded)

ILLUSTRATIONS

ILLUSTRATIONS

Figures **Page**

ILLUSTRATIONS

TABLES

ACKNOWLEDGMENTS

The authors are indebted to their SRI colleagues F. Galimba, M. Merritt, T. Lovelace, J. Regnere, L. Alaura-Malinis, M. Saunders, J. Berry, and K. Baxter for their invaluable contributions.

INTRODUCTION

Developments in the field of materials science are making possible the design of materials with prescribed properties. In a growing number of situations, materials can be tailored for specific applications. Such engineered materials are contributing to the design of lighter, more maneuverable, and more fuel-efficient aircraft and lighter, more precise, and more lethal munitions. Thus, engineered materials are a significant element in the effort to maintain a superior U.S. Air Force. Engineered materials often combine several monolithic materials or phases to obtain overall desired properties. Understanding and modeling the influence of each component material or phase on the composite properties are important steps in optimizing the performance of advanced engineered materials.

The influence of loading rate on the behavior of materials must also be recognized. Changing the rate at which materials are stressed may change their flow properties and also the micromechanisms leading to their fracture. Quantitative evaluation of the effect of loading rate is therefore essential for designing structures that will be subjected to a wide range of in-service loading rates.

Titanium airframe structural components and high strength steel hard target penetrators are two examples of components which are subjected to high loading rates and in which improvements in properties associated with optimized microstructural design can result in better products with significantly improved performance at a reduced cost to the Air Force.

This report presents the results of a three-year research project in which SRI International addressed the need for predicting the influence of microstructure on material performance at high loading rates. The focus of the research was primarily on a promising advanced titanium alloy (Ti-10V-2Fe-3Al), but the understanding and experience gained in the work with titanium were also applied to two high-strength, quenched-and-tempered steels (300M and D6ac).

The research on the two high strength steels was the subject of a separate report, which was submitted in November 1991 and is appended here. The following sections present the objectives, general approach, and main accomplishments of the project; the details of our approach and results for the research on Ti-10V-2Fe-3Al; our first attempt at microstructural modeling based on our experimental observations; and lists of personnel, activities, and publications and presentations associated with this and related previous AFOSR-sponsored projects.

RESEARCH OBJECTIVES AND ACCOMPLISHMENTS

OBJECTIVES

The long term objective of this research was to develop capabilities for predicting the influence of microstructural parameters on the mechanical and fracture behavior of engineered multiphase materials. We sought to accomplish this overall objective for a given material by

1. Establishing the influence of grain size on the static and dynamic fracture behavior of different Ti-10V-2Fe-3Al microstructures with a given strength and comparable primary alpha phase (α_p) content.
2. Developing a model relating the influence (or lack thereof) of microstructural parameters such as α_p content and grain size to the fracture behavior of multiphase alloys.

APPROACH

In previous research programs[1,2] funded by the Air Force Office of Scientific Research (AFOSR), SRI developed reliable testing methods to characterize the dynamic fracture behavior of high strength metallic alloys and investigated the dynamic fracture behavior of three Ti-10V-2Fe-3Al microstructures. Further, we established how, for a given strength level, changes in the α_p-phase content influence the micromechanisms of deformation and fracture and affect macroscopic static and dynamic fracture properties.

In the current research program, to establish the influence of other microstructural parameters on the dynamic fracture behavior of Ti-10V-2Fe-3Al, we produced and tested microstructures with approximately the same mechanical strength and α_p content but with different grain sizes (fine, intermediate, and coarse, varying from less than 10 μm up to 1 mm). To characterize the dynamic fracture behavior of these microstructures in terms of continuum fracture mechanics parameters (such as the stress-intensity factor), we conducted crack initiation and propagation experiments using the one-point-bend test developed under AFOSR sponsorship.[1] We also measured the dynamic stress strain curve and the shear-banding properties of the selected microstructures in torsion Hopkinson bar experiments.[3] To verify and interpret the continuum characterization of the dynamic fracture properties, we applied advanced fractographic techniques such as fracture surface topography analysis (FRASTA)[4] to deduce microfailure mechanisms from fracture surface observations of laboratory specimens.

On the basis of our observations, we developed a first simple finite element model, including a void damage constitutive relation, to simulate some of the microdeformation and microfailure features we observed in the microstructures we investigated.

ACCOMPLISHMENTS

The work performed in this research program has resulted in the following significant accomplishments:

- We have extended classical dynamic fracture mechanics to a class of new, commercially useful titanium microstructures and demonstrated that their dynamic fracture behavior differs significantly from that of previously studied model materials.
- We established a very strong rise in the crack propagation toughness with crack extension for velocities as low as 100 m/s. This rate dependent resistance curve effect is an intrinsic material property (in contrast to a structural effect) and a strong function of microstructure.
- We demonstrated that the formation of shear lips is also a strongly rate dependent phenomenon and that shear lips make only a relatively small contribution to the propagation toughness (about 20%).
- We demonstrated that, in general, there is no direct correlation between dynamic initiation and propagation toughnesses.
- We independently verified the continuum results with fractographic measurements of crack tip opening displacements (CTODs) and angles and obtained, to our knowledge for the first time, a crack opening displacement resistance curve directly from fracture surface topography measurements.
- We identified rate dependent and microstructure dependent mechanisms that provide partial explanations for the observed dynamic toughness behavior.
- We developed a two-dimensional finite element model of one of the investigated microstructures, incorporating different constitutive models for different regions of the microstructure and introducing a damage model to simulate microfailure processes. With the model, we investigated how the strength and defect density in the α grain boundary film of a Ti-10V-2Fe-3Al microstructure affect the tendency for grain boundary fracture and shear localization across the grains. We predicted ductile failure and strain localization locations consistent with our experimental observations.

This study has made a significant contribution to dynamic fracture mechanics by establishing a strong link between microscopic observations and continuum measurements, and by successfully demonstrating an approach for modeling the effects of microstructural constituents on microfailure processes. Thus the research program has improved our ability to design multiphase materials with engineered mechanical properties.

EFFECT OF GRAIN SIZE ON THE STATIC AND DYNAMIC FRACTURE PROPERTIES OF Ti-10V-2Fe-3Al

BACKGROUND

Ti-10V-2Fe-3Al is a relatively new β titanium alloy of interest to the aerospace community for use in structural components of aircraft. Extensive descriptions of the alloy's metallurgy and mechanical behavior can be found in References 5 through 15. In particular, Reference 10 reports on a recent study of the effect of microstructure on the static fracture properties of Ti-10V-2Fe-3Al, whereas Reference 11 gives to our knowledge the only available results of dynamic strength and fracture tests on the alloy.

Ti-10V-2Fe-3Al has deep hardenability and a low β-transus temperature. The low β-transus facilitates isothermal forging and results in reduced wear of the forging dies and in material savings. Ti-10V-2Fe-3Al also has a better combination of strength and toughness than α or α-ß alloys.

Precipitation strengthening is possible in Ti-10V-2Fe-3Al by solution treatment at a temperature near the β-transus, quenching to retain metastable β, and aging to precipitate the α phase within the β grains. The α-ß interfaces tend to retard the dislocation motion necessary for plastic deformation and thus provide strengthening.

The final microstructure of the alloy depends on the thermomechanical processing and the heat-treating schedule. Solution treatment above the β-transus results in equiaxed β-grains after quenching, whereas solution treatment below the β-transus results in microstructures containing a relatively coarse distribution of soft α phase, termed primary α (α_p), distributed within the β-grains and, in some cases, also in a continuous or discontinuous film at the grain boundaries. The morphology of the α_p phase is controlled mainly by the thermomechanical processing, whereas its volume fraction depends on the solution treatment temperature: the lower the solution treatment temperature, the higher the α_p-phase content. The aging treatment precipitates a secondary α phase that is much finer than the α_p phase and is not resolvable optically. In some cases, an α phase film develops along the β-grain boundaries during the aging treatment.

The strength level of the alloy is controlled by the secondary α phase produced during aging.

The ductility and fracture toughness depend predominantly on the volume fraction and morphology of the α_p phase. Therefore, strength and toughness properties of the alloy can be varied independently, to within certain limits, by varying the heat-treatment steps of the alloy. Terlinde et al.[10] and Campagnac[14] have shown that, for a given strength level, the static ductility and toughness of the alloy decrease with increasing α_p-phase content. Both ductility and toughness decrease strongly as a function of the strength level. For a given strength level and α_p-phase content, microstructures with globular α_p phase have better ductility but lower toughness than microstructures with an elongated α_p phase.[10, 15] This inverse relationship between ductility and toughness, which is usually not encountered in ferrous alloys, is typical of many titanium alloys.[15] The reason for this behavior is that ductility is controlled by void nucleation at the interface of α_p-phase particles with the matrix, whereas crack path tortuosity strongly affects resistance to crack extension which controls toughness. For a given volume fraction, elongated α_p-phase particles offer a larger surface area for void nucleation while at the same time inducing larger crack deflections. Similarly, the prior β-grain size also affects the (static) fracture properties through its influence on the crack path.[10] This anticipated grain size effect has motivated the study presented in this report.

MICROSTRUCTURES

The Ti-10V-2Fe-3Al alloy studied in the present investigation was acquired from Timet Corporation for a previous project[2] in which we investigated the influence of the α_p-phase content on the static and dynamic fracture behavior of the alloy. The original material was in the form of a 200-kg, 0.2-m-diameter billet. The chemical composition of the billet is reported in Table 1. The billet was first α–β forged to 50-mm-thick slabs and β-annealed at 843°C. All the slabs except one were then β-rolled to 30 mm thick and α–β finish-rolled at 760°C to 25 mm thick. Figure 1 shows a three-orientation low magnification view of this as-received β-processed microstructure, which reveals banding due to rolling. The remaining slab was processed entirely at 760°C in the α–β domain to achieve a fine grain size. Figure 2 shows micrographs of the as-received α–β processed fine-grain microstructure, which also displays banding due to rolling. We established that the alloy had a β-transus of 810°-815°C.

We prepared three materials with different grain sizes [coarse-grain (CG), intermediate-grain (IG), and fine-grain (FG)] from the as-received slabs and selected the same solution and aging treatment for the three microstructures, so as to achieve approximately the same strength levels in all three materials. Table 2 summarizes the processing and heat treatment selected for each

Table 1

INGOT CHEMISTRY (wt %) FOR Ti-10V-2Fe-3Al

	Fe	O_2	V	Mo	B	C	H	Sn	Cu	N	Al	Zr	Mn	Si
Top	1.850	0.096	9.670	0.031	.001	0.014	1 ppm	0.010	0.001	0.007	3.020	0.001	0.001	0.034
Bottom	2.040	0.098	9.920	0.031	.001	0.021	1 ppm	0.010	0.002	0.009	3.030	0.001	0.007	0.044
Average	1.945	0.097	9.795	0.031	.001	0.017	1 ppm	0.010	0.001	0.008	3.025	0.001	0.004	0.039

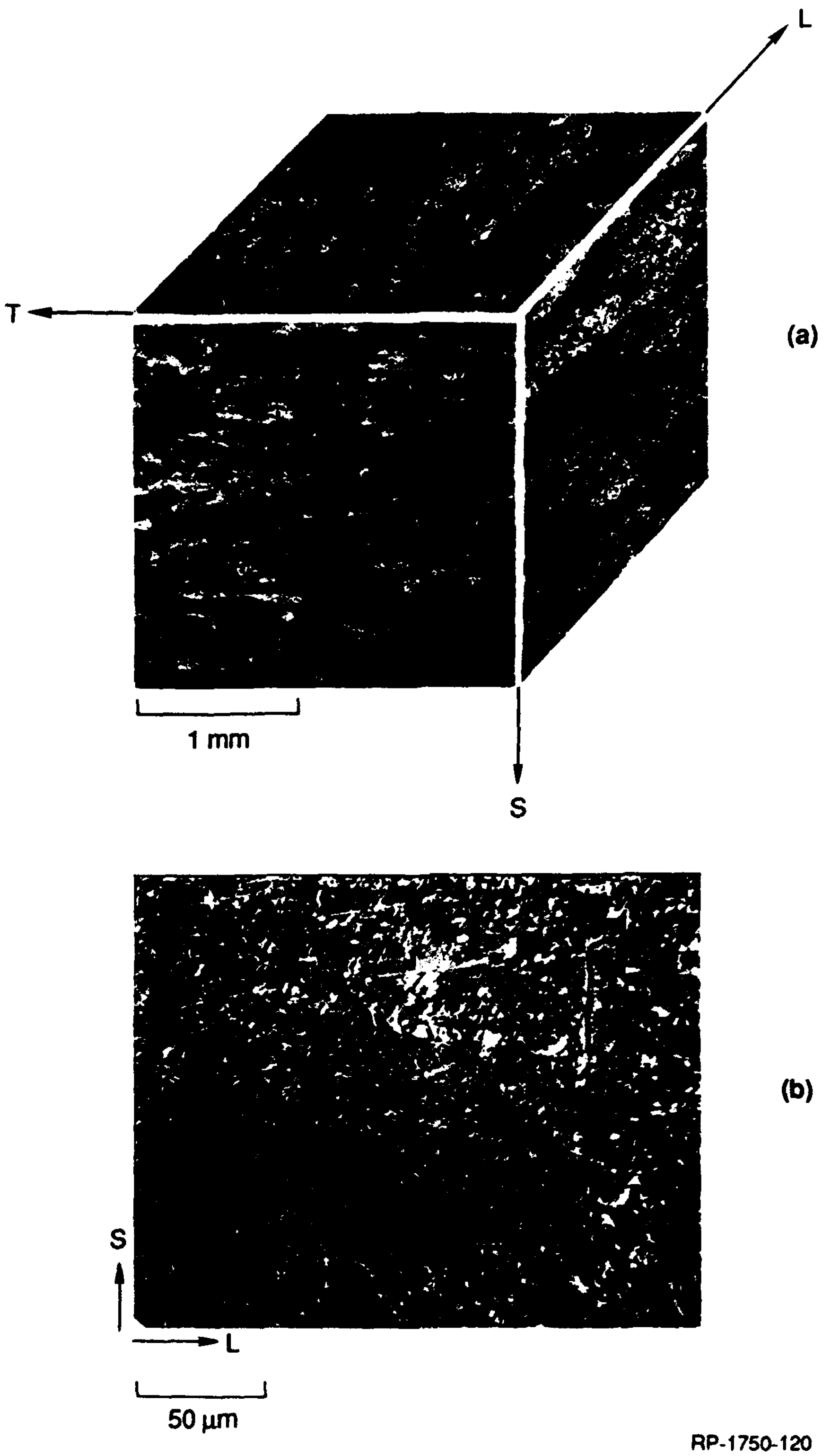

RP-1750-120

Figure 1. As-received β-processed microstructure of Ti-10V-2Fe-3Al.

(a) Three-orientation view.

(b) Detail of microstructure.

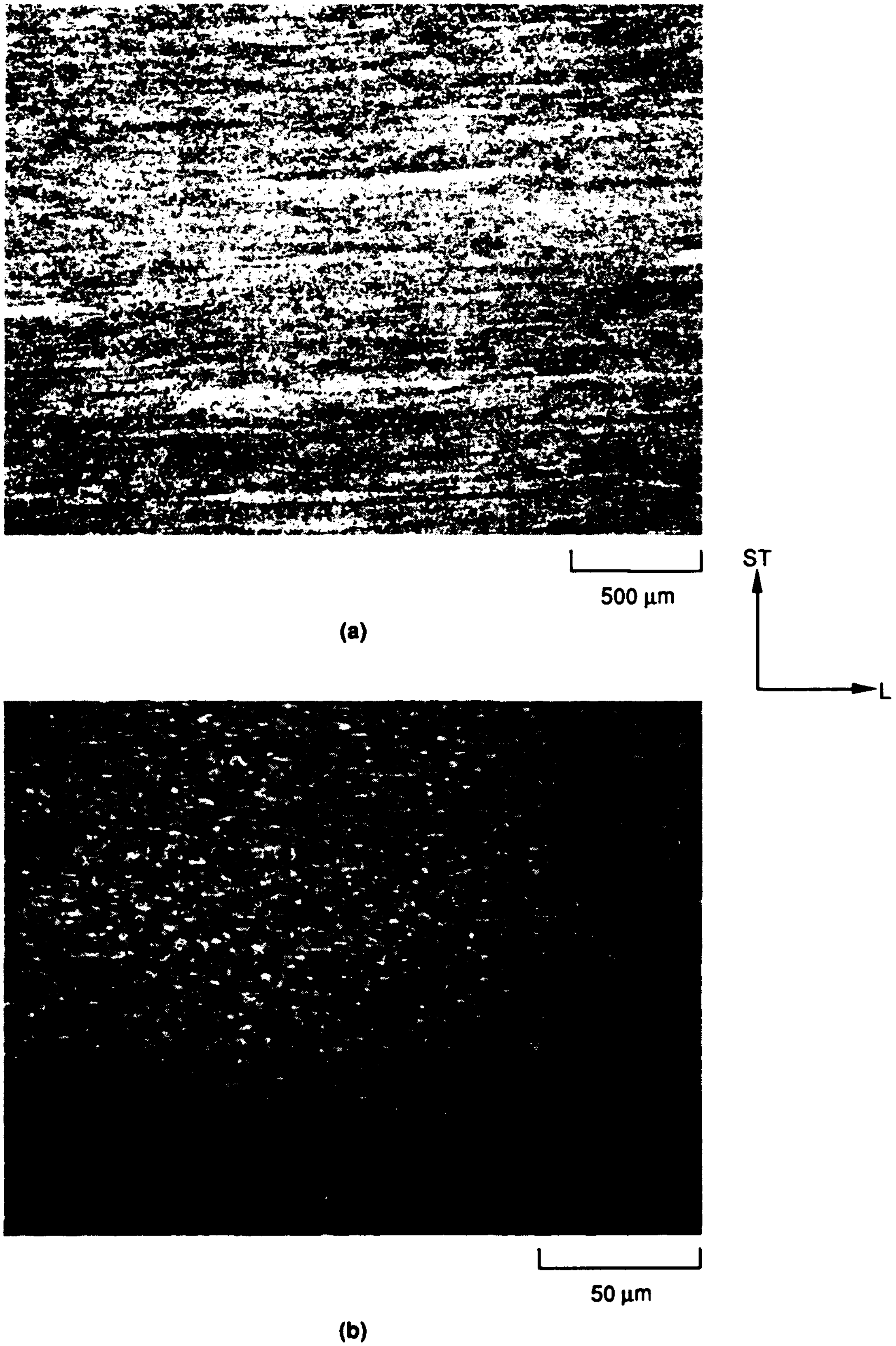

RP-7294-45

Figure 2. As-received α-β-processed microstructure of Ti-10V-2Fe-3Al.

Table 2

HEAT TREATMENT CONDITIONS FOR THREE MATERIALS WITH DIFFERENT GRAIN SIZES

Heat Treatment Steps	Coarse-Grain (CG) Microstructure	Intermediate-Grain (IG) Microstructure	Fine-Grain (FG) Microstructure
Thermomechanical treatment	α–β-forged to 50-mm-thick slabs and β-annealed at 843°C, β-rolled to 30 mm-thick plates, α–β-finished to 25-mm-thick plates		Processed entirely at 760°C in the α–β domain
Grain-growth treatment	Heated to 975°C and held for one hour, water-quenched	—	—
Solution treatment	Heat to 760°C, hold for one hour, water quench (same for all three materials)		
Aging treatment	Heat to 500°C, hold for eight hours, air cool (same for all three materials)		

of the three materials. Because of the different processing histories, the resulting α_p-phase contents, although similar, are not identical and the α_p-phase morphology is quite different. To grow coarse grains in the β-processed material, we held it at 975°C for 1 hour and then water quenched it. The intermediate grain size and the fine grain size resulted directly from the β- and α–β-thermomechanical processing, respectively. All three materials were solution-treated at 760°C for 1 hour, water quenched, aged at 500°C for 8 hours, and air cooled. The IG microstructure, which was produced, characterized, and tested in the previous program,[2] served as our baseline microstructure. In the present project, we performed complementary dynamic strength and fracture tests and fractographic analyses for this IG microstructure.

Figure 3 shows the resulting microstructures and Table 3 summarizes their characteristics. The CG microstructure has equiaxed grains 300-1000 μm in size (Figure 3a.). The α_p phase is mainly globular, with some particles being more elongated (roughly 1:4 aspect ratio), as illustrated in Figure 3b. Figure 3b also reveals the presence of either thick continuous or thinner discontinuous grain boundary α phase.

The IG microstructure has a more elongated grain structure resulting from the thermomechanical treatment, with a grain aspect ratio of roughly 1:2 to 1:4 and a grain size varying between roughly 50 and 300 μm (Figure 3c). We observed a variety of morphologies for the α_p phase, ranging from fine globular particles to elongated platelets. Some regions contained large globular α_p particles, while others had an agglomeration of thick platelets adjacent to an α_p-depleted region. The IG microstructure also has continuous and discontinuous grain-boundary and sub-grain boundary α films (Figure 3d). The FG microstructure has grains smaller than 10 μm (barely discernible in Figure 3e) and a regular distribution of globular α_p. The size and spacing of the globular α_p particles are on the order of the grain size. The globular α_p-phase particles of the FG material are considerably coarser than those of the CG microstructure (compare Figures 3b and 3e).

From the metallographic characterization of the three microstructures, we see that we were able to vary the grain size over several orders of magnitude. However, this variation is also (unavoidably) accompanied by variations in the morphology of the α_p particles and, possibly, of the volume fraction. As we discussed above, these metallurgical factors may also have a significant impact on the fracture behavior of the alloy and hence must be taken into account in analyzing the results of the present study.

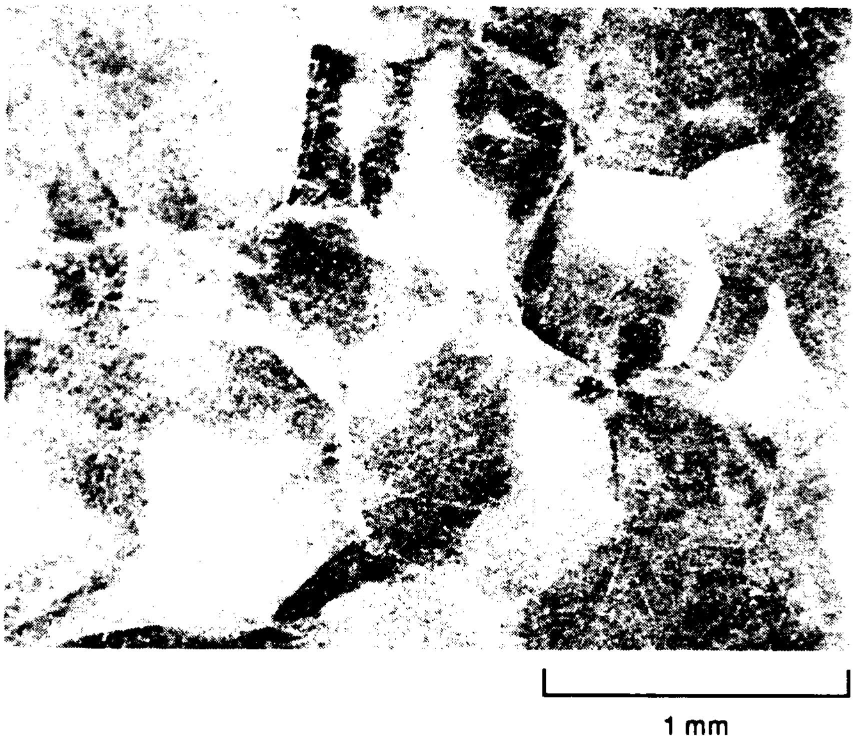

(a) Coarse Grain

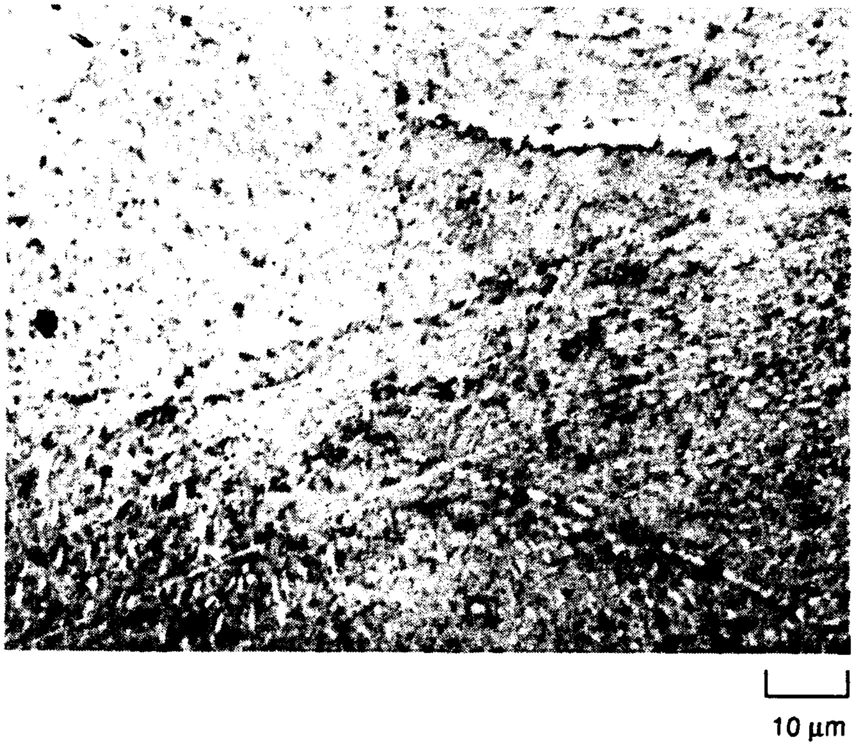

(b) Coarse Grain

RP-7294-78

Figure 3. Investigated Ti-10V-2Fe-3Al microstructures. (Continued)

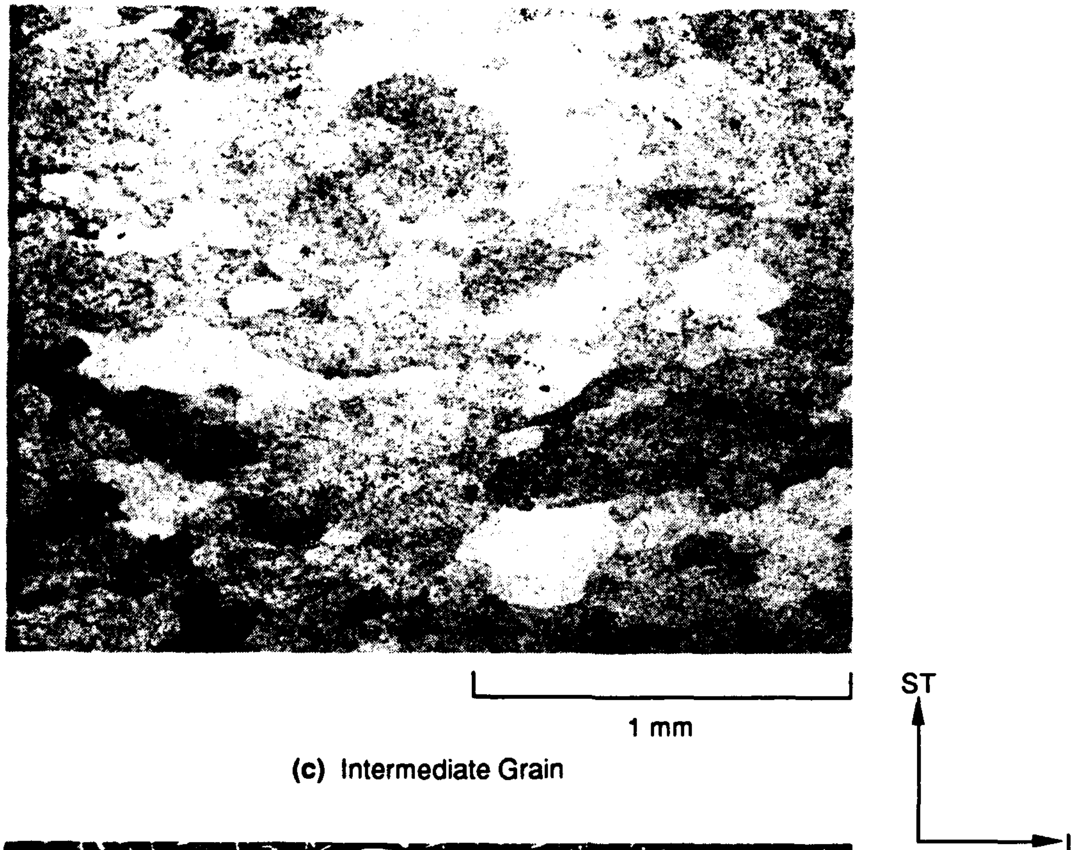

(c) Intermediate Grain

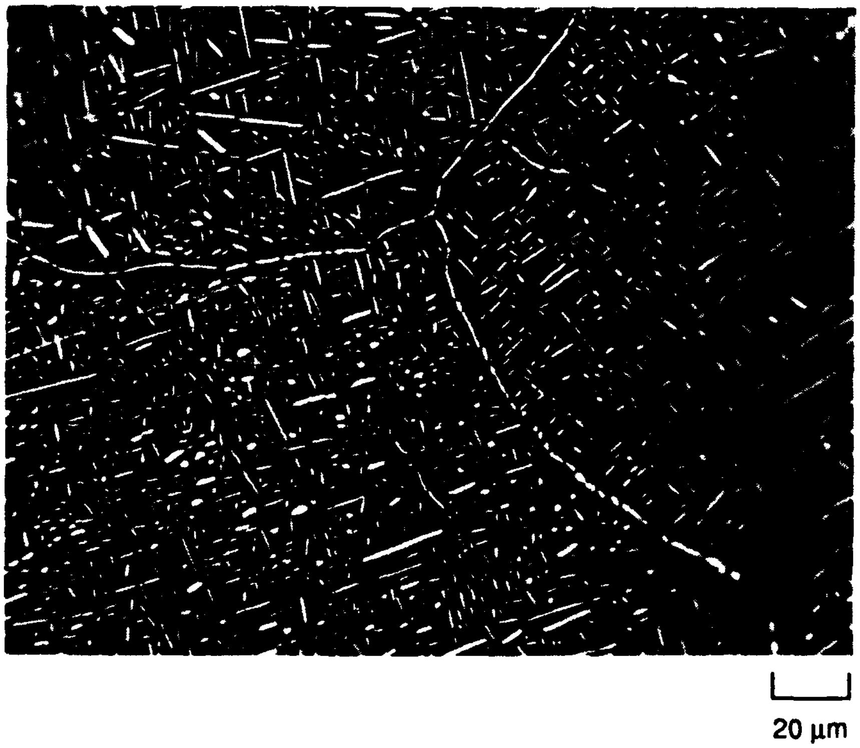

(d) Intermediate Grain

RP-7294-79

Figure 3. Investigated Ti-10V-2Fe-3Al microstructures. (Continued)

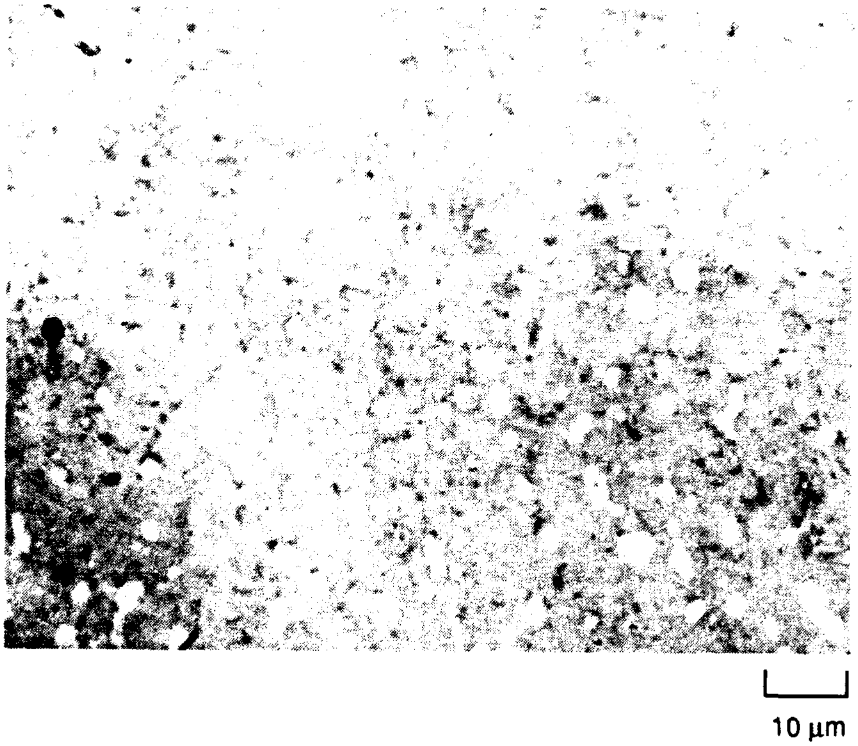

(e) Fine Grain

RP-7294-80

Figure 3. Investigated Ti-10V-2Fe-3Al microstructures. (Concluded)

Table 3

CHARACTERISTICS OF INVESTIGATED MICROSTRUCTURES

	CG Microstructure	IG Microstructure	FG Microstructure
Grain size (μm)	300-1000	50-300	<10
α_p Phase	Globular or slightly elongated	Mainly elongated with some globular	Globular
Grain boundary α phase	Thick continuous and thinner discontinuous	Mainly thin continuous	None

EXPERIMENTAL METHODS

Strength Properties Characterization

We characterized the strength properties of the three microstructures by performing conventional round bar tension tests (ASTM Standard E-8, Standard Methods of Tension Testing of Metallic Materials) and high strain rate torsion split Hopkinson bar tests. The torsion split Hopkinson bar test method is a well established technique and is described in detail in Reference 3. Both the tensile specimens and the high rate torsion specimens were cut from broken halves of fracture specimens. The orientation of the specimens with respect to the as-received plate is indicated in Figure 4. We performed three static tensile tests and two high strain rate torsion tests for each microstructure.

Fracture Properties Characterization

We characterized the fracture properties of the three microstructures by performing conventional static three-point-bend fracture tests (ASTM Standard E399, Standard Test Method for Plane-Strain Fracture Toughness of Metallic Materials) and dynamic one-point-bend fracture tests.

The static three-point-bend tests utilized 25.4-mm-wide specimens, and an elastic analysis was used to evaluate the initiation toughness and the resistance curve of the materials.

The one-point-bend impact test was proposed and developed by Kanninen et al.[16] and Kalthoff et al.[17] and further developed at SRI.[1, 18, 19] In this test, a single-edge-cracked rectangular specimen is impacted by a moving hammer as in a conventional three-point-bend impact test, except that the specimen supports are omitted (Figure 5a). The crack is loaded in bending solely by the inertia of the unsupported ends of the specimen. The resulting stress intensity history (at the stationary crack tip) is a smoothly varying function of time (Figure 5b) and can conveniently be measured with a strain gage mounted near the original crack tip. We relate the measured strain to the stress intensity by performing a static calibration before the dynamic experiment or by using the elastic singularity solution for the crack tip fields.

To obtain the dynamic propagation toughness, additional experimental parameters are required. We measured the impact velocity, the impact force (with strain gages mounted on the

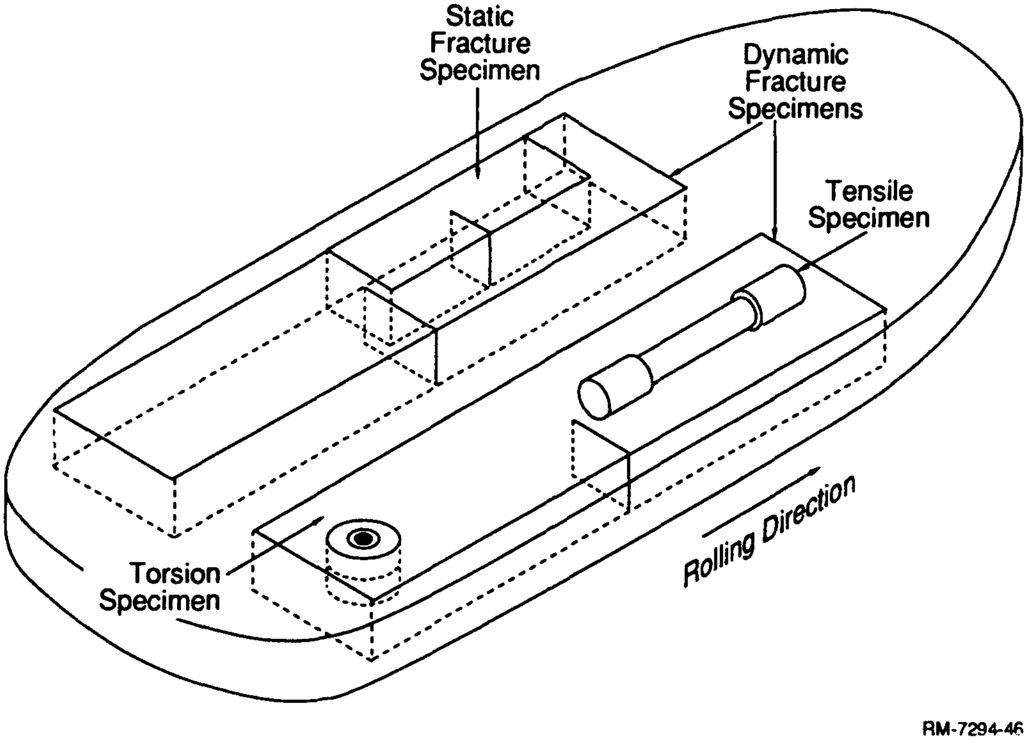

Figure 4. Orientation of specimens in as-received plate.

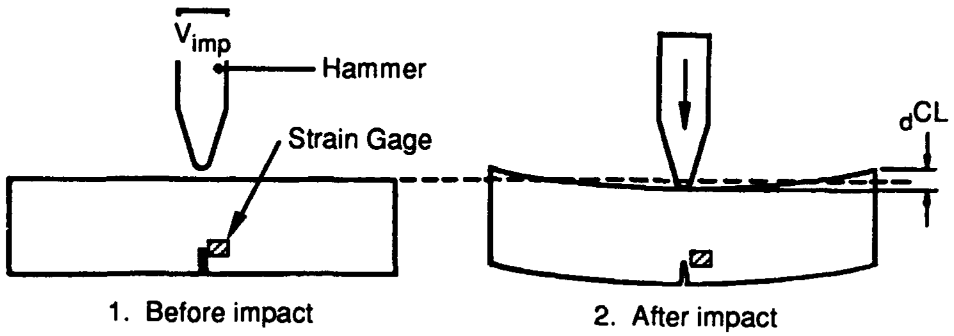

(a) Test arrangement and loading mechanism

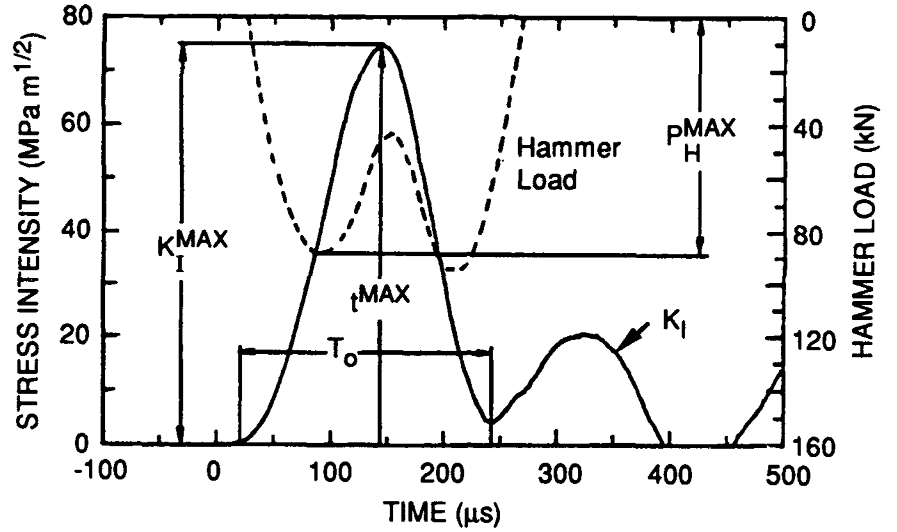

(b) Typical stress intensity and load histories

JM-2777-17

Figure 5. One-point-bend impact experiment.

hammer), and the crack propagation history (by taking high-speed photographs, typically using a 5-μs interframe time). We then used the impact load and the crack propagation history as input for numerical simulations of the experiments, in which we calculated the energy release rate by means of a path-independent domain integral.[20] We performed the simulations with the explicit DYNA2D finite element code,[21] using a two-dimensional plane strain approximation. We also measured strains normal to the crack plane at several locations along the crack path. These strain records provided independent verification of the crack propagation histories and coarse estimates of the stress intensity factor during crack propagation.

In the one-point-bend experiment, we controlled the crack propagation speed by varying the impact velocity and by changing the acuity of the initial notch in the specimen.

The orientation of the fracture specimens with respect to the as-received plate is indicated in Figure 4. We fabricated the static fracture specimens from broken halves of the dynamic fracture specimens. In preparing the fracture specimens after heat treatment, we machined approximately 1 mm from the top and bottom surfaces to remove any possible α-case. All the fracture specimens were 23 mm thick and had no side-grooves, except for two specimens that were made from the IG microstructure and had 2-mm-deep, 0.25-mm-wide side grooves. These grooved specimens were used in dynamic crack propagation experiments designed to evaluate the propagation toughness in the absence of shear lips.

The dynamic initiation toughness data for the CG, IG, and FG microstructures were obtained from 4, 8, and 4 experiments, respectively, and the dynamic crack propagation data from 4, 9, and 4 experiments, respectively. Of the latter set of experiments, we only fully analyzed one for the CG and one for the FG microstructures, with the other experiments used to ascertain repeatability of the results. The fracture data for the IG microstructure were obtained in the previous program,[2] except for the crack propagation experiments with side-grooved specimens, which were performed and evaluated in the present program.

FRASTA Technique

FRASTA (fracture surface topography analysis), a technique[4] developed at SRI, was used to obtain independent toughness estimates from microscopic measurements on the fracture surface. FRASTA also provided insight into the micromechanisms leading to crack initiation and growth.

Simply stated, FRASTA compares quantitative three-dimensional topographies of conjugate fracture surfaces, reconstructs the details of the fracture process, and graphically presents the results as a series of plots. FRASTA was conceived from a kinetic interpretation of microfracture processes in materials, as discussed below.

Consider the development of a microcrack in a material under application of a load. Initially, the material undergoes local plastic flow before failure begins, at some weak spot or stress concentrator, in the form of a microvoid or microcrack. The newly formed microfracture surfaces are free surfaces, and so the stresses on those surfaces fall to zero. Thus, the material immediately beneath the surfaces undergoes no further plastic deformation. The applied load is redistributed to unfractured material in front of the crack tip, which continues to deform plastically until it, too, fractures.

Microfracture extension results from the sequential process of deformation, microfracture, and redistribution of stresses. This sequential deformation and microfracture process produces differences in the amount of plastic deformation experienced locally by the material as a function of distance from the microfracture nucleation site and as a function of time after the initiation of microfracture nucleation. Thus, this difference in the amount of plastic deformation experienced by local material is a record of the history of the microfracture events.

However, the difference in local plastic deformation cannot be determined by examining one fracture surface alone. When a crack front moves through the plastic zone at the crack tip, the crack front interacts with local microstructural features so that the total amount of plastic deformation developed at the crack tip is divided unevenly between the two fracture surfaces. This interaction of the crack tip with the local microstructure and the uneven division of plastic deformation results in irregularities on the fracture surface. The total amount of plastic deformation occurring during fracture can be determined only by assessing the deformation on mating surfaces. Indeed, it is only by matching the topography of conjugate surfaces that the nucleation sites and sequence of microcracking can be established.

The FRASTA technique accesses information on microfracture evolution by obtaining precise, quantitative, three-dimensional topographic profiles (maps) of conjugate fracture surfaces—either by using a confocal optic scanning laser microscope or from stereo photographs produced with a scanning electron microscope—and matching them, with the aid of a computer, to determine the development of local plastic deformation accompanying fracture. The information on differences in local plastic deformation is used to reconstruct the microfracture sequence from beginning to end.

The results of FRASTA are presented in two ways: a series of fractured-area projection plots (FAPPs) and a series of cross-sectional plots (XSPs) as a function of map separation. The FAPP is equivalent to a radiograph of the microcracks taken in the direction perpendicular to the fracture plane at one instant during crack extension. This plot provides information on the location(s) of the microcrack initiation site(s) and the projected area(s) of the microcrack(s) or crack(s). A detailed picture of crack propagation is obtained by examining a series of FAPPs produced as a function of map separation.

The fractured area in a FAPP can also be computed and converted into the average crack length. By plotting the area or crack length as a function of map displacement, we can assess the crack growth rate.

The XSP shows a cross section made perpendicular to the fracture surface, displaying how the two surfaces match each other, the amount of overlap (plastic deformation necessary before fracture), and the amount of crack face opening displacement. The crack tip opening displacement (CTOD) determined from the plot can be related to the J-integral or stress intensity factor K to assess the fracture toughness of the material or the loading conditions. We relate the crack opening displacement to J and K through the equation

$$K^2(1-\nu^2)/E = \mathrm{CTOD} * \sigma_{\mathrm{flow}} = J \qquad (1)$$

where ν is Poisson's ratio, E is Young's modulus, and σ_{flow} is the flow stress, defined as the average of the yield and ultimate stresses.

RESULTS

Strength Properties

The strength properties of the CG, IG, and FG microstructures are summarized in Table 4 and Figures 6 and 7. Figure 6 shows the static tensile true stress-true strain curves up to the onset of necking. Figure 7 shows the dynamic shear stress-shear strain curves. In Table 4, we converted the shear stress data to equivalent tensile data by multiplying by $\sqrt{3}$.

The static yield strengths for the three microstructures differ by less than 4%, and the flow curves for the IG and FG microstructures are also very similar up to necking, with an elongation of

Table 4

SUMMARY OF STRENGTH PROPERTIES OF CG, IG, AND FG MICROSTRUCTURES

Microstructure	Static Yield Strength (0.2% Offset) (MPa)	Static Tensile Strength (MPa)	1-in. Gage Length Elongation (%)	Static Tensile Failure Strain	Dynamic Yield Strength[1] (MPa)	Dynamic Flow Strength[1] (MPa)	Dynamic Shear Strain at Failure
CG	1158	1170	1.0	0.014	1400	1515	0.055
IG	1140	1227	9.0	0.29	1125	1385	0.071
FG	1179	1236	8.0	0.29	1390[2]	1515[2]	0.030[2]

[1] Converted from the measured shear stress by multiplying by $\sqrt{3}$.

[2] Data from only one test.

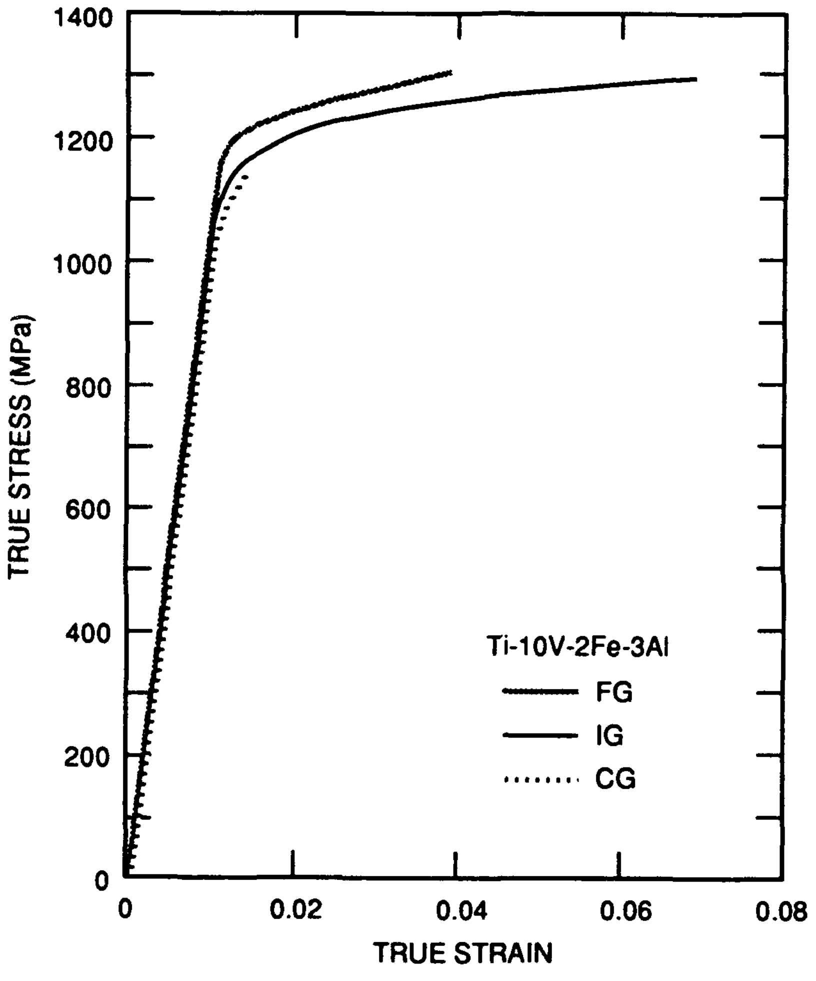

RM-7294-47

Figure 6. Static tensile true stress-true strain curve for the CG, IG and FG microstructures.

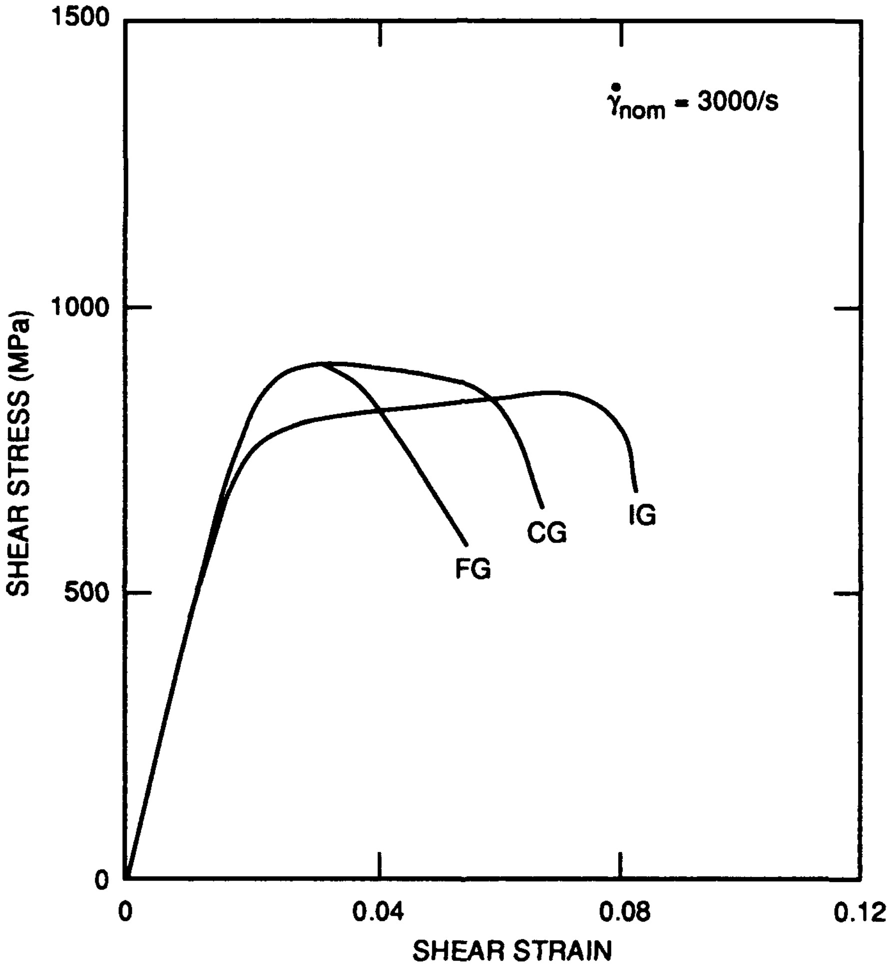

RM-7294-48

Figure 7. Dynamic torsion stress-strain curve for the CG, IG and FG microstructures.

9% and 8%, respectively, and failure strains (obtained from the final neck diameters) of about 0.29. The CG microstructure, on the other hand, has very low ductility (1% elongation and 0.014 failure strain) and fails without necking.

The strain rate for the torsion experiments was 2500-3000/s engineering shear strain rate (1500-1700/s equivalent tensile strain rate). The CG and FG microstructures have very similar shear stress-shear strain curves and display a marked strain rate sensitivity, whereas the flow properties of the IG microstructure are less strongly influenced by strain rate. Shear strains to failure are small (<0.1) suggesting that the specimens failed by adiabatic shear banding. The IG microstructure has the largest shear strain to failure, about 0.07.

Fracture Properties

Initiation Toughness. Table 5 summarizes the results of the initiation fracture toughness tests. Because of the limited number of tests we performed, the standard deviations listed in Table 5 are only rough estimates, particularly the static data.

The static initiation toughness (K_{Ic}) values, obtained at a loading rate of about 2×10^{-1} MPa$\sqrt{m}$/s, range from 54 MPa$\sqrt{m}$ for the FG microstructure to 58 MPa$\sqrt{m}$ for the CG microstructure and 63 MPa$\sqrt{m}$ for the IG microstructure. This ranking is also preserved for the dynamic initiation toughness values (K_{Id}), which range from 58.2 MPa$\sqrt{m}$ to 60.2 MPa$\sqrt{m}$ and 75 MPa$\sqrt{m}$, respectively. The loading rate for the dynamic one-point-bend test ranged from 1×10^{6} to 1.4×10^{6} MPa$\sqrt{m}$/s for impact velocities ranging from 17 to 30 m/s. The data indicate that the loading rate does not strongly influence the initiation fracture toughness of either the CG or the FG microstructure. The IG microstructure shows a stronger rate sensitivity (about 20%) but also a larger scatter of the initiation toughness.

Propagation Toughness. When the static experiments were evaluated using linear elastic fracture mechanics analysis, a modest resistance curve effect was seen for all three materials, as indicated by the data in Table 6. For the CG and IG microstructures, the stress intensity factor remains constant after 2-3 mm of extension and the steady-state value is about 20% higher than the value at initiation.

For the FG microstructure, the stress intensity rises more slowly but continuously with crack extension. Because the amount of crack growth was limited by the specimen size, we could not verify the existence of a constant steady-state value. No shear lips formed in the static fracture specimens.

Table 5

INITIATION FRACTURE TOUGHNESS OF CG, IG, AND FG MICROSTRUCTURES

Microstructure	Static Initiation Toughness K_{Ic} $(MPa\sqrt{m})$	Dynamic Initiation Toughness K_{Id} $(MPa\sqrt{m})$
CG	58 ± 1	60.2 ± 3.8
IG	63 ± 6	75 ± 15
FG	54 ± 5	58.2 ± 5.7

Table 6

MAXIMUM STRESS INTENSITY REACHED IN THE STATIC FRACTURE EXPERIMENTS

Microstructure	K_{Ic} ($MPa\sqrt{m}$)	K_{Imax} ($MPa\sqrt{m}$)	Δa (mm)
CG	59.0	71.0	2.0
IG	68.6	82.6	2.8
FG	54.0	64.0	5.4

The results of the dynamic crack propagation experiments are illustrated in Figure 8. Figure 8a shows crack propagation histories for experiments with one of each of the three microstructures, and Figure 8b shows the corresponding stress intensity factor as a function of crack propagation distance. In the dynamic crack propagation experiments, the crack velocities ranged from about 70 m/s to 350 m/s, depending on the test conditions. The crack velocity also varied during a single experiment, as illustrated in Figure 8a. Figure 9 shows the typical appearance of the fracture surface of dynamically loaded specimens for the three Ti-10V-2Fe-3Al microstructures.

For all three microstructures, we found that the resistance to dynamic crack propagation is significantly larger than the resistance to dynamic crack initiation. For the range of velocities investigated, we were not able to establish a clear dependence of the dynamic propagation toughness on crack velocity. Rather, the propagation toughness appears to increase as a function of crack extension distance, leading to the development of a dynamic resistance curve. Therefore, in Figure 8b, we present the dynamic crack propagation toughness results in terms of the stress intensity at the running crack tip as a function of the crack extension distance, an approach we had already taken (for the same reasons) in the preceding study.[2]

Figure 8b shows that, for the CG microstructure, the stress intensity rises steadily with crack extension until it reaches a value of about 100 $\mathrm{MPa}\sqrt{\mathrm{m}}$ after about 15 mm of extension. This steady-state value is significantly higher than the value reached in the static experiments (see Table 6). Thus we observe that the propagation toughness increases 65% over the initiation toughness for initiation from a fatigue crack. The fracture surfaces of the CG microstructure produced in the dynamic crack propagation experiments have a uniformly rough appearance but do not display shear lips (Figure 9).

For the IG microstructure results shown in Figure 8b, the crack initiated at a fatigue crack at a stress intensity value of 96 $\mathrm{MPa}\sqrt{\mathrm{m}}$ (compared to an average value of 75 $\mathrm{MPa}\sqrt{\mathrm{m}}$ for K_{Id}, an indication of the large scatter in fracture data for the IG microstructure). After a short extension, the stress intensity rapidly rose to a steady-state value of about 120 $\mathrm{MPa}\sqrt{\mathrm{m}}$, which is again significantly higher than the static steady-state value and also 60% larger than the dynamic initiation toughness value. This result was verified in many additional experiments (see below).

The fracture surfaces of dynamically loaded IG specimens have an increasing roughness with increasing crack length and display shear lips several millimeters wide (Figure 9). These fractographic features are consistent with a propagation toughness increasing with crack extension.

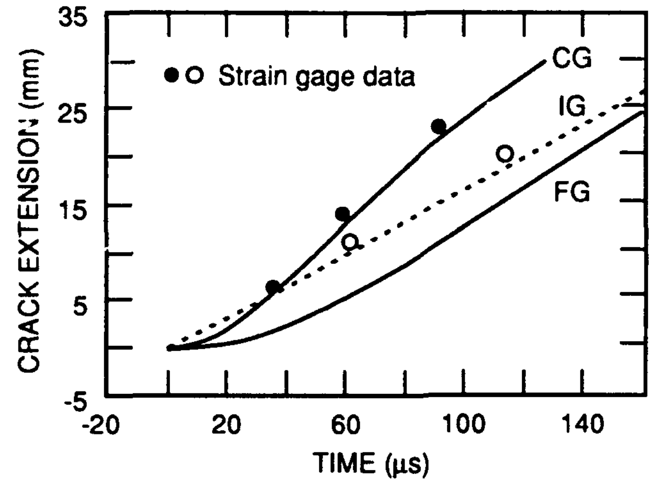

(a) Crack propagation histories.

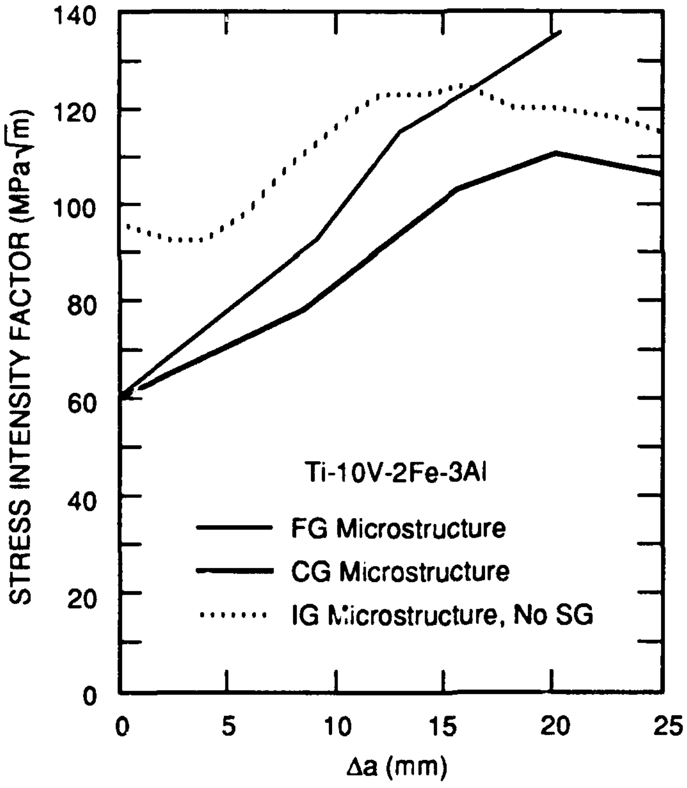

(b) Corresponding stress intensity factor versus crack propagation distance.

RM-7294-49

Figure 8. Selected results of dynamic crack propagation experiments for three Ti-10V-2Fe-3A microstructures with different grain sizes.

SG = side grooves.

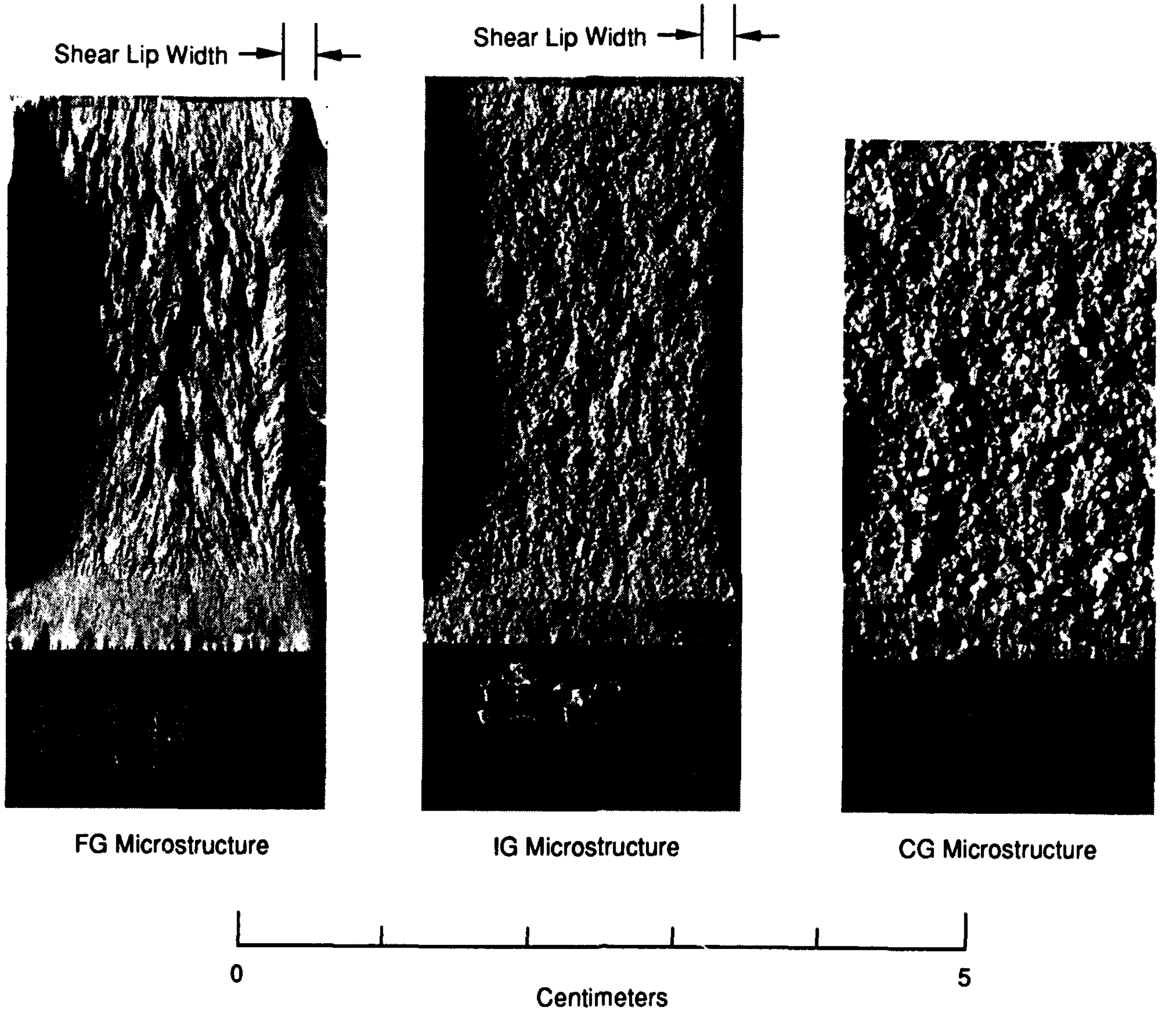

RP-7294-51

Figure 9. Fracture surface appearance of dynamically loaded specimens for the three Ti-10V-2Fe-3Al microstructures.

The stress intensity factor for the FG microstructure increases similarly with crack length, but it does not reach a steady-state value over the range of crack extension observed. For an equivalent amount of crack extension, the dynamic propagation toughness is significantly higher than the static propagation toughness; in other words, the dynamic resistance curve is well above the static resistance curve. The dynamic propagation toughness reaches values more than double the value of the initiation toughness. The roughness of the fracture surface also increases with extension of the crack, and significant shear lips develop at the specimen edges (Figure 9).

Figure 10, which compares the fracture surfaces of three FG microstructure specimens loaded at different rates, demonstrates that the formation of shear lips is a strongly rate-dependent process. One specimen was loaded during the static fracture test (2 x 10^{-4} MPa$\sqrt{m}$/s) and no shear lips formed during the crack growth phase of the experiment. As pointed out earlier, the toughness increased only by a small amount with crack extension during the static experiments. The second specimen was accidentally broken during fatigue precracking (under load-control conditions), so the crack extended significantly faster than during the static fracture experiment. This specimen shows approximately 1-mm-wide shear lips. The third specimen was broken in a one-point-bend crack propagation experiment (loading rate $\approx 10^6$ MPa$\sqrt{m}$/s) and has significantly wider shear lips. We also made similar observations for the IG microstructure. To our knowledge, the dependence of shear lip formation on the loading rate, at least in titanium alloys, as never been reported before and is a significant finding in understanding the interaction between deformation and fracture processes, as we discuss further below.

Effect of Shear Lips. In earlier work,[2, 22, 23] we postulated that the strong rise (above the initiation toughness value) of the dynamic propagation toughness observed in α_p-containing microstructures was due to the formation of significant shear lips during the early stage of crack extension. The experiments with side-grooved specimens of the IG microstructure were designed to verify this interpretation. The presence of side grooves eliminates the formation of shear lips. Therefore, if the shear lips contribute significantly to the dynamic propagation toughness, we should measure a much lower value with the side-grooved specimens.

Figure 11 compares the results of crack propagation experiments with flat and side-grooved (SG) specimens having the IG microstructure. Figure 11a shows the crack propagation histories and indicates that crack velocities ranged from 70 to 300 m/s. In one experiment (marked 3 in Figure 11), the crack arrested after a 13 mm extension. Figure 11b compares the corresponding

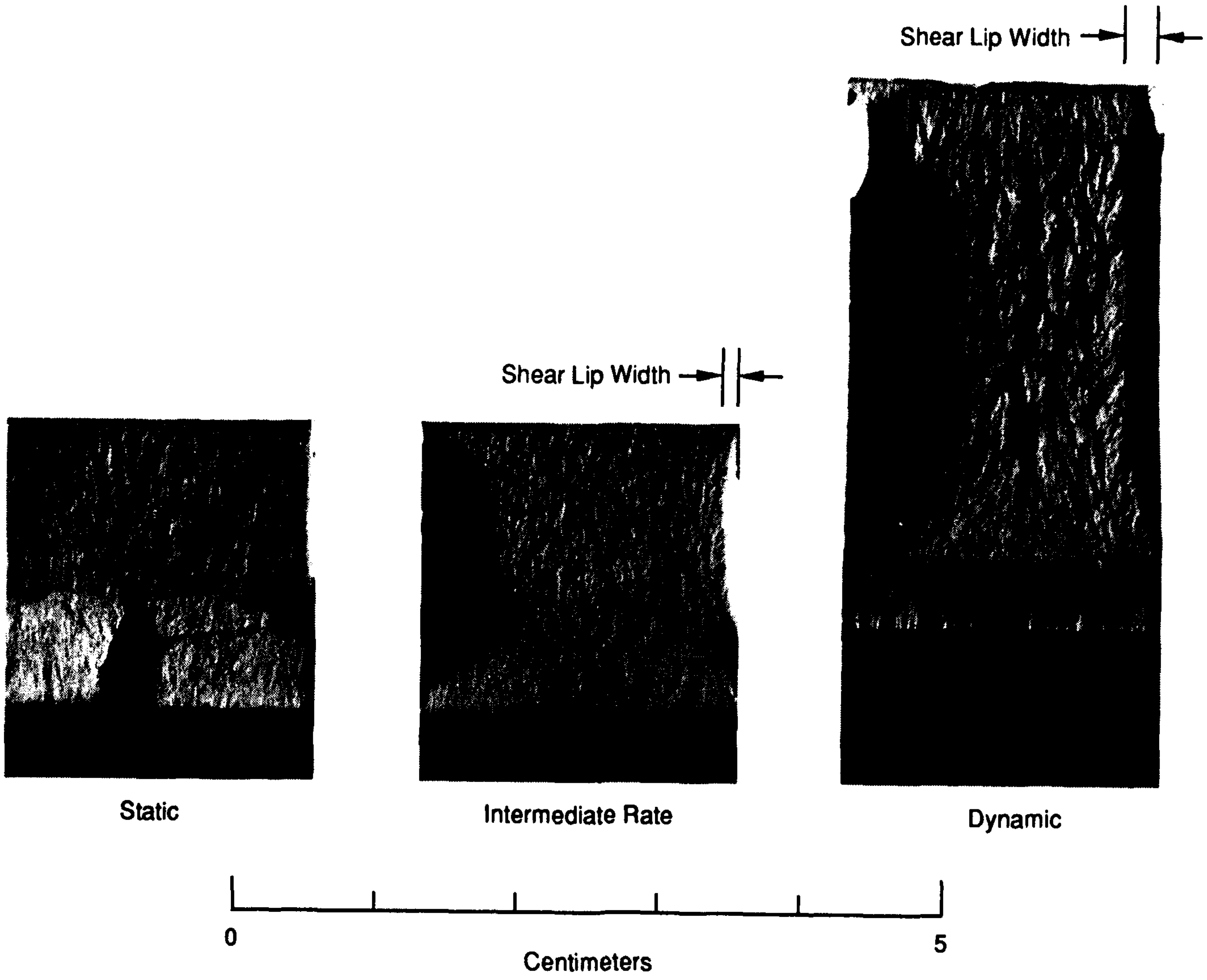

RP-7294-52

Figure 10. Fracture surface appearance of FG microstructure loaded at three different rates.

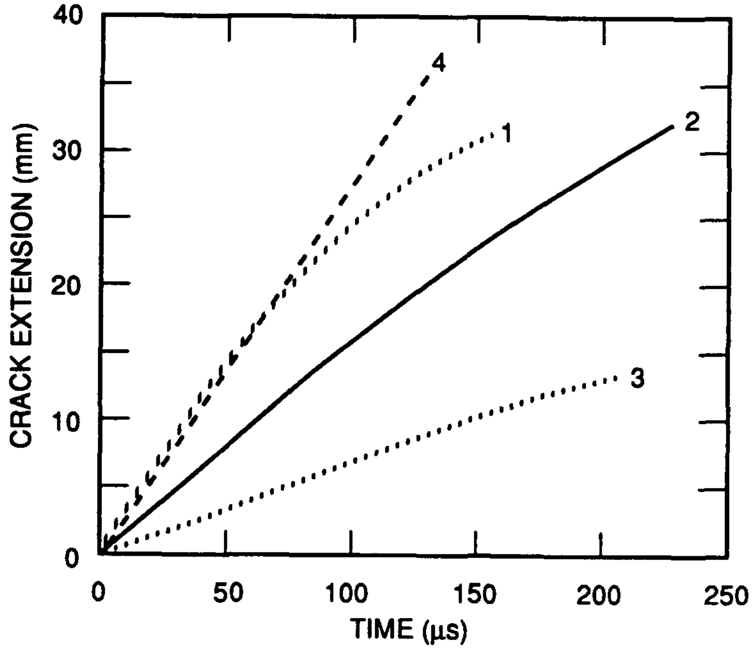

(a) Crack propagation histories

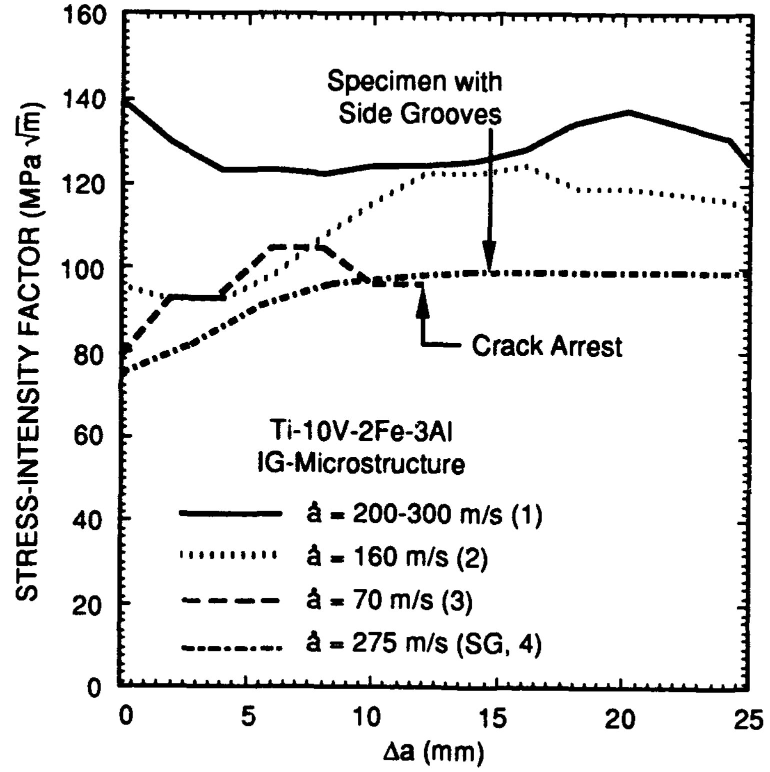

(b) Corresponding stress intensity factor versus crack propagation distance

RM-7294-50A

Figure 11. Results of dynamic crack propagation experiments for IG microstructure.

plots of stress intensity factor as a function of crack propagation distance. As previously discussed, for the flat specimens we observe an adjustment of the stress intensity factor from the value at the onset of crack initiation to the steady-state value of about 120 MPa$\sqrt{m}$. In the experiment labeled (3), although the stress intensity rises after initiation, the steady-state value is never reached, perhaps because the crack arrested or possibly because the crack velocity was substantially lower in this experiment. The striking result illustrated by Figure 11b is that crack propagation in the specimen with side grooves (and hence without shear lips) occurs at stress intensities of about 100 MPa$\sqrt{m}$, substantially higher than the average dynamic initiation toughness[*] and only 20% lower than the steady-state value for the flat specimens, in which shear lips formed.

Therefore, we conclude from the experiments with flat and side-grooved IG specimens that the large value of the stress intensity factor during crack extension, compared to the initiation toughness, reflects mainly the actual resistance of the material to dynamic crack extension and is not due only to structural effects such as the development of shear lips. This conclusion is further supported by the observation that, although no shear lips formed in the CG microstructure, we estimated a substantial rise in the stress intensity factor during extension in this microstructure.

The difference in the steady-state dynamic propagation toughness for the flat and side-grooved specimens (curves 1 and 4 in Figure 11b) indicates that the contribution of the shear lips to the crack propagation resistance of the specimen is smaller than anticipated in our earlier work.[22, 23] The contribution of the shear lips to the increase in propagation toughness above initiation toughness is only about 45%, instead of 100% as assumed originally.

Discussion of Continuum Observations. The continuum measurements reported in this section, as well as those in our previous work on microstructures with different α_p contents,[2, 22, 23] demonstrate that the dynamic propagation toughness is a function of microstructure: the FG microstructure achieves the highest values and the CG microstructure the lowest values. This trend differs from the trend for initiation toughness reported in Table 5, where the FG microstructure has

---

[*] The initiation toughness value for this fatigued pre-cracked specimen is unusually high (109 MPa$\sqrt{m}$), so there is a question whether it was measured correctly in the experiment. The CTOD value measured with FRASTA (23 μm; see Table 7 and text below) suggests that this value is indeed too high and inconsistent with the rest of the data measured for this IG microstructure. Therefore, in performing the finite element simulation to evaluate the propagation toughness, we used the average initation toughness value for this microstructure 75 MPa$\sqrt{m}$, as the value of the stress intensity at crack initiation. Had we used the initiation value determined in the one-point-bend test in the calculations, we would have estimated a steady-state toughness of 110 MPa$\sqrt{m}$.

We believe that the excessively high value of the stress intensity at initiation is due to uncertainties in the static strain gage calibration procedure we used to account for the presence of the shear lips.

the lowest initiation toughness values and the IG microstructure the highest. Therefore, a direct correlation between the dynamic initiation and propagation toughnesses does not seem to exist in this alloy system.

The results of static and dynamic experiments further indicate that the rise in dynamic propagation toughness is also dependent, in still undetermined ways, on the loading rate or the crack velocity. Either micromechanical or loading rate effects may cause the rise in toughness. Our combined continuum observations suggest that the micromechanisms responsible for toughening the three microstructures do not prevent crack initiation as effectively as they do crack extension and that there must be a certain amount of crack extension for them to develop fully. This situation may be analogous to the situation in transformation toughened ceramics or ceramics toughened by microcracking and crack path deflection. Terlinde et al.[10] have previously alluded to this behavior for the static fracture toughness of Ti-10V-2Fe-3Al microstructures. On the other hand, we estimate from strain gage records that the loading rate of the process zone ahead of the crack during propagation is at least one order of magnitude higher than the loading rate for the stationary crack up to initiation in the one-point-bend experiment. Therefore, the increase in toughness during dynamic propagation above the value at initiation may be due to this order-of-magnitude change in loading rate. Similarly, the more significant resistance curve effect observed in the dynamic fracture experiments (compared to the effect in the static experiments) may also be due to differences in loading rate.

In the next section, which reports the results of the fractographic investigation, we present independent evidence for the intrinsic microstructural nature of the high resistance to crack propagation observed in the three microstructures. We also point out rate-dependent microdeformation and microfailure features that help in understanding how loading rate and crack extension can contribute to an elevation in toughness.

Fractographic Observations

Scanning Electron Microscope Observations.

Figures 12 through 14 summarize our scanning electron microscope (SEM) observations of the fracture surfaces for the three microstructures. For each microstructure, we show views at two magnifications of the fracture surface of the static and dynamic specimens. We complemented our SEM observations with observations of polished and etched metallographic cross sections normal to the crack plane and the crack front; these sections revealed the microfailure initiation sites, the collateral damage, and the crack path with respect to microstructural features.

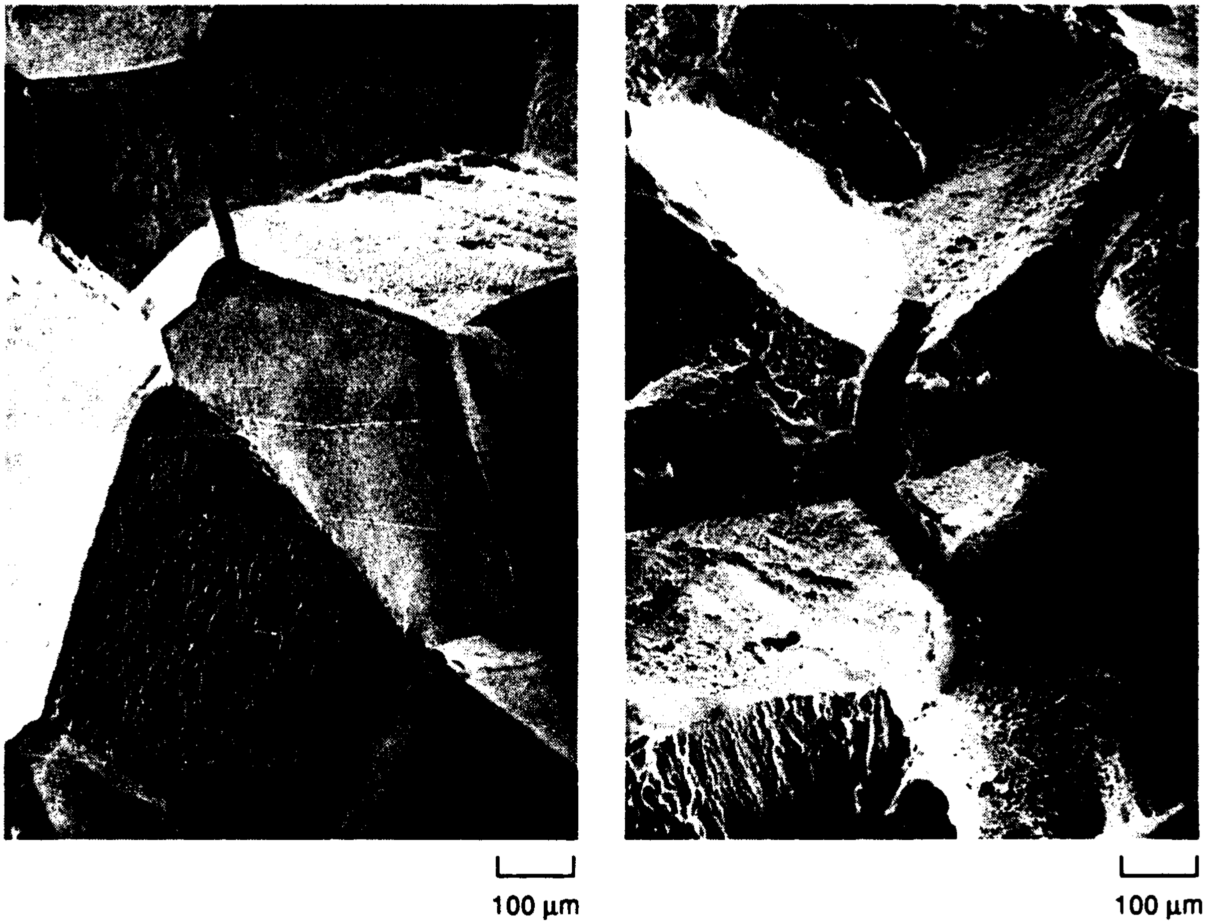

(a) Static

(b) Dynamic

Figure 12. Fracture surface appearance of CG microstructure. (a) and (c), static fracture specimen; (b) and (d), dynamic fracture specimen. (Continued)

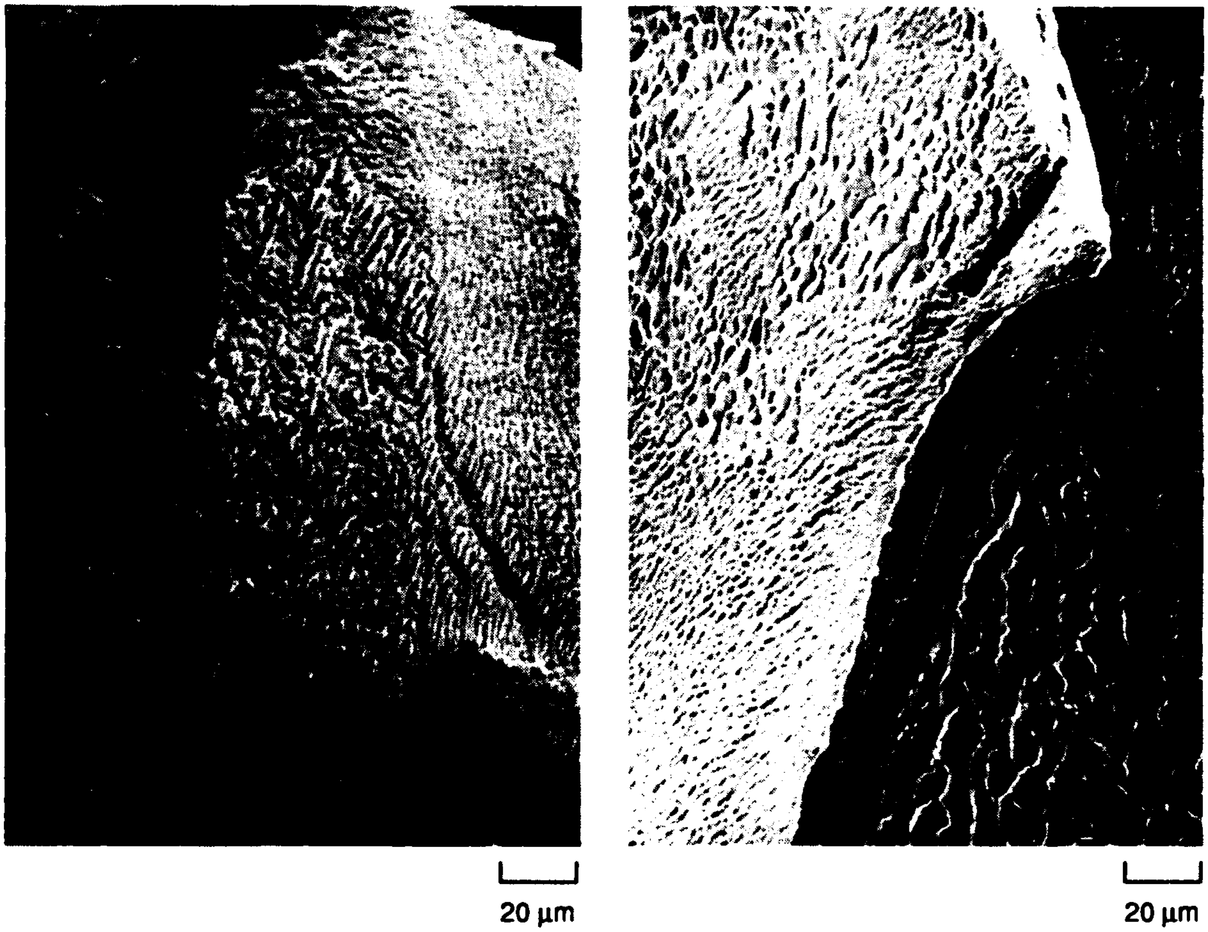

(c) Static

(d) Dynamic

RP-7294-54

Figure 12. Fracture surface appearance of CG microstructure. (a) and (c), static fracture specimen; (b) and (d), dynamic fracture specimen. (Concluded)

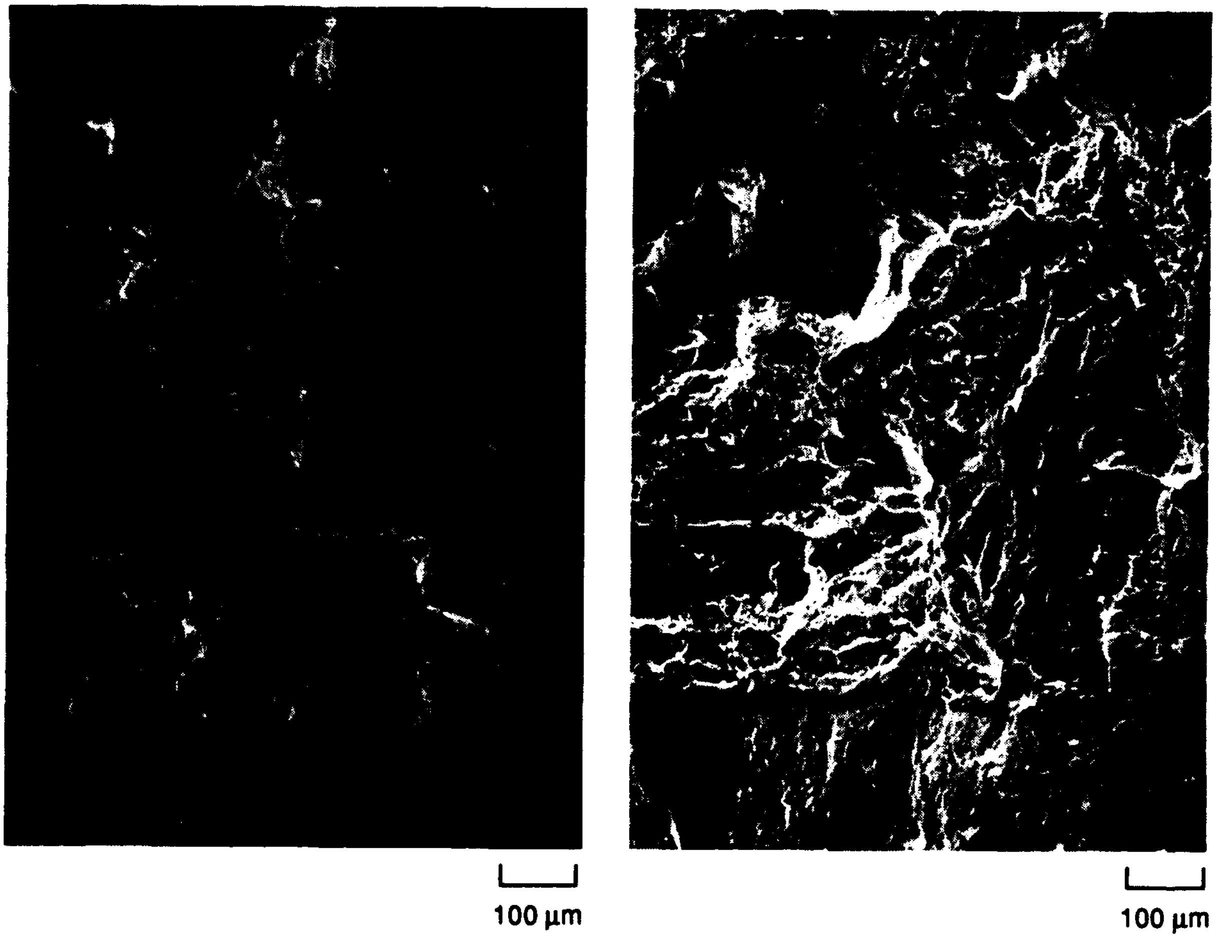

(a) Static

(b) Dynamic

Figure 13. Fracture surface appearance of IG microstructure. (a) and (c), static fracture specimen; (b) and (d), dynamic fracture specimen. (Continued)

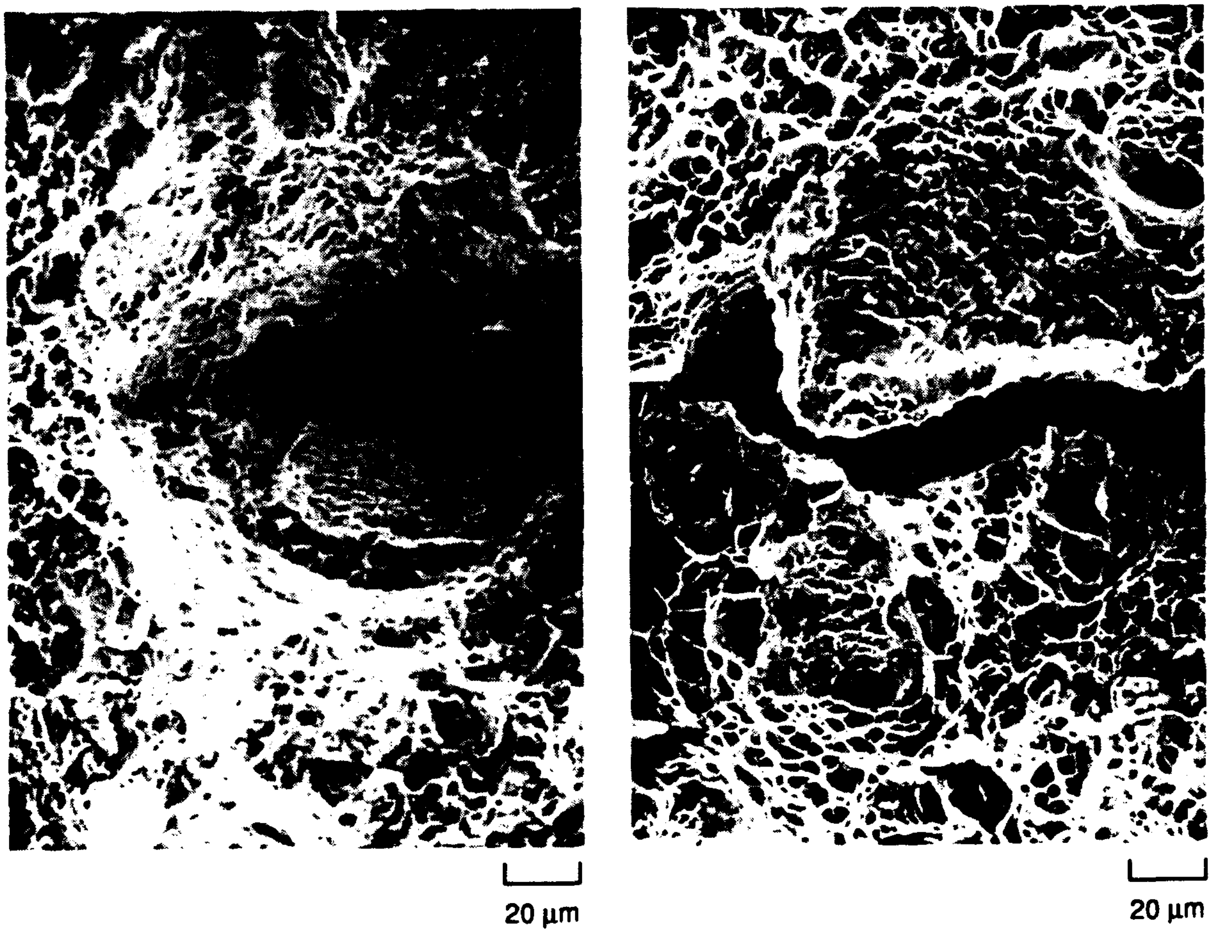

(c) Static

(d) Dynamic

RP-7294-56

Figure 13. Fracture surface appearance of IG microstructure. (a) and (c), static fracture specimen; (b) and (d), dynamic fracture specimen. (Concluded)

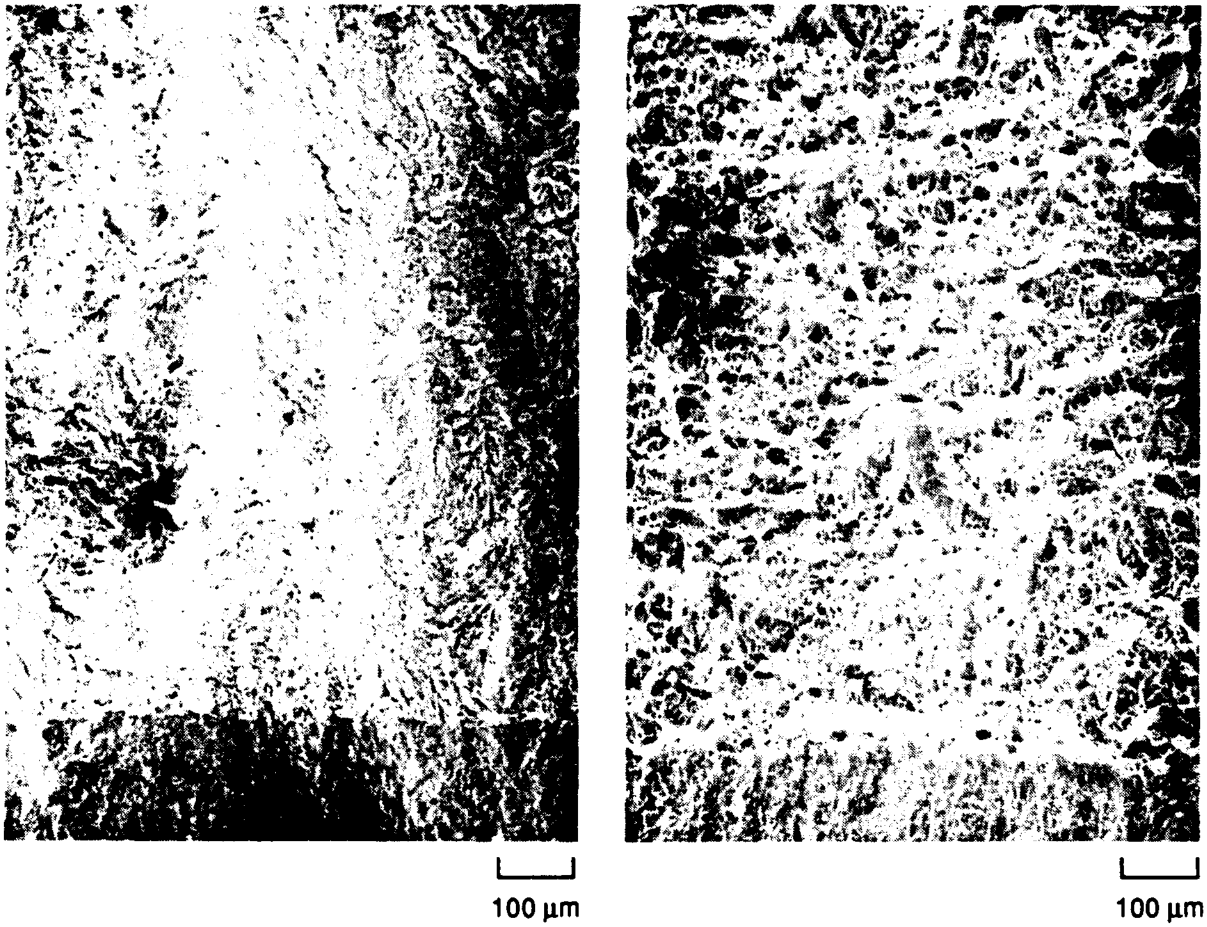

(a) Static **(b)** Dynamic

RP-7294-58

Figure 14. Fracture surface appearance of FG microstructure. (a) and (c), static fracture specimen; (b) and (d), dynamic fracture specimen. (Continued)

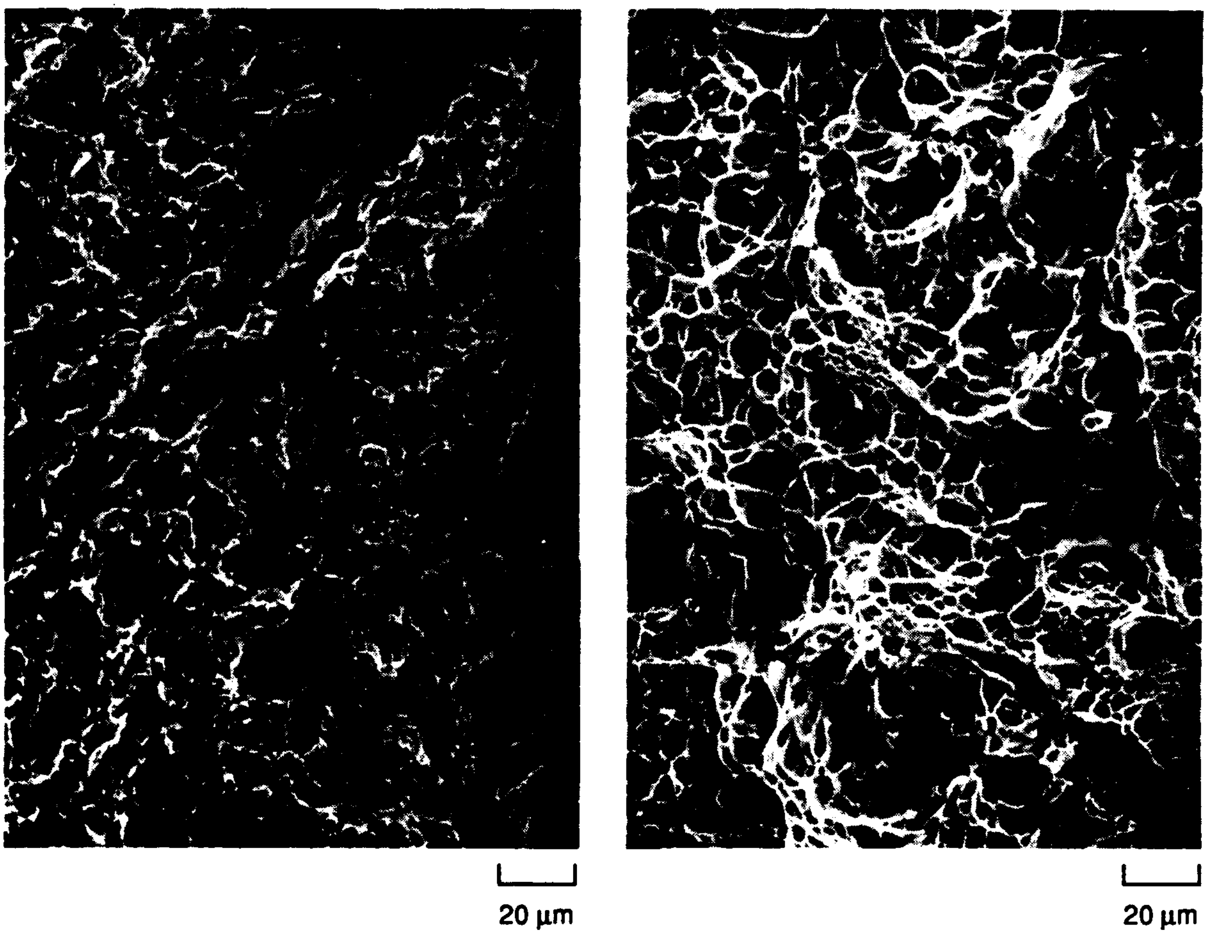

(c) Static

(d) Dynamic

RP-7294-59

Figure 14. Fracture surface appearance of FG microstructure. (a) and (c), static fracture specimen; (b) and (d), dynamic fracture specimen. (Concluded)

All three microstructures present some common features, which we summarize first. Visual inspection of the dynamic fracture surfaces reveals roughness features with a length scale on the order of 1 mm. These features are particularly visible in the FG microstructure (see Figure 9) and tend to be aligned parallel to the crack propagation direction. They reflect the increase in dynamic propagation toughness with crack extension and the enlargement of the fracture process zone. Observation at higher magnification (Figures 12a and b, 13a and b, and 14a and b) reveals a second characteristic roughness scale associated with the grain size of the microstructures, as evidenced by grain facets (Figure 12) or transgranular fracture surfaces (Figure 13). In the FG microstructure, the grain size and the α_p particle spacing are similar, so both affect the fracture surface roughness, over a characteristic length of several tens of micrometers.

At yet a finer size scale, fracture invariably occurs by nucleation and growth of microvoids that nucleate either in the continuous grain boundary α film or at α_p particles within the grains (Figures 12c and d, 13c and d, and 14c and d). Microvoids nucleated in grain boundary α films result in much shallower dimples than voids nucleated at α_p particles.

In all three microstructures, we observe microcracks more or less normal to the main fracture plane. The length of the intersection of these microcracks with the main crack plane is of the same order as the grain size. Finally, localized shear deformation within grains or grain boundaries is evident. This localized deformation appears to play a key role in the formation and opening of transverse cracks.

The increase in loading rate from the static value of 2×10^{-4} MPa$\sqrt{m}$/s to 1.4×10^{6} MPa$\sqrt{m}$/s induces a striking increase in the local ductility of the three microstructures. In Figures 12 through 14, this increase is evidenced by (1) a coarser network of microvoids (compare, for instance, Figures 13c and d and 14c and d), (2) the appearance of larger smooth regions resulting from plastic slip and local stretching (compare Figures 13a and b and 14a and b), and (3) wider opening of the microcracks normal to the main fracture plane (compare Figures 12a and b). The larger size of the dimple network on the fracture surface suggests larger growth of fewer of the voids before coalescence. A patch of several coalesced voids forms a larger cavity, which in turn continues to grow by plastic flow and coalescence with smaller adjacent voids. This mechanism, which may also be observed in statically loaded specimens, is enhanced in the case of dynamic loading and apparently leads to the formation of the larger, smoother regions on the fracture surface. We believe that this rate-dependent enhanced ductility may be associated with deformation-induced adiabatic heating effects and that these two processes are at least in part associated with the increase in the dynamic propagation toughness above the dynamic initiation toughness.

The CG microstructure fails in a predominantly intergranular mode by the nucleation, growth, and coalescence of voids in the grain boundary α phase. The shallow void network resulting from this failure mechanism is illustrated in Figures 12c and d. As a consequence of intergranular fracture, the crack path zigzags strongly, with excursions of several hundreds of micrometers away from the average crack plane. From place to place the fracture path deviates from the grain boundary and proceeds transgranularly, leaving a network of voids that are nucleated at α_p particles within the grain. The intersection of main crack and secondary cracks can result in a very complex local crack path around and through grains, so interference of separated grains and interlocking of those grains may occur as the main crack opens up. These processes can in turn contribute to propagation toughness elevation by reducing the effective stress intensity at the crack tip. A rate-induced increase in the local ductility allows the transverse crack to open up or blunt more. This larger opening must be accommodated by deformations in neighboring grains or grain boundaries, and these deformations result in the spread of the process zone, possibly over several grains.

The IG microstructure fails predominantly in a transgranular mode, except in isolated locations where the crack follows the boundary of a grain. Microvoids invariably nucleate at α_p particles, either within the grains or at the grain boundary. In our previous work, we reported the tendency for shear localization. Figures 13a and b show the appearance of smooth regions on the fracture surface of the IG microstructure. The smooth regions are much larger in the dynamically loaded specimen than in that of the statically loaded specimen. Matching of the two fracture surfaces demonstrates that these regions correspond to tubular cavities. Figure 13c and d demonstrate the larger dimples on the fracture surface that result from an increase in loading rate.

The observations made for the IG microstructure also hold true for the FG microstructure, as demonstrated in Figure 14. Note, however, that in the FG microstructure, the α_p particles are located between the fine β-grains and are of a size comparable to the grain size, so it is difficult to assess whether fracture is inter- or transgranular. The smooth regions and the dimples are larger in the fracture surfaces of dynamically loaded specimens. The dimples of the FG microstructure are comparable to those of the IG microstructure but the smooth regions are significantly smaller, suggesting some relationship between the size of these smooth regions and the grain size. The microcracks normal to the fracture surface are also significantly smaller in size and number than for the IG microstructure.

FRASTA Results. Four specimens were examined by FRASTA using a scanning laser microscope. We analyzed the crack initiation region of one flat-sided specimen for each of the microstructures, and we report the results of these analyses in detail. In addition, we analyzed the crack initiation region for one side-grooved specimen of the IG microstructure to validate independently the dynamic propagation toughness results.

Figure 15 shows SEM photographs of the conjugate fracture surfaces of the CG microstructure specimen analyzed with FRASTA. The fatigue crack front is represented by the vertical line at the center of the photographs, and the dynamic crack propagation is to the left of the fatigue crack front. Because of the large size of the grains in this microstructure, we analyzed only what appears to be transgranular extension (as opposed to the more common intergranular extension in this microstructure) of the crack across one single grain. Figure 15 shows how the fatigue crack extended through almost an entire grain (at the right side of the photographs), leaving only a narrow band of fatigue-damaged but not completely failed material in the grain (60-80 μm, at center of photographs). During dynamic loading, this narrow band fractured first and then the crack extended into a new grain. Note in Figure 15 the large inclined bands of smooth stretched material in the failed grain at the left of the photographs. These regions correspond to tubular cavities, several hundred micrometers long, developing between unbroken ligaments.

Figure 16 portrays the dynamic crack initiation and extension into one grain from the end of the fatigue crack in another grain. Figures 16a and b represent fracture of the narrow vertical band in Figure 15. In Figures 16c through e, we observe the nucleation, growth, and coalescence of the tubular cavities that appeared as smooth regions in Figure 15. The final link-up of the cavities occurs by the growth of a row of smaller spherical voids.

Figure 17 shows XSPs along the horizontal dashed line in Figure 16 and reveals the crack path and profile during the dynamic fracture event. At the end of the fatigue crack growth (which almost corresponds to the end of a grain), the crack path abruptly changes direction as it extends into a new grain. As the crack propagates downward and across the grain, it maintains a small, more or less constant, crack opening angle (Figures 17c through e). Cavities open up ahead of the main crack, as also indicated in Figures 16c through e. At the end of the propagation through the grain (Figure 17f), there is a significant blunting of the crack tip, initiation of a crack ahead of the blunted tip, and vertical shearing of the ligament between the main crack and the newly reinitiated crack. This sequence of events is associated with the extension of the crack from one grain to another grain or to a grain boundary. The presence of a (vertical) grain boundary with a soft film of α phase stops the advance of the crack and thus locally increases the toughness. As revealed in

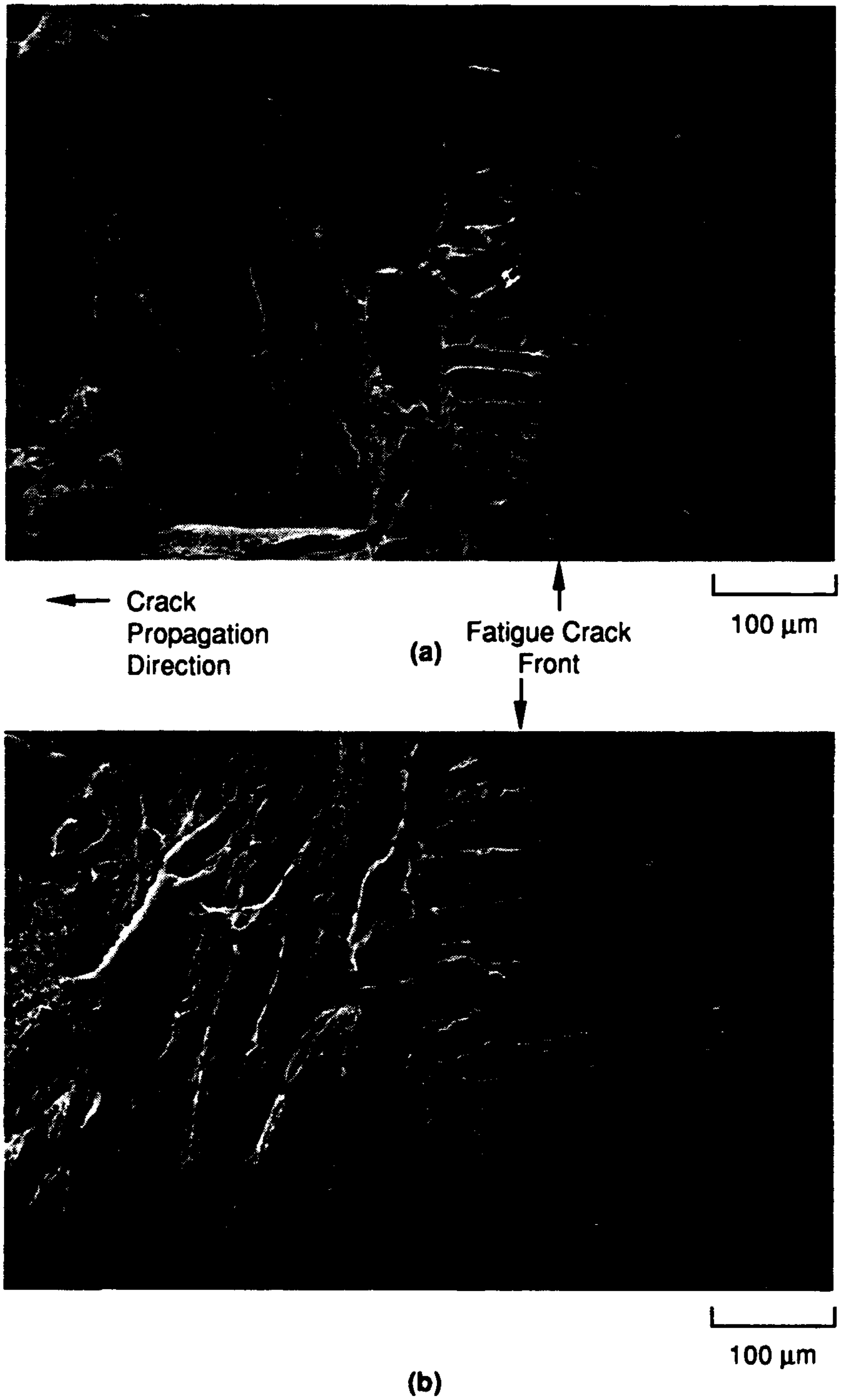

RP-7294-57

Figure 15. Conjugate fracture surfaces of dynamically loaded CG microstructure used in FRASTA.

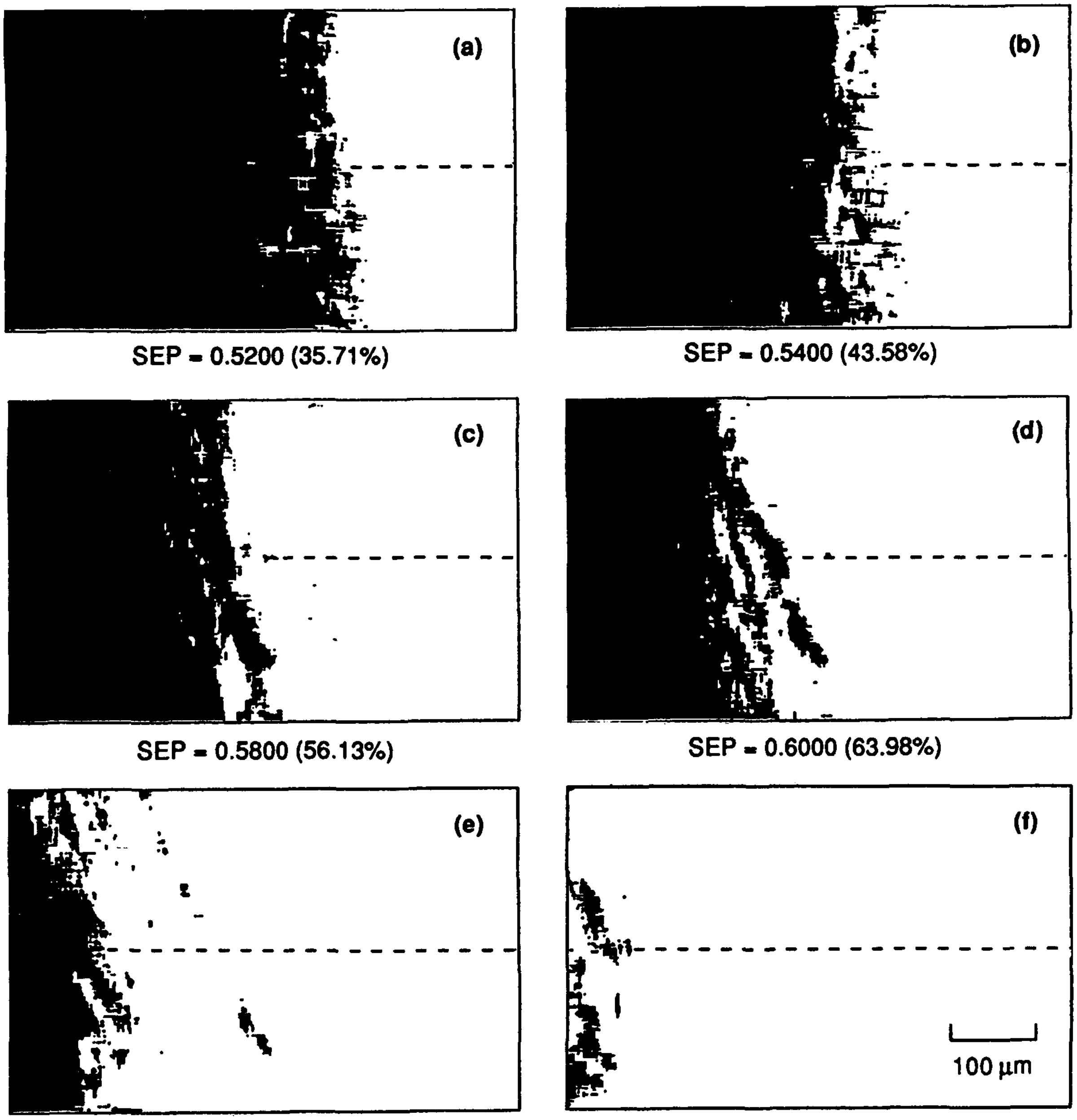

SEP = 0.5200 (35.71%)

SEP = 0.5400 (43.58%)

SEP = 0.5800 (56.13%)

SEP = 0.6000 (63.98%)

SEP = 0.6400 (84.46%)

SEP = 0.7100 (97.78%)

RA-7294-62

Figure 16. FAPPs of dynamic crack propagation in CG microstructure used in FRASTA. (a) through (f) correspond to profiles (a) through (f) in Figure 17. SEP = separation.

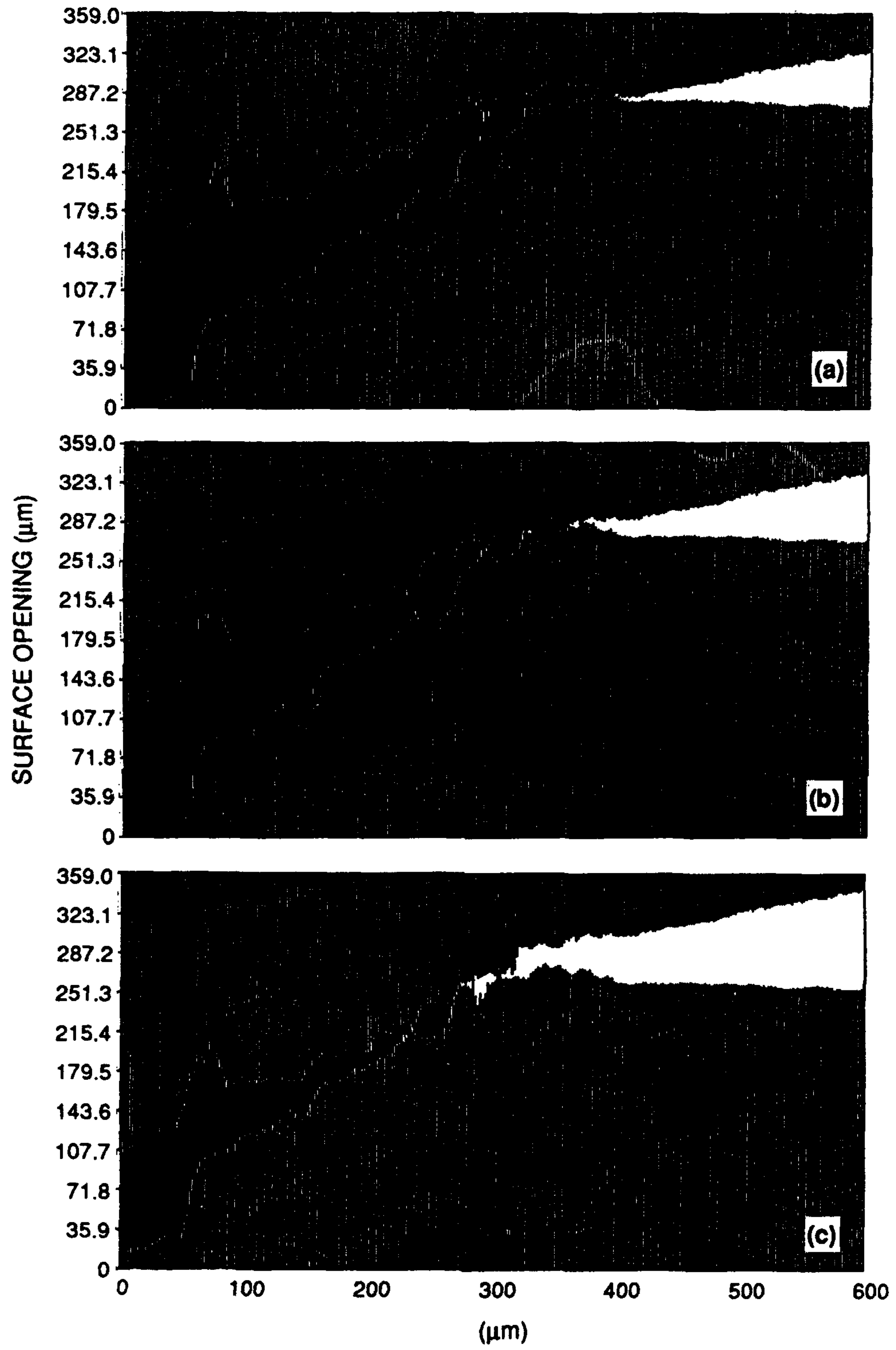

RA-7294-60

Figure 17. XSPs showing crack opening profiles during dynamic crack initiation an
propagation in CG microstructure. (Continued)

(a) end of fatigue, (b) propagation of crack across remaining portion of grain facet, (c) through (e) low resistance crack propagation across new grain, (f) blunting and high resistance crack propagation through a locally tough region.

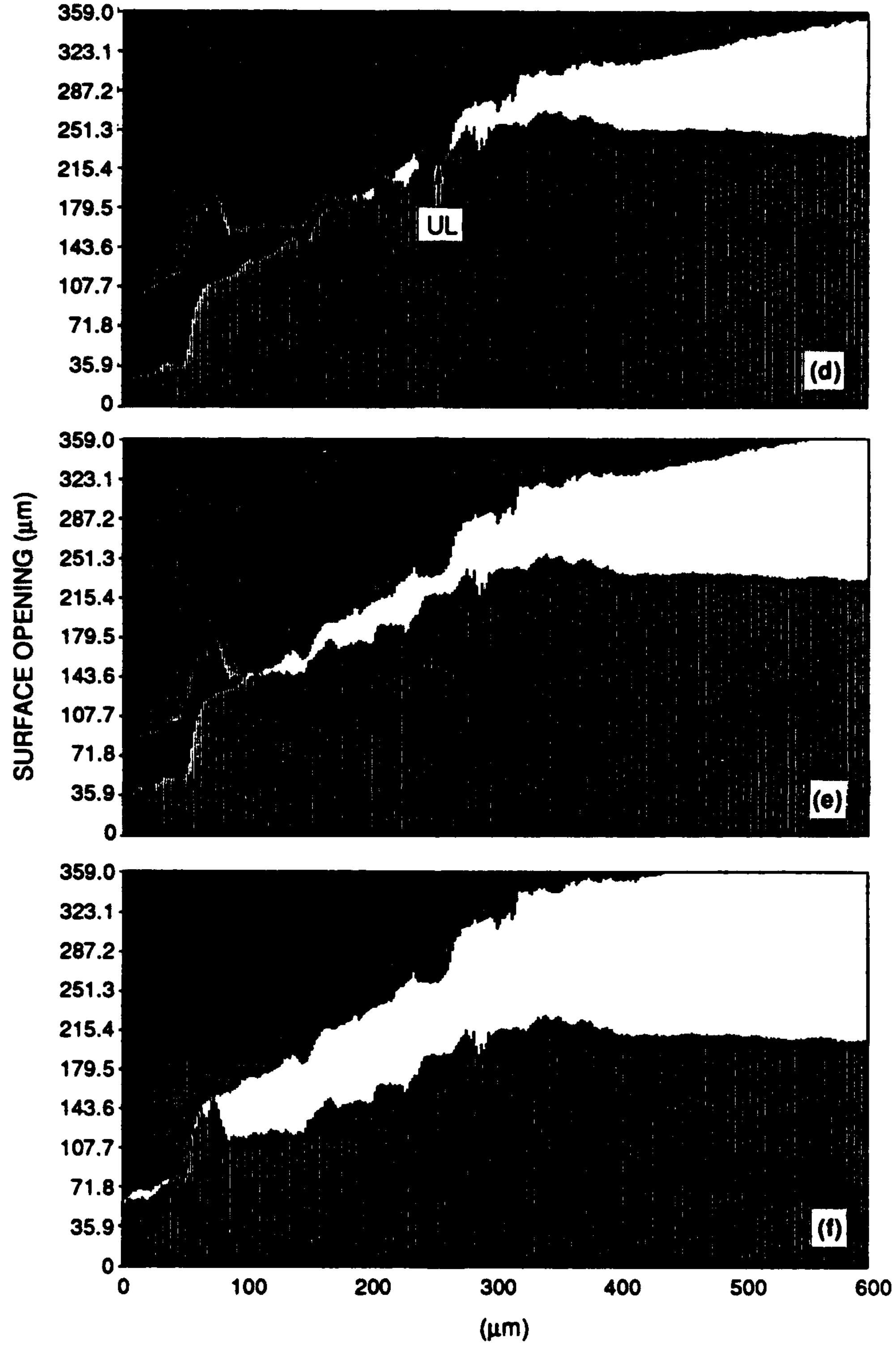

RA-7294-61

Figure 17. XSPs showing crack opening profiles during dynamic crack initiation and propagation in CG microstructure. (Concluded)

(a) end of fatigue, (b) propagation of crack across remaining portion of grain facet, (c) through (e) low resistance crack propagation across new grain, (f) blunting and high resistance crack propagation through a locally tough region.

(UL = unbroken ligament. See Figure 16 for location of cross section.)

Figure 15, the grain boundary appears to have fractured, forming a crack normal to the main crack plane and locally blunting the crack front. In addition, the change in crack path associated with extension into a new grain or grain boundary also contributes to the local increase in toughness. Thus, FRASTA reveals the micromechanisms of crack extension contributing to the increase in dynamic propagation toughness inferred from the continuum measurements. In the CG microstructure, the process zone clearly extends at least over one grain and must be on the order of 1 mm in size.

Figure 18 shows SEM photographs of the conjugate fracture surfaces of the dynamically loaded IG microstructure (specimen without side-grooves) that was examined using FRASTA. Figure 19 portrays the dynamic crack extension through the IG microstructure. Microfailure initiation and growth are very nonuniform along and ahead of the fatigue crack front (Figures 19b and c) and result in a very tortuous dynamic crack front with many trailing unbroken ligaments (Figure 19d). The regions of failed material ahead of the main crack front are smaller than the grain size, suggesting that microdamage nucleates within grains or grain boundaries and requires substantial additional deformation to extend across a whole grain or grain boundary. In Figures 19e and f, we observe a straightening of the crack front, apparently associated with crack extension through a locally tough region. This point is illustrated in Figure 20, which presents the crack opening profile (along the dashed line in Figure 19) during dynamic crack initiation and propagation. Figure 20a shows the blunted crack tip profile just before dynamic crack initiation. Figures 20b through d show a phase of dynamic crack extension during which the advancing crack maintains a sharp tip while some unbroken ligaments trail the main crack front (Figure 20c). In Figure 20d, the crack has reached a locally tough region and blunts significantly before reinitiating and extending ahead of an unbroken ligament (Figures 20e and f). Figure 20 further reveals vertical deviations of the crack path on the order of 100 μm over distances of several hundred micrometers. These lengths are consistent with the grain size of this microstructure and suggest that the deviations in the crack path are associated with crack tip interaction with grains.
The FAPPs of Figure 19 also indicate that the process zone of the IG microstructure is on the order of several hundred micrometers in size. Similar observations were made for the side-grooved specimen.

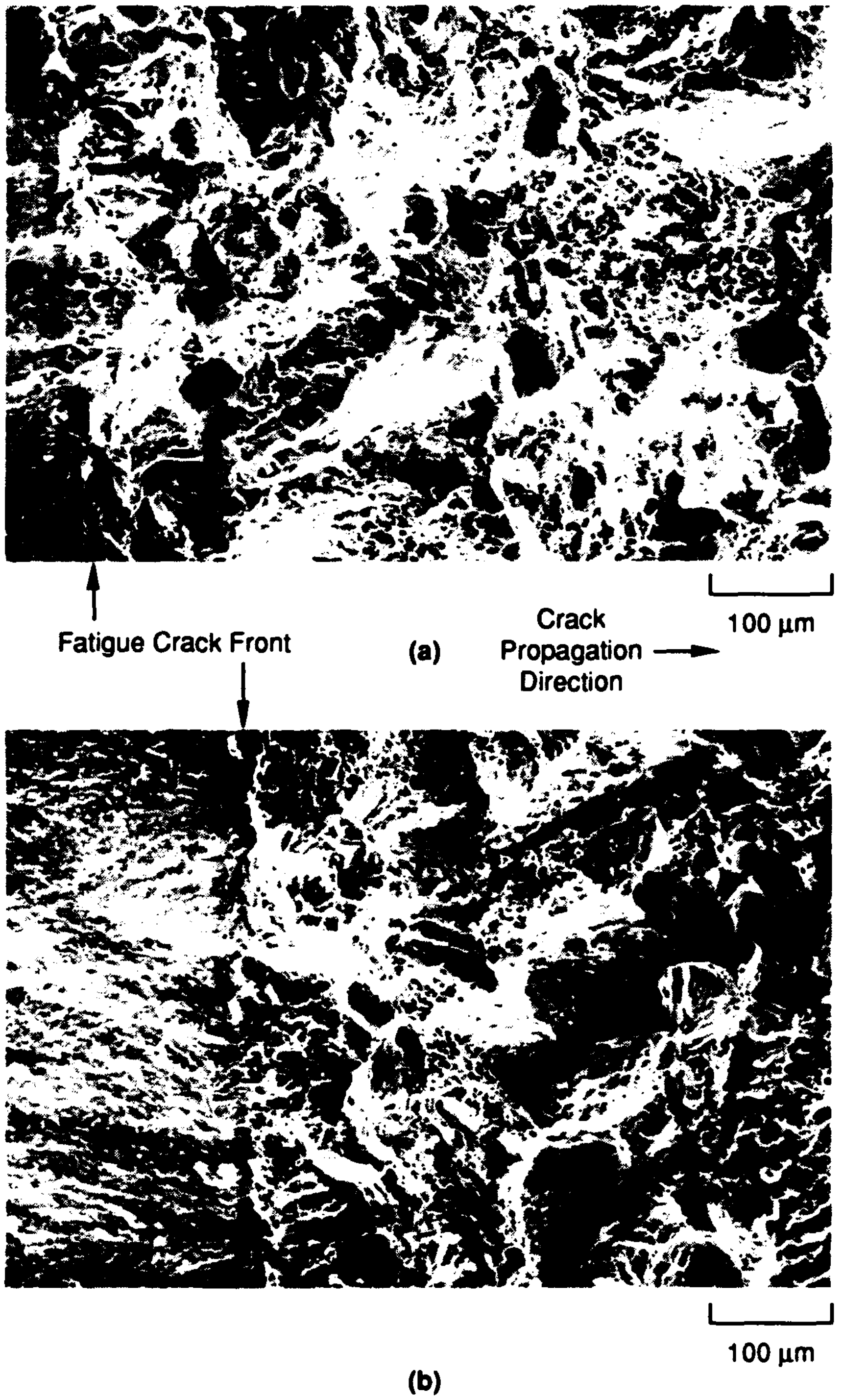

RP-7294-63

Figure 18. Conjugate fracture surfaces of dynamically loaded IG microstructure used in FRASTA.

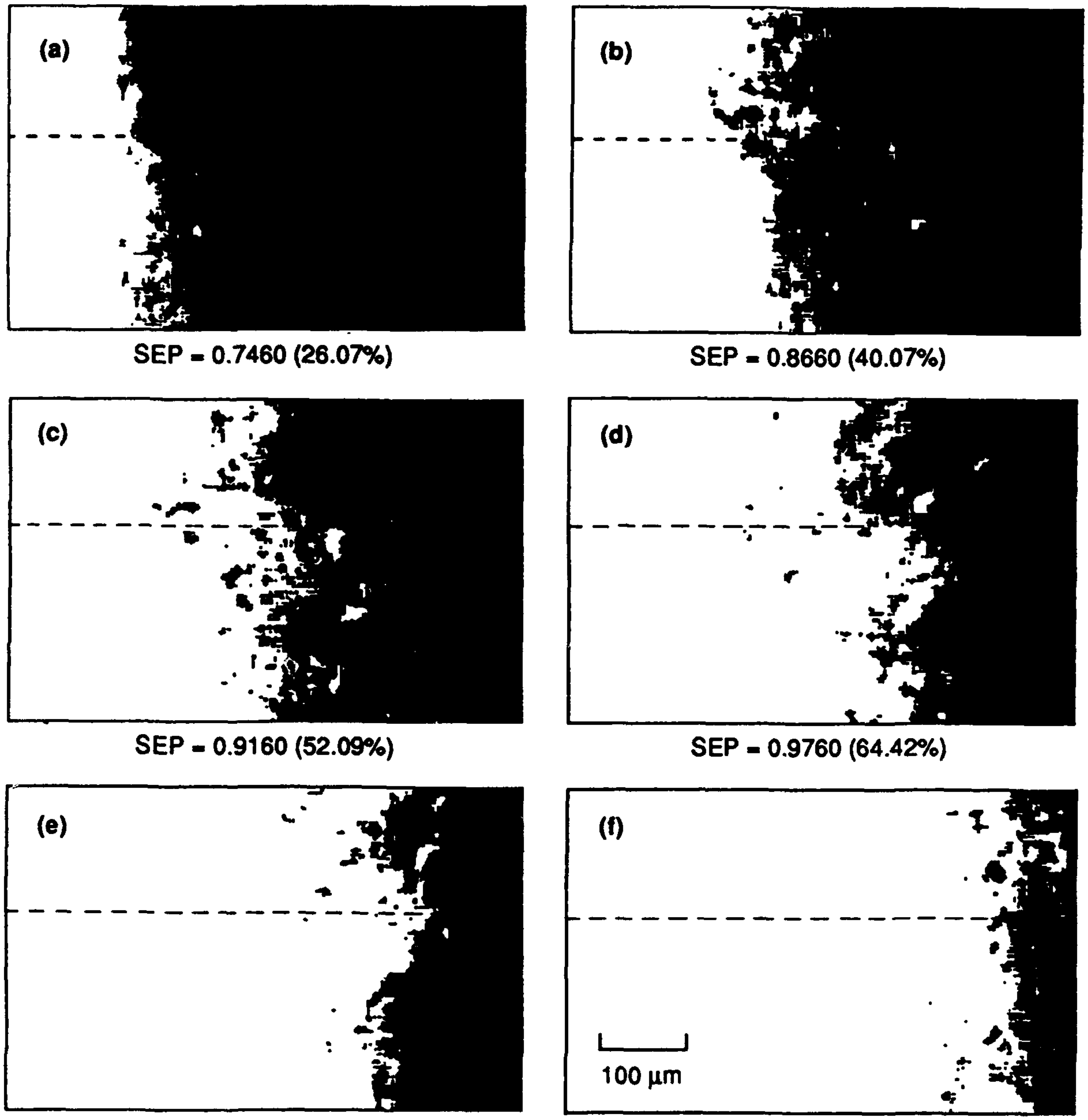

SEP = 0.7460 (26.07%)

SEP = 0.8660 (40.07%)

SEP = 0.9160 (52.09%)

SEP = 0.9760 (64.42%)

SEP = 1.0460 (75.24%)

SEP = 1.1460 (88.43%)

RM-7294-66

Figure 19. FAPPS of dynamic crack propagation in IG microstructure.

(a), (b), (d), and (e) correspond to profiles (a) through (d) in Figure 20. SEP = separation.

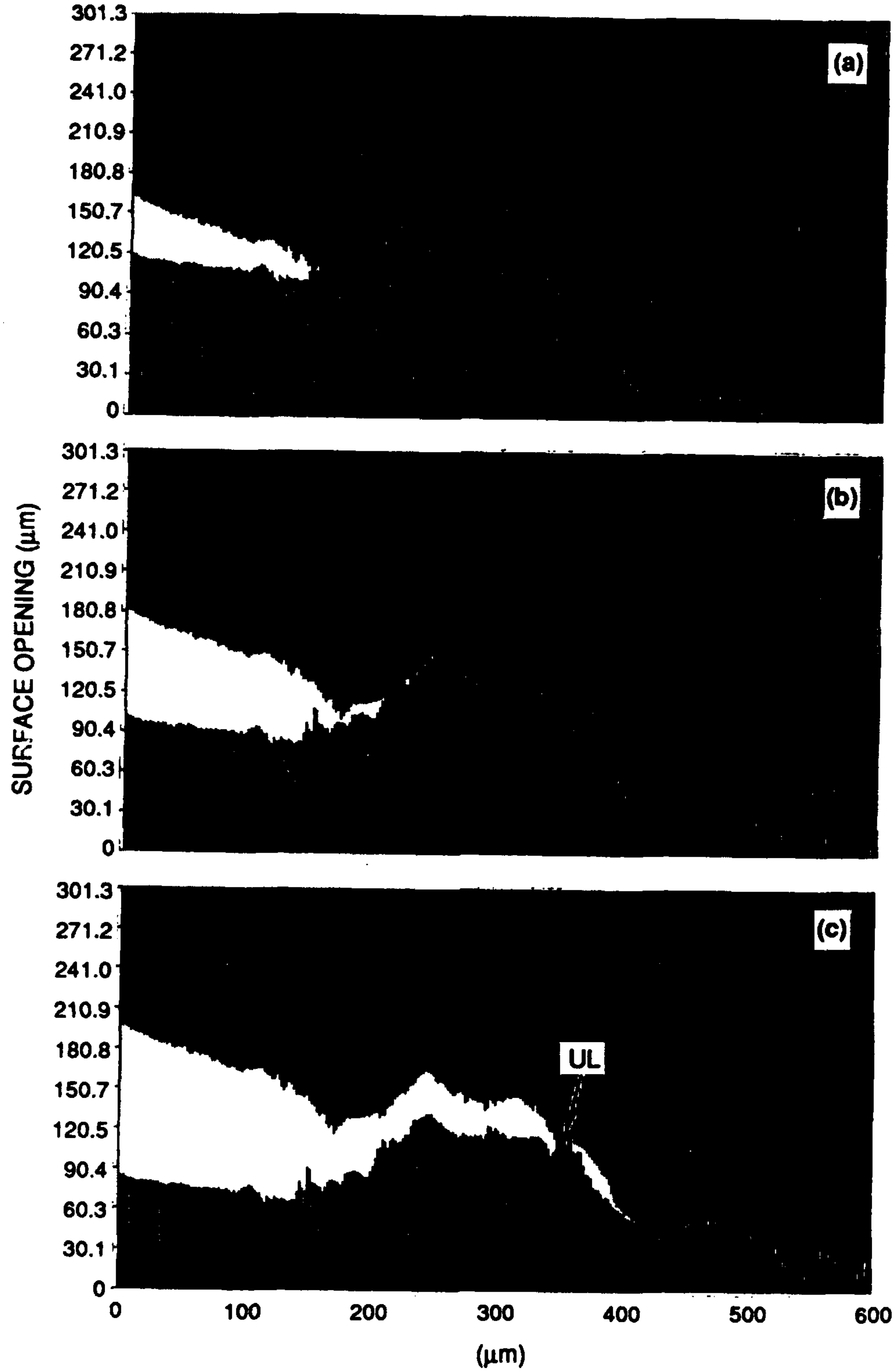

RA-7294-64

Figure 20. XSPs showing crack opening profile during dynamic crack initiation and propagation in IG microstructure (specimen without side grooves). (Continued)

(a) blunted fatigue crack just before initiation, (b) through (d) low resistance crack propagation, (e) and (f), blunting and high resistance crack propagation through a locally tough region.

(UL = unbroken ligament. See Figure 19 for location of cross section.)

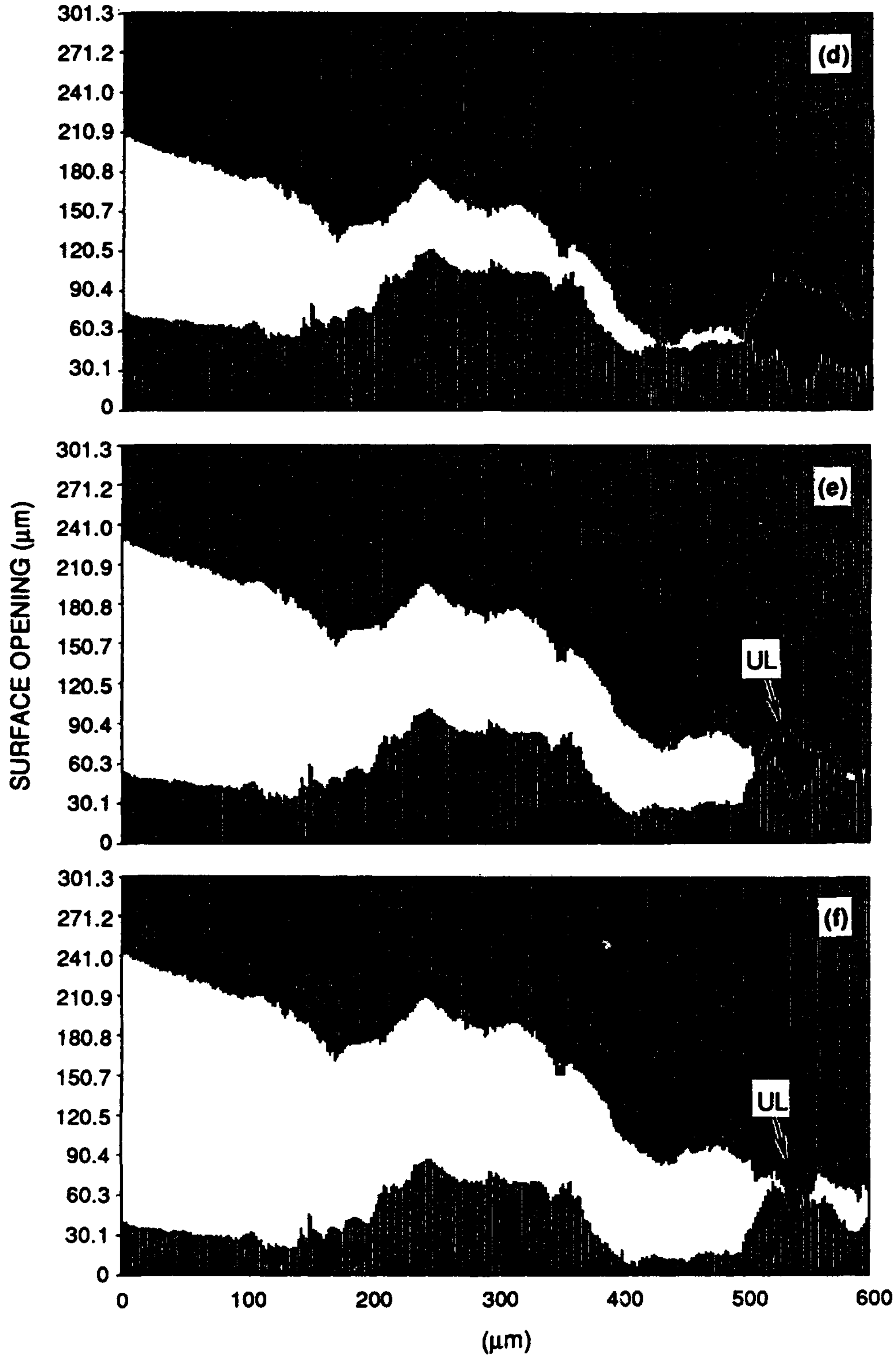

RA-7294-65

Figure 20. XSPs showing crack opening profile during dynamic crack initiation and propagation in IG microstructure (specimen without side grooves). (Concluded)

a) blunted fatigue crack just before initiation, (b) through (d) low resistance crack propagation, (e) and (f), blunting and high resistance crack propagation through a locally tough region.

(UL = unbroken ligament. See Figure 19 for location of cross section.)

Figure 21 shows the conjugate fracture surfaces of the dynamically loaded FG microstructure used for FRASTA examination. Figure 22 portrays the dynamic crack extension through the FG microstructure. Crack extension proceeds by the nucleation and growth of microvoids in regions ahead of the main crack front; the microvoids eventually link up with the crack front to advance the crack. The failed regions have an elongated shape, with the long axis oriented parallel to the main crack front. The size of a failed region is on the order of many tens of micrometers, and these regions correspond to the larger, smoother regions seen in the SEM photographs of the fracture surface (see Figure 21). These smooth regions form by growth and coalescence of many smaller voids and then continue to grow as larger voids.

Figure 23 presents the crack opening profile (along the dashed line in Figure 21) during dynamic crack initiation and propagation in the FG microstructure. Figure 23b shows the blunted fatigue crack tip just before the onset of crack growth. During crack extension, the crack profile varies substantially from location to location. In Figure 23c, the crack opening angle is very large (36 degrees) and the crack tip is blunted, suggesting a temporary arrest when the crack front engulfs one of the regions that have failed ahead of the main front. Once the tougher material ahead of these regions fails, the crack propagates with a smaller crack opening angle (17°) and a sharp tip (Figures 23d and e) until it again encounters a tougher region (Figure 23f). The interactions between the main crack front and damaged or tougher regions ahead of it provide a mechanism for elevating the dynamic propagation toughness. To be operable, this mechanism requires the crack to propagate and thus would not effect the initiation toughness. The FAPPs of Figure 22 suggest that the process zone size is about 50 μm, near the fatigue crack tip.

Table 7 summarizes quantitatively the FRASTA results on crack initiation in the three different microstructures. Table 7 lists the CTOD at crack initiation, the corresponding value of the toughness calculated using Equation (1) (and the dynamic flow stress), and the dynamic initiation toughness measured in the particular experiment. The CTOD is measured in the XSPs of Figures 17, 20, and 23 and is defined as the crack face separation 50 μm behind the fatigue crack tip at the point of first tearing of the crack tip material. We need to view the CTOD values with some care since they reflect the crack opening only at one location along the crack front. Nevertheless, the K_{Id} values calculated with Equation (1) are in good agreement with the values measured directly in the experiments. Table 7 also indicates that the presence of side grooves appears to reduce the crack opening displacement (COD) at initiation (32 μm without side grooves, 23 μm with side grooves), with a corresponding reduction in the stress intensity factor value of about 16%. In view of this latter result, we believe that the high initiation toughness value recorded in the

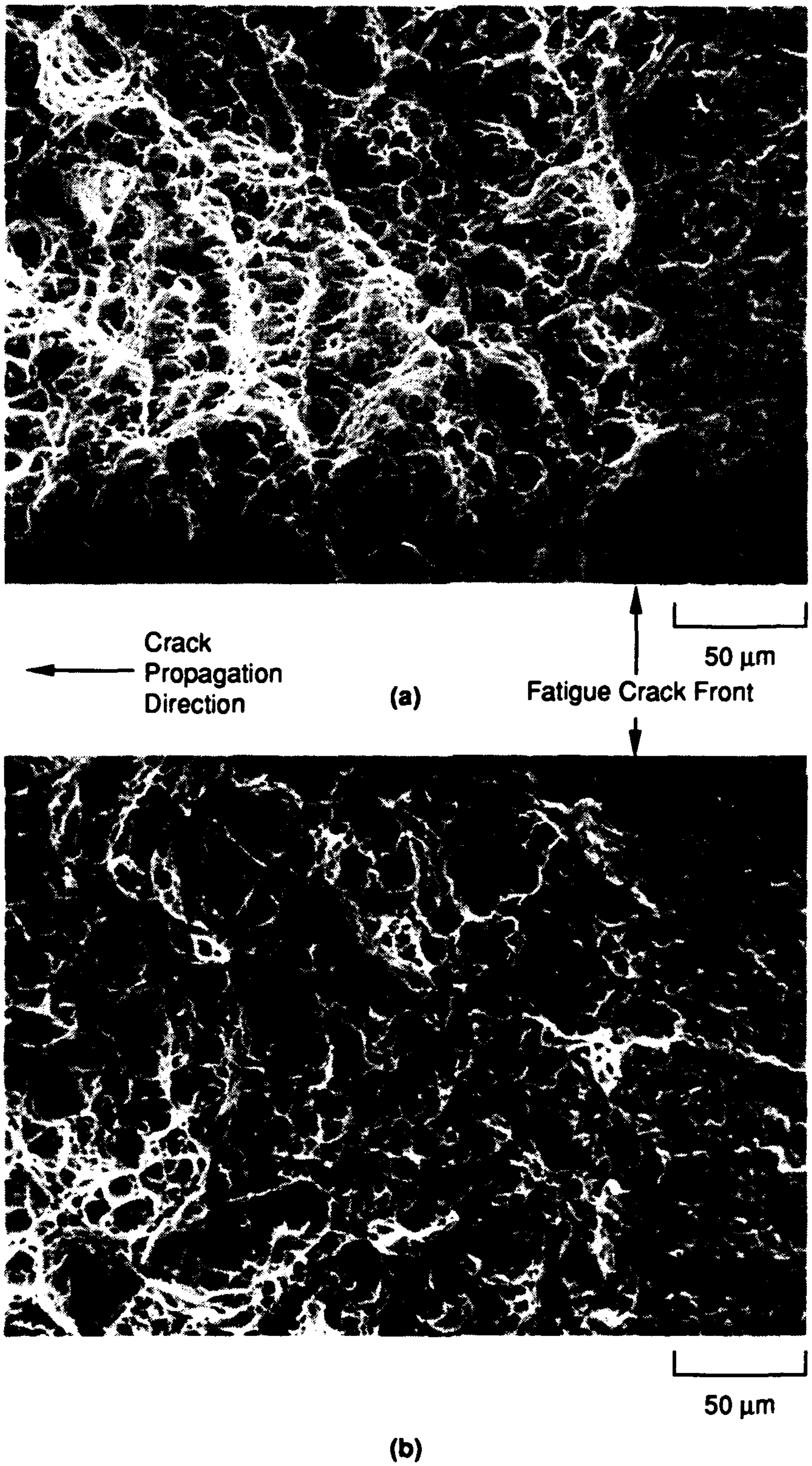

RP-7294-100

Figure 21. Conjugate fracture surfaces of dynamically loaded FG microstructure used in FRASTA.

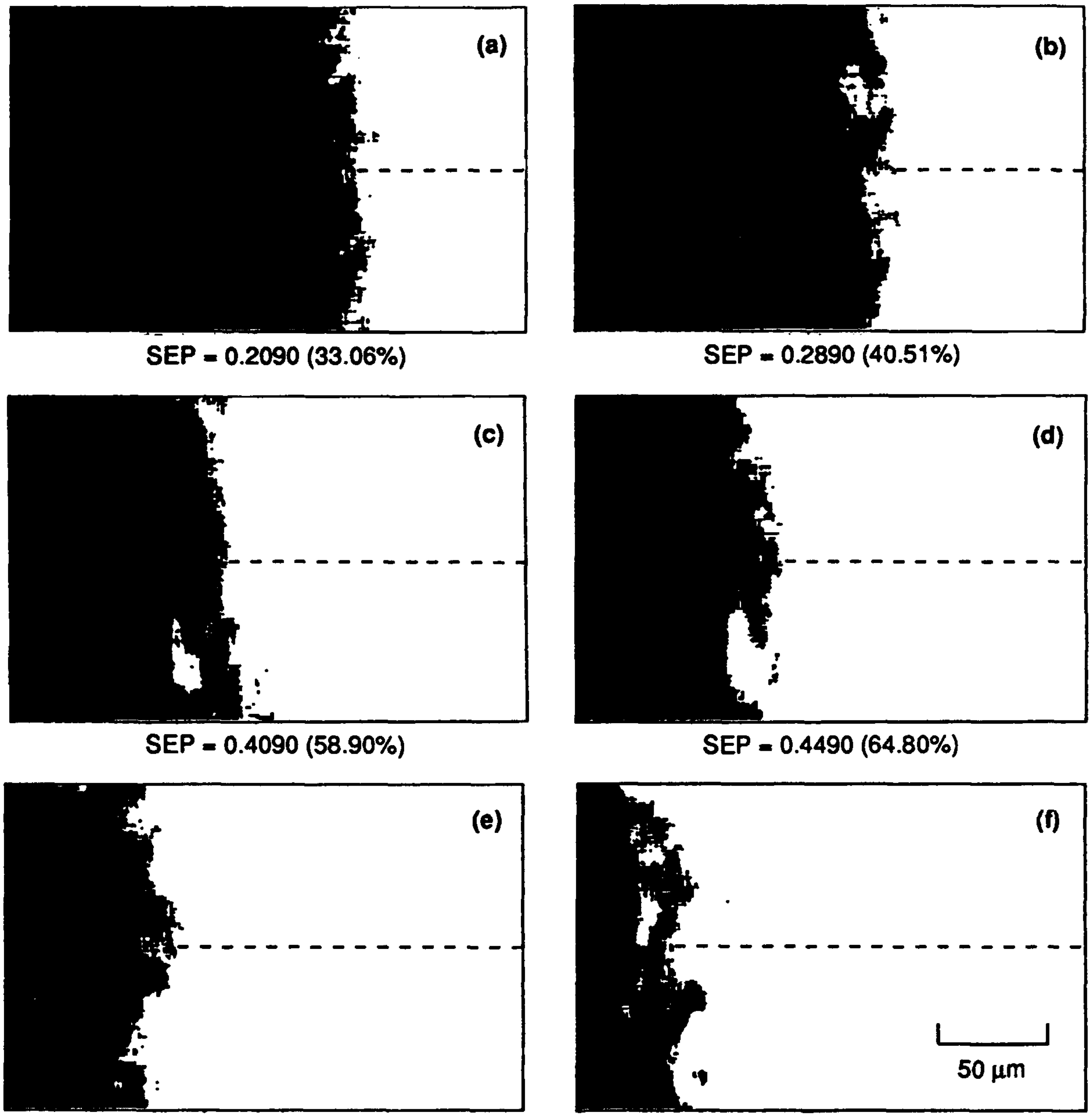

SEP = 0.2090 (33.06%)

SEP = 0.2890 (40.51%)

SEP = 0.4090 (58.90%)

SEP = 0.4490 (64.80%)

SEP = 0.5090 (71.92%)

SEP = 0.5690 (81.49%)

RM-7294-69

Figure 22. FAPPS of dynamic crack propagation in FG microstructure.

(a), (b), (d), (e), and (f) correspond approximately to profiles (a), (b), (c), (d), and (e) in Figure 23. SEP = separation.

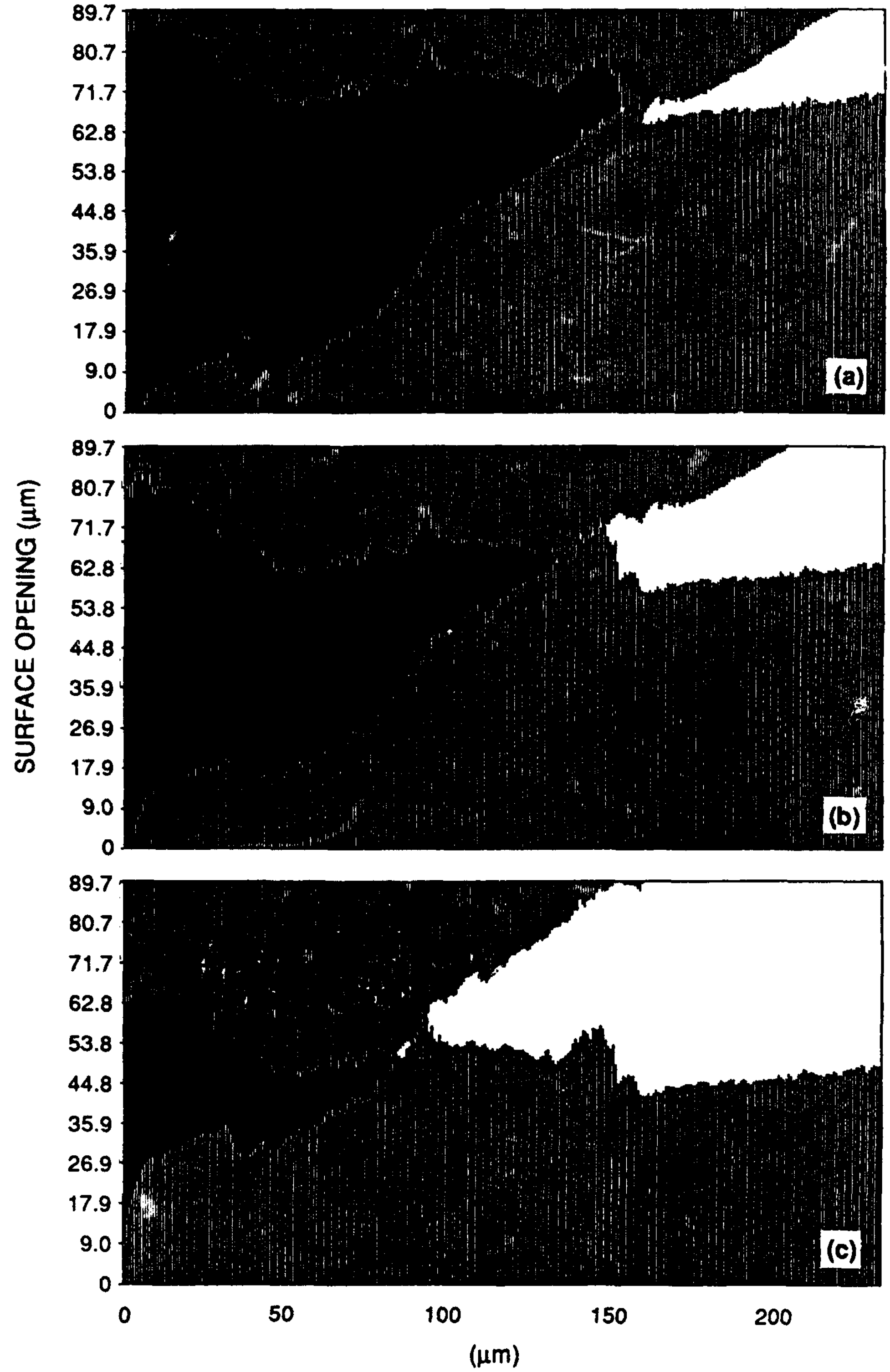

RA-7294-67

Figure 23. XSPs showing crack opening profile during dynamic crack initiation and propagation in FG microstructure. (Continued)

(a) end of fatigue, (b) blunted crack tip just before initiation, (c) through (f) crack propagation through alternating regions of high and low resistance.

(See Figure 22 for location of cross section.)

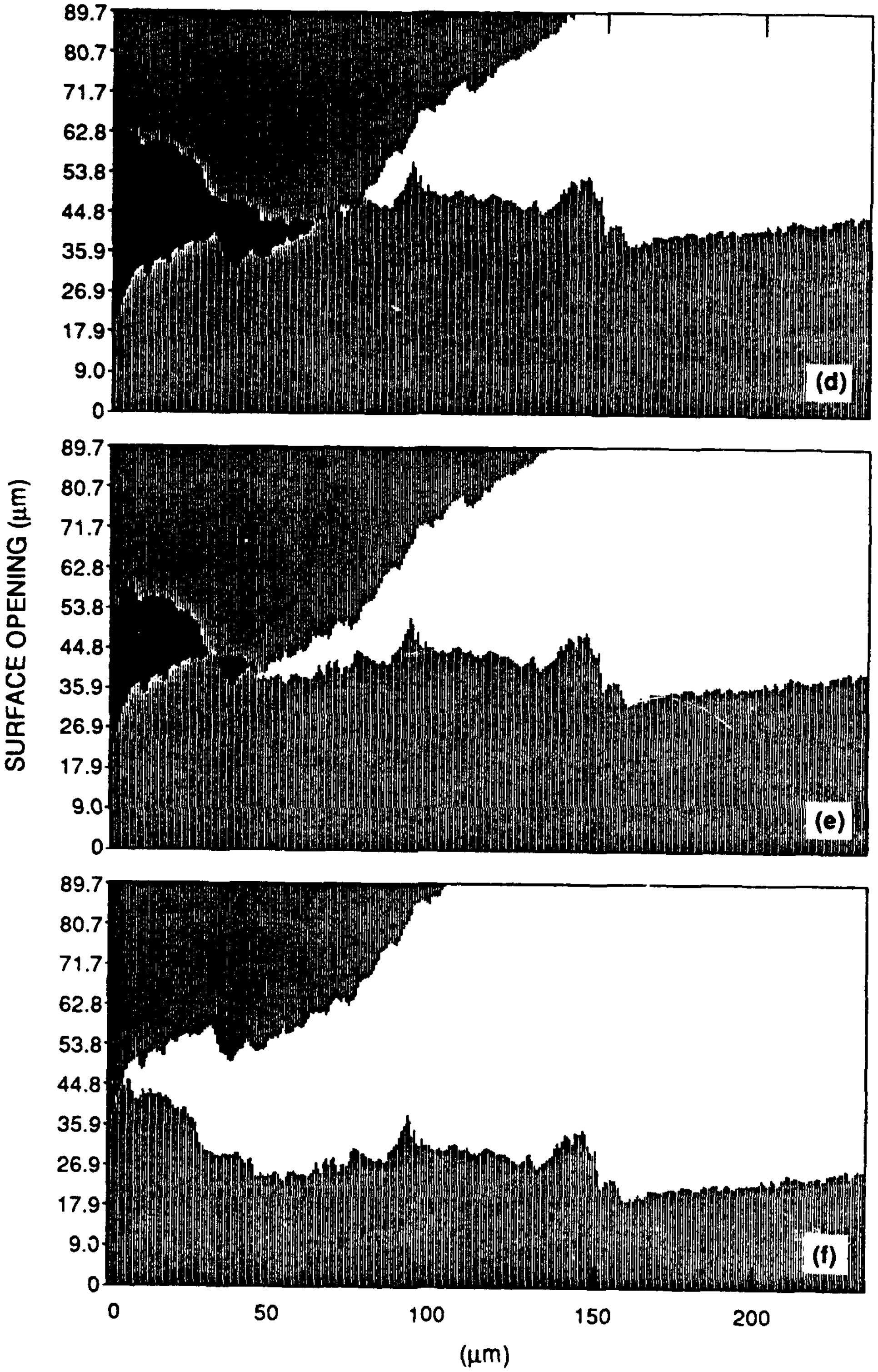

Figure 23. XSPs showing crack opening profile during dynamic crack initiation and propagation in FG microstructure. (Concluded)

(a) end of fatigue, (b) blunted crack tip just before initiation, (c) through (f) crack propagation through alternating regions of high and low resistance.

(See Figure 22 for location of cross section.)

Table 7

CRACK TIP OPENING DISPLACEMENT AT INITIATION OF DYNAMIC FRACTURE MEASURED WITH FRASTA AND CORRESPONDING STRESS INTENSITY FACTOR

Microstructure	CTOD (μm)	K_{Id} from Eq. (1) ($MPa\sqrt{m}$)	K_{Id} from 1PBT* ($MPa\sqrt{m}$)
CG	27	69.3	63.0
IG (no side grooves)	32	70.0	71.5
IG (with side grooves)	23	59.4	109.0
FG	18	56.5	63.0

* 1 PBT = one-point-bend test.

one-point-bend experiment for the side-grooved specimen is probably in error, and therefore, as explained above, we used the average initiation toughness value for the IG microstructure in the simulation of the experiment.

Figure 24 summarizes the FRASTA results on crack propagation. Figure 24 plots the COD at the original fatigue crack front position as a function of the average crack extension for the three microstructures. We obtained the average crack extension by calculating the surface area of the fractured regions in the FAPPs of Figures 16, 19, and 22 and dividing by the width of the regions. We also applied this procedure to the FRASTA results for the side-grooved specimen of the IG microstructure. The COD is obtained by subtracting the topographic map separation at the end of the fatigue crack growth from the current map separation corresponding to an average crack extension. Thus, Figure 24 presents COD resistance curves obtained directly from microscopic fracture surface measurements. The slope of each curve is a measure of the crack opening angle (COA). To our knowledge, it is the first time that such measurements have been performed, and they represent a significant advance in fracture mechanics.

Figure 24 clearly reveals differences in the slope of the COD-crack extension (COD-Δa) curves for the three microstructures and hence in their resistance to crack propagation as measured by the COA. In particular, Figure 24 establishes the same ranking among the microstructures as the continuum data presented in the previous section, i.e., the FG microstructure has the highest resistance to dynamic crack propagation and the CG microstructure the lowest. Therefore, this result provides a partial verification of our continuum measurements. However, since we analyzed only a small increment of crack extension (100 to 400 μm), we are not able to demonstrate with FRASTA that the fracture resistance increases with crack extension—i. e., that the COA becomes larger, which would provide a complete verification of the continuum measurements.

Figure 24 also indicates that the COA for the side-grooved IG microstructure specimen is comparable to and only slightly lower than that for the specimen without side grooves. This similarity of the COA is another indication that the high resistance to dynamic crack extension observed in this IG microstructure is indeed an intrinsic material property and is not associated with the formation of shear lips. Had the shear lips alone been responsible for the high propagation toughness of the specimen without side grooves, we might have expected a much flatter COD-Δa curve for the specimen with side grooves. However, the crack extension distance over which FRASTA reconstructed fracture is only about 0.5 mm, or about a tenth of the propagation distance to reach the steady-state value shown in the continuum results (Figure 11). It is not clear that the shear lips can have a significant effect on the resistance to dynamic crack

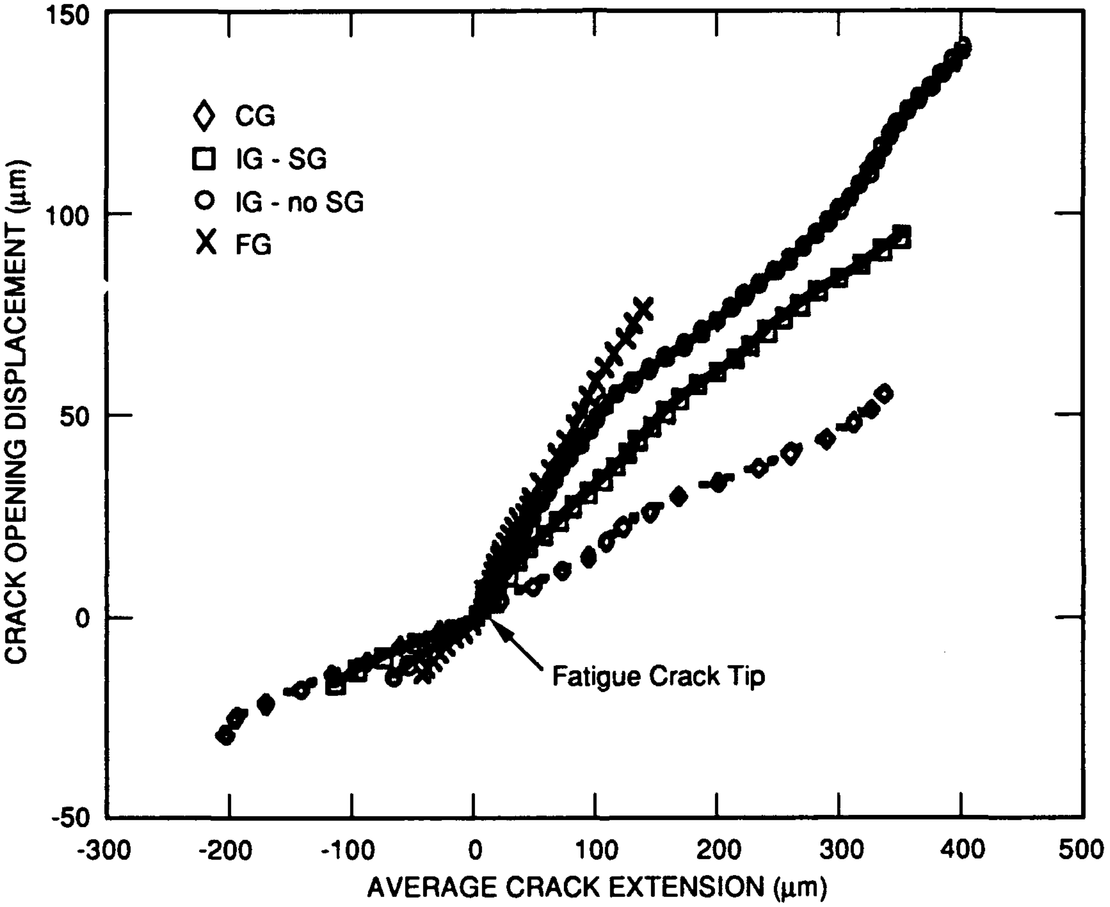

RM-7294-70

Figure 24. Crack opening displacement versus crack extension curve obtained with FRASTA for three Ti-10V-2Fe-3Al microstructures.

extension over such a short propagation distance. Therefore, the FRASTA results provide strong support for the intrinsic increase in dynamic crack propagation toughness but not unequivocal proof.

Microstructural Estimates of Dynamic Propagation Toughness. To obtain independent dynamic propagation toughness estimates for the flat region and shear lip or slant region of the IG microstructure and provide additional validation of our continuum measurements, we performed a two dimensional FRASTA analysis in the dynamic crack propagation region of a typical dynamic fracture specimen of the IG microstructure. We also used the results of the torsion split Hopkinson bar experiment to obtain estimates of the fracture energy of the shear lips.

We produced two matching metallographic cross sections of a specimen of the IG microstructure in the region of dynamic crack propagation. The plane of the cross sections was normal to both the fracture plane and the crack propagation direction. We photographed the cross sections to obtain contours of the edge of the fracture surface and then overlapped the contours in a process analogous to the process shown in Figures 17, 20, and 23, except that the cross section orientation is turned 90°. Figure 25 shows the reconstruction we obtained with this process and illustrates how the crack propagates first at the center of the specimen and how the shear lips then fail. The main direction of crack extension is normal to the plane of the figure.

Using the procedure illustrated in Figure 26, we integrated the fracture edge overlap δ, at a relative separation of the two cross sections corresponding to the appearance of the first microcrack in the flat center region and calculated the fracture energy G per unit area (essentially the plastic work) and the fracture toughness K_{ID}, by using the following relationships

$$G = \frac{\sigma_0}{L} \int_0^L \delta(x)\, dx \qquad (2)$$

$$K_{ID} = \sqrt{G\, E/(1-\nu^2)} \qquad (3)$$

where σ_0 is the flow stress and L and x are defined in Figure 26.

The procedure illustrated in Figure 26 can be performed over part or all of the cross section to estimate the fracture resistance of each individual region (flat fracture region or shear lip region). In performing this toughness estimate, we assumed that the displacement (i.e., the map separation) required to nucleate the first observable microvoids is much smaller than the displacement required

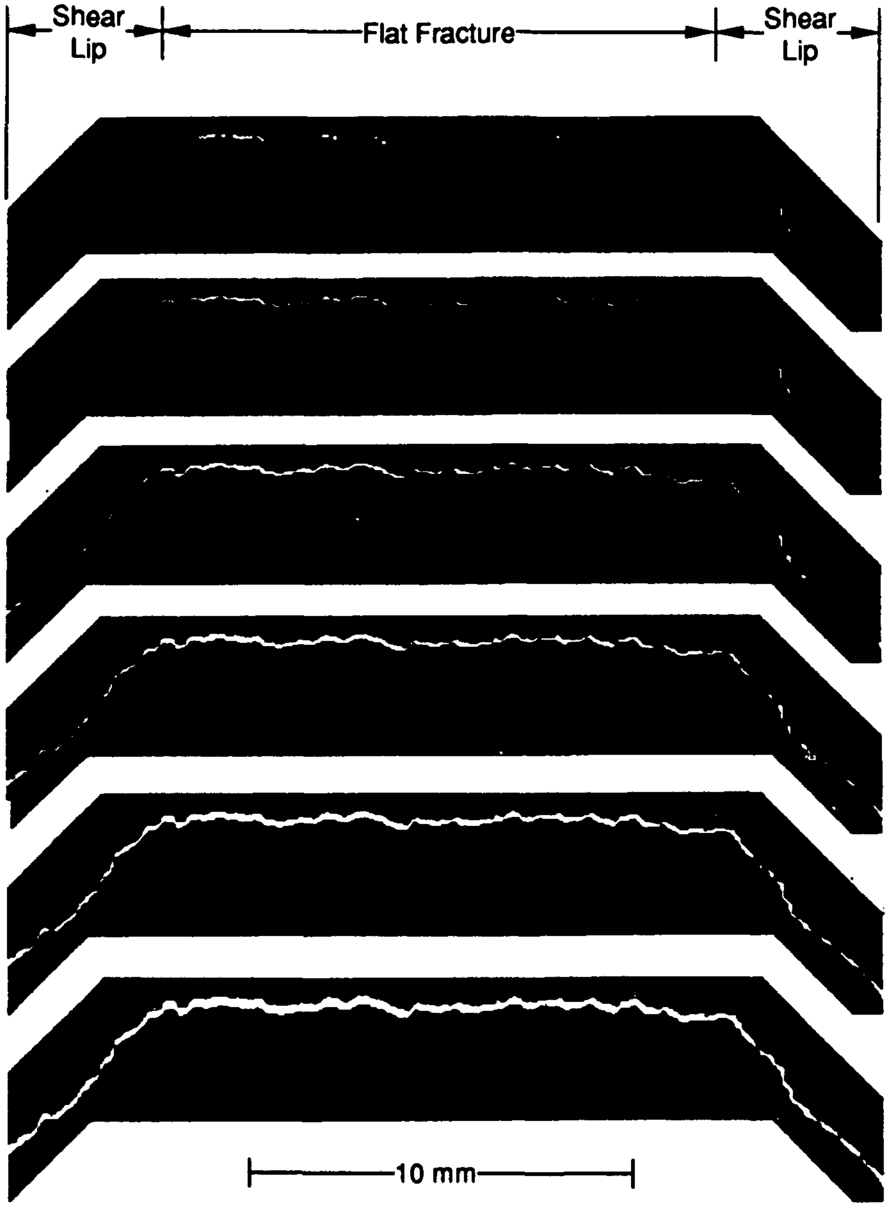

RM-7294-81

Figure 25. Two-dimensional FRASTA reconstruction of crack extension through the thickness of an IG microstructure specimen in the dynamic crack propagation region.

(0.055 mm vertical displacement between successive views.)

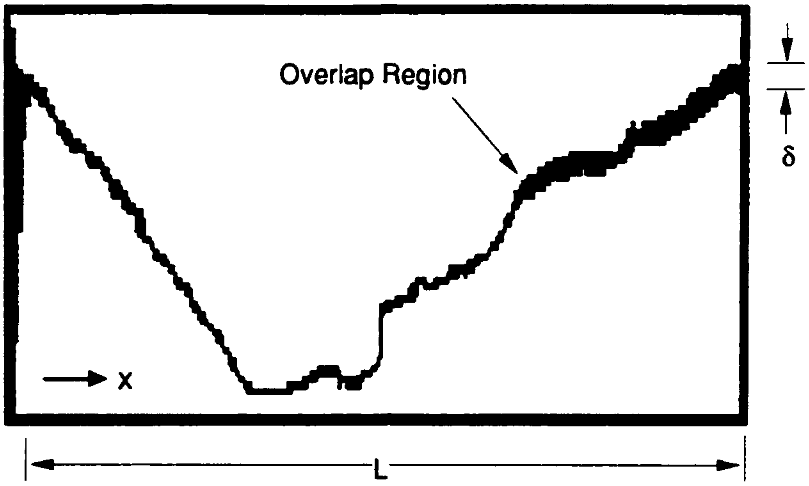

- $G = \frac{\sigma_o}{L}\int_0^L \delta(x)\,dx$

G = fracture energy per unit crack area

$\delta(x)$ = overlap thickness as a function of distance

σ_o = dynamic flow stress

- $K = \sqrt{GE}$ = propagation toughness

E = Young's modulus

RAM-7294-40A

Figure 26. Estimation of fracture energy per unit area and of the fracture toughness with two-dimensional FRASTA.

to grow and coalesce them. In other words, void nucleation strains are negligible compared to the strain accumulated during void growth.

Table 8 lists the toughness values obtained from two-dimensional FRASTA and compares it with values obtained from continuum measurements. In the latter data set, the value for the combined contributions of the flat region and the shear lip region is the propagation toughness value measured with the flat -sided specimen, and the value for the flat fracture region is the propagation toughness measured with the side-grooved specimens. We estimated the continuum value of the toughness associated with the shear lips by (1) integrating the stress-strain curve measured in the torsion split Hopkinson bar experiments to obtain the dissipated energy density and (2) integrating this dissipated energy density over the entire volume of the shear lips (i.e., assuming a constant value over this volume). In performing these estimates, we assumed the value of the flow stress σ_0 to be 1385 MPa (See Table 4).

Toughness values estimated with two-dimensional FRASTA are in remarkable agreement with the toughness values from continuum measurements. Such an excellent agreement may be somewhat fortuitous given the simplifying assumptions that were made in performing the two-dimensional FRASTA analysis. Nevertheless, the two-dimensional FRASTA data provide additional evidence for the intrinsically high dynamic propagation toughness of the IG microstructure and for the relatively modest contribution of the shear lips.

DISCUSSION

As in the Results section above, we will first discuss the results from a continuum point of view and then consider the implications of our microscopic observations.

Strength and Fracture Properties

Most of the previous linear elastic fracture studies of dynamic crack initiation and propagation were performed on model materials such as epoxy resins and PMMA or on high strength steels (see, for instance, References 24 through 26). Some studies have also addressed dynamic crack propagation in ductile steels.[27,28]

For materials amenable to linear elastic fracture analysis, previous work indicates that the dynamic crack propagation toughness varies with crack velocity. At lower velocities, typically up to 20% of the Rayleigh wave speed (i.e., velocities up to 700 m/s for high strength steel), the propagation toughness is approximately equal to or somewhat smaller than the dynamic initiation

Table 8

COMPARISON OF DYNAMIC PROPAGATION TOUGHNESS OBTAINED FROM TWO-DIMENSIONAL FRASTA AND FROM CONTINUUM MEASUREMENTS FOR IG MICROSTRUCTURE

	Toughness from 2D-FRASTA $(\mathrm{MPa}\sqrt{\mathrm{m}})$	Toughness from Continuum Measurement $(\mathrm{MPa}\sqrt{\mathrm{m}})$
Flat fracture	109	100
Shear lips	149	152
Combined flat fracture/shear lips	125	120

toughness, indicating a correlation between the two toughnesses. As the crack velocity approaches about a third of the Rayleigh wave speed (about 1000 m/s for high strength steels), the propagation toughness rapidly increases to several times the value of the initiation toughness. Two complementary explanations can be invoked to explain this rise. First, as the crack speed increases, both the rate of energy release available in the crack tip process zone to damage the microstructure and the size of the region with large strains decrease.[25] Second, the material response itself may change because of the extremely high strain rates at the propagating crack tip (estimates are difficult, but strain rates of 10^6/s may not be unreasonable) and because of associated adiabatic heating effects, which may induce changes in the local flow and deformation behavior. In addition to these considerations, there are also some questions regarding the dominance of the singular elastic field (K-field) at the tip of rapidly propagating cracks and the effect of specimen geometry (i.e., higher order terms in the elastic solution) on the analysis of the experimental results.

The formation of shear lips has often been observed in both static and dynamic crack propagation experiments. The tendency to form shear lips is usually correlated to plastic zone size for the material, which is estimated in terms of the square of the ratio of toughness to yield strength. In general, shear lips have been considered to raise the effective propagation toughness significantly because they act as trailing uncracked ligament and cause curving of the crack front.

The formation of shear lips is associated with materials having lower yield strength, which are often no longer strictly amenable to an elastic analysis. Lower strength steels display a very steep rise in propagation toughness with crack velocity for velocities in the range 0 to 300 m/s (see Reference 26 for typical examples). Usually these materials also have a high static toughness and a steep static resistance curve.

The results of this study, augmented by our earlier results,[2] extend classical dynamic fracture to a new class of practical materials and open new perspectives on dynamic fracture. One of the most significant features of our study is that it has generated one of the first extensive sets of dynamic strength and fracture properties for a titanium alloy. It shows that titanium alloys with commercially useful microstructural conditions have a rather different behavior than previously studied brittle polymers and high strength steels. Although the initiation toughness does not appear overly sensitive to the loading rate (at most, the initiation toughness increases about 20% for a ten-orders-of-magnitude increase in loading rate), the propagation toughness is strongly sensitive to crack speed in some titanium microstructures. Whereas the propagation toughness (resistance curve) increases only modestly (20%) over the initiation toughness at quasi-static loading rates, crack speeds as low as 100 m/s are sufficient to raise the propagation toughness by as much as 100%. The development of a steady-state dynamic propagation toughness also appears to require a certain amount of crack extension (many millimeters). This dynamic resistance curve behavior is in strong contrast to the previously observed behavior of brittle polymers and high strength steels. Our study provided evidence that the rate sensitivity of the propagation toughness of the titanium alloys is an intrinsic material property rather than a result of structural phenomena such as the formation of shear lips. Some microstructures of the same alloy have a high dynamic propagation toughness, whereas others—such as the β-quenched microstructure investigated in our earlier work,[2, 22, 23] with comparable initiation toughness and 17% higher strength—do not display any increase in propagation toughness over initiation toughness for the crack velocities investigated. This dependence on strength and microstructural condition further demonstrates the intrinsic nature of the high dynamic propagation toughness in some titanium microstructures.

Indeed, our second significant finding is that the shear lips are a consequence rather than a cause of the increase in propagation toughness, in contrast to our interpretation of earlier results.[2, 22, 23] Our estimates show that shear lips only contribute a fraction (about 20%) of the total elevation of the propagation toughness above the initiation toughness. Further, we have demonstrated that the process of forming shear lips is highly rate dependent, an observation consistent with the propagation toughness results.

Third, our dynamic measurements indicate that the initiation and propagation toughnesses are not simply correlated. For instance, the FG microstructure has the lowest initiation toughness of the three microstructures but develops the highest steady-state dynamic propagation toughness. Therefore, how dynamic initiation and propagation toughnesses relate to each other depends on the toughening mechanisms and consequently on microstructure.

Microstructural Observations

Microstructural observations made during this investigation provide support for the continuum results and indicate what mechanisms contribute to the dynamic toughness. Here we attempt to answer the following questions: (1) Why do the investigated microstructures develop a resistance curve effect? (2) Why are the dynamic fracture properties superior to the static properties? (3) How do the investigated microstructural variations affect the micromechanisms of fracture and the fracture properties?

Our study shows that all three microstructures have a modest static resistance curve effect. Therefore, independent of rate effects, micromechanisms exist that increase the resistance to crack propagation over the initiation toughness. Similarities in the fracture surface appearance for the static and dynamic experiments further suggest that the mechanisms remain the same under dynamic loading but are enhanced by the rate sensitivity of microdeformation processes.

For all three microstructures, our fractographic observations provide evidence for the role of rate-induced changes in microductility. In addition, the Hopkinson bar experiments demonstrate that the flow strength of the aged β-matrix is rate sensitive. Simply considering plastic work dissipation, it is easy to see how rate-enhanced microductility and flow strength in all three microstructures can lead to their enhanced dynamic fracture resistance.

Besides the common rate sensitivity, FRASTA reveals that all three microstructures have a common general mechanism for developing a resistance curve, namely, the presence of tough "microregions" which locally arrest and blunt the crack front. However, the nature of these tough microregions and the details of the deformation mechanisms associated with these microregions differ from one microstructure to the other, because the microstructures have different grain sizes, different α_p-phase morphologies, and different amounts of grain boundary α.

For instance, in the CG microstructure, which fractures mainly intergranularly, debonded grain boundaries ahead of the main crack or encounters with new grains with different grain boundary orientations may act as tough regions and force the crack to follow a new propagation direction. Rate-induced changes in the microductility and flow strength of the grain boundary material will lead to a higher energy dissipation for this crack tortuosity mechanism under dynamic loading than under static loading.

In the IG microstructure, which has a predominantly transgranular fracture mode, interactions between the extending crack and aged β-grains may also play the role of a tough microregion, forcing the crack to blunt and deviate from its main path. However, in contrast to the case of the CG microstructure, we believe that activation of slip within each grain and not grain boundary crack propagation is the process controlling crack tortuosity in the IG microstructure.

In the FG microstructure, the crack path is much straighter, consistent with the much smaller grain size. Therefore, crack deflection does not appear to be a significant toughening mechanism. A possible origin for the tougher microregions in this microstructure could be local variations in the distribution of void nucleating α_p particles. Considering Figure 3e, which shows rather homogeneously distributed α_p particles, we would expect the effect to be small, which is consistent with the rather small slope of the resistance curve in the static fracture experiments.

It is interesting that the ranking of the microstructures in terms of dynamic propagation toughness is the reverse of what we might anticipate if crack path tortuosity were the only active toughening mechanism. In that case, the microstructure with the larger grain size should have the greatest propagation toughness. Therefore, we conclude that different mechanisms must be active, particularly since fracture is not intergranular in all microstructures. Thus, in the FG microstructure, the dynamic resistance curve effect may be due almost entirely to the rate-induced microductility effect, which leads to the growth of larger voids and their delayed coalescence.

The above comments are still somewhat speculative and fall far short of providing a complete and consistent explanation of the observed crack propagation behaviors. For instance, the characteristic length scale of the discussed toughening mechanisms is on the order of the grain size, and therefore we should see the achievement of a steady state in the resistance curve after at most several millimeters of crack extension. Nevertheless, we obtained an increasing dynamic resistance curve for crack extensions of 10 to 15 mm. Although the development of shear lips can account for part of the toughness elevation for larger crack extensions, at present we do not have a satisfactory explanation of the phenomenon. The roughening of the fracture surface of the dynamically loaded FG microstructure attests to the increasing size of the process zone as the crack extends. What leads to this increase remains to be explained and warrants further research.

SUMMARY AND CONCLUSIONS

We extended classical dynamic fracture mechanics to a class of new commercially useful titanium microstructures and demonstrated that their dynamic fracture behavior differs significantly from that of previously studied model materials. By combining continuum measurements (obtained using the torsion split Hopkinson bar and one-point-bend fracture test methods) and fractographic measurements (obtained using fracture surface topography analysis, FRASTA), we generated a complete static and dynamic strength and fracture toughness data base for various microstructures of the alloy Ti-10V-2Fe-3Al.

Whereas the dynamic initiation toughness was only moderately higher than the static initiation toughness (at most 20%), we established a very strong rise in the crack propagation toughness with crack extension (as much as a 100% increase) for velocities as low as 100 m/s. This rate dependent resistance curve effect is an intrinsic material property (in contrast to a structural effect) and a strong function of microstructure. We demonstrated that the formation of shear lips is also a strongly rate dependent phenomenon and that shear lips, when they develop, make only a modest contribution to the propagation toughness (on the order of 20% for the case studied here). Our results also showed that, in general, there is not a direct correlation between the dynamic initiation and propagation toughnesses.

We independently verified the continuum results with fractographic measurements of crack tip opening displacements and angles and obtained, to our knowledge for the first time, a crack opening displacement resistance curve directly from fracture surface topography measurements. We have demonstrated in several independent ways that it is possible to extract from fractographic measurements parameters useable in continuum fracture mechanics analyses.

For a given strength level, the microstructure of the alloy (primary alpha content and morphology, grain size, grain boundary alpha film) influences the fracture mode and the fracture properties in a complex way. Void nucleation and growth at primary alpha particles or in grain boundary alpha films is always the dominant microfailure mode, but decreasing the grain size by two orders of magnitude changes the fracture path from intergranular to transgranular. We identified rate dependent and microstructure dependent mechanisms (such as interactions of the main crack tip with secondary transverse cracks or with unfavorably oriented grains or grain boundaries) which provide partial explanations for the observed dynamic toughness behavior.

Several experimental observations, such as the long crack extension needed for achieving a steady state value of the dynamic propagation toughness, remain without conclusive detailed micromechanical explanation and will require additional research.

MODELING MICROSTRUCTURES

The primary motivation for this project is the development of microscopic models that will be able to predict the mechanical behavior of multiphase microstructures

In Reference 2, we outlined an approach for modeling Ti-10-2-3 microstructures by using finite element simulations. In this approach, the microstructure is represented by an array of two-dimensional grains containing one or more phases and by a continuous film of material at the grain boundaries. In the model, each phase can be assigned different constitutive behaviors and failure behaviors to simulate different microstructural failure processes such as void nucleation and growth, shear localization, or inter- and transgranular cracking.

In the present work we made a first attempt at applying this approach to model one of the microfailure processes observed in the alloy Ti-10V-2Fe-3Al. As we described in reporting the fractographic results above and in Reference 2, grain boundary fracture by the nucleation and growth of microvoids in the soft α film was often observed in the microstructures studied in this and the previous project (see, for instance, Figure 12). Indeed, Williams et al.[15] point out that this mechanism of fracture is a very common one in all commercial titanium alloys and plays a key role in controlling their ductility and fracture properties. It is believed that the relative strengths and hardening rates of the grain boundary α film and the grain matrix in turn control the growth rate of cavities in the grain boundary. Therefore, in view of the importance of the grain boundary (ductile) failure mechanism, we modeled in the present project an array of grains surrounded by a continuous grain boundary film that fails by growth of microvoids and investigated the influence of the relative grain/grain boundary strengths on the deformation and failure of the grain array. To represent the growth of voids in the grain boundary, we used the Gurson-Tvergaard plasticity model for porous materials.[29,30]

This section of the report describes finite element calculations of the two-dimensional grain core/grain boundary problem. We first describe the grain arrangement and the symmetry properties used to reduce the geometry to a unit cell, then describe the finite element mesh used to discretize the unit cell and the constitutive models assigned to the boundary and core materials. We then compare results obtained with both the NIKE2D quasi-static, implicit finite element code[31] and the DYNA2D dynamic, explicit finite element code,[21] briefly discussing issues of convergence and precision for each. Finally, we present the results of a NIKE2D parametric study in which the relative strengths of the grain boundary and core materials were varied and discuss the implications for strain localization and microstructural failure.

MODELING APPROACH

Geometrical Configuration and Computational Mesh

For all the calculations we performed, we chose the grain arrangement shown in Figure 27, which consists of a uniform array of elongated hexagonal grains separated by a thin layer of grain boundary material. The choice of elongated hexagonal grains was serendipitous, as will be shown below, and is a reasonable representation of the real microstructures (see, for instance, Figures 3a and c) when they are viewed in terms of a unit cell.

The main difficulty in modeling the grain array arises because, in the Ti-10V-2Fe-3Al microstructures studied, the thickness of the α grain boundary layer is less than 2% of the grain size. Because we are interested in what happens to the grain boundary, we need to use small cells to discretize this region in order to achieve a reasonable resolution of field quantities in the thickness direction. However, because the length/thickness ratio of the grain boundary is very high, the use of small cells results in a large number of elements in the mesh and thus in long computational times. To try to optimize the accuracy with which we model the problem at hand, as well as to minimize the computational time, we utilized two finite element codes (NIKE2D and DYNA2D) to study a baseline problem and compare the results.

For globally affine deformations having a principal axis aligned with the long axis of the grains (by globally affine, we mean that, although deformation gradients may vary locally, they are affine when averaged over a large volume of grains), symmetry allows us to discretize only parts of two grains. These parts are located inside the shaded rectangle shown in Figure 27. We assume that boundary loads are applied remotely and any body forces are applied uniformly.

Figure 28 shows the mesh used to discretize the problem. The mesh contains 717 nodes and 666 elements, 130 of which belong to the grain boundary. The grain boundary has two cells across the thickness. We tried a higher resolution mesh with four cells across the grain boundary, but it required five times as much computer time, which was impractical.

Except for wave propagation effects, the grain core/grain boundary problem, when modeled with the constitutive models we chose, is scale-invariant. Thus, the choice of 36.5 cm for the height of the unit cell was made strictly for convenience.

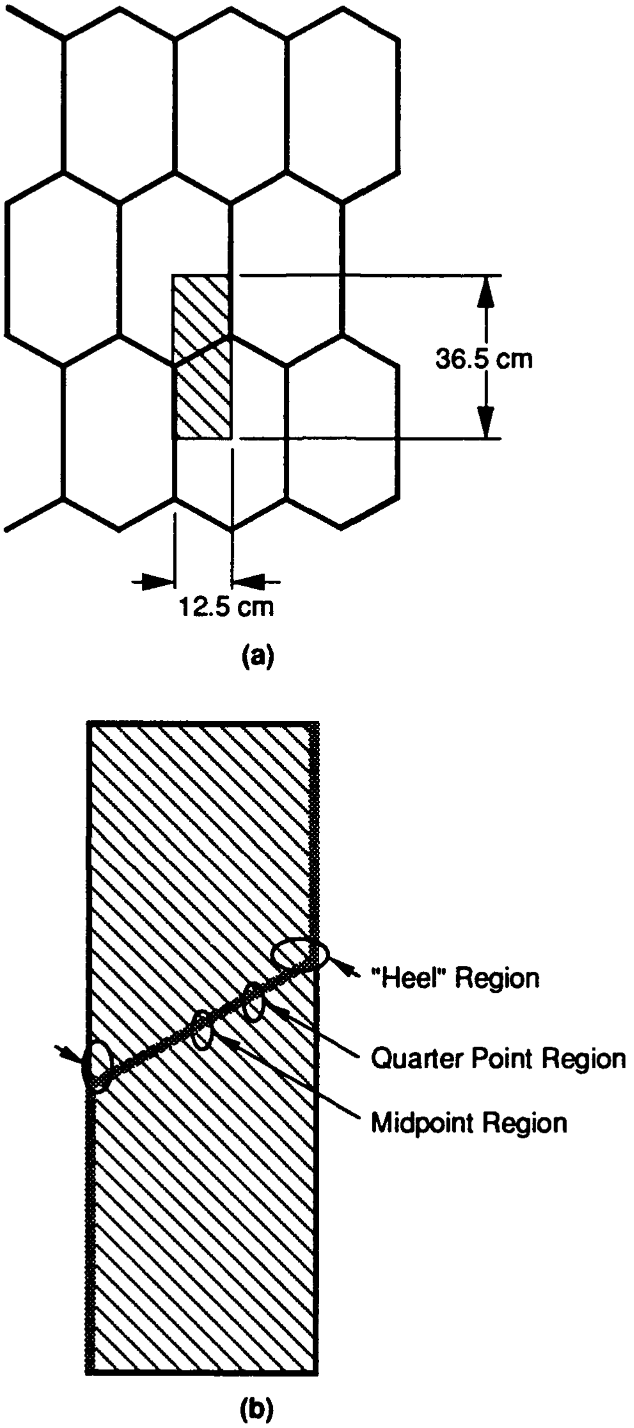

R-7294-82

Figure 27. Hexagonal grain array used to simulate Ti-10V-2Fe-3Al microstructures.

(a) Overall array, with shaded rectangle representing region that was discretized, (b) definition of "heel," "toe," midpoint, and quarter point locations.

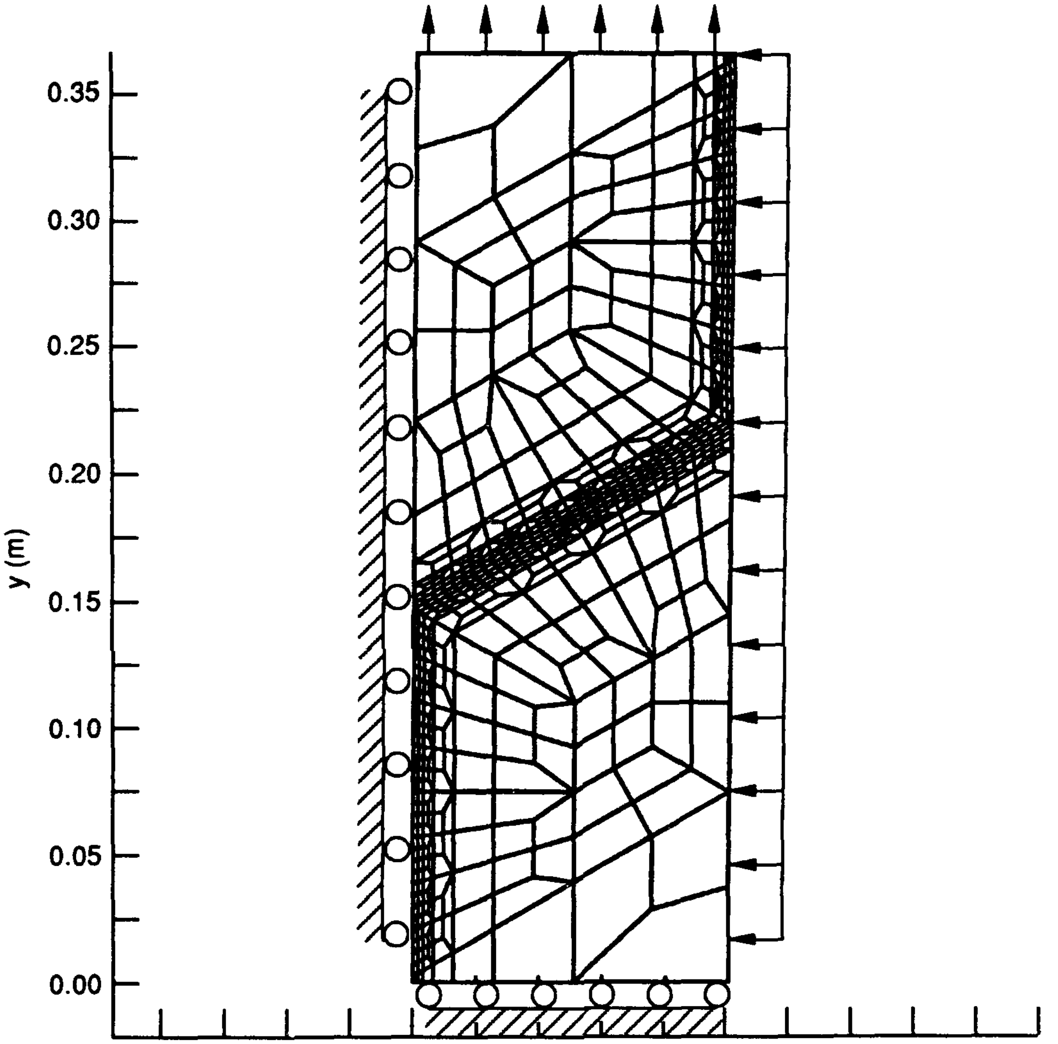

RM-7294-83

Figure 28. Finite element mesh.

Baseline Constitutive Models and Material Properties

We used an elastic-plastic model with linear, isotropic hardening for the grain core. Table 9 lists the material parameters for the grain core, which we kept the same for all the simulations. We only varied the material parameters for the grain boundary.

Tvergaard's version[30] of the Gurson plasticity model[29] is used for the grain boundary. The yield condition is given by

$$\left(\frac{\bar{\sigma}}{\sigma_Y}\right)^2 + 2 f q_1 \cosh\left(\frac{\mathrm{tr}\sigma}{2\sigma_Y}\right) - \left(1 + q_3 f^2\right) = 0 \qquad (4)$$

where $\bar{\sigma}$ is the effective stress, σ_Y is the current yield strength, $\mathrm{tr}\sigma$ is the trace of σ, f is the void volume fraction, and q_1 and q_3 are the first and third Tvergaard-Gurson parameters, respectively. The density, Young's modulus, Poisson's ratio, and the tangent modulus are the same as for the grain core. The baseline values of the Tvergaard-Gurson model parameters are given in Table 10.

There are only two differences between the grain core and the grain boundary in the baseline calculations. First, the initial yield strengths are different. We chose the yield strength of the grain core as that of the IG microstructure, and the yield strength of the grain boundary as a lower value to represent the α phase, which we know is softer than the aged β-matrix. Second, we modeled the grain boundary with the Tvergaard-Gurson flow law, which accounts for the growth of voids in the plastically deforming material. The grain core was modeled using conventional Von-Mises flow theory with linear hardening. Each of these differences makes the grain boundary softer than the grain core in the baseline calculations.

Depending on the initial void volume fraction, the Tvergaard-Gurson model does not accurately model strength when void volume fractions grow beyond $f = 4\sim12\%$ (see Reference 32). However, the model will behave in a physically reasonable way, until the void volume fraction reaches $f = q_1/q_3$. This limitation to the model can be understood by considering Equation (4). According to Equation (4), the maximum equivalent stress $\bar{\sigma}$ can be sustained when $\mathrm{tr}\sigma = 0$ and is equal to

$$\bar{\sigma} = \sigma_Y \left(1 + q_3 f^2 - 2 f q_1\right)^{\frac{1}{2}} \qquad (5)$$

Table 9

MATERIAL PARAMETERS FOR GRAIN CORE

Parameter	Nomenclature	Value
Density	ρ	4.65 g/cm^3
Young's modulus	E	106.0 GPa
Poisson's ratio	ν	0.315
Initial yield strength	Y_0	1.37 GPa
Tangent modulus	h	1.0 GPa

Table 10

MATERIAL PARAMETERS FOR THE GRAIN BOUNDARY, INCLUDING PARAMETERS FOR THE TVERGAARD-GURSON YIELD MODEL

Parameter	Nomenclature	Value
Density	ρ	4.65 g/cm^3
Young's modulus	E	106.0 GPa
Poisson's ratio	v	0.315
Initial yield strength	Y_0	1.15 GPa
Tangent modulus	h	1.0 GPa
First Gurson parameter	q_1	1.5
Third Gurson parameter	q_3	2.25
Initial void volume fraction	f_0	0.0082

As f increases in Equation (5), the flow stress $\bar{\sigma}$ decreases until $f = q_1/q_3$ (= 2/3 for our choice of parameters), at which point $\bar{\sigma}$ begins to increase, which is non physical.

Boundary Conditions

We prescribed boundary conditions such that the grain array undergoes a biaxial strain-triaxial stress deformation, when we take into account the fact that the calculations are performed in plane strain. The grain array is extended in the vertical direction while being compressed in the horizontal direction. The horizontal compression is less than that required to conserve volume, so a net volume increase occurs. We selected this type of deformation to approximate the deformation state of a material element ahead of a crack tip. All four boundaries of the mesh (Figure 28) are free of shear (tangential) traction. The left and bottom boundaries are fixed in the direction normal to the surface. The top boundary is moved uniformly in the outward normal direction and the right boundary is moved uniformly in the inward normal direction. The top and right boundary motions are obtained differently with the NIKE2D and the DYNA2D codes: With NIKE2D the *displacement* of the boundary nodes is imposed, whereas with DYNA2D the *velocity* of these nodes is imposed.

The deformation of the mesh is parameterized by ε, which is the vertical displacement of the top boundary divided by the initial height of the mesh, i.e., the global, axial, engineering strain. For both codes, the calculation is set to halt at $\varepsilon = 3.3\%$.

Calling β the positive ratio of transverse extension to horizontal compression, let us express the (elastic) path to yielding. The strain components are

$$\varepsilon = \begin{pmatrix} \varepsilon & 0 & 0 \\ 0 & -\beta\varepsilon & 0 \\ 0 & 0 & 0 \end{pmatrix} \tag{6}$$

and the stress components are

$$\sigma = \begin{pmatrix} \lambda(1-\beta)+2\mu & 0 & 0 \\ 0 & \lambda(1-\beta)-2\mu\beta & 0 \\ 0 & 0 & \lambda(1-\beta) \end{pmatrix} \varepsilon \tag{7}$$

where λ and μ are the Lamé constants. The stress path to yielding in $\left(\bar{\sigma}, \mathrm{tr}\sigma\right)$ space is described by

$$\bar{\sigma} = \frac{\sqrt{1 + \beta + \beta^2}}{1 - \beta} \frac{1 - 2\nu}{1 + \nu} \mathrm{tr}\sigma \tag{8}$$

In our problem, $\beta = 1/20$, so

$$\bar{\sigma} \approx 1.080 \frac{1 - 2\nu}{1 + \nu} \mathrm{tr}\sigma \tag{9}$$

This path is quite close to uniaxial strain ($\beta = 0$), for which

$$\bar{\sigma} = \frac{1 - 2\nu}{1 + \nu} \mathrm{tr}\sigma \tag{10}$$

and far from uniaxial stress, for which

$$\bar{\sigma} = \mathrm{tr}\sigma \tag{11}$$

and even farther from pure shear, for which $\beta = 1$, $\mathrm{tr}\sigma = 0$, and $\bar{\sigma} = 2\mu\varepsilon$.

Thus, for any $\beta < 1$, the volume of the sample will increase because the lateral compression is not fully compensating the axial extension.

With NIKE2D, the imposed global strain rate is 5.5×10^{-3}/s, making the NIKE2D problem quasi-static. With DYNA2D, the imposed global strain rate is 27.4/s. Over the 1.2-ms duration of the DYNA2D problem, a longitudinal wave makes approximately eight round trips over the length of the mesh, so the modeled grain region is probably not far from static equilibrium. Thus, the problems simulated with the NIKE2D and DYNA2D codes should be comparable. We chose such a relatively high strain rate for DYNA2D to minimize the central processing unit (CPU) time and reduce truncation errors. The NIKE2D and DYNA2D problems each need about 25 hours on a MicroVAX. When DYNA2D is run with a global strain rate of 5.5/s, about 125 hours are needed, and nodal position errors become important. The errors are important because, at low strain rates, the nodal displacement increment per time step can be very small relative to the nodal position. When the displacement is added to the old position to obtain a new position, the added increment is smaller than the least significant digit of the old position as stored in the computer memory, so the nodal position is not changed. Many such displacement increment truncations lead to significant errors.

DYNA2D, being an explicit finite element code, is able to handle nearly any mesh distortion and material model instability and still provide numerical results. The user must judge the physical relevance of these results. NIKE2D, on the other hand, is an implicit finite element code and thus will halt when mesh distortions become too large or material models become unstable. Modifying the analytical parameters will not help solve the problem. Thus, with NIKE2D, we have never been able to advance as close to, or past, softening instabilities that arise in the investigated problems, as we have with DYNA2D. The NIKE2D results, however, are smoother and more easily interpreted because wave propagation is removed from the problem. From considerations of the grain size and the time to fracture, we know that wave propagation on the scale of individual grains, as modeled here by DYNA2D, is not important at the ~10^6 MPa$\sqrt{m}$/s loading rates in our fracture experiments, because even at these loading rates waves would have time to traverse the grains many times before fracture.

Problems Analyzed

We first analyzed a baseline problem (defined by the combination of material properties in Tables 9 and 10) by using the NIKE2D and DYNA2D codes. The purpose of these analyses was to select the most appropriate code to investigate the failure behavior of the grain array in a computationally efficient way.

We then performed simulations in which we varied the parameters of the constitutive model to give physical insight into the microfailure behavior of the grain array when the relative strengths of the grain core and grain boundary are varied. In particular, we were interested in studying the effect of the relative strength of the grain boundary on strain localization and failure location, since this parameter has been shown to play a controlling role in the fracture of titanium alloys.[15]

We selected three variations of the material parameters, as listed in Table 11. In the first calculation, referred to as denser grain boundary calculation, the initial void volume fraction in the grain boundary, f_0, was decreased from the baseline value of 0.0082 to 0.0050. In the second calculation, referred to as porous grain boundary calculation, f_0 was reset to the baseline value of

0.0082, but the initial yield strength in the grain boundary, Y_0, was increased from the baseline value of 1.15 GPa to 1.37 GPa, the same as the grain core initial yield strength. Both of these variations were intended to make the grain boundary harder than in the baseline case, but still softer than the core; we expected that this change would suppress or at least delay divergences. In the third calculation, referred to as hard grain boundary calculation, f_0 remained at 0.0082 but Y_0 in the grain boundary was increased to 1.60 GPa, making the boundary initially harder than the core. This calculation was expected to give significantly different results and extend our understanding of core/boundary interaction.

The denser grain boundary calculation ($f_0 = 0.005$) ran until $\varepsilon = 2.86\%$, which is about 0.3% farther than the baseline calculation ran, and the porous grain boundary calculation ran to completion ($\varepsilon = 3.29\%$). The hard grain boundary calculation ran beyond the usual completion point, diverging at $\varepsilon = 4.57\%$.

RESULTS

Baseline Calculations

We present and compare the results of our various calculations in terms of void volume fraction histories in the grain boundary and effective plastic strain time histories and contour maps in the grain core. We compare the maps at equivalent imposed global strains. Because of the different output plotting intervals in the various calculations, equivalent strains are not always exactly equivalent, the difference being generally lower than 1% and never higher than 4%.

We first compare NIKE2D and DYNA2D results for the baseline calculations. As shown in Figure 29a, void volume fractions begin to increase at the same global strain for both codes (approximately 1.4%). Shortly after the start of void growth, effective plastic strains in the grain core material also begin to increase (Figure 29b), once again at the same global strain for both codes. The grain boundary material begins to deform inelastically before the grain core material because of the difference in the initial yield strengths of the materials. The void volume fraction and effective plastic strain values at the beginning of plastic deformation are very similar for DYNA2D and NIKE2D results. Maximum void volume fractions are slightly higher with DYNA2D and maximum effective plastic strains somewhat higher with NIKE2D. Figure 30 shows plastic strain contours for an early time in a DYNA2D calculation. A "plastic deformation wave" is moving from top to bottom of the grain array and clearly demonstrates wave propagation phenomena that only appear in the DYNA2D simulations.

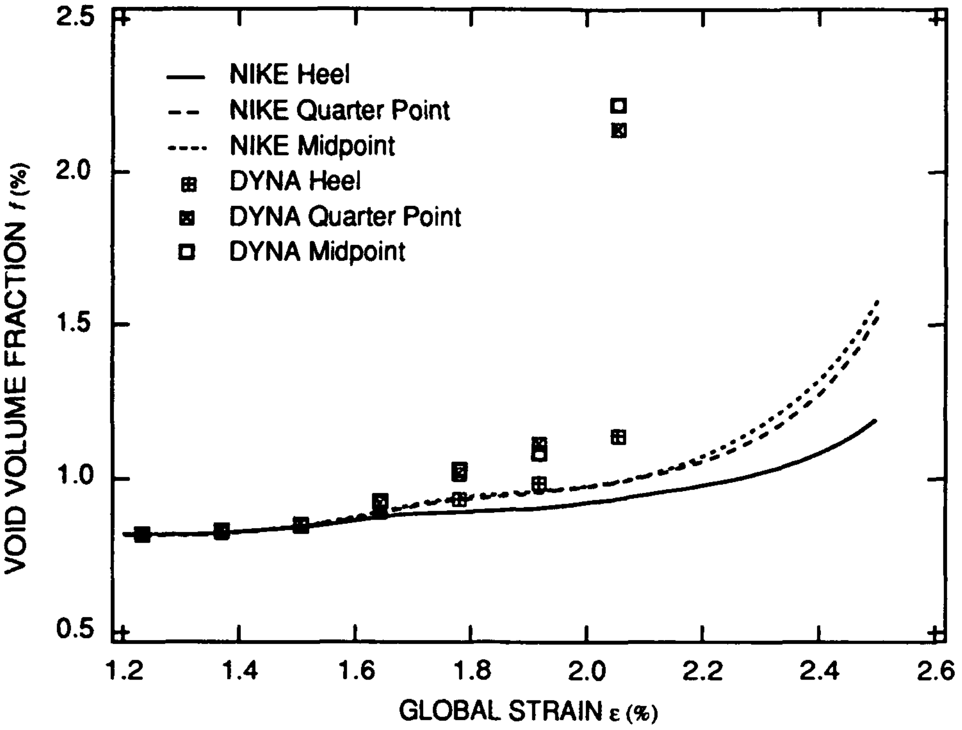

(a) Void volume fraction

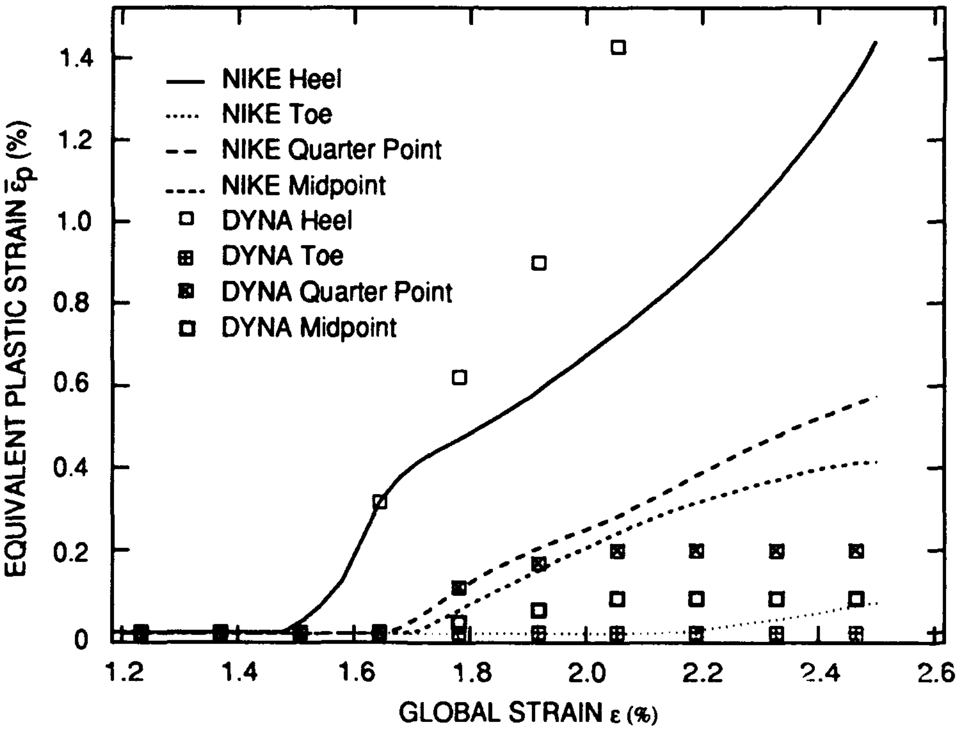

(b) Equivalent plastic strain

RAM-7294-84

Figure 29. Comparison of DYNA2D and NIKE2D results for baseline calculations. (a) void volume fraction versus imposed global strain, (b) equivalent plastic strain in the grain core versus imposed global strain.

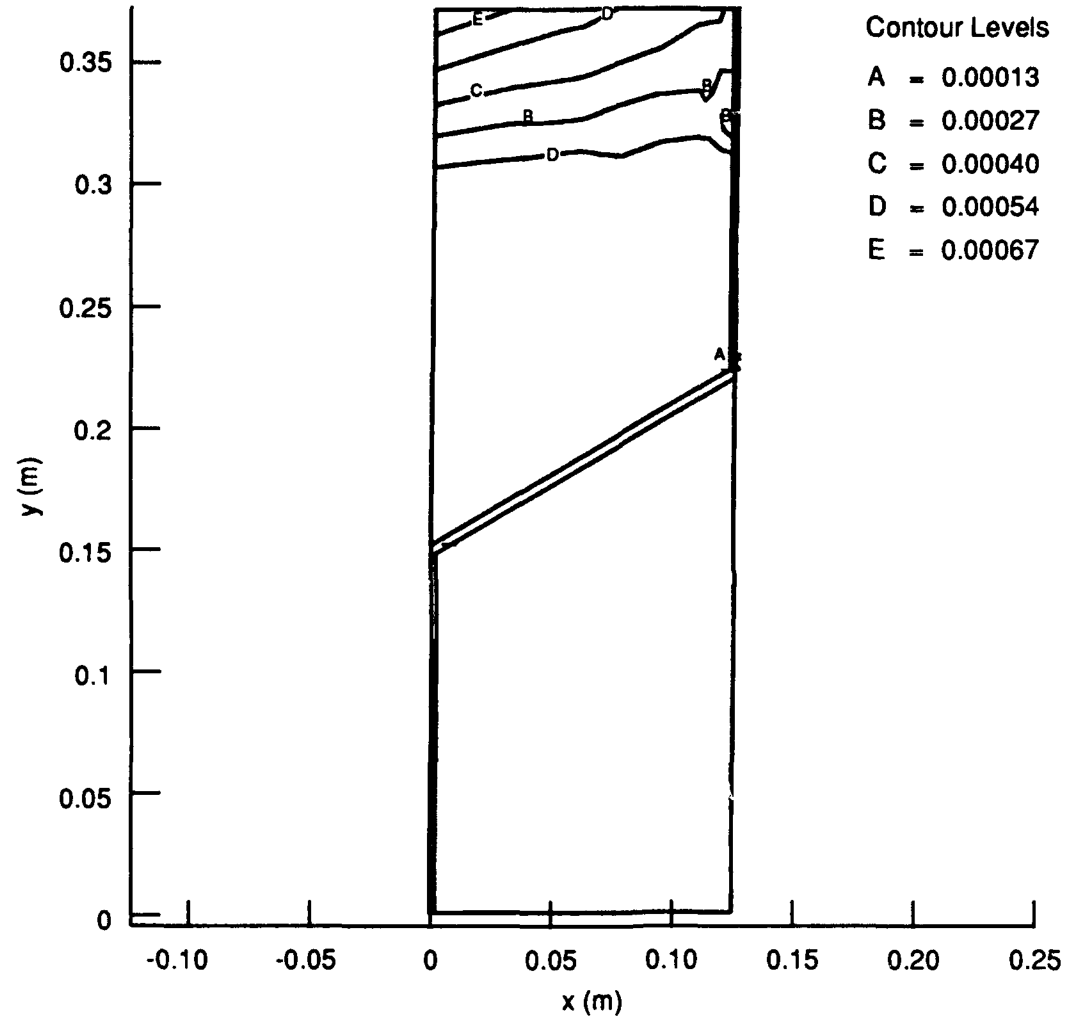

RM-7294-85

Figure 30. Effective plastic strain contours for DYNA2D calculation of the baseline case.

(10 ms problem, time 0.55 ms, ε = 1.51%.)

The greatest deformation occurs near the "heels" of the grain core, which are the right and left pairs of corners of the hexagons (see Figure 27b), and the least deformation occurs near the "toes," which are the top and bottom corners of the hexagons. In the heels, from $\varepsilon = 1.6\%$ to $\varepsilon = 1.9\%$, both boundary void volume fractions and core effective plastic strains increase faster with DYNA2D. The differences between DYNA2D and NIKE2D remain on the order of 10–20%, and the two problems still give quite similar results.

At $\varepsilon = 2.0\%$, differences in the results of the two codes become very significant. In the transverse part (the part between the toe and heel regions, see Figure 27b) of the grain boundary, any void volume fraction calculated with NIKE2D is smaller than any calculated with DYNA2D (Figure 29a). Maximum effective plastic strains calculated with NIKE2D are as much as twice those calculated with DYNA2D (Figure 29b).

At $\varepsilon = 2.2\%$, DYNA2D results can no longer be trusted, since unstable void growth has probably occurred; and by $\varepsilon = 6.6\%$, all the deformation has concentrated into the middle of the transverse boundary cells (Figure 31). NIKE2D void volume fractions and effective plastic strains continue to increase smoothly until the NIKE2D solution diverges at $\varepsilon = 2.56\%$. In contrast with the DYNA2D results, we do not observe any sharp increase in the void volume fraction calculations of NIKE2D.

Because the NIKE2D results are smoother and because wave propagation is not relevant for the problem we wanted to investigate, we used NIKE2D for the remainder of the calculations discussed here, wherein we varied parameters from the baseline calculation. The results of the parametric study, which were obtained by varying the parameters of the constitutive model as indicated in Table 11, are compared and discussed below. The comparison is based on the NIKE2D baseline calculation described above and is intended to give physical insight into the grain core/grain boundary problems and how variations in the material parameters might lead to fracture by different mechanisms.

NIKE2D Parametric Study: Denser and Porous Grain Boundary Cases

Let us first compare the evolution of the void volume fraction in the boundary material for the denser and porous grain boundary cases, which both can be looked at as representing soft grain boundaries. Figure 32 shows the locations of elements to which we will refer often in the following discussion. Elements 80, 65, and 72 are located in the middle of the transverse

Table 11

MATERIAL PARAMETERS FOR INVESTIGATED PROBLEMS

Calculation	Y_0 (GPa)	f_0
Baseline grain boundary	1.15	0.0082
Denser grain boundary	1.15	0.0050
Porous grain boundary	1.37	0.0082
Hard grain boundary	1.6	0.0082

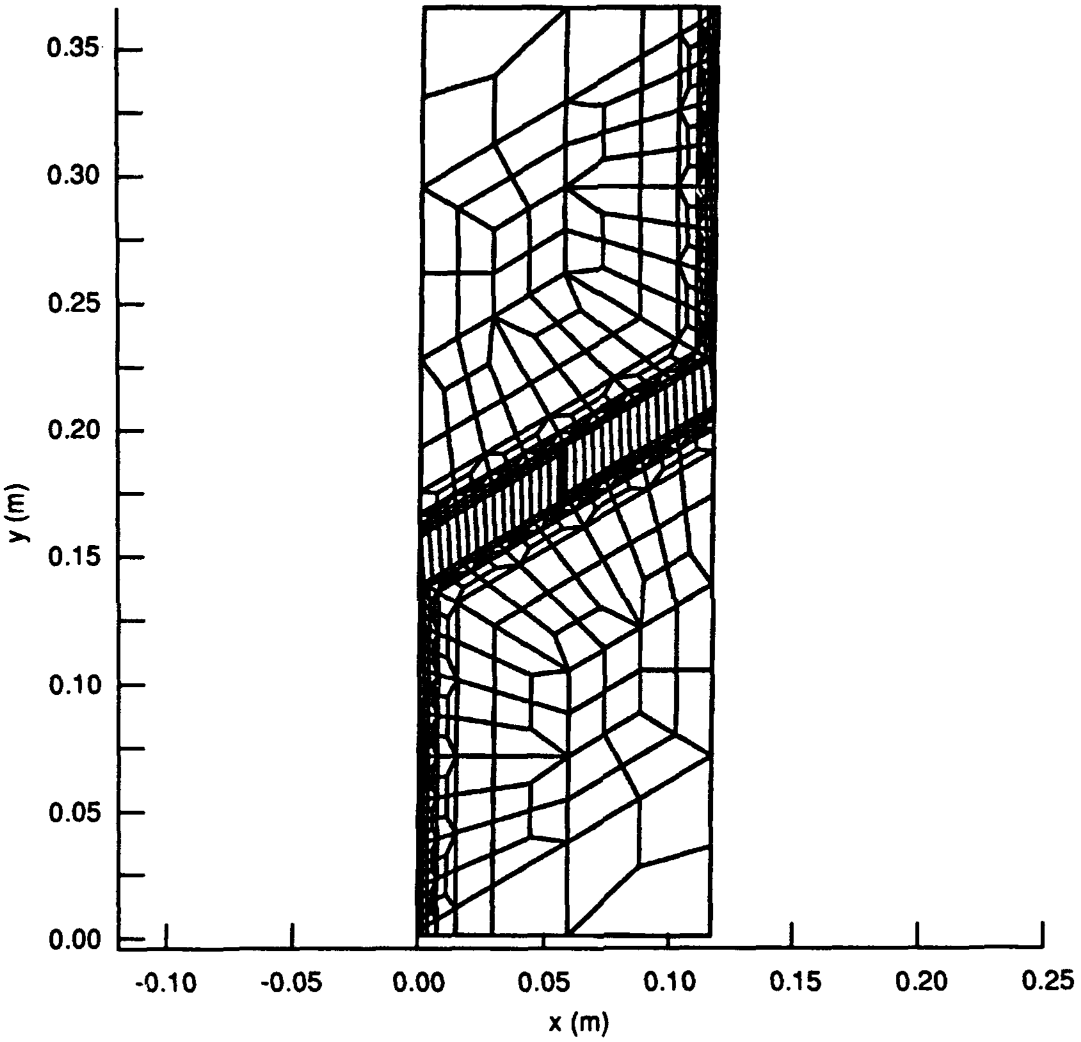

RM-7294-86

Figure 31. Deformed mesh for DYNA2D simulation of the baseline problem ($\varepsilon = 6.58\%$).

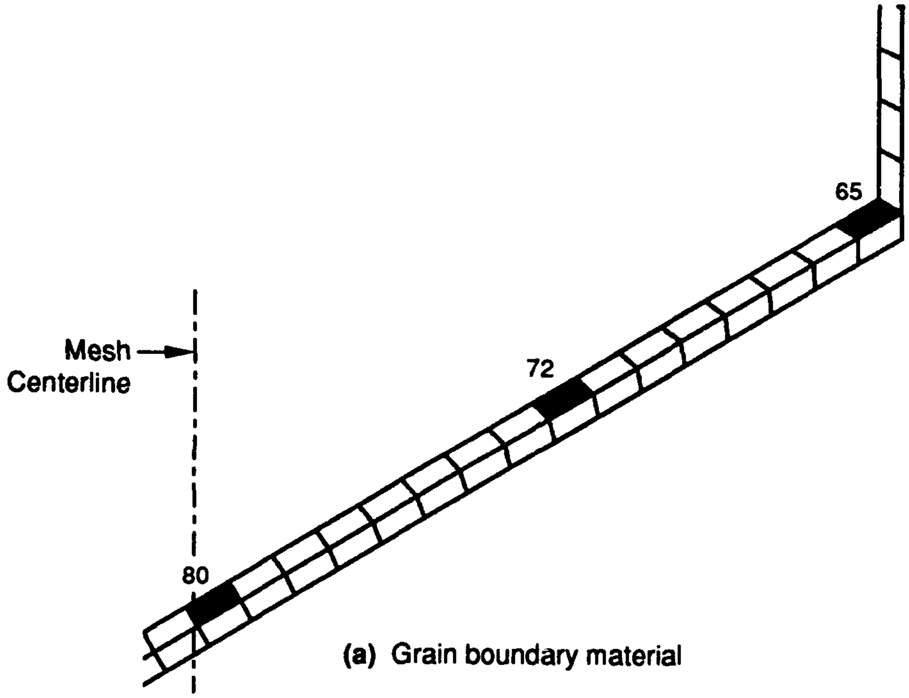

(a) Grain boundary material

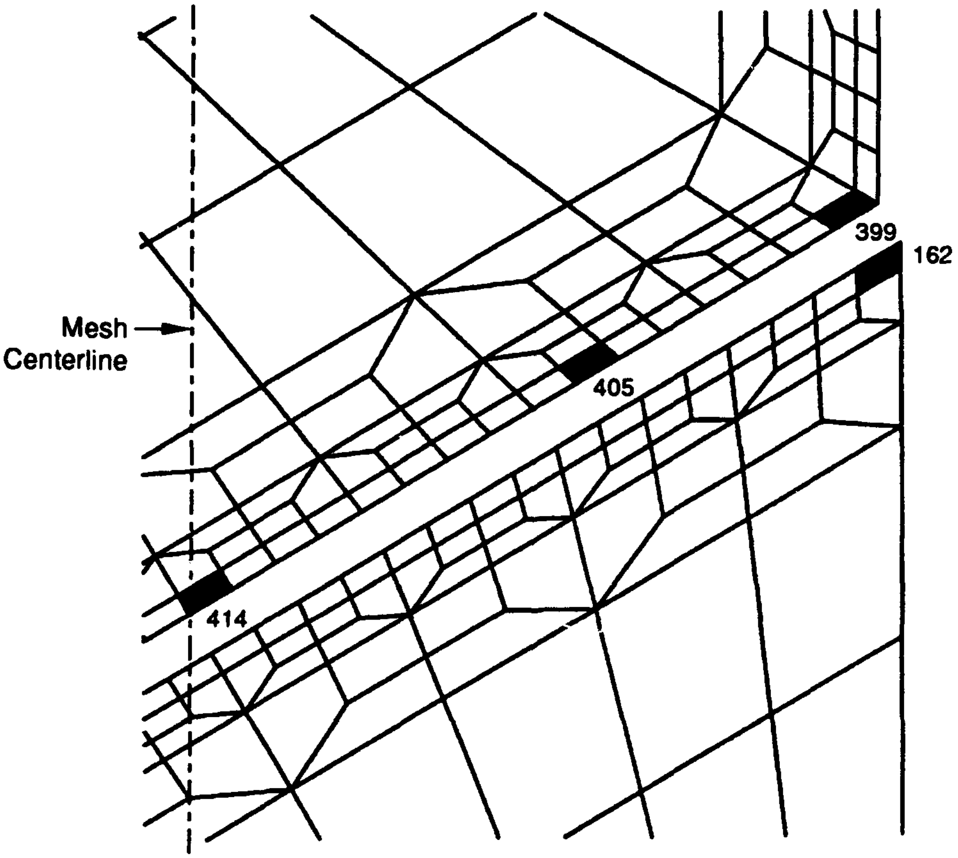

(b) Grain core material

RM-7294-87

Figure 32. Element locations for midpoint (80, 414), quarter point (72, 405), heel (65, 399), and toe (162).

boundary, within the triple point between the top core material (heel) and bottom core material (toe), and about halfway between, respectively. Elements 414, 399, 162, and 405 are located just above the middle of the transverse boundary, in the heel near the triple point, in the toe near the triple point, and about halfway between, respectively. The void volume fraction histories for boundary elements 65, 72, and 80 are reported in Figure 33 for all four studied conditions.

Void volume fractions increase earlier in the denser grain boundary case ($f_0 = 0.0050$, $Y_0 = 1.15$ GPa) than in the porous grain boundary case ($f_0 = 0.0082$, $Y_0 = 1.37$ GPa) because of the lower initial yield strength of the boundary material in the former. They also increase faster and in a less homogeneous way: in Figure 33 the three curves for elements 65, 72, and 80 for the porous case almost overlay which is not the case for the denser case. As in all cases presented in this report, the void volume fractions always increase faster in the center of the boundary layer than at the edges: Element 80 always has the highest void volume fraction, albeit only toward the end of the calculation for the hard grain boundary case ($f_0 = 0.0082$, $Y_0 = 1.60$ GPa).

At a global strain close to $\varepsilon = 1.64\%$, the increase in void volume fraction slows briefly for all but the hard grain boundary case. This slowing may be due to the beginning of plastic deformation in the grain core material. However, these plastic deformations harden the grain core material, and subsequently the grain boundary void volume fractions increase again at an accelerated rate.

The solution to the denser grain boundary case diverges at $\varepsilon = 2.79\%$. The maximum void volume fraction is about twice the initial one. Meanwhile, the porous grain boundary case continues past $\varepsilon = 2.79\%$, and void volume fractions continue to increase. The void volume fractions actually differ only slightly from each other at $\varepsilon = 2.79\%$.

The effective plastic strains in the grain core material also differ amongst the calculations. They are less homogeneous and their maximum is higher in the baseline calculation, although the denser grain boundary case is very similar (compare Figures 34 and 35). In any case, the evolution of the strain is qualitatively the same, with maxima located inside the heel and minima located in the toe. As shown in Figure 36, the effective plastic strains appear to concentrate in a band aligned with the diagonally opposed corners of the grains.

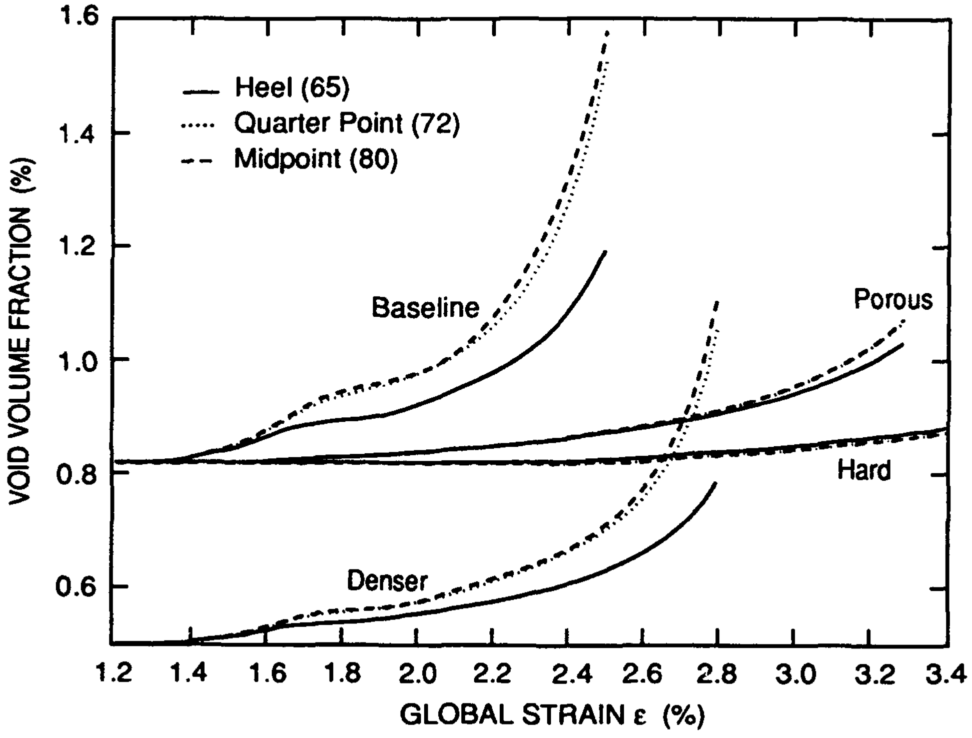

RAM-7294-88

Figure 33. Void volume fraction histories.

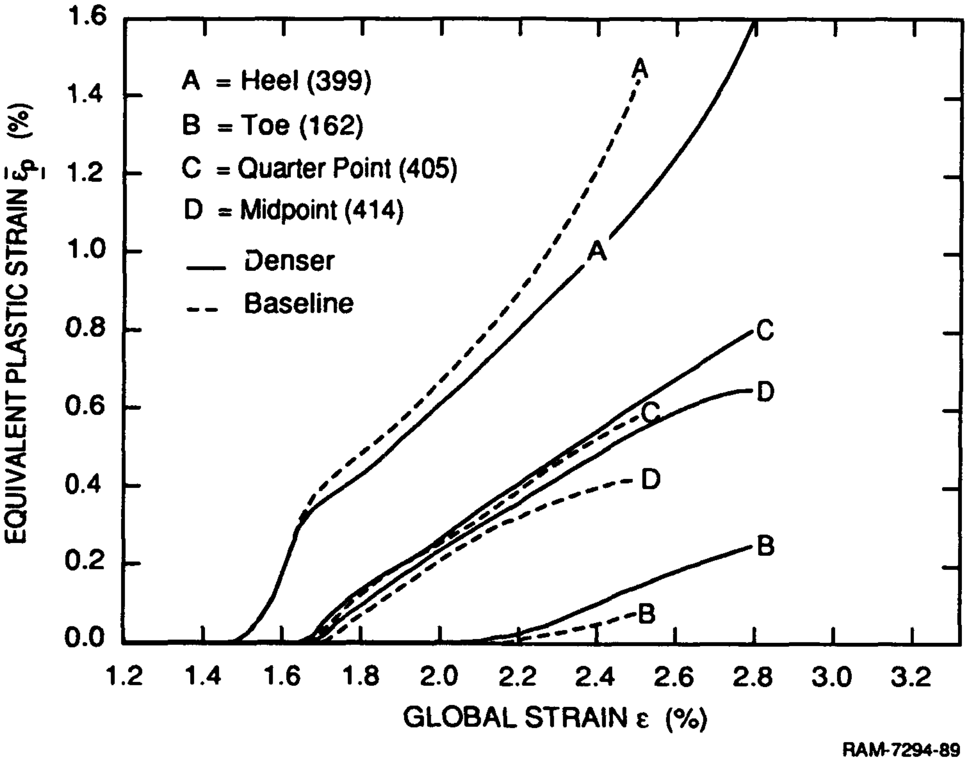

Figure 34. Equivalent plastic strain histories in the grain core for baseline and denser grain boundary calculations.

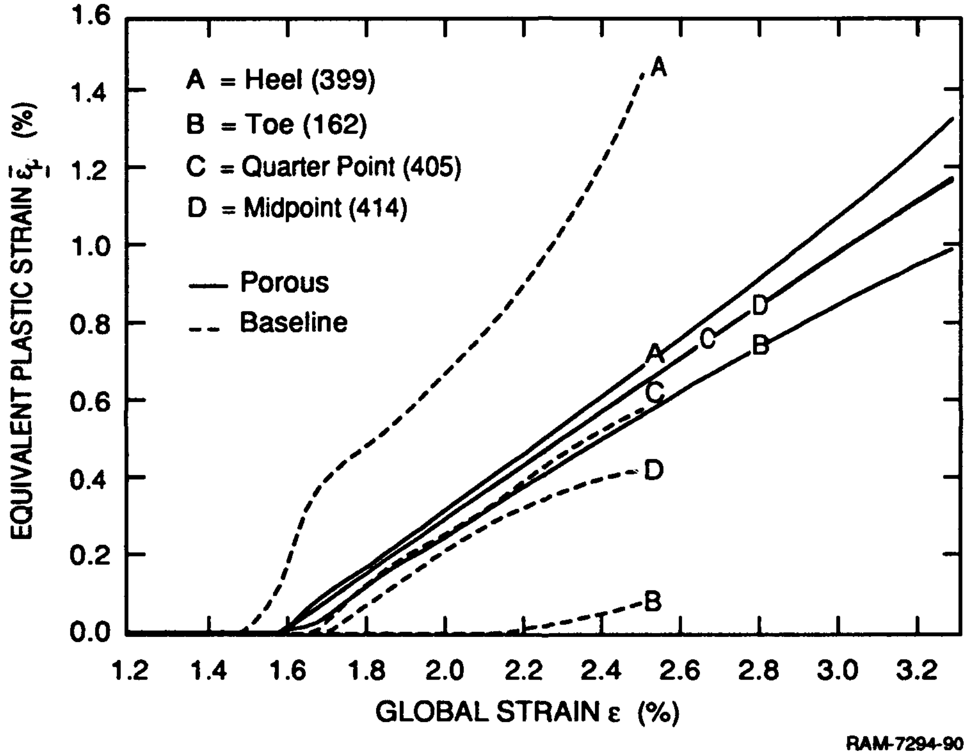

Figure 35. Equivalent plastic strain histories in the grain core for baseline and porous grain boundary calculations.

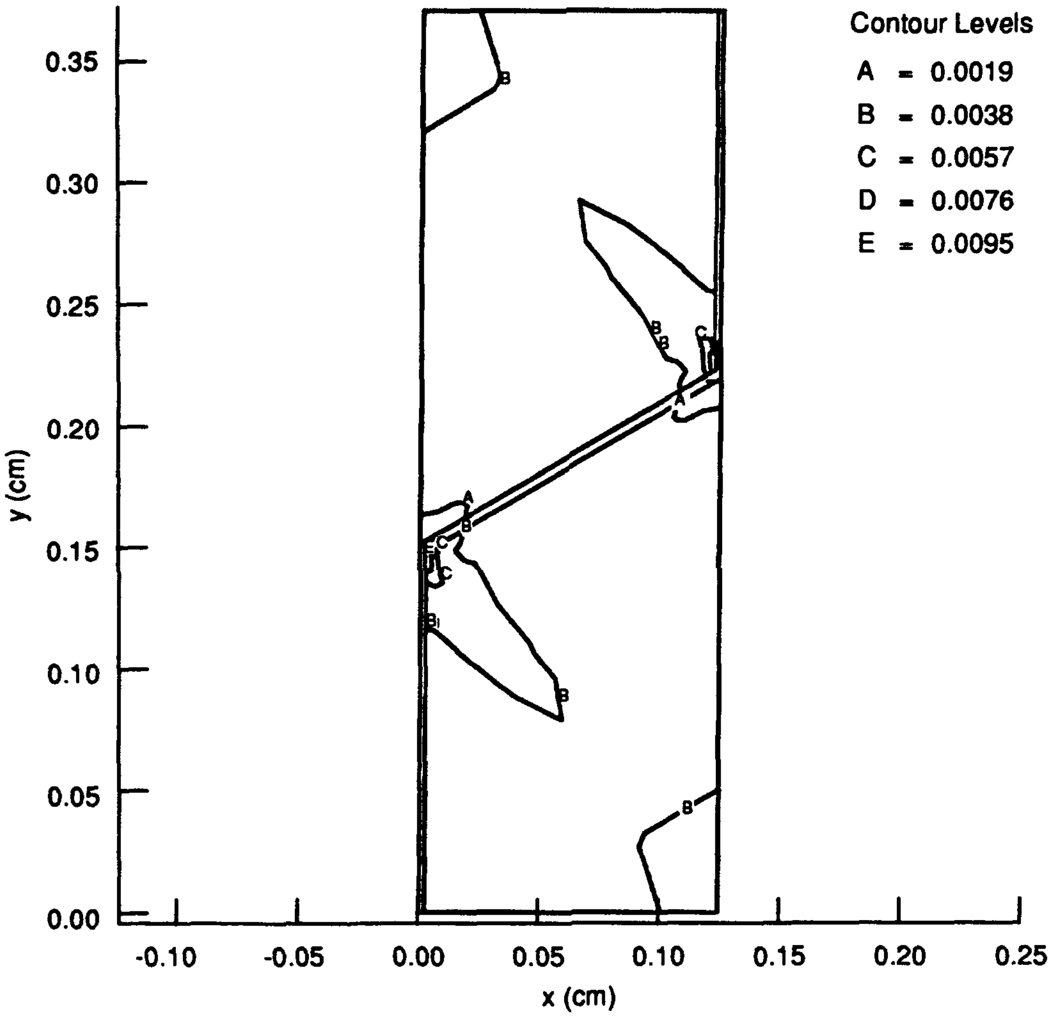

RM-7294-92

Figure 36. Effective plastic strain contours for the denser grain boundary calculation, ε = 2.10%.

NIKE2D Parametric Study: Hard Grain Boundary Case

If our interpretation is correct, making the boundary material initially harder than the core material should provide results opposite to those described above. In particular, we expect the void volume fractions to be higher at the edges of the transverse boundary layer instead of in the middle of it. Also, we expect minimum and maximum plastic deformations in the core material to shift locations. Of course, since the core material can only harden and the boundary material can only soften, these assumptions will only hold as long as the boundary material stays harder than the core material.

The numerical results confirm our expectations. Plasticity (concomitant with void growth in the boundary) begins significantly earlier in the grain core material (Figure 37) than in the boundary material (Figure 33). In the grain core material, plasticity is now maximum in the toe of the core and aligned with the vertical boundaries of the grains, because the strong vertical boundary layer forces this part of the core material to undergo more horizontal stretching (Figure 38). Plasticity is now smaller in the heel (Element 399) because the strong vertical and transverse parts of the boundary layer protect this part of the core material from deformations. In the grain boundary material, void volume fractions are now maximum at the edges of the transverse boundary layer (Figure 33) and in the vertical boundary layers. Also, void volume fractions are more homogeneous than in the other three problems because of the higher initial strength of the boundary material.

DISCUSSION

We now discuss the above results and attempt to relate the calculated responses to those observed in experiments.

Comparison of DYNA2D and NIKE2D Results

DYNA2D and NIKE2D results for the baseline case are not strictly comparable. The reason for this is at least partially physical, since the DYNA2D simulation includes wave propagation (because of the higher imposed boundary velocity) whereas the NIKE2D problemdoes not. Thus, even though the constitutive models used are not rate sensitive, the load is not distributed in exactly the same way in the two types of simulations, which may cause some differences in the results. But the reason for these differences may also be numerical, since the

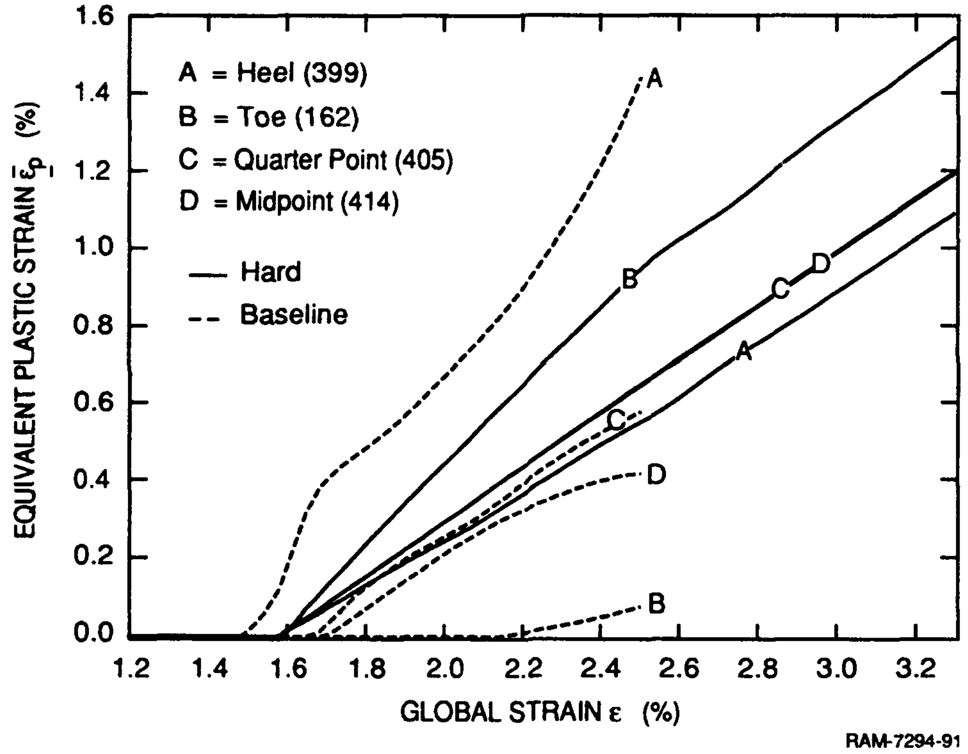

Figure 37. Equivalent plastic strain histories in the grain core for baseline and hard grain boundary calculations.

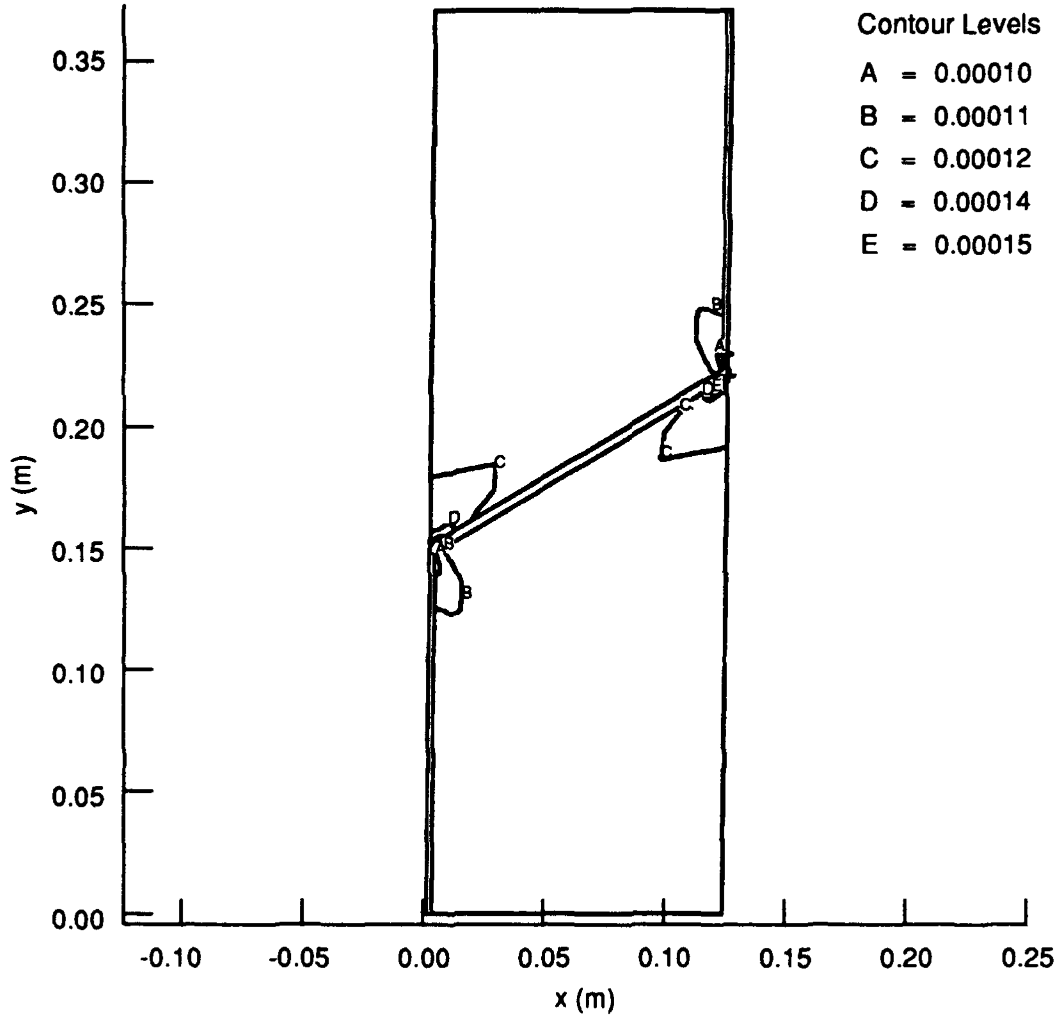

RM-7294-93

Figure 38. Effective plastic strain contours for the hard grain boundary case, $\varepsilon = 3.29\%$.

two codes are very different. However, the main difference between the two types of simulations is the way the ductile failure process develops. Roughly speaking, after a phase where results are very similar, failure happens quickly but stably in the DYNA2D simulation, whereas the NIKE2D simulation continues running smoothly until finally divergence occurs from one computational step to the other, before we can really know what happens in terms of damage localization. We presume that the divergence of the NIKE2D simulation is associated with a failure via bifurcation, which causes the solution to diverge because NIKE2D cannot handle the nonequilibrium increase of void volume fractions and deformations that accompany this process. Whether the divergence can be delayed by altering implementation of the Gurson/Tvergaard model into NIKE2D or by altering the solution search parameters used by NIKE2D has not been clarified, but it appears unlikely. Bifurcation will be discussed more below.

On the basis of these results we conclude that, as far as the choice of a code is concerned, NIKE2D is preferable to describe what happens in static problems up to, but not including, failure. But if the process of interest is failure itself, the DYNA2D code is preferable, because it can simulate the mechanisms of failure whereas the NIKE2D code cannot.

NIKE2D Parametric Study

The results of the parametric NIKE2D study only differ from a quantitative point of view. Qualitatively, all of them show the same kind of phenomena. Minor modifications of the parameters, however, change the results significantly in terms of timing and amplitude. The baseline NIKE2D calculation showed an early divergence of the solution, probably due to a very fast increase of void volume fractions. Decreasing the initial void volume fraction from $f_0 = 0.0082$ to 0.0050 delayed divergence, and a 20% increase of the initial yield strength of the grain boundary material was enough to obtain a solution to $\varepsilon = 3.3\%$. This behavior shows that results are quite sensitive to constitutive parameters. It also emphasizes the need for precise constitutive models, if quantitative results are expected.

All of the analyzed problems begin with an elastic deformation phase. Since the elastic moduli of the grain core and the grain boundary materials are identical, both materials behave the same way during this phase (this would not be the case for the real titanium microstructure, since the grain core and the grain boundary contain different crystallographic phases). Then plasticity begins in the most severely loaded softer cells.

In the baseline and denser grain boundary cases, the softer cells are the boundary cells. So the Gurson/Tvergaard model begins to increase void volume fractions and effective plastic strains in the boundary material. Increasing void volume fractions further soften the material and increasing effective plastic strains harden it. These two mechanisms compete, but the overall effect is a softening of the boundary material. Figure 33 shows that not all grain boundary cells react the same way: void volume fractions (and effective plastic strains) increase faster in the middle of the transverse boundary layer and slower at the edges of the transverse boundary layer and in the vertical boundary layers. We think that this strain distribution is due to the presence of the two vertical boundary layers: on both sides of the mesh there are many more boundary material cells than on any other line parallel to these sides. So plasticity is shared by many more cells, thus making effective plastic strains and void volume fractions increase more slowly. The result of this deformation phase, which is plastic for the grain boundary material and elastic for the core material, is a softening of the boundary material, with more pronounced softening in the middle of the mesh. The boundary material, which was initially softer than the core material, is now even softer and no longer homogeneous.

The plastic grain boundary/elastic grain core deformation phase does not take place in the porous grain boundary case, because the initial yield strengths of both materials are equal.

In the next deformation phase, both the core and boundary deform plastically. The initial conditions of this phase are different for the baseline and denser grain boundary case on the one hand and the porous grain boundary case on the other hand, because of the preliminary plastic grain boundary/elastic grain core deformation phase taking place for the baseline and denser grain boundary cases. However, the subsequent deformation phase is qualitatively the same for all three problems. The only difference between the porous grain boundary, baseline, and denser grain boundary cases is that, at the onset of the plastic/plastic deformation phase, failure develops more quickly in the baseline and denser grain boundary cases, owing to a softer and less homogeneous boundary layer.

During the plastic/plastic deformation phase, two noticeable things happen. First, void volume fractions increase in the inhomogeneous way described for the plastic/elastic deformation phase (when it exists). The reasons for the inhomogeneous void growth are the same as those invoked earlier for the plastic/elastic deformation phase. As a consequence of inhomogeneous damage accumulation, the boundary material becomes increasingly softer, and this process is not stable: the softest regions of the grain boundary soften faster than the less soft parts. The situation becomes as if the transverse part of the grain boundary was "pinned" at the edges.

The second noticeable process consists of concentrated plastic deformation bands appearing and growing in the grain core material. The bands are formed in the heel and aligned with diagonally opposed corners of the grain. Our explanation for this localization relies on the presence of the vertical grain boundary regions. The grain core material located in the toe (see, for instance, curve B for Element 162, in Figure 34) is less deformed because the softer vertical grain boundary layer with which it is aligned protects it. The grain boundary layer absorbs much of the deformation. The grain core material located in the "heel" (see, for instance, curve A for Element 399, in Figure 34) is more deformed because the softer vertical grain boundary tends to make it move faster than the rest of the grain core material, thus developing shear stresses.

We are not certain why deformations concentrate in the directions of the diagonally opposite corners of the mesh (see Figure 36). This direction could be physical or nonphysical: the deformations might simply grow toward the corners of the mesh regardless of the physics involved. We intuitively expected the deformations to grow in the direction of the transverse grain boundary regions (Figure 39). Nevertheless, if we assume that deformations should grow in the direction of diagonally opposite corners, as shown in Figure 39, this direction is likely to be privileged for the growth of damage because deformations arising from two opposite corners of the hexagonal grain would meet each other, generating a weak direction in the grain. We note that if the grains had been regular instead of elongated hexagons, we would not have noticed the misalignment between the strain concentration direction and the boundary angle bisector, since mesh corner directions and boundary bisector directions would have coincided.

Our interpretations of the plastic/plastic deformation phase rely on the presence of vertical grain boundary regions that are softer than the grain core material. These vertical boundary regions were suggested as the reason why plasticity concentrates in the middle of the transverse grain boundary region. They were also suggested as the cause of the localization of plasticity inside the grain core material. If these explanations are correct, our conclusions should be reversed if we make the boundary layer initially harder than the core. Below we will see that this is indeed the case.

The denser grain boundary case diverges at $\varepsilon = 2.79\%$, whereas the porous grain boundary case continues beyond $\varepsilon = 3.3\%$. Earlier, we assumed that divergence was due to a sudden (unstable) increase of void volume fractions that NIKE2D was not able to simulate. We are still not certain, however, why the void volume fractions suddenly increase or how this can result in a divergence.

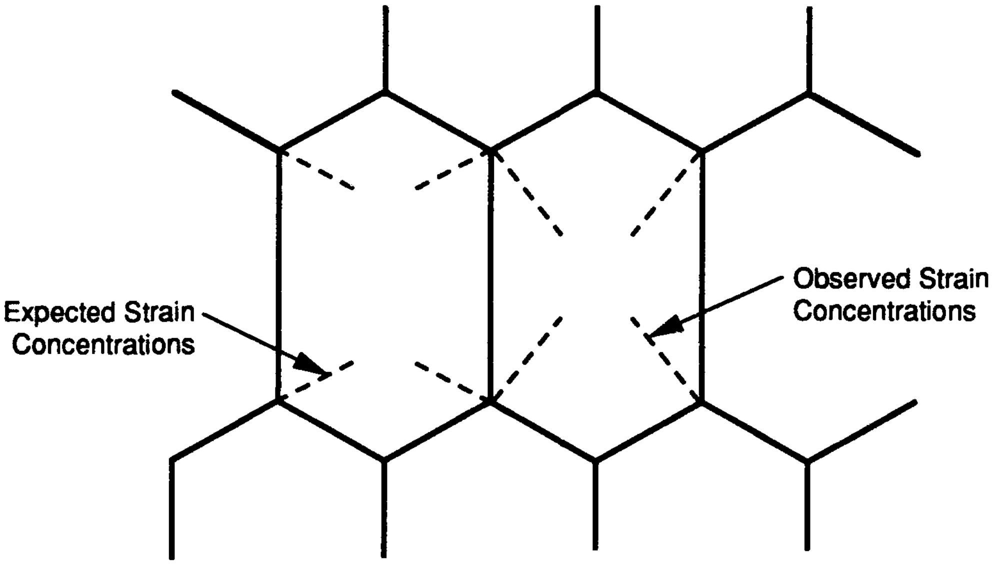

RAM-7294-94

Figure 39. Strain concentration locations, soft grain boundary cases.

The sudden increase in void volume fraction is probably a bifurcation. During the plastic/plastic deformation phase, both the grain core and boundary materials harden, with the hardening probably continuing until the point where the hardening of the transverse grain boundary, in a globally averaged sense, stops and softening sets in. In other words, the load-displacement relationship for the transverse boundary reaches a local maximum and the core material suddenly recovers some of its elastic deformations. Of course, this change causes very large and sudden deformations: the void volume fraction increases dramatically in the grain boundary layer, and NIKE2D diverges. Because of its divergence, NIKE2D cannot show the strain recovery occurring in the core material, but the DYNA2D code can. Figure 40 shows the vertical displacements of the corner nodes of Element 80, located in the middle of the transverse grain boundary region (see Figure 32), and demonstrates that the grain core material indeed recovers. In the beginning of the calculation, all four displacements increase together. Then, as plastic deformations increase and voids grow, these displacements gradually increase at different speeds. Finally, at about $\varepsilon = 2.06\%$, the displacement of the two top nodes suddenly increases whereas the displacement of the two bottom nodes reverses direction. Thus, the recovery of the grain core material drives the huge deformation (in fact, probably the failure) of the transverse grain boundary region.

The exact conditions for the onset of instability in the transverse grain boundary region have not been investigated. They may be related to a critical softening of the hardest parts of the transverse boundary region, i.e., its edges. Bifurcation probably occurs when global softening sets in, by which we mean that the load-displacement relation for the top edge of the grain boundary region passes through a maximum. Insertion into NIKE2D of a test for bifurcation along the lines of that used by Tvergaard[30] would increase understanding of the grain array failure process.

The nonequilibrium nature of bifurcation explains why NIKE2D diverges. As the imposed displacement of the top edge increases, the corresponding load increases, both during the plastic/elastic deformation phase and during the beginning of the plastic/plastic deformation phase (because of hardening). Then the load suddenly decreases as shown schematically in Figure 41. The suddenload drop is not an equilibrium process, and NIKE2D fails to find a solution. DYNA2D finds a solution because it uses a different solution scheme that does not rely on finding equilibrium states.

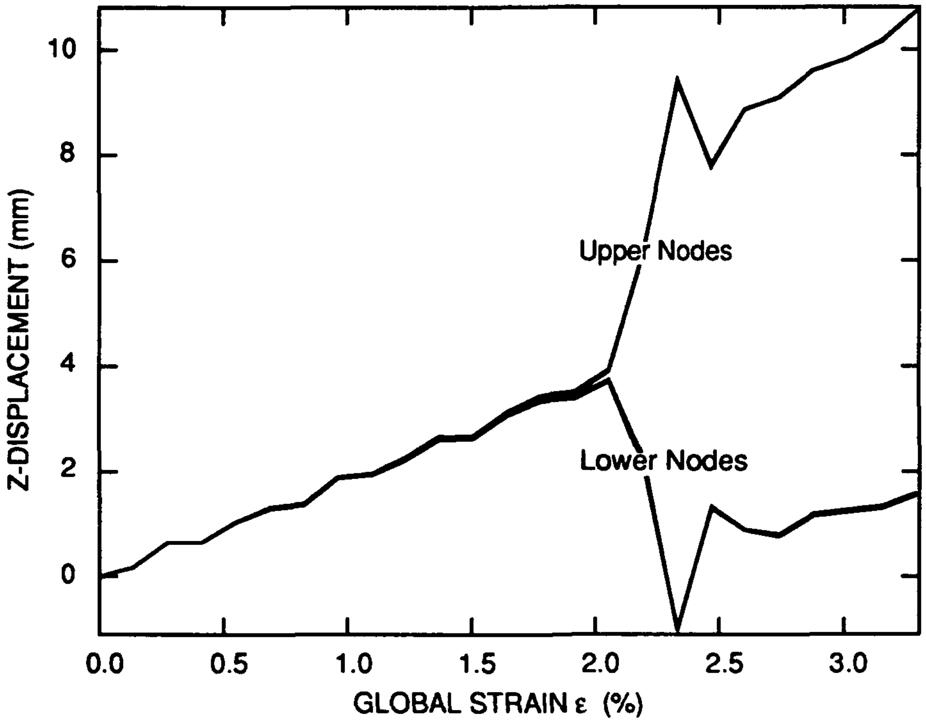

RAM-7294-95

Figure 40. Vertical displacement of the upper and lower nodes of the midpoint, Element 80, for the DYNA2D calculation.

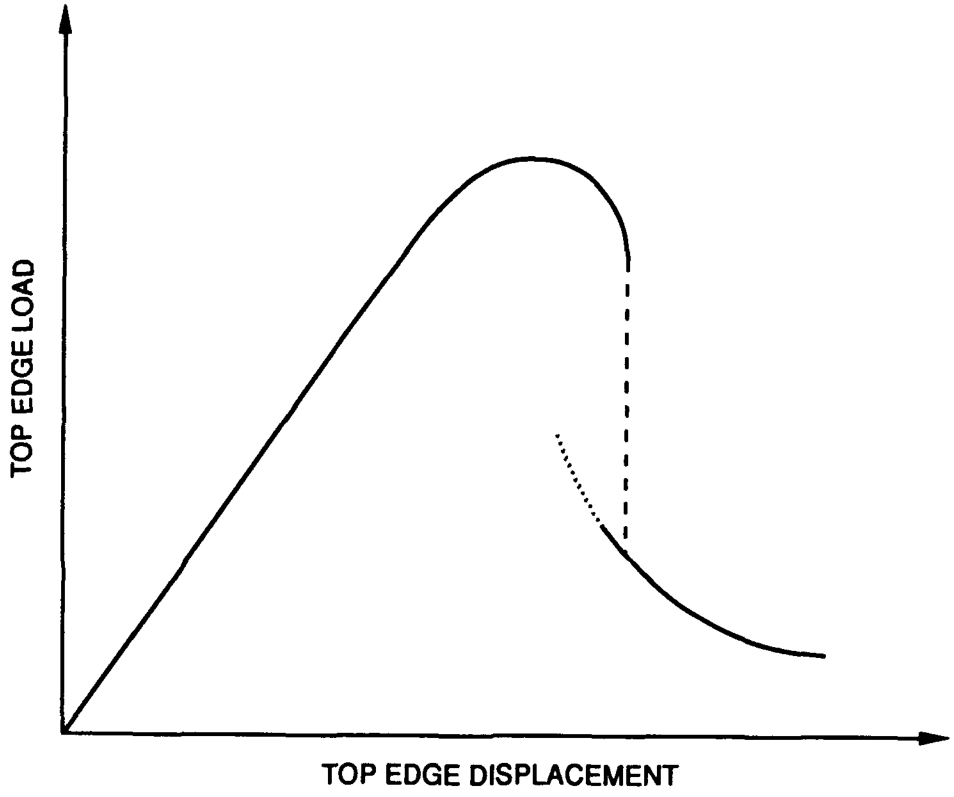

RAM-7294-96

Figure 41. Load-displacement path for the top edge of the finite element mesh.

The solution for the hard grain boundary case is essentially opposite to the solution for the soft boundary cases (compare Figures 33, 36, 38, and 42). The grain core yields first, plastic strains concentrate in the toe, and void volume fractions are now maximum at the edges of the transverse boundary and in the vertical boundaries. Therefore, it is possible that the damaged direction in the core material will now be the one shown in Figure 43 instead of that shown in Figure 39 for the soft boundary cases. Thus, a different kind of failure mechanism may appear in this case. However, since the grain core material can only harden and the grain boundary material eventually softens, this situation does not persist. The difference between the highest and the lowest void volume fractions or effective plastic strains does not keep increasing as fast as it did in the other cases (see Figures 33 and 36). At the end of the calculation, it actually begins to decrease (Figure 42).

The boundary material eventually becomes softer than the core material, and what happens subsequently appears qualitatively the same as what happens in the cases with initially soft boundaries (baseline and denser and porous grain boundary cases). The void volume fractions finally become higher in the middle of the transverse boundary layer at $\varepsilon = 4.11\%$. Unlike what happens to the void volume fractions, however, the locations of plastic strain maxima and minima do not have time to concentrate along diagonal bands before divergence, as they do in the soft boundary cases. The curves in Figure 42 show that effective plastic strains always remain quite homogeneous. Divergence finally occurs at $\varepsilon = 4.54\%$.

What happens in the hard boundary problem can be summarized as follows. First, deformation and void growth happen opposite to the way they happen in the soft boundary cases and a different weak direction develops (Figure 43), but then the deformation phenomena that took place in the soft boundary problems develop, and these deformation phenomena dominate the problem.

Because we have not attempted to model the actual failure process, we cannot tell whether the plastic strain concentrations that develop in the grain core would really lead to failure. For example, the strain concentration that develops and then disappears in the hard boundary problem may persist in the actual alloy and lead to a fracture of the grain. Note also that, the direction in which plastic strains localize in the actual microstructure will also be influenced by the crystallography of the grain and by the orientation of the slip systems with respect to the external loading axis.

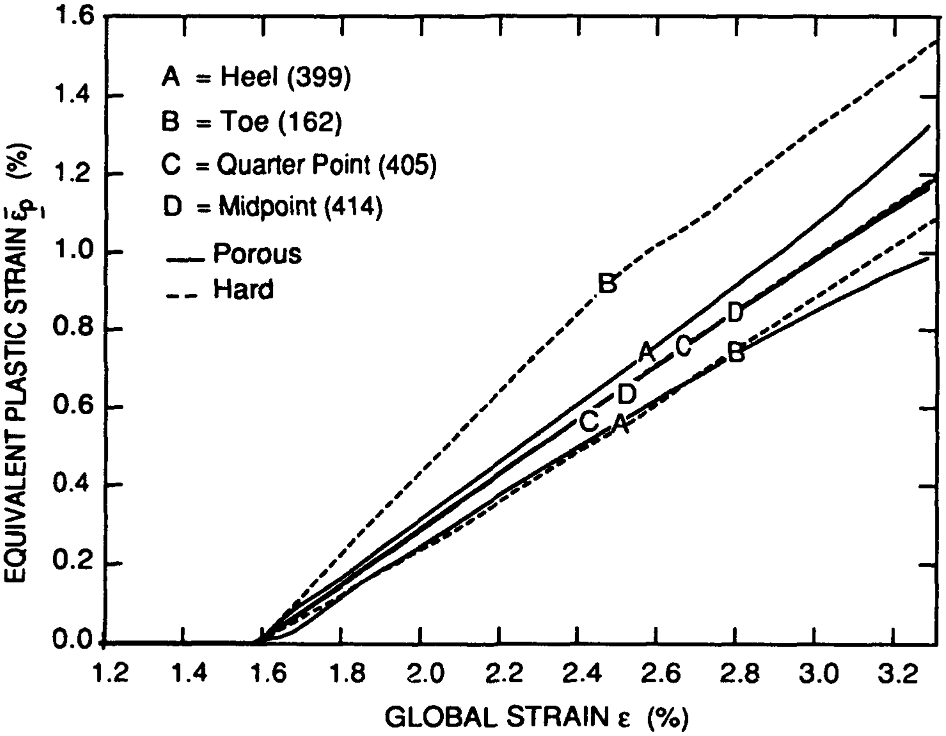

RAM-7294-97

Figure 42. Equivalent plastic strain histories in the grain core for the porous and hard grain boundary cases.

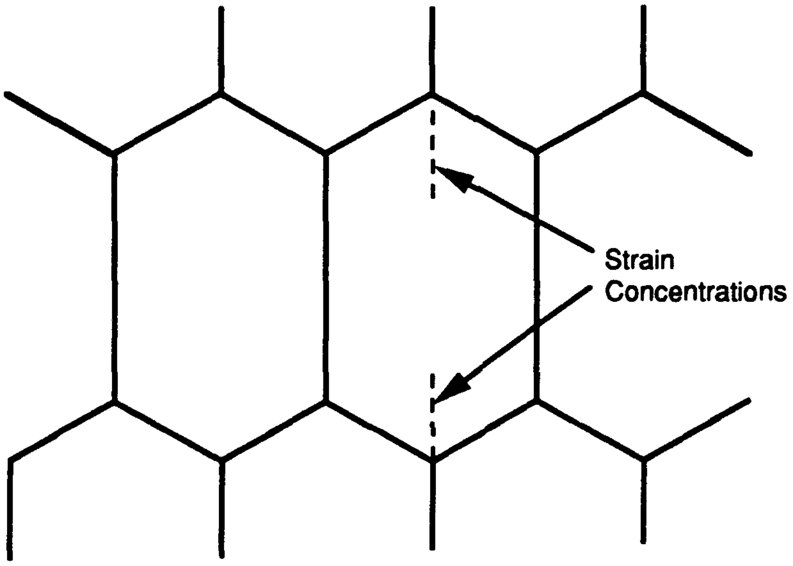

RAM-7294-98

Figure 43. Strain concentration locations, hard grain boundary case.

CONCLUSIONS

The objective of this work was to simulate with finite element codes (NIKE2D and DYNA2D) the behavior of an array of grains of a titanium alloy, with separate material models used for the grain cores and grain boundary layers. We sought to develop an understanding of the interaction between heterogeneous grain core and boundary material under conditions of highly triaxial stress and quasi-uniaxial strain extension. We used a modified Gurson model for the grain boundary and a strain-hardening plasticity model for the cores.

With this relatively simple microstructural model, we were able to reproduce some microfailure features observed in the alloy Ti-10V-2Fe-3Al and to rationalize the effect of the relative grain boundary/grain core strength on the fracture behavior of this alloy and of Titanium alloys more generally. For instance we showed that voids grow at a faster rate in the mid portion of soft grain boundaries than at the triple points and that void softening in the grain boundary may be accompanied by strain localization in the grain core. By considering elastic strain recovery of the grain core we identified a mechanism for inducing unstable void growth in the grain boundary (a process that would lead to void coalescence in the actual microstructure) and forming a grain boundary crack. The consistency between the experimental microfracture observations and the results of the simulations is encouraging and indicates that the approach taken here hold some promise. We should however emphasize that several important micromechanisms of deformation and fracture were not modeled at all in the finite element simulations. First, void nucleation was not considered. It is conceivable that certain void nucleation mechanisms could significantly alter the predicted void distribution, shifting the maximum void activity from the mid region of the grain boundary to the triple points, and also affecting the strain distribution in the grain core. Second, we did not model the grain core crystallography and the details of the slip properties. Again, a more detailed description of the core material, may result in a significantly different strain localization pattern. More over, the activation of specific slip systems in the grain core may result in the nucleation of voids on specific parts of the grain boundary (slip-induced grain boundary nucleation) and therefore in a somewhat different failure mode for the grain boundary.

We also showed that both qualitative and quantitative results were sensitive to minor changes of the properties of the core and boundary and that it is desirable to characterize these properties better in order to achieve more representative predictions.

The next steps to improve the finite element models should be to represent the distribution of α_p particles in the grain core, to simulate the influence of the crystal structure on the grain deformation, and to introduce void nucleation models. Simulating the distribution of α_p particles might be achieved by introducing a finer mesh and assigning different material properties to selected, randomly distributed elements in the grain core. This approach may not be computationally practical because of the large number of elements that would be required. A multiplane plasticity model, SHEAR4,[33] could serve to model the influence of the crystal orientation on strain localization within the grain core as well as failure along a strain localization band. To our knowledge, no reliable void nucleation model relevant for grain boundary nucleation is currently available and considerable development is needed in this area.

From a computational point of view and for the purpose of future modeling efforts along the lines of the modeling presented in this study, we note that NIKE2D diverges, apparently when the boundary layer softens globally and the core recovers elastically. Since the bifurcation is not an equilibrium process, divergence seems unavoidable. However, this may not matter since divergence seems to happen at the onset of a very fast failure process that currently is not the most interesting part of the problem.

Unlike NIKE2D, DYNA2D is able to describe the failure process. But when used instead of NIKE2D for quasi-static calculations, DYNA2D has precision problems. Also DYNA2D and NIKE2D results are not quantitatively identical. Thus, care should be taken when using DYNA2D to extend solutions beyond NIKE2D divergences.

REFERENCES

1. J. H. Giovanola and D. A. Shockey, "Dynamic Fracture Behavior of Structural Materials, " Final Report prepared for Air Force of Scientific Research, Contract No. AFOSR/F49620-81-K-0007, SRI Project No. 2777, SRI International, Menlo Park, CA, July 1986.

2. J. H. Giovanola, R. W. Klopp, J. W. Simons, T. Kobayashi, and D. A. Shockey, "Influence of Microstructure and Microdamage Processes on Fracture at High Loading Rates," Final Report prepared for Air Force of Scientific Research, Contract No. AFOSR/F49620-86-K-0010, SRI Project No. 1750, June 1989.

3. K. A. Hartley, J. Duffy, and R. H. Hawley, "The Torsional Kolsky (Split-Hopkinson) Bar," in *Metals Handbook,* Ninth Ed., Vol. 8, *Mechanical Testing* (American Society for Metals, Metals Park, OH), pp. 218-228

4. T. Kobayashi and D. A. Shockey, "FRASTA: A New Way to Analyze Fracture Surfaces, Part 1: Reconstructing Crack Histories," Advanced Materials & Processes **140**, No. 5 (1991); "FRASTA: A New Way to Analyze Fracture Surfaces, Part 2: Determining Fracture Mechanisms and Parameters," Advanced Materials & Processes **140**, No. 6 (1991).

5. T. W. Duerig and J. C. Williams, "Overview: Microstructure and Properties of Beta Titanium Alloys," in *Beta Titanium Alloys in the 1980s*, R. R. Boyer and H. W. Rosenberg, Eds. (The Metallurgical Society, Warrendale, PA, 1984), pp. 19-67.

6. T. W. Duerig, "Phase Transformations and Properties of Ti-10V-2Fe-3Al," Ph.D. Dissertation, Carnegie-Mellon University, Pittsburgh, PA, 1980.

7. T. W. Duerig, G. T. Terlinde, and J. C. Williams, "Phase Transformations and Tensile Properties of Ti-10V-2Fe-3Al," Met. Trans.A, **11**, 1987-1998 (1980).

8. G. T. Terlinde, T. W. Duerig, and J. C. Williams, "Microstructure, Tensile Deformation, and Fracture in Aged Ti-10V-2Fe-3Al," Met. Trans. A, **14**, 2101-2115 (1983);
T. W. Duerig, J. E. Allison, and J. C. Williams, "Microstructural Influences on Fatigue Crack Propagation in Ti-10V-2Fe-3Al," Met. Trans. A, **16**, 739-751 (1985).

9. R. R. Boyer and G. W. Kuhlman, "Processing Properties Relationships of Ti-10V-2Fe-3Al," Met. Trans. A, **18**, 2095-2103 (1987).

10. G. Terlinde, H. J. Rahjen, and K. H. Schwalbe, "Microsuucture and Fracture Toughness of the Aged β-Ti Alloy Ti-10V-2Fe-3Al," Met. Trans. A, **19**, 1037-1049 (1988).

11. J. D. Bryant and H. G. F. Wilsdorf, "The Effect of Increasing Loading Rate on Tensile Properties and Fracture Toughness of Ti-10V-2Fe-3Al," in *Proceedings of Impact 87, International Conference on Impact Loading and Dynamic Behavior of Materials, May 18-21,1987*, C. Y. Chiem et al., Eds. (DMG Informationsgesellschaft, Oberursel, Germany, 1988), 145-152.

12. K. Toyama and T. Maeda, "The Effect of Heat Treatment on the Strength and Fracture Toughness of Ti-10V-2Fe-3Al," Trans. Iron Steel Inst. Japan, 26, 814-821 (1986).

13. M. H. Campagnac and A. Vassel, "Transformations Structurales et Propriétés Mécaniques des Alliages de Titane Ti-10V-2Fe-3Al et Ti-10V-3Cu-3Al," Rapport Technique N^{o} 5/3578 M, Office National d'Etudes et de Recherches Aerospatiales, 92320 Châtillon, France, February 1986.

14. M. H. Campagnac, " Structures et Propriétés Mécaniques d'Alliages de Titane à Bas Transus Ti-10V-2Fe-3Al et Ti-10V-3Cu-3Al," Note Technique 1989-3, Office National d'Etudes et de Recherches Aerospatiales, 92320 Châtillon, France, September 1989.

15. J. C. Williams, J. C. Chesnutt, and A. W. Thomson, "The Effects of Microstructure on Ductility and Fracture Toughness of $\alpha+\beta$ Titanium Alloys," in *Microstructure Fracture Toughness and Fatigue Crack Growth in Titanium Alloys*, A. K. Chakrabarti and J. C. Chesnutt, Eds. (The Metallurgical Society, Inc., Warrendale, PA, 1987), pp. 255-271.

16. M. F. Kanninen, P. C. Gehlen, C. R. Barnes, R. G. Hoagland, G. T. Hahn, and C. H. Popelar, "Dynamic Crack Propagation Under Impact Loading," in *Nonlinear and Dynamic Fracture Mechanics*, N. Perrone and S. N. Atluri, Eds. (American Society of Mechanical Engineers, New York, 1979), pp. 185-200.

17. J. F. Kalthoff, S. Winkler, W. Böhme, and D. A. Shockey, "Mechanical Response of Cracks to Impact Loading," in *Proceedings of the International Conference on Dynamical Properties and Fracture Dynamics of Engineering Materials* (Czechoslovak Academy of Sciences, Institute of Physical Metallurgy, Brno, Czechoslovakia, June 1983).

18. J. H. Giovanola, "Investigation and Application of the One-Point-Bend Impact Test," in *Fracture Mechanics*, Vol. 17, ASTM STP 905, J. G. Underwood, R. Chait, C. W. Smith, D. P. Wilhelm, W. A. Andrews, and J. Newman, Eds. (American Society for Testing and Materials, Philadelphia, 1986), pp. 307-328.

19. J. H. Giovanola, "The One-Point-Bend Test," in *ASM Metals Handbook*, 9th ed., Vol. 8, *Mechanical Testing* (American Society for Metals, Metals Park, OH, 1985), p. 271.

20. T. Nakamura, C. F. Shih, and L. B. Freund, "Analysis of a Dynamically Loaded Three-Point-Bend Ductile Fracture Specimen," Brown University Report ONR0365/1, Brown University, Providence, RI, 1985.

21. J. O. Hallquist, "User's Manual for DYNA2D—An Explicit Two-Dimensional Hydrodynamic Finite Element Code with Interactive Rezoning," Lawrence Livermore National Laboratory, Report UCID-18756 (1980).

22. J. H. Giovanola, R. W. Klopp, D. A. Shockey, and A. T. Werner, "Effect of Microstructure and Loading Rate on the Fracture Behavior of Titanium-10V-2Fe-3Al," in *Advances in Fracture Research*, Vol. 1, *Proceedings of the Seventh International Conference on Fracture, Houston, March 20-24, 1989*, K. Salama et al., Eds. (Pergamon Press, New York, 1989), pp. 643-650.

23. J. H. Giovanola, R, W. Klopp, and J. W. Simons, "Effect of Shear Lips on Dynamic Crack Propagation," in *Dynamic Fracture, Proceedings of the Oji International Seminar on Dynamic Fracture, Toyohashi, August 1-4, 1989*, H. Homma and Y. Kanto Eds. (Chuo Technical Drawing Co. Ltd.), pp. 93-102.

24. W. L Fourney, R. Chona, and R. J. Sanford, "Dynamic Crack Growth in Polymers," in *Proceedings of Workshop on Dynamic Fracture,* W. G. Knauss et al. Eds. (California Institute of Technology, Pasadena, CA, 1983), pp. 75-99.

25. J. F. Kalthoff, "On Some Current Problems in Experimental Fracture Dynamics," in *Proceedings of Workshop on Dynamic Fracture,* W. G. Knauss et al. Eds. (California Institute of Technology, Pasadena, CA, 1983), pp. 11-35.

26. A. J. Rosakis and A. T. Zehnder, "On the Dynamic Fracture of Structural Metals," *Int. J. Fracture* **27**, 169-186 (1985).

27. T. Kanazawa, S. Machida, T. Teramoto, and H. Yoshinari, "Study on Fast Fracture and Crack Arrest," *Exp. Mech. 21*, 78-88 (February 1981).

28. W. Klemm, "Material Resistance Against Fast Ductile Fracture in Pipeline Steels," in Dynamic Fracture for the 1990s, H. Homma, D. A. Shockey, and G. Ygawa Eds. (The American Society of Mechanical Engineers, New York, 1989), pp. 99-104.

29. A. L. Gurson, "Continuum Theory of Ductile Rupture by Void Nucleation and Growth: Part I—Yield Criteria and Flow Rules for Porous Ductile Media," *J. Eng. Mat. Tech.* **99**, 2-15 (1977).

30. V. Tvergaard, "On Localization in Ductile Materials Containing Spherical Voids," *Int. J. Fracture* **18**(4), 237-252 (1982).

31. J. O. Hallquist, "NIKE2D: A Vectorized, Implicit, Finite Deformation, Finite Element Code for Analyzing the Static and Dynamic Response of 2-D Solids," Lawrence Livermore Laboratory, Report UCID-19677 (1983)

32. R. Becker, A. Needleman, O. Richmond, and V. Tvergaard, "Void Growth and Failure in Notched Bars," J. Mech. Phys. Solids **36**(3), 317-351 (1988).

33. D. R. Curran, L. Seaman, and D. A. Shockey, "Dynamic Failure of Solids," Physics Reports, Vol. 147, Nos. 5 & 6 (March 1987).

PERSONNEL, ACTIVITIES, PUBLICATIONS, AND PRESENTATIONS

PERSONNEL

The following professional personnel were associated with this research effort:

Dr. J. H. Giovanola, Co-Principal Investigator

Dr. D. A. Shockey, Co-Principal Investigator

Dr. R. W. Klopp

Dr. T. Kobayashi

Mr. S. W. Kirkpatrick

Dr. Patrick Touzé

Dr. Alain Marchand

Dr. C. G. Schmidt

Mr. D. C. Erlich

Ms. C. Kanazawa

Mr. J. Crocker

Dr. T. Duerig, consultant

ACTIVITIES

The work performed in this program will be presented at the 29th Annual Meeting of The Society of Engineering Science (September 14-16, 1992), and six publications resulting from this work are in preparation. These activities are included in the publications and presentations listed below.

Dr. Shockey has been invited for the past several years to lecture on micromechanical aspects of dynamic fracture at the University of Nantes, France. Dr. Giovanola has transferred some of the results and experience gained in this research program to the Air Force Armament Technical Laboratory at Eglin Air Force Base, to support their analysis and modeling effort aimed at developing better hard target penetrators. Dr. Giovanola also collaborated with the California Institute of Technology, providing well characterized materials for complementary dynamic fracture experiments on the alloys tested in this program. He has also been interacting with the dynamic fracture working groups of the European Structural Integrity Society (ESIS) and of the EuroDymat Society.

Extensive oral reviews of the program results were presented to Dr. A. H. Rosenstein of the Air Force Office of Scientific Research during his yearly visits to SRI and to Dr. T. Nicholas of the Air Force Wright Materials Laboratory.

The following lists of publications and presentations include those resulting from this and related earlier work.

PUBLICATIONS

J. F. Kalthoff and D. A. Shockey, "Instability of Cracks Under Impulse Loads, " J. Appl. Phys. 48, 984-993 (March 1977).

D. A. Shockey, J. F. Kalthoff, H. Homma, and D. C. Erlich, "Criterion for Crack Instability Under Short Pulse Loads," in *Advances in Fracture Research*, D. Francois et al., Eds. (Oxford and Pergamon Press, New York, 1980), pp. 415-423.

D. A. Shockey, J. F. Kalthoff, and D. C. Erlich, "Evaluation of Dynamic Crack Instability Criteria," Int. J. Fract. Mech. 22, 217-229 (1983).

D. A. Shockey, J. F. Kalthoff, W. Klemm, and S. Winkler, "Simultaneous Measurements of Stress Intensity and Toughness for Fast Running Cracks in Steel," Exp. Mech. 23, 140-145 (1983).

H. Homma, D. A. Shockey, and Y. Murayama, "Response of Cracks in Structural Materials to Short Pulse Loads," J. Mech. Phys. Solids 31, 261-279 (1983).

D. A. Shockey, J. F. Kalthoff, H. Homma, and D. C. Erlich, "Response of Cracks to Short Pulse Loads," in *Proceedings of the Workshop on Dynamic Fracture*, a workshop held at the California Institute of Technology, Pasadena, CA, February 17-18, 1983, under sponsorship of the National Science Foundation and the Army Research Office, W. G. Knauss, Ed. (California Institute of Technology Press, 1983), pp. 57-71.

J. H. Giovanola, "Investigation and Application of the One-Point-Bend Impact Test," in *Fracture Mechanics*, Vol. 17, ASTM STP 905, J. G. Underwood, R. Chait, C. W. Smith, D. P. Wilhelm, W. A. Andrews, and J. Newman, Eds. (American Society for Testing and Materials, Philadelphia, 1986), pp. 307-328.

J. H. Giovanola, "The One-Point-Bend Test," in *ASM Metals Handbook*, 9th ed., Vol. 8, *Mechanical Testing* (American Society for Metals, Metals Park, OH, 1985), pp. 271-275.

D. A. Shockey, "Short-Pulse-Duration Tests," in *ASM Metals Handbook*, 9th ed., Vol. 8, *Mechanical Testing* (American Society for Metals, Metals Park, OH, 1985), pp. 282-284.

D. A. Shockey, J. F. Kalthoff, H. Homma, and D. C. Erlich, "Short Pulse Fracture Mechanics," in *Dynamic Fracture, The Albert S. Kobayashi Anniversary Volume of the International Journal of Fracture*, M. F. Kanninen and S. N. Atluri, Eds. (Pergamon Press, New York, 1986), pp. 311-319.

J. H. Giovanola, "Crack Initiation and Extension in Steel for Short Loading Times," in *Proceedings of DYMAT 85 Conference on Mechanical and Physical Behavior of Materials under Dynamic Loading, Paris, September 2-5, 1985* (Les Editions de Physique, France, 1985), pp. C5-171 through C5-178.

D. A. Shockey, "Recent Progress in Dynamic Fracture Testing and Treatment" in *International Conference on Impact Loading and Dynamic Behavior of Materials*, C. Y. Chiem et al., Eds. (DGM Informationsgeselschaft mbH, Oberursel, FRG, 1988), pp. 3-21.

J. H. Giovanola, T. Kobayashi, R. W. Klopp, T. Gaines, and R. Arwood, "A Note on Dynamic Displacement Measurements Using Hall Effect Sensors," J. Testing Eval., **17**, 196-200 (1989).

J. H. Giovanola, R. W. Klopp, D. A. Shockey, and A. T. Werner, "Effect of Microstructure and Loading Rate on the Fracture Behavior of Titanium-10V-2Fe-3Al," in *Advances in Fracture Research*, Vol. 1, *Proceedings of the Seventh International Conference on Fracture, Houston, March 20-24, 1989*, K. Salama et al., Eds. (Pergamon Press, New York, 1989), pp. 643-650.

J. H. Giovanola, R, W. Klopp, and J. W. Simons, "Effect of Shear Lips on Dynamic Crack Propagation," in *Dynamic Fracture, Proceedings of the Oji International Seminar on Dynamic Fracture, Toyohashi, August 1-4, 1989*, H. Homma and Y. Kanto, Eds. **(publisher, city, year)**, pp. 93-102

J. H. Giovanola, R. W. Klopp, and T. Kobayashi, "Effect of Primary Alpha Content and Grain Size on the Static and Dynamic Fracture Behavior of Titanium-10V-2Fe-3Al: Properties Measurement," in preparation. To be submitted to Metallurgical Transactions A.

J. H. Giovanola, T. Kobayashi, and R. W. Klopp, "Effect of Primary Alpha Content and Grain Size on the Static and Dynamic Fracture Behavior of Titanium-10V-2Fe-3Al: Fractographic Observations," in preparation. To be submitted to Metallurgical Transactions A.

J. H. Giovanola, T. Kobayashi, R. W. Klopp, and S. W. Kirkpatrick, "Estimation of Dynamic Propagation Toughness in Ti-10V-2Fe-3Al Microstructures by Continuum and Microscopic Approaches, " in preparation. To be submitted to International Journal of Fracture.

J. H. Giovanola, R. W. Klopp, and S. W. Kirkpatrick, "On the Role of Shear Lips in Dynamic Crack Propagation," in preparation. To be submitted to Engineering Fracture Mechanics.

T. Kobayashi and J. H. Giovanola, "Effect of Constraint on the Dynamic Fracture Toughness of a High Strength Steel," in preparation. To be submitted to Engineering Fracture Mechanics.

J. H. Giovanola, R. W. Klopp, and S. W. Kirkpatrick, "One-Point-Bend Dynamic Fracture Toughness Test Using Curved Specimens," in preparation. To be presented at an ASTM Symposium on Fracture and to appear in *Proceedings*.

PRESENTATIONS

D. C. Erlich and D. A. Shockey, "Instability Conditions for Cracks Under Short-Duration Pulse Loads," Topical Conference on Shock Waves in Condensed Matter, Meeting of the American Physical Society, Washington State University, Pullman, WA, June 11-13, 1979.

D. A. Shockey, "Instability Conditions for Cracks Loaded by Short Stress Pulses," Poulter Laboratory Seminar, SRI International, Menlo Park, CA, December 12, 1979.

D. A. Shockey, "Dynamic Crack Instability," Institut CERAC, Ecublens, Switzerland, May 19, 1980.

D. A. Shockey, "Dynamic Crack Instability," Institut für Werkstoffmechanik, Freiburg, Germany, May 21, 1980.

D. A. Shockey, "Simultaneous Measurements of Stress Intensity and Toughness for Fast Running Cracks in Steel," Poulter Laboratory Seminar, SRI International, Menlo Park, CA, June 1980.

D. A. Shockey, "Criterion for Crack Instability Under Short Pulse Loads," Fifth International Conference on Fracture (ICF5), Cannes, France, March 29-April 3, 1981.

D. A. Shockey, "Simultaneous Measurements of Stress Intensity and Toughness for Fast Running Cracks in Steel," 18th Annual Meeting of the Society for Engineering Science, Inc., Brown University, Providence, RI, September 2-4, 1981.

D. A. Shockey, "Short Pulse Fracture Mechanics," Seminar for the Department of Applied Mechanics, Stanford University, Stanford, CA, March 3, 1983, C. Steele, Chairman.

D. A. Shockey, "Short Pulse Fracture Mechanics," Poulter Laboratory Seminar, SRI International, Menlo Park, CA, April 11, 1983.

J. H. Giovanola, "Mechanics of Fracture Under Pulse Loads; Minimum Time Theory Revisited," Poulter Laboratory Seminar, SRI International, Menlo Park, CA, April 1984.

J. H. Giovanola, "Material Failures at High Strain Rates, " two lectures given at the Department of Materials Science and Engineering of Stanford University, Stanford, CA, May 1984.

J. H. Giovanola, "Material Failures at High Strain Rate," Materials Science and Engineering Graduate Seminar, University of California at Berkeley, Berkeley, CA, November 1984.

J. H. Giovanola, "Investigation and Analysis of the One-Point-Bend Impact Test," presented at the ASTM Seventeenth National Symposium on Fracture Mechanics, Albany, NY, August 7-9, 1984.

D. A. Shockey, D. R. Curran, and L. Seaman, "Fracture Under Impact Loads," presented at the International Conference on Dynamic Fracture Mechanics, San Antonio, TX, November 7-9, 1984.

J. H. Giovanola,"The One-Point-Bend Test: Experiment and Analysis," Poulter Laboratory Seminar, SRI International, Menlo Park, CA, March 1985.

D. A. Shockey, J. F. Kalthoff, M. Homma, and J. H. Giovanola, "Recent Results in Short Pulse Fracture Mechanics," presented at the SEM Spring Meeting, Las Vegas, NV, June 1985.

J. H. Giovanola, "Crack Initiation and Extension in Steel for Short Loading Times," presented at DYMAT International Conference on Mechanical and Physical Behavior of Materials under Dynamic Loading, Paris, September 2-5, 1985.

J. H. Giovanola: "Fracture at High Loading Rates," presented at the University of California at Berkeley short course entitled Fracture and Fatigue: Approaches for Analysis and Control of Failure, June 1986.

J. H. Giovanola, "Fracture at High Loading Rates," invited lecture for graduate fracture mechanics course (ME 225) at the University of California at Berkeley, April 14, 1987.

D. A. Shockey, "Recent Progress in Dynamic Fracture Testing and Treatment" invited lecture, Impact 87, International Conference on Impact Loading and Dynamic Behaviour of Materials, Bremen, FRG, May 18-22, 1987.

J. H. Giovanola "Review of Recent Dynamic Fracture Research at SRI International," presented to the Fatigue and Fracture Branch of the David Taylor Naval Ship Research and Development Center, Annapolis, MD, June 3, 1988.

J. H. Giovanola, "Effect of Strain Rate and Microstructure on the Fracture Behavior of Ti-10V-2Fe-3Al," Poulter Laboratory Seminar, SRI International, Menlo Park, CA, November 1988.

J. H. Giovanola, "Effect of Strain Rate and Microstructure on the Fracture Behavior of Ti-10V-2Fe-3Al," 7th International Conference on Fracture, Houston, TX, March 20-24, 1989.

J. H. Giovanola, " Dynamic Fracture of Ti-10V-2Fe-Al," Poulter Laboratory Seminar, SRI International, Menlo Park, CA, May 11, 1992

J. H. Giovanola, " Microstructural Effects on the Dynamic Fracture Behavior of Ti-10V-2Fe-3Al," to be presented at the Swiss Federal Institute of Technology, Lausanne, July 8, 1992.

J. H. Giovanola, T. Kobayashi, R. W. Klopp, and S. W. Kirkpatrick,"Dynamic Fracture Behavior of a Near-Beta Titanium Alloy," to be presented at the 29th Annual Meeting of The Society of Engineering Science, La Jolla, CA, September 14-16, 1992.

Appendix

MODELING OF MICROSTRUCTURAL EFFECTS ON FRACTURE PROCESSES AT HIGH LOADING RATES: DYNAMIC FRACTURE OBSERVATIONS IN HIGH STRENGTH STEELS

SRI International

Technical Report • January 1992

MODELING OF MICROSTRUCTURAL EFFECTS ON FRACTURE PROCESSES AT HIGH LOADING RATES

Dynamic Fracture Observations in High-Strength Steels

J. H. Giovanola, Program Manager
D. R. Curran , Scientific Director
T. Kobayashi, Senior Research Engineer
R. W. Klopp, Research Engineer
S. W. Kirkpatrick, Research Engineer
D. C. Erlich, Research Physicist
J. E. Crocker, Material Scientist
Poulter Laboratory

SRI Project 7294
Contract No. F49620-89-K-0003

Prepared for:

Dr. A. H. Rosenstein Air Force Office of Scientific Research AFOSR/NE Bolling AFB, DC 20332	Captain E. Staubs, Program Manager Mr. W. Cook AFATL/MNW Eglin AFB, FL 32542

Approved:

James D. Colton, Director
Poulter Laboratory

David M. Golden
Vice President
Physical Sciences Division

333 Ravenswood Avenue • Menlo Park, CA 94025-3493 • (415) 326-6200 • FAX (415) 326-5512 • Telex 334486

REPORT DOCUMENTATION PAGE

Form Approved
OMB No. 0704-0188

1. AGENCY USE ONLY ***(Leave blank)***

2. REPORT DATE
1992 January

3. REPORT TYPE AND DATES COVERED
Technical Report

4. TITLE AND SUBTITLE
MODELING OF MICROSTRUCTURAL EFFECTS ON FRACTURE PROCESSES AT HIGH LOADING RATES—Dynamic Fracture Observations in High Strength Steels

5. FUNDING NUMBERS

6. AUTHOR(S)
Jacques H. Giovanola, Donald R. Curran, Takao Kobayashi, Richard W. Klopp, Steve W. Kirkpatrick, David C. Erlich, James E. Crocker

7. PERFORMING ORGANIZATION NAME(S) AND ADDRESS(ES)

SRI International
333 Ravenswood Avenue
Menlo Park, CA 94025-3493

8. PERFORMING ORGANIZATION REPORT NUMBER

SRI Project 7294

9. SPONSORING/MONITORING AGENCY NAME(S) AND ADDRESS(ES)
Air Force Office of Scientific Research
AFOSR/NE, Bldg. 410
Bolling Air Force Base
Washington, DC 20332

10. SPONSORING/MONITORING AGENCY REPORT NUMBER

11. SUPPLEMENTARY NOTES

12a. DISTRIBUTION/AVAILABILITY STATEMENT

12b. DISTRIBUTION CODE

13. ABSTRACT ***(Maximum 200 words)***

Present understanding of the penetration of hard targets indicates that improved performance of the penetrator will be achieved by judiciously selecting the ratio of strength to toughness of the case material or by increasing both these properties. Currently, the design and optimization process is mostly empirical—i.e penetrator cases are fabricated from selected steels and then sled tested to evaluate their performance. Moreover, the mechanical properties specified for the case material—i.e. strength, hardness and occasionally Charpy energy—do not allow the optimization of the penetrator to be based on analytical methods.

The shortcomings of the empirical approach were illustrated in a recent development program in which higher strength penetrators (300M steel) failed to perform as well as the lower strength penetrators (D6ac steel) that they were designed to replace. To accelerate the design process of new penetrators and decrease the design cost, it is therefore important to develop micromechanical failure models that can serve to analyze the behavior of penetrator cases in numerical simulations and to measure the material properties that enter these models.

14. SUBJECT TERMS

300M steel	Initiation Toughness	FRASTA
D6ac steel	Propagation Toughness	microfailure
Dynamic Fracture	COD	

15. NUMBER OF PAGES

16. PRICE CODE

17. SECURITY CLASSIFICATION OF REPORT	**18. SECURITY CLASSIFICATION OF THIS PAGE**	**19. SECURITY CLASSIFICATION OF ABSTRACT**	**20. LIMITATION OF ABSTRACT**
UNCLASSIFIED	UNCLASSIFIED	UNCLASSIFIED	SAME AS REPORT

NSN 7540-01-280-5500

Standard Form 298 (Rev. 2-89)
Prescribed by ANSI Std. 239-18

CLASSIFIED BY:

DECLASSIFY ON:

13. Abstract (continued)

This report presents the results of a preliminary program aimed at measuring the dynamic strength and fracture properties controlling the penetration behavior of two penetrator materials (300M and D6ac steels) by means of advanced mechanical testing and fractographic techniques.

We established significant differences in the dynamic strength (37%) and fracture toughness (close to 100%) of the two materials and demonstrated that differences in microstructural failure mechanisms controlled the difference in dynamic fracture toughness. Further, the results of this program indicated which micromechanical material properties should be measured for the development of damage models. Finally we demonstrated how the new techniques used in the program can be used to measure these key micromechanical properties.

Therefore approaches and tools to implement these approaches are now available that will eliminate the empiricism in the design of hard target penetrators and provide a better, more fundamental understanding of the case behavior during penetration.

CONTENTS

ILLUSTRATIONS

ILLUSTRATIONS
(CONTINUED)

ILLUSTRATIONS

(CONCLUDED)

TABLES

INTRODUCTION

BACKGROUND

Many warheads in the United States Air Force arsenal are fabricated from high-strength steels. Recent tests with hard-target penetrators fabricated from several high-strength steels indicated that, although the alloys were similar and essentially met conventional material specifications, they behaved quite differently under impact loading. Cases made of certain steels successfully penetrated targets, whereas cases made from other steels broke up during penetration. These results suggest that material processing and microstructure have a profound effect on the dynamic deformation and fracture behavior of these alloys and that this effect cannot be satisfactorily evaluated with conventional mechanical properties tests. Rather, a more fundamental understanding is needed of how microstructure influences microdeformation and microfailure processes and how, in turn, these processes affect macroscopic dynamic fracture phenomena and the performance of the components.

This report describes the results of a preliminary research program aimed at addressing these issues.

OBJECTIVES

In this perspective, the long-term objectives of the preliminary work described in this report are

(1) To determine the relationship between microstructure and dynamic mechanical properties of ferrous alloys to facilitate the microstructure selection and optimization process for specific applications involving high loading rates.

(2) To develop material and damage models that can be used in numerical simulations of penetration events to help the design of improved penetrators.

More specifically, in this initial investigation we focused on two candidate high-strength steels for penetrator case applications and established their behavior under dynamic loading from both the macroscopic and microscopic points of view.

APPROACH

To achieve the project objectives, we analyzed fragments from actual penetration experiments and compared our findings with observations made on specimens fractured in controlled laboratory experiments. This approach allowed us to establish the microscopic and macroscopic deformation and fracture properties and relate them to penetrator performance.

We used advanced metallographic and fractographic techniques, such as fracture surface topography analysis (FRASTA), to identify the microfailure mechanisms and to elucidate the contribution of individual microstructural constituents to the failure process. To characterize the macroscopic dynamic fracture behavior of high-strength steels heat-treated to various microstructures, we used the one-point-bend impact test. Finally, we measured the dynamic stress-strain curves for the alloys and assessed their shear banding behavior by using Hopkinson torsion bar experiments.

SUMMARY OF RESULTS

During this research program, we analyzed a fractured 300M penetrator case, developed a procedure for measuring dynamic fracture toughness with curved specimens, measured the dynamic fracture toughness of 300M and D6ac steels, performed a detailed fractographic analysis of these two steels by using the FRASTA method, and measured their dynamic stress-strain curve.

We found that D6ac steel has a dynamic initiation toughness almost twice that of 300M steel (116.7 MPa$\sqrt{m}$ versus 60.1 MPa$\sqrt{m}$). This large difference is consistent with fractographic observations, which reveal significant differences in the microscopic crack growth mode in the two microstructures. In 300M steel, cracks propagate at a rapid rate as soon as they initiate, whereas in D6ac steel we observe a transient regime after initiations during which cracks seem to grow at a slow rate over a short distance before rapid crack growth sets in. We have also found evidence that for both materials, resistance to crack extension is higher than resistance to crack initiation, even at moderate speeds of a few hundred meters per second.

300M steel has a significantly higher dynamic shear flow strength than D6ac steel (1300 MPa versus 950 MPa), but the shear strains at failure for the two materials are similar (0.10 versus 0.13).

FAILURE ANALYSIS OF 300M STEEL PENETRATOR CASE

The Air Force Armament Laboratory (AFATL) provided SRI with parts of field-tested penetrator cases made from two high-strength steels, D6ac and 300M. We have no information on the processing or mechanical properties of these materials. Preliminary hardness measurements indicated that the D6ac steel is somewhat softer than the 300M steel (Rockwell hardness C 46 versus 51).

Our objective in performing the failure analysis of the case was to establish the mechanisms of loading and the fractographic details of the case material when failed under actual service conditions so that we could then compare the observations with failures produced in laboratory experiments. With this comparison we ascertained that the observations and measurements made in the laboratory were indeed relevant for the deformation and fracture of the penetrators.

We did not perform a failure analysis of a D6ac case because only one case failed during testing, and that case was tested under conditions outside the envelope of test parameters. We inspected 300M case sections that had failed in an earlier sled test. The case consisted of three parts that had been previously sectioned at AFATL and fragments from the tail section (Figure 1).

We cleaned the 300M case parts, established the cracking pattern by highlighting the cracks with dye penetrants, then sectioned the parts at two locations (I-B and I-A/II-A in Figure 1) to inspect the interior. We measured the ovalization of the case and correlated case deformation and fracture observations. We selected several cracked regions (including some tail fragments) and cut out the fracture surfaces in preparation for detailed fractographic analysis by FRASTA.

Figure 2 shows the external cracking pattern of part I-B/II-B of the case (before sectioning) from different perspectives, whereas Figure 3 shows the interior surface of parts I-B/I-A and II-A/II-B (after sectioning). We found that most cracks initiate from the outside of the case and propagate across the thickness toward the inside and around the circumference. Many of these cracks did not completely penetrate the case thickness, as demonstrated by a comparison of Figures 2 and 3. The cracks that do not break through the inside of the case leave a small unbroken ligament. The external cracks form a complex network, with one crack propagating the whole length of the case in a more or less axial direction (Figure 2).

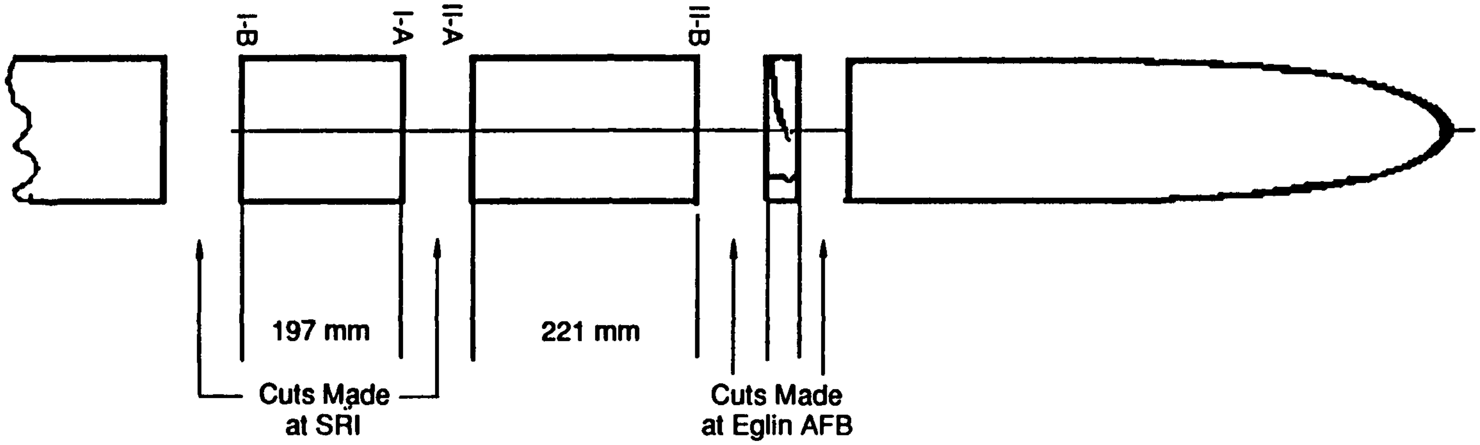

RAM-7294-13

Figure 1. Map of sections from 300M penetrator case.

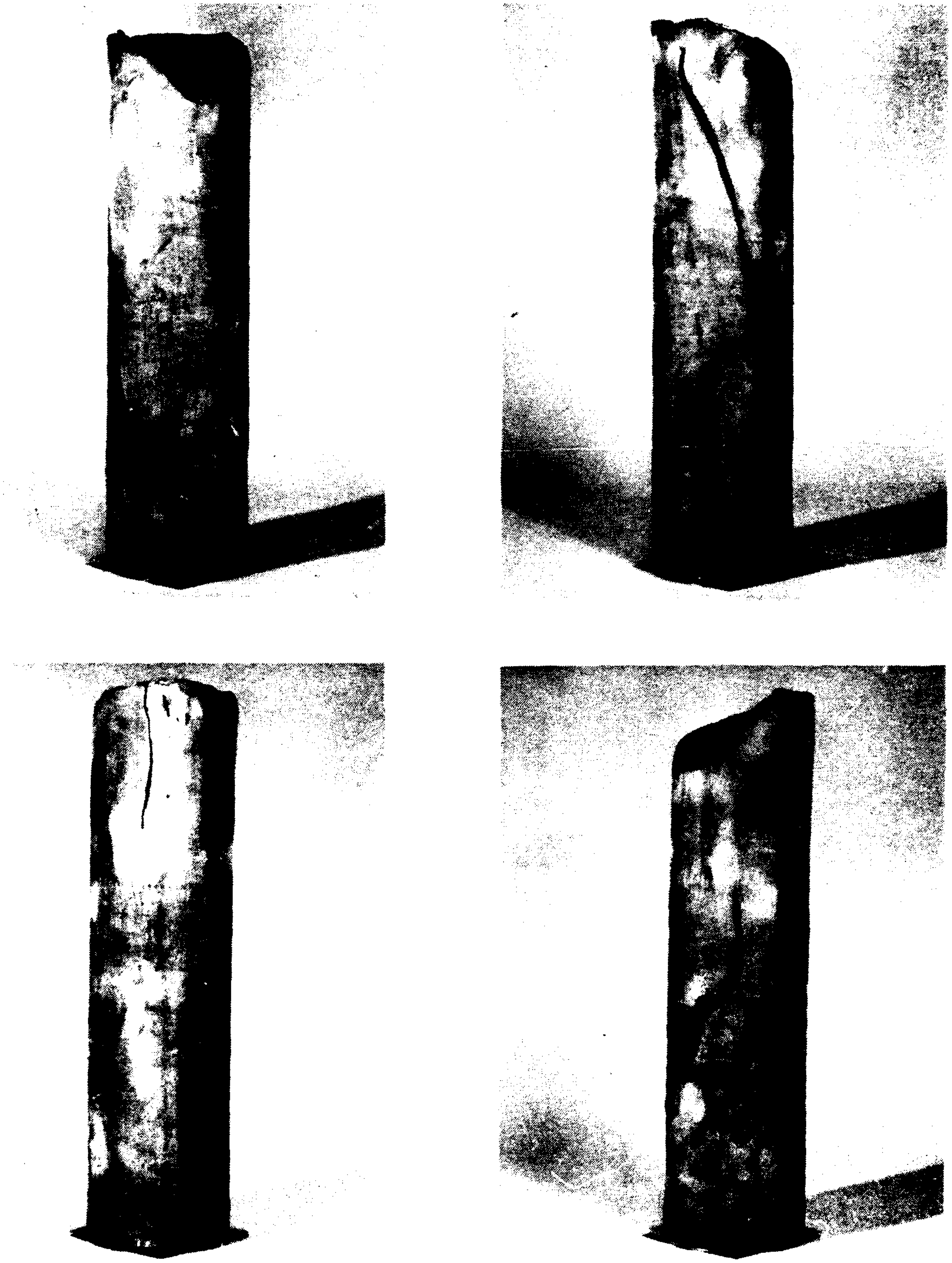

RPM-7294-14

Figure 2. External crack pattern for 300M penetrator case seen from different perspectives.

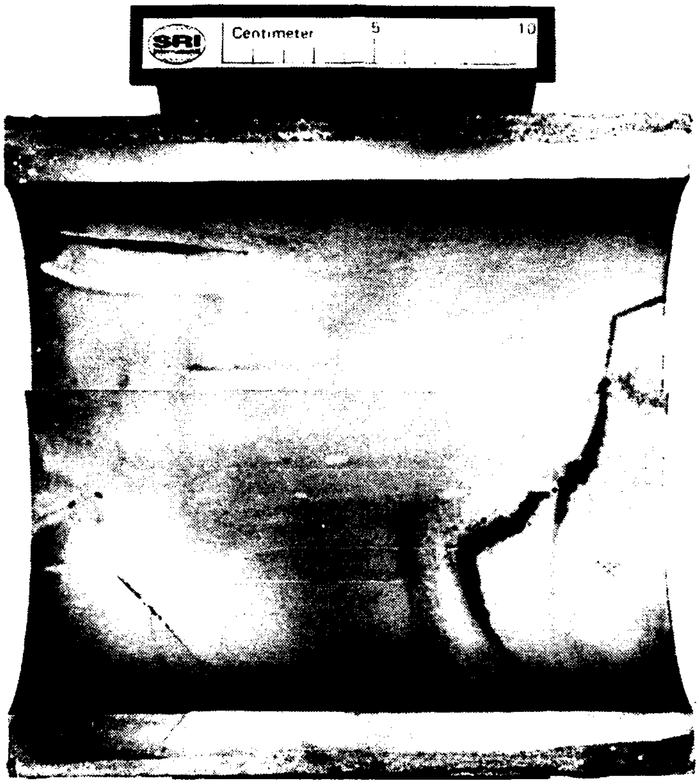

(a) Part II-B/II-A

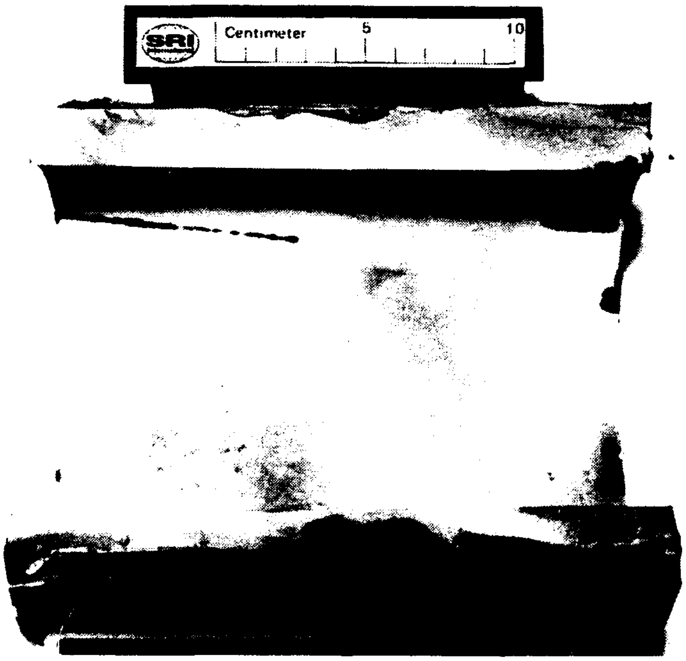

(b) Part I-B/I-A

RP-7294-12

Figure 3. Internal crack pattern for 300M penetrator case.

(View of part II-B/II-A is assembled from two photographs to show the entire view of the case inside wall.)

Two fragments of the penetrator tail are shown in Figure 4. The thickness of these fragments is significantly less than that of the rest of the case.

Figure 5 shows a plot of the external diameter of the case measured at four locations along the case axis as a function of angular position. The measurement locations are indicated in Figure 1. Locations I-A and II-A are essentially the same. The arrows in Figure 4 indicate locations at which cracks intersect the plane where we measured the case diameters. Figure 4 clearly indicates that the case ovalized significantly as a result of the impact. The amount of ovalization is smaller toward the penetrator nose (position II-B) than in the aft part of the case (positions I-B and I-A/II-A). The forward part of the long axial crack indicated in Figure 2 falls in a region of tensile bending strains on the outer case fiber.

From the preceding observations, we may speculate on a scenario for the case failure. A slight yaw or pitch during penetration may have induced a bending moment normal to the case axis, which in turn caused ovalization of the cross section. The long axial crack in Figure 2 may then have initiated because of case ovalization. The other cracks represent collateral damage that occurred after the initiation of the long axial crack. The breakup of the tail fragment might be explained this way: The cover that screws into the tail of the case makes it stiffer and prevents ovalization. This restraint induces circumferential bending that might explain the fracture pattern observed in the aft region. Clearly, we need more experimental evidence to verify this somewhat speculative explanation.

We cut out several regions of the case to observe selected fracture surfaces in the scanning electron microscope (SEM) and to establish the microscopic morphology of the fracture surface. Figure 6 shows the matching surfaces of a thumbnail crack that initiated on the outside of the mid-region of the case, propagated partially through the wall, and stopped. The dark regions correspond to the surfaces of the crack that propagated during the sled test, then corroded during storage at Eglin Air Force Base. The lighter fracture surface regions were produced when we broke open the remaining ligament. The fracture surfaces are very flat and quite smooth. We removed the corrosion products from the fracture surfaces and unsuccessfully attempted a fractographic analysis using FRASTA. The surface had been too badly corroded to allow reliable observations.

Details of the fracture surface of fragments from the tail region are presented in Figures 7 through 10. Figure 7 presents a low-magnification fractograph of matching surfaces (region B in Figure 4) and demonstrates that the crack in this part of the case has a very rough surface, which

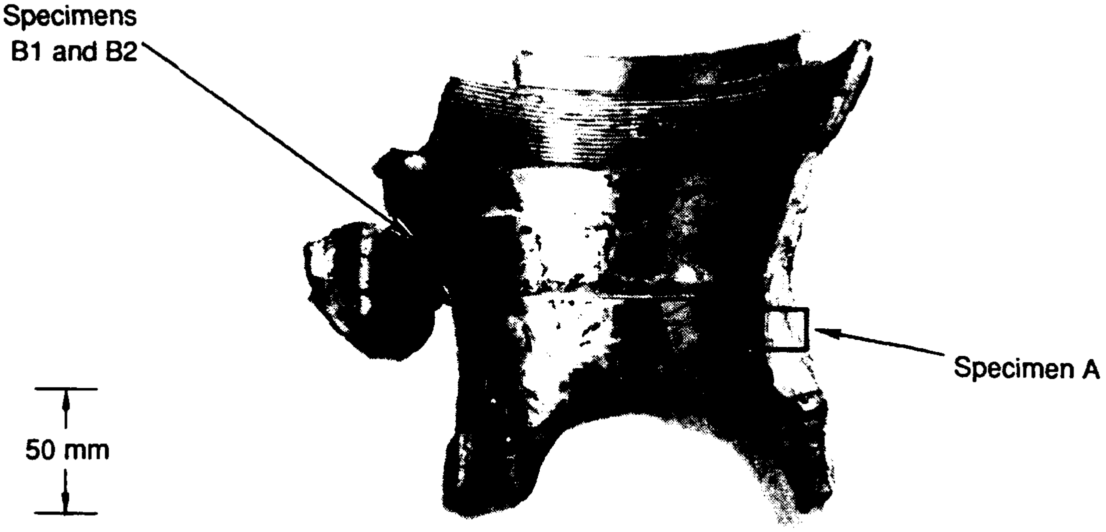

(a) Inside surface

(b) Outside surface

CP-314582-4

Figure 4. Fragments from the tail region of the penetrator.

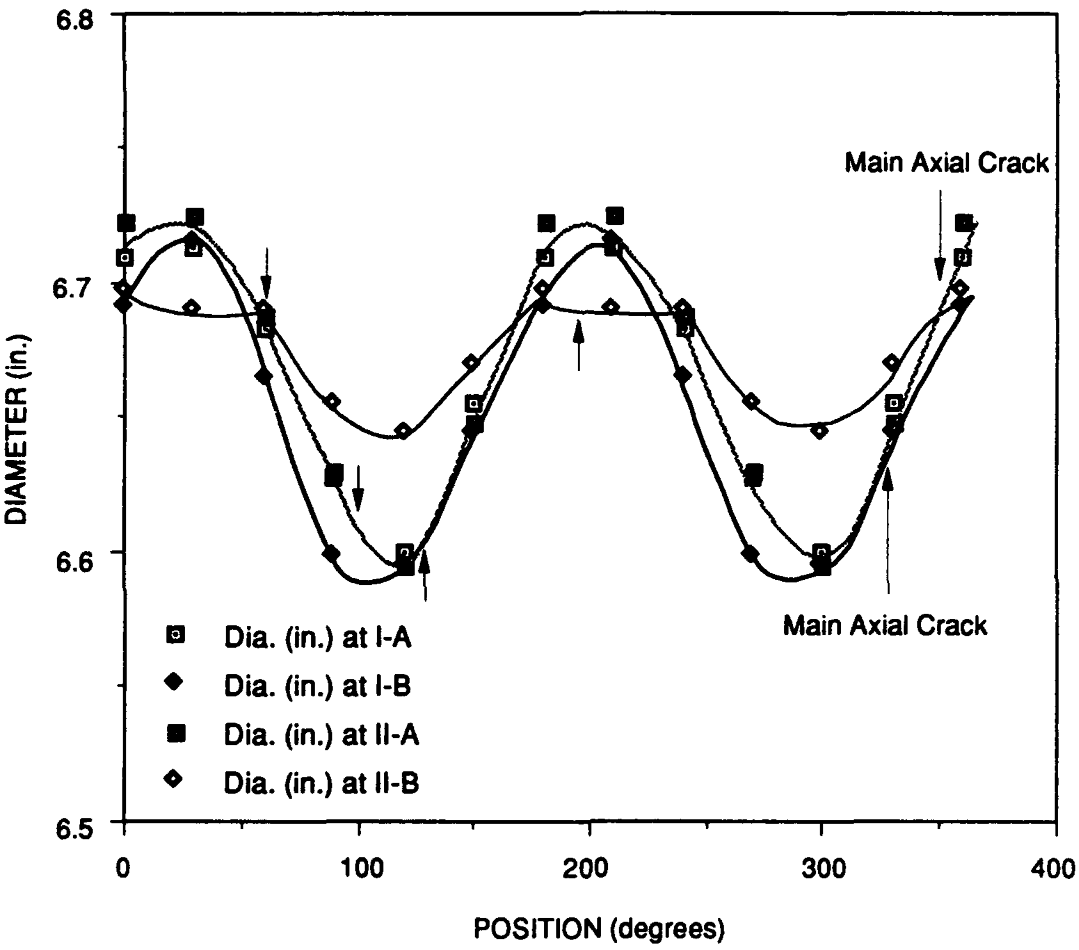

RAM-7294-15

Figure 5. External case diameter as a function of angular position around the circumference.

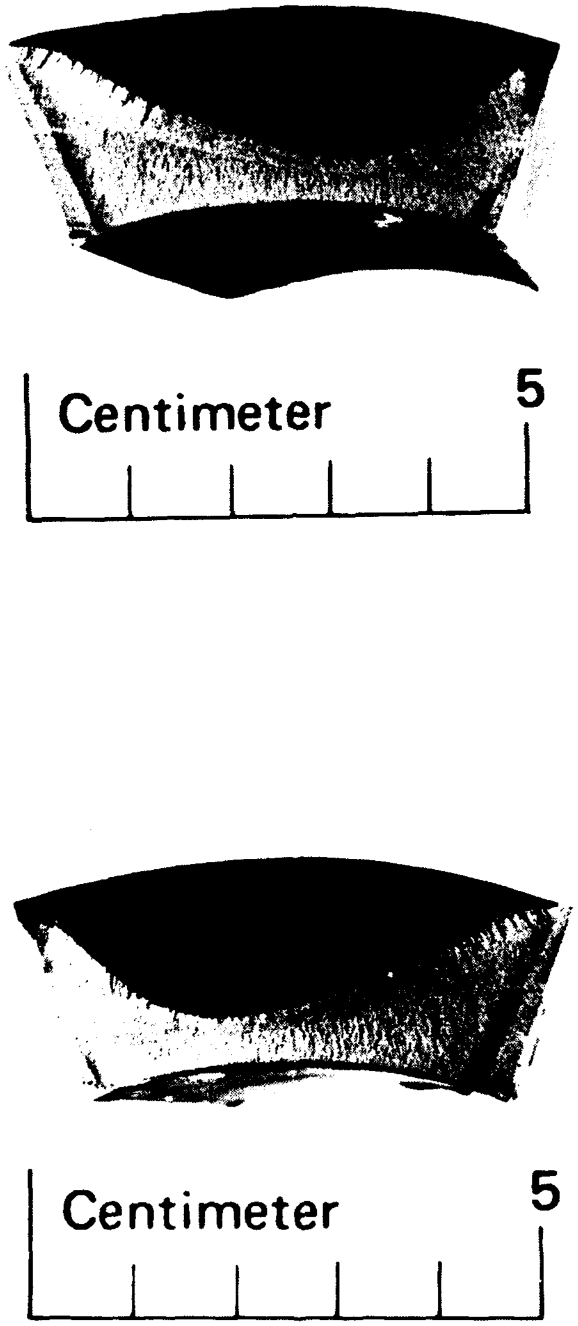

RPM-7294-16

Figure 6. Matching fracture surfaces of a thumbnail crack that partially propagated through the case wall.

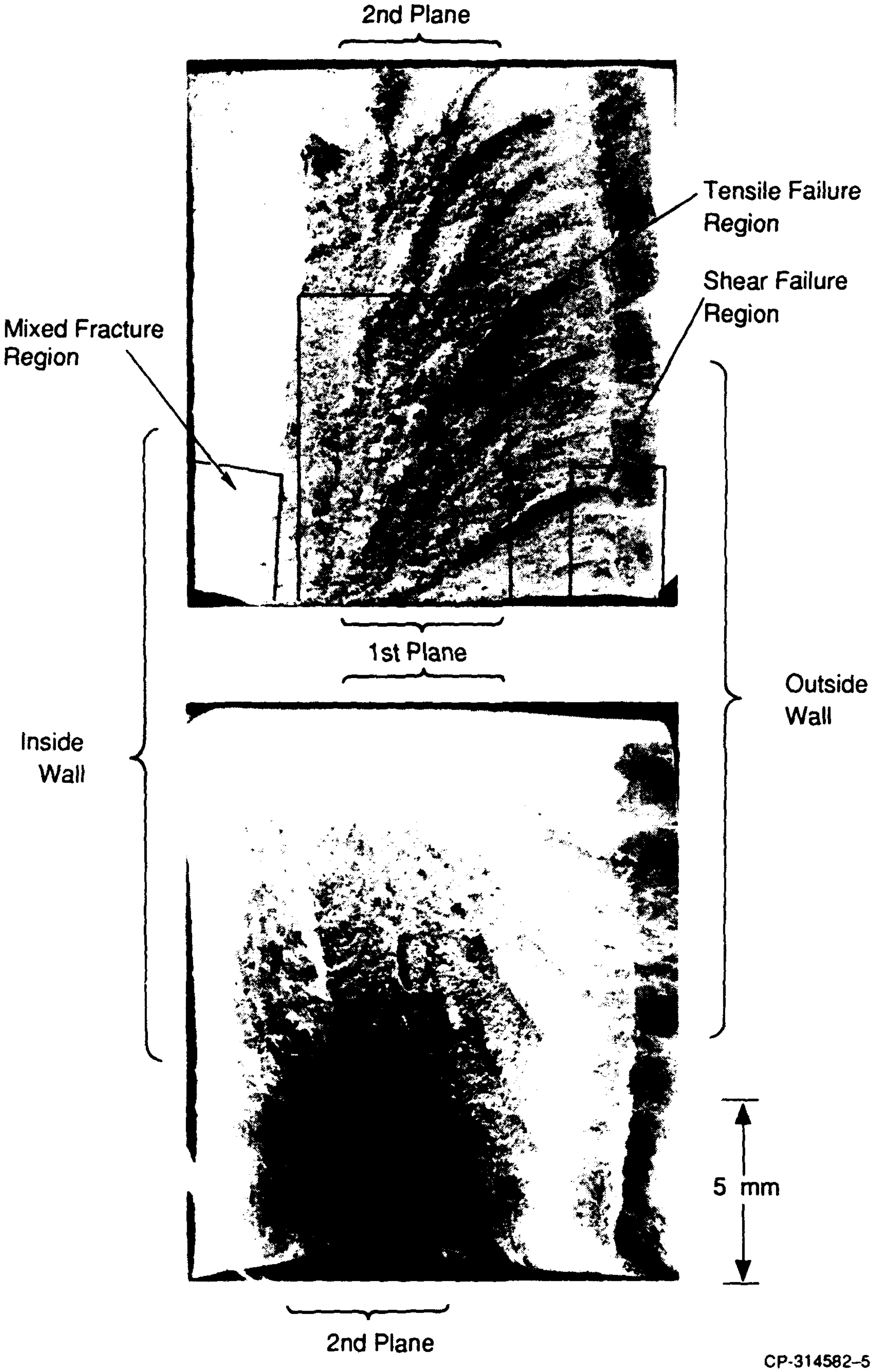

CP-314582-5

Figure 7. Low magnification fractographs of region B of the fragments in Figure 4.

contrasts with the flat appearance of the thumbnail crack in Figure 6. We defined three regions of the fracture surface from the macroscopic deformation mode that appears to have controlled their morphology: (1) tensile region, (2) mixed fracture region, and (3) shear region.

The tensile region occupies most of the fracture surface and has many high steps. These steps form a curved fan pattern and were produced by segments of flat cracks propagating at different levels in the material, then linking up with one another by localized shear deformation (shear walls). The fan pattern indicates that, as shown in the top photograph in Figure 7, the crack propagated from the lower left corner (inside wall) toward the top and right side of the picture (outside wall). This propagation path in turn suggests that a circumferential bending moment loaded the fracture region, putting the inner wall in tension and the outer wall in compression. The mixed mode and shear regions are inclined with respect to the tensile fracture region. This slant of the fracture surface is probably due to the difference in the state of stress near the free surface of the specimen and to the mode of loading.

Higher-magnification SEM photographs of the tensile region (Figure 8) indicate that, at the microscopic level, fracture proceeds by nucleation, growth, and coalescence of microvoids. The morphology of a shear wall is clearly illustrated in Figure 8. We also find microvoids in the mixed mode region but with a more elongated shape, which results from the superimposition of tensile and shear stresses (Figure 9). Finally, in the shear region we once again find microvoids that have been partly or completely obliterated by rubbing of the matching surfaces against each other. Rubbing causes the large smooth smeared regions seen in Figure 10.

Additional fractographic observations are reported below in the section presenting the results of the FRASTA analysis.

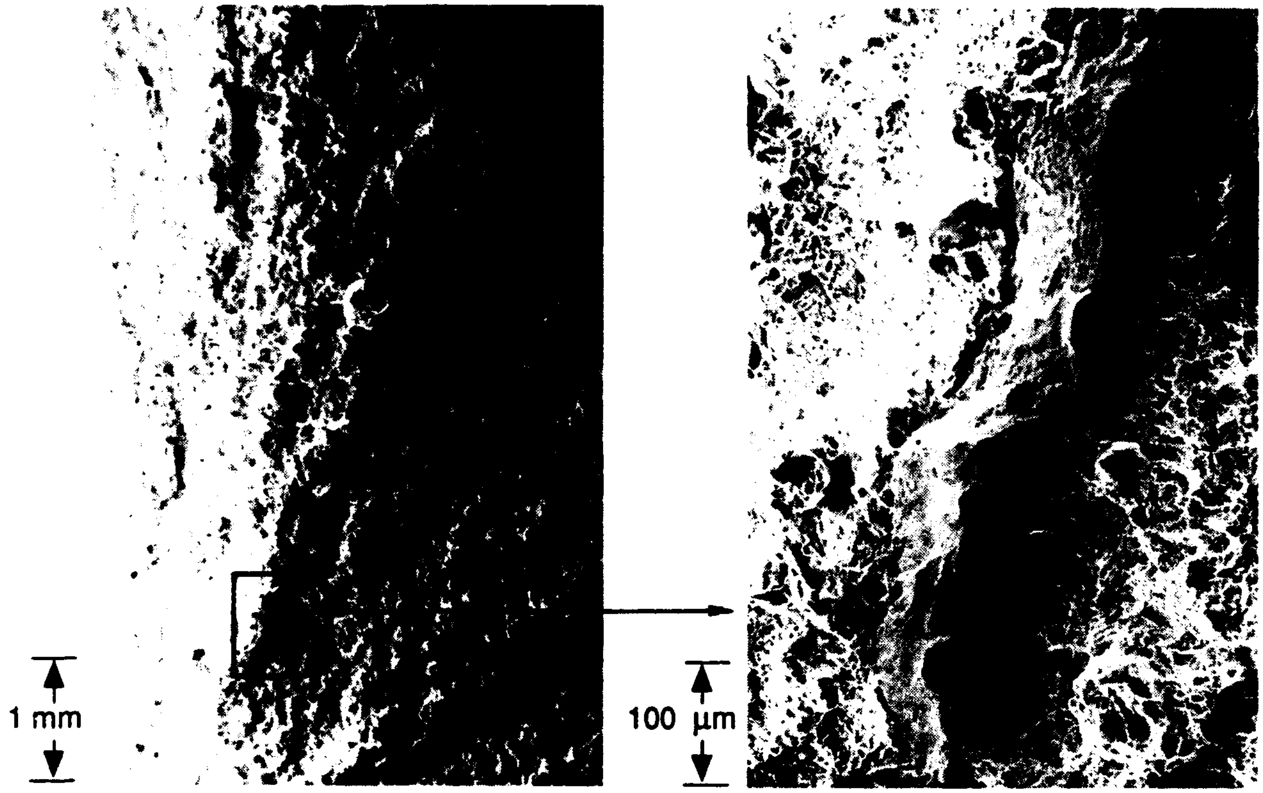

(a) Region noted in macro photo

(b) Detail of shear wall connecting two layers of tensile cracks

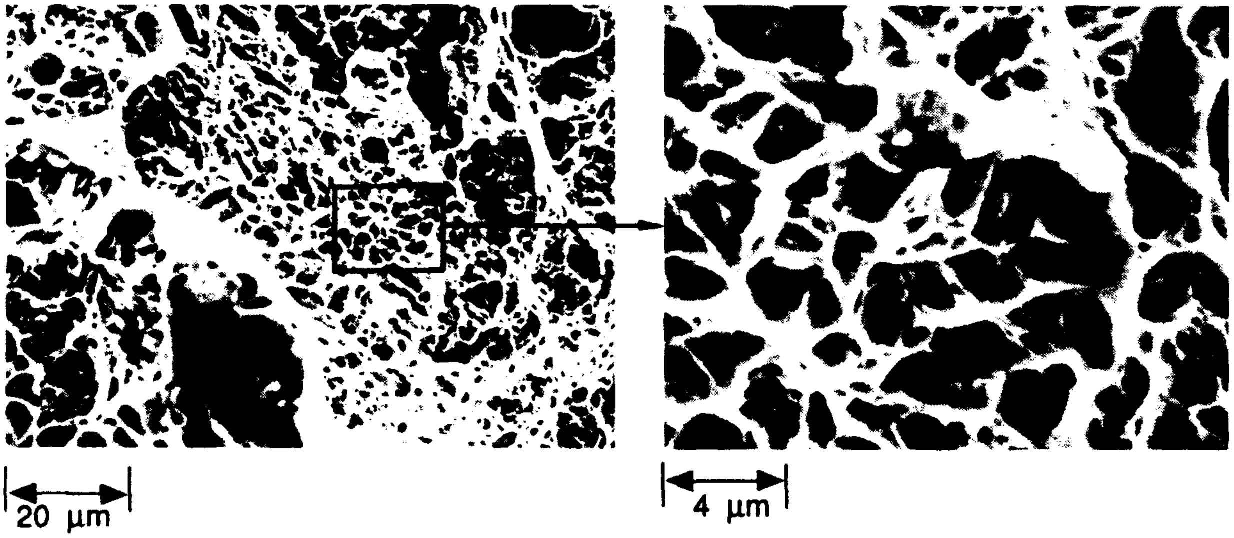

(c) Closer views of fracture surface

CP-314582-6

Figure 8. Details of the fracture surface morphology of the tensile region in Figure 7.

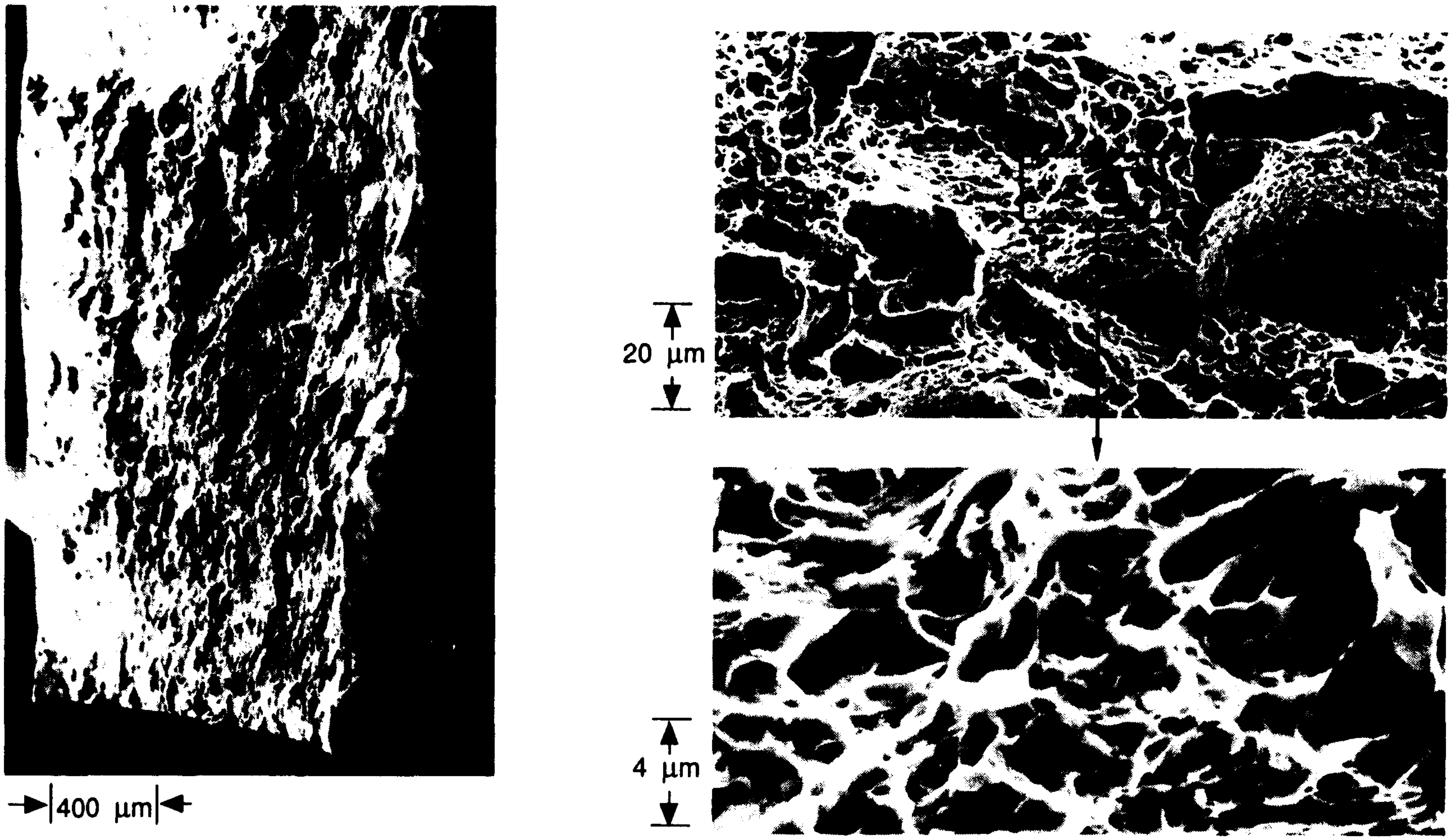

(a) Region noted in macrophoto

(b) Closer views of fracture surface

CP-314582-8

Figure 9. Details of the fracture surface morphology of the mixed-mode region in Figure 7.

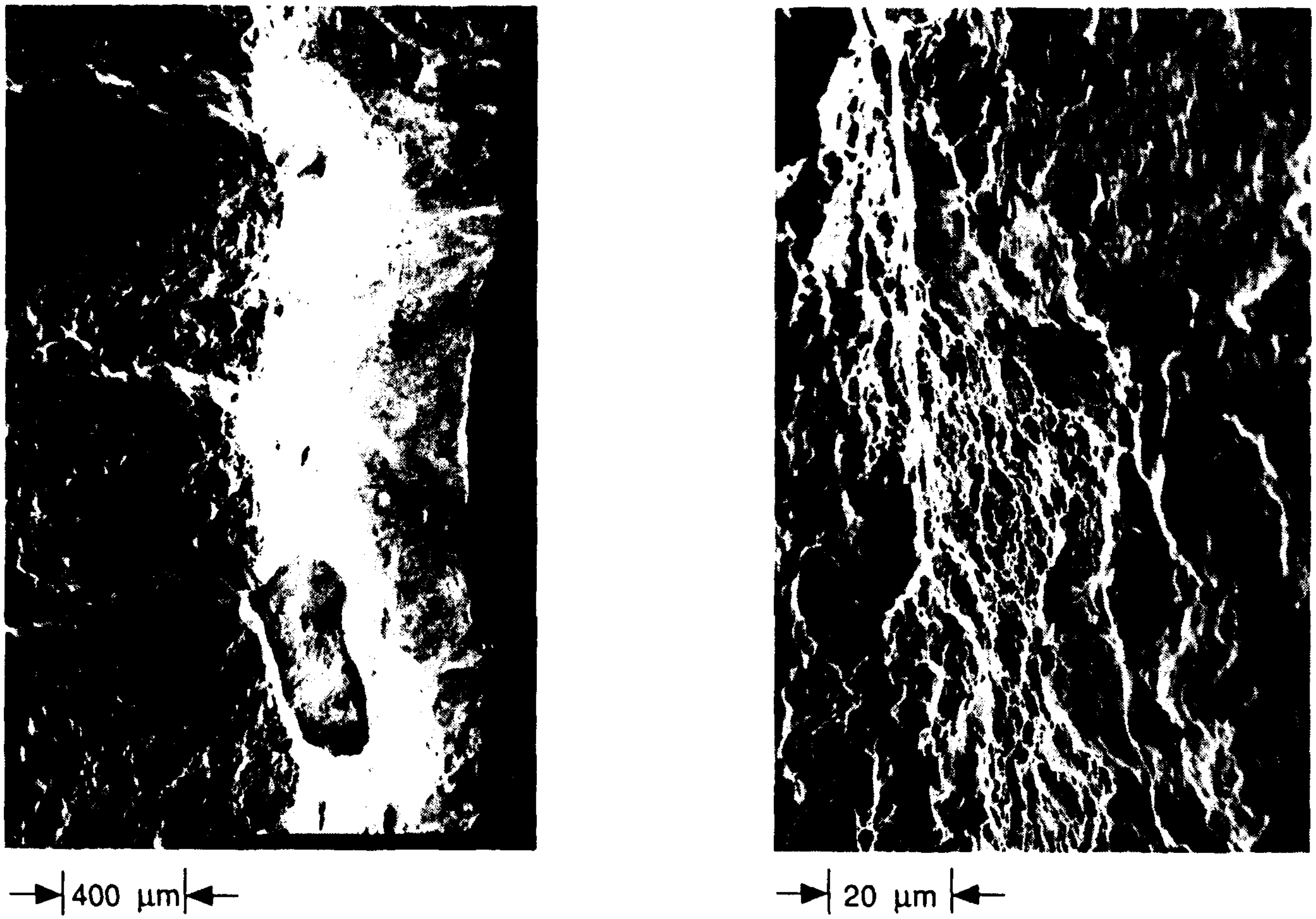

(a) Region noted in macrophoto

(b) Close-up view of edge of shear failure region

CP-314582-7

Figure 10. Details of the fracture surface morphology of the shear region in Figure 7.

DYNAMIC FRACTURE EXPERIMENTS

To characterize the dynamic fracture behavior of 300M and D6ac steels, we performed one-point-bend (1PB) impact experiments. We measured both the dynamic initiation and propagation toughness of 300M steel and the initiation toughness of D6ac steel. To accommodate the cylindrical shape of the starting materials, we developed and validated a new procedure for testing curved specimens.

ONE-POINT-BEND TEST PROCEDURE

The 1PB impact test was proposed and developed by Kanninen et al.[1] and Kalthoff et al.[2] and further developed at SRI.[3] In this test, a single-edge-cracked rectangular specimen is impacted by a moving hammer as in a conventional three-point-bend impact test, except that the specimen supports are omitted [Figure 11(a)]. The crack is loaded in bending solely by the inertia of the unsupported ends of the specimen. The resulting stress intensity history (at the stationary crack tip) is a smoothly varying function of time [Figure 11(b)] and can conveniently be measured by a strain gage mounted near the original crack tip. We relate the near tip strain to the stress intensity by performing a static calibration before the dynamic experiment or by using the elastic singularity solution for the crack tip fields.

Additional experimental parameters are required to obtain the dynamic propagation toughness. We measured the impact velocity, the impact force (with strain gages mounted on the hammer), and the crack propagation history (by taking high-speed photographs of the ligament region of the specimen; the interframe time was typically 5 μs). We then used the impact load and the crack propagation history as input for numerical simulations of the experiments, in which we calculated the energy release rate by means of a path-independent domain integral.[4] We performed the simulations with the explicit DYNA2D[5,6] finite element code by using a two-dimensional plane strain approximation. We also measured strains normal to the crack plane at the initial crack or notch tip and at several locations along the crack path. These strain records provided independent verification of the crack propagation histories and coarse estimates of the stress intensity factor during crack propagation.

In the one-point-bend experiment, we controlled the crack propagation speed by varying the impact velocity and changing the acuity of the initial notch in the specimen.

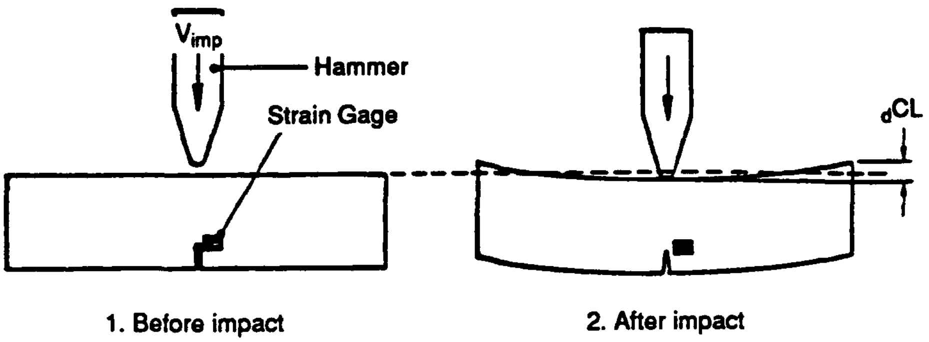

(a) Test arrangement and loading mechanism

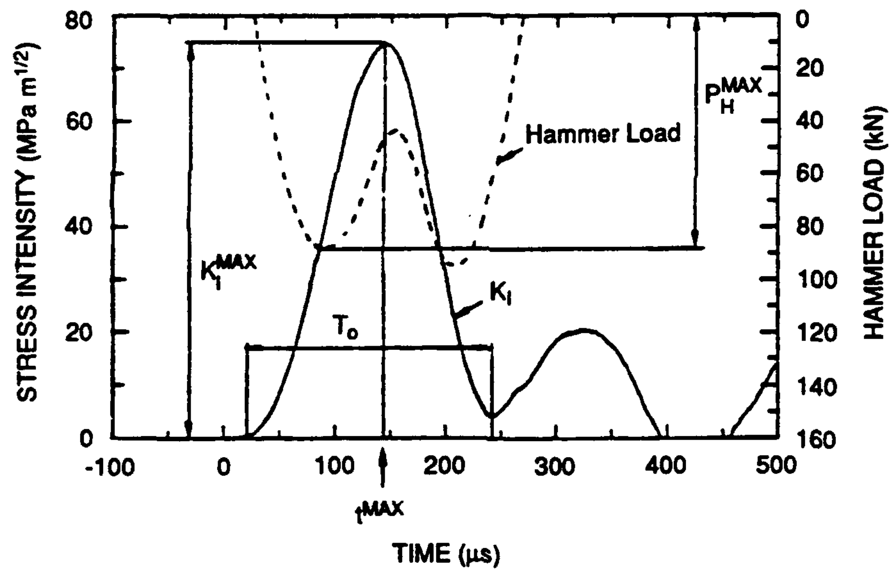

(b) Typical stress intensity and load histories

JA-2777-17

Figure 11. One-point-bend impact experiment.

ONE-POINT-BEND EXPERIMENT WITH CURVED SPECIMENS

When measuring the toughness of materials produced in the shape of hollow cylinders, as are penetrator materials, a specimen in the shape of a ring segment would be convenient to use. Therefore, we developed and validated a modification of the one-point-bend test that enables us to test curved specimens cut directly from the cylindrical penetrator case.

The specimen geometry is illustrated in Figure 12(a) and consists of a 110-degree circular segment with a fatigue crack on the convex side of the specimen. We instrument the specimen with a strain gage at the crack tip and impact on the concave side. In that way, we can propagate the crack in the same orientation as the cracks observed in the penetrator case.

The test procedure and data analysis are the same as for the conventional one-point-bend test. In particular we expect that the stress intensity response curve for a given specimen, material, and impact velocity can be applied to other geometrically similar specimens of different sizes or materials and impact velocities using similar scaling rules. Figure 12(b) shows the stress intensity response curve for the specimen in Figure 12(a) impacted at 1.15 m/s, a velocity too low to cause crack initiation. The curve was obtained by relating the strain measured near the crack tip to the stress intensity factor by using the elastic singularity solution and was normalized by using the procedure described by Giovanola.[3] In the figure, W is the width of the segment, ρ is the density and E is Young's modulus.

We validated the one-point-bend test procedure for curved specimens by (1) comparing initiation toughness values measured for the curved specimens with values measured for the rectangular specimens and (2) comparing the measured stress intensity history with that calculated in numerical simulations of the experiments with the DYNA2D[5,6] finite element code. The experimental results presented in the next section demonstrate that curved and rectangular specimens yield identical toughness results. The measured and calculated stress intensity histories up to the point of fracture initiation are also in excellent agreement, as illustrated in Figure 13. Therefore, we are confident that one-point-bend tests with curved specimens give reliable dynamic initiation toughness values.

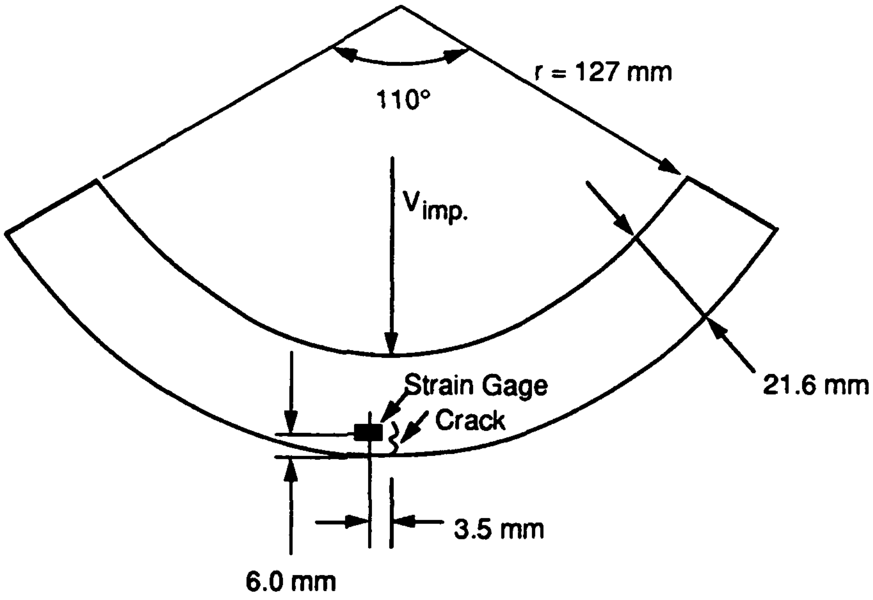

(a) Specimen

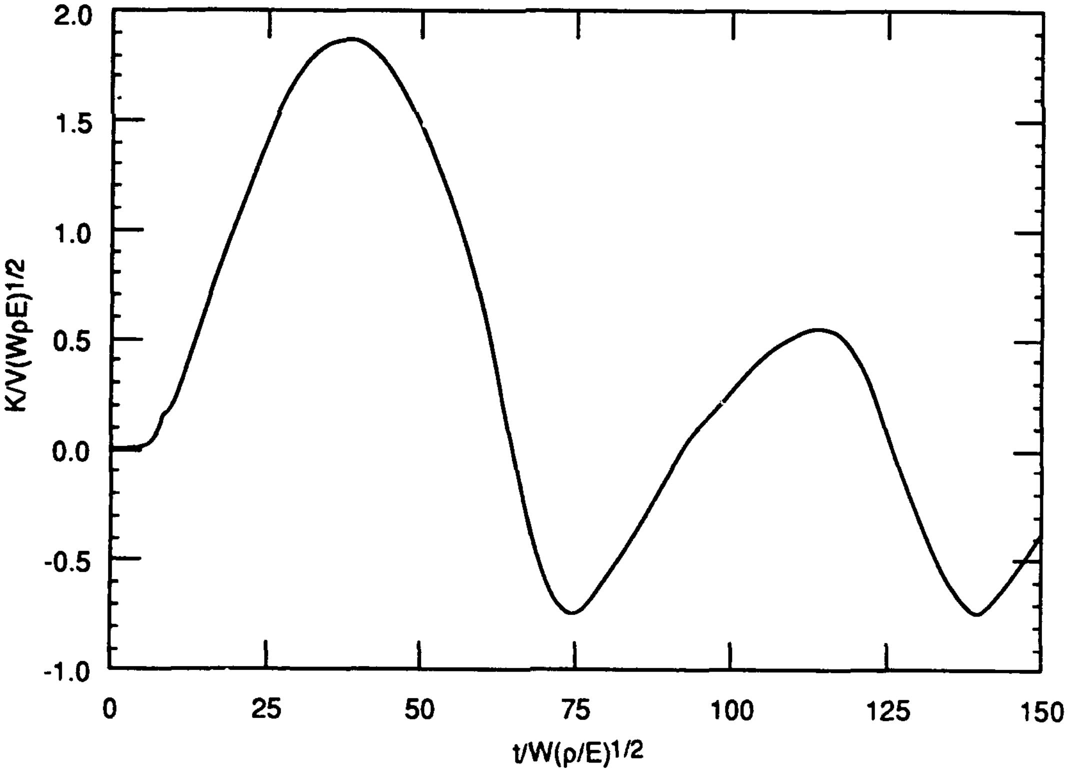

(b) Elastic response curve

RAM-7294-8

Figure 12. Curved one-point bend test method.

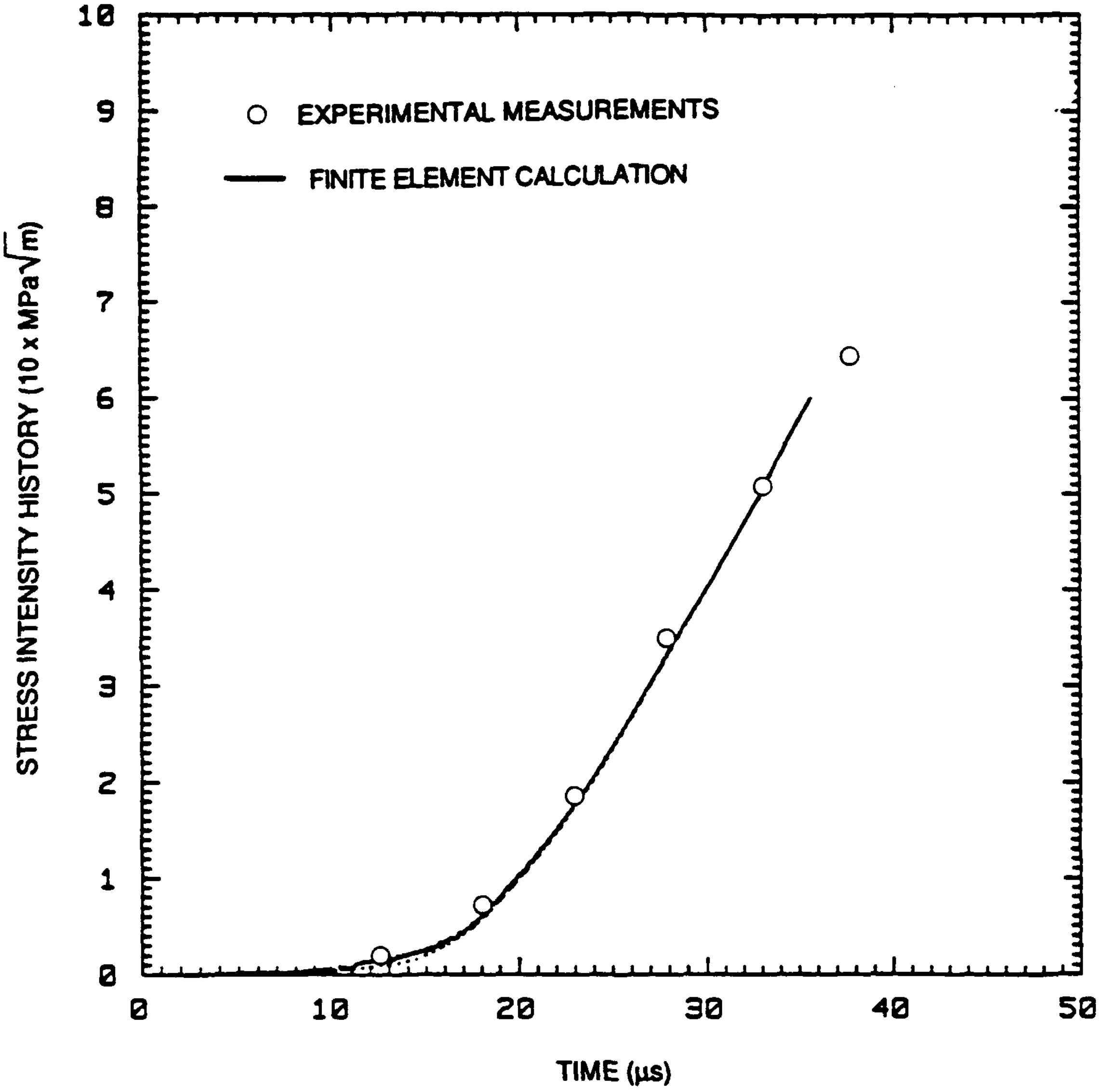

RA-7294-17

Figure 13. Comparison of the measured and calculated stress intensity histories for the curved one-point-bend fracture specimen in Figure 12a.

We fabricated and tested four 300M and three D6ac curved specimens to measure their dynamic initiation toughnesses. We tested three conventional rectangular one-point-bend specimens to measure the dynamic propagation toughness of 300M steel and to verify the data obtained with the curved specimens (Figure 14). The long dimension of the rectangular specimens was oriented along the penetrator axis, so that the crack propagated in the equivalent of the circumferential direction of the case. Two of the rectangular specimens were fatigue-precracked, whereas the third one had a blunt notch with a 0.13-mm root radius. We also tested one curved D6ac curved specimen which had 6.3-mm deep, 1-mm wide side-grooves. Because of the side-grooves, we did not instrument this specimen with a strain gage and we did not measure the initiation toughness.

FRACTURE TOUGHNESS RESULTS

Initiation Toughness for 300M and D6ac Steels

Table 1 compares the dynamic initiation toughness of 300M and D6ac steels. As we mentioned earlier, the average toughness values measured for 300M steel with the curved and rectangular specimens are essentially the same (60 $\mathrm{MPa}\sqrt{\mathrm{m}}$). The average value of the fracture toughness of D6ac steel is almost double the value for 300M steel (116.7 versus 60.1 $\mathrm{MPa}\sqrt{\mathrm{m}}$). Significant shear lips formed at the surface of the D6ac specimens (2-3 mm), whereas the shear lips were either small (<1 mm) or absent in the 300M specimens.

The good agreement between the toughness values for 300M steel obtained with the curved and rectangular specimens validates the curved specimen test and indicates that the crack orientation does not affect the toughness results.

Inspection of the crack tip strain records for D6ac steel reveals that the strain drops off only slowly (several tens of microseconds) and that the drop rate is directly related to the impact velocity. This behavior suggests that, at least initially, the crack propagated rather slowly in a dynamically stable manner under a rising applied stress intensity factor. The formation of large shear lips probably also influenced the drop-off in the strain records. In the 300M specimen, the crack tip strain drop-off was much more rapid. This observation implies that we may not readily detect the onset of crack initiation in D6ac. In other words, the crack tip strain may still be rising while the crack has already started to propagate, driven by an increasing stress intensity factor. Therefore, the value of K_{Id} we quote for D6ac steel may have been affected by a small amount of crack growth.

Thickness = 0.675 (15.9)
Dimensions: inch (mm)

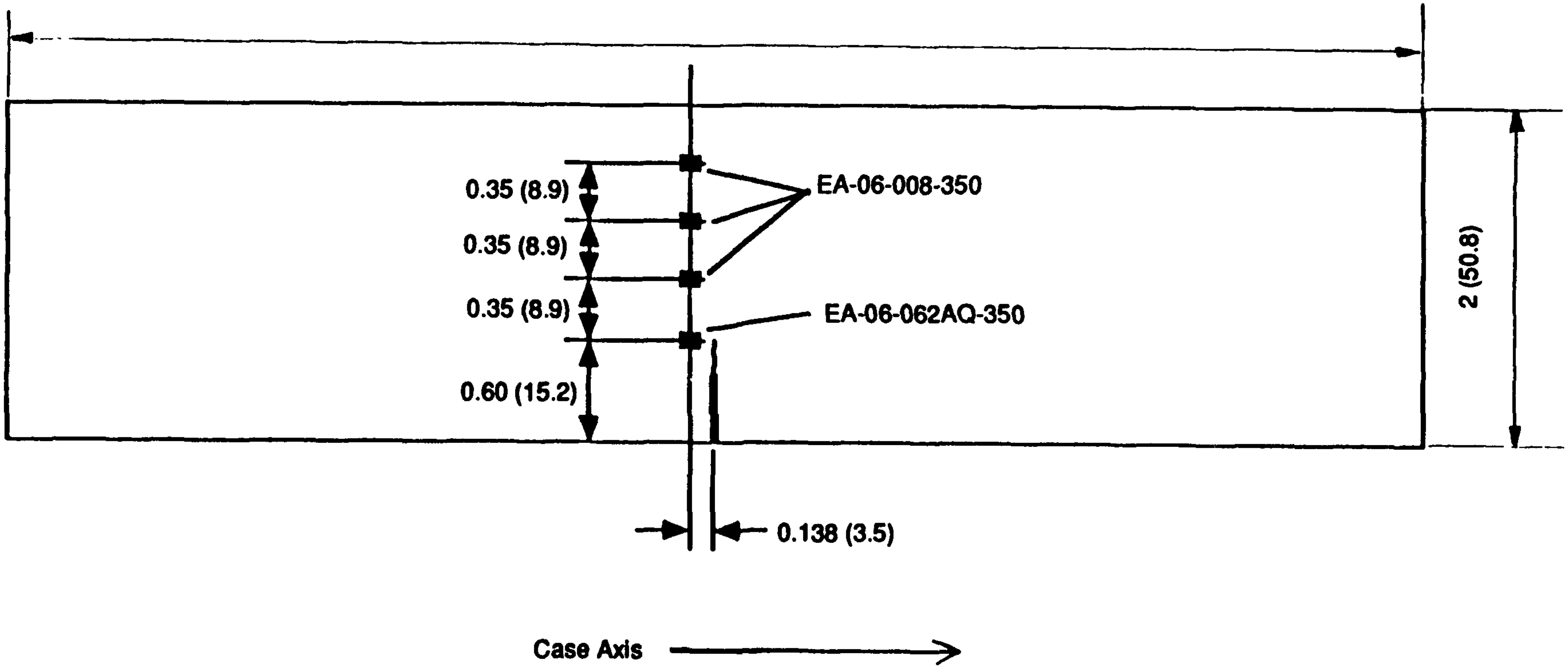

RAM-7294-18

Figure 14. Rectangular cracked bend bar used for crack propagation experiments with 300 M steel.

Table 1

SUMMARY OF DYNAMIC INITIATION TOUGHNESS RESULTS

Specimen Number		K_{Id} (MPa$\sqrt{m}$)		
300M steel	Curved-1	58.9	Average of four values = 60.4	Average of six values = 60.1
	Curved-2	59.7		
	Curved-3	65.5		
	Curved-4	57.3		
	Rectangular-1	57.4	Average of two values = 59.7	
	Rectangular-2	62		
D6ac steel	Curved-1	105.0	Average of three values[a] = 116.7	
	Curved-2	135.0		
	Curved-3	110.0		

[a] The high toughness values for D6ac are at the limit of validity for the use of elastic testing and analysis procedures.

This important difference in fracture behavior between 300M and D6ac steels provides a first indication of why the penetrator cases behaved so differently in sled tests.

Propagation Toughness for 300M Steel

Table 2 summarizes the test conditions for the three crack propagation experiments with 300M steel. The experiments covered a range of velocities of roughly 250 to 540 m/s. During the third experiment (Rectangular-3) with the blunt notch, the impacting hammer partially failed so that we have no reliable load record for this experiment; we were unable to simulate it to calculate the stress intensity history.

Figures 15 through 18 present the experimental data obtained from measurements performed during experiment 300M-steel Rectangular-1. The load history of Figure 15 is similar to the double-humped curve of Figure 11(b), except that the second hump is truncated by fracture of the specimen. Figure 16 shows strain records measured with strain gages along the crack path. Figure 14 gives the position of the gages with respect to the initial fatigue crack tip (specimens Rectangular-1 and -2) or notch (specimen Rectangular-3*). Strain gage 1 recorded the strain history at the stationary crack tip or notch tip, and we used it to establish the time of fracture initiation and the corresponding value of the stress intensity factor. The crack propagation history estimated from the strain records (using the time at which the strain is maximum and the gage locations) is in reasonable agreement with the photographic measurements. Figure 17 shows a time sequence of digitized crack propagation records. The notched tip and the fatigue crack lie to the left of the vertical axis, and the crack propagates toward the right. The spacing between records is proportional to the interframe time. The small kinks along the crack path represent deviations caused by the formation of very small shear lips (less than 1 mm in height). Figure 18 plots the crack extension history obtained from Figure 17. We can approximate the history as three regions of constant velocity.

We used the data in Figures 14 through 16 and 18 as input for a DYNA2D[5,6] finite element simulation of the experiment, and we calculated the stress intensity history at the propagating crack tip. Figure 19 presents the results of the simulation. The initial loading portion of the curve, during which the crack is still stationary, is compared with the experimental measurements, the

---

*The notch depth for specimen Rectangular-3 was only 10 mm compared with a fatigue crack length of 15.2 mm for the other two specimens.

Table 2

CONDITIONS FOR DYNAMIC FRACTURE TOUGHNESS EXPERIMENTS WITH 300M STEEL

Specimen Number	Notch Root Radius	Impact Velocity (m/s)	Stress Intensity Factor at Initiation (MPa$\sqrt{m}$)	Average Crack Velocity (m/s)
Rectangular-1	Fatigue-precracked	15.2	57.4	450
Rectangular-2	Fatigue-precracked	7.2	62.0	250 (crack arrest)
Rectangular-3	Blunt notch (notch depth: 10 mm)	15.9	182.0	540

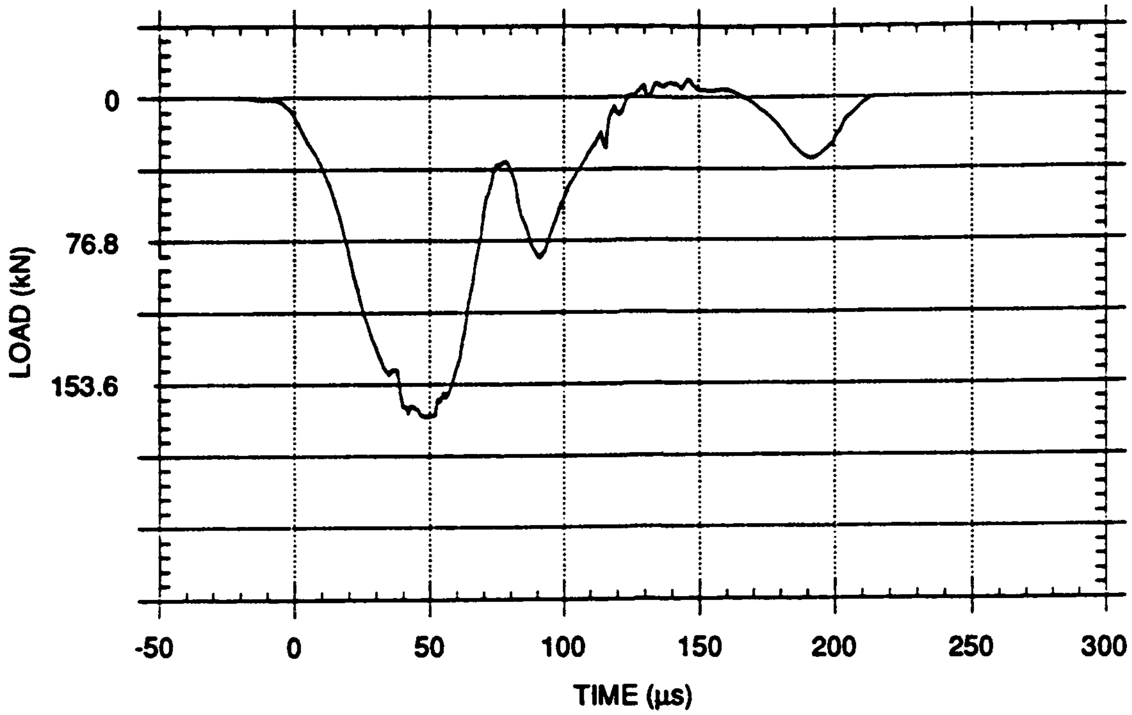

Figure 15. Hammer load history for experiment 300 M-Rectangular-1.

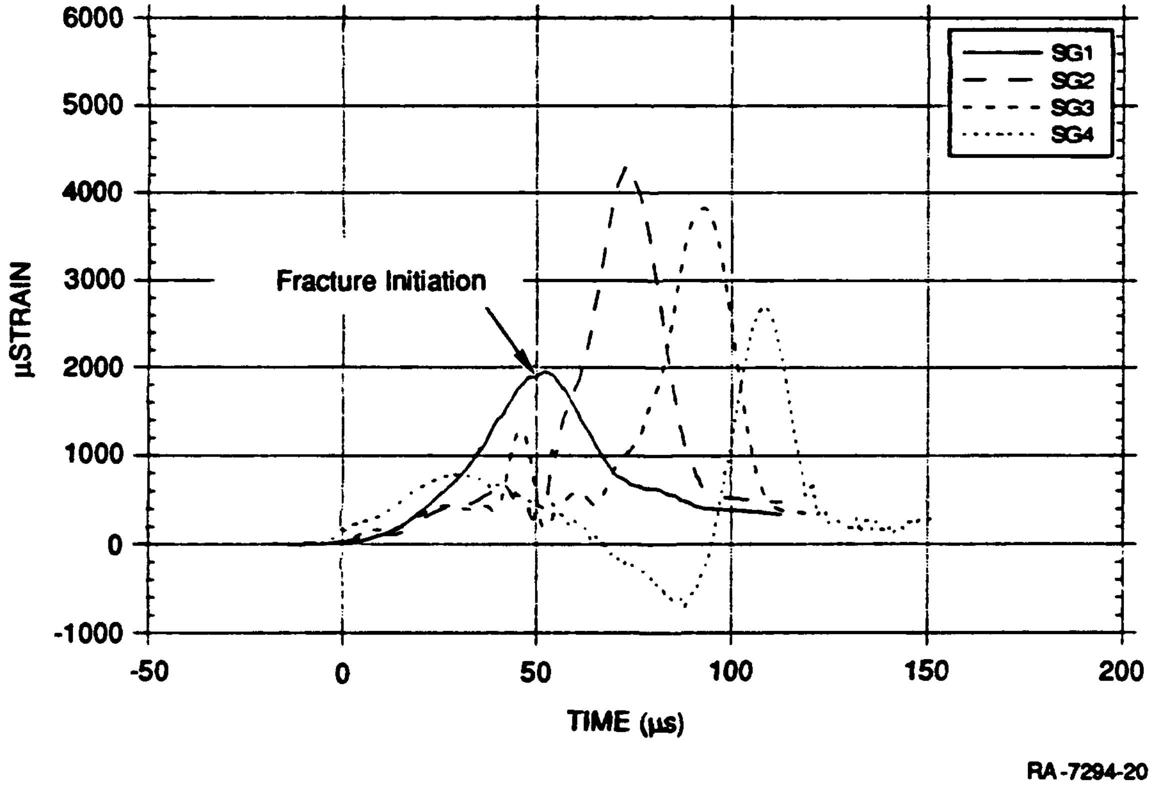

Figure 16. Strain histories at crack tip and along crack path for experiment 300M steel Rectangular-1.

(Strain gages position is indicated in Figure 14.)

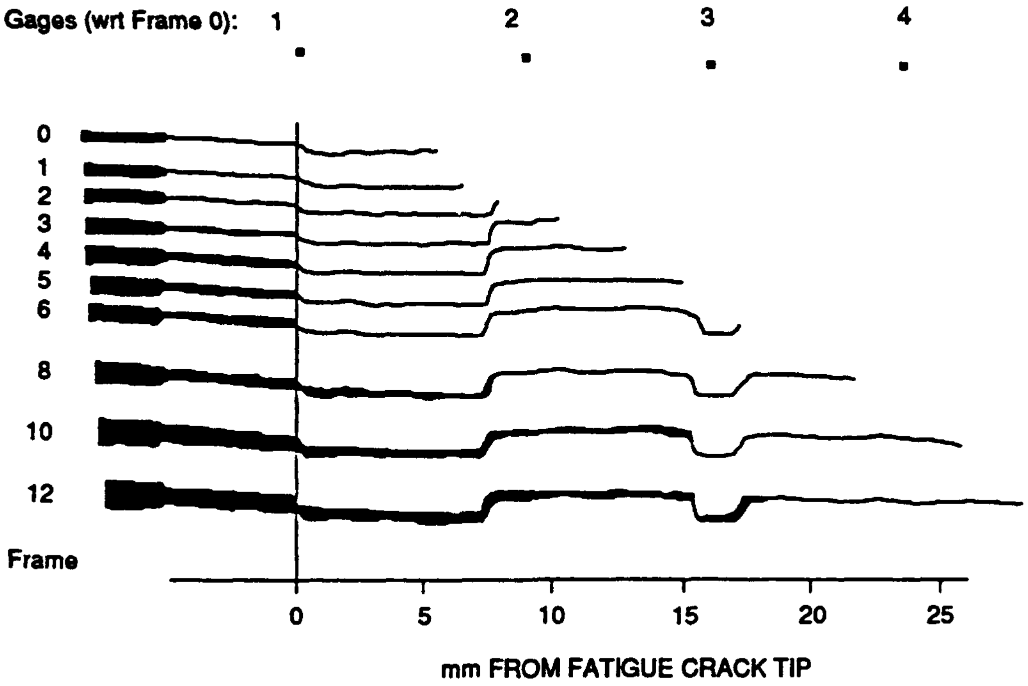

Figure 17. Digitized crack propagation records for experiment 300M steel Rectangular-1.

(The vertical axis is equivalent to a time axis with the time increasing downward; interframe time, 5μs)

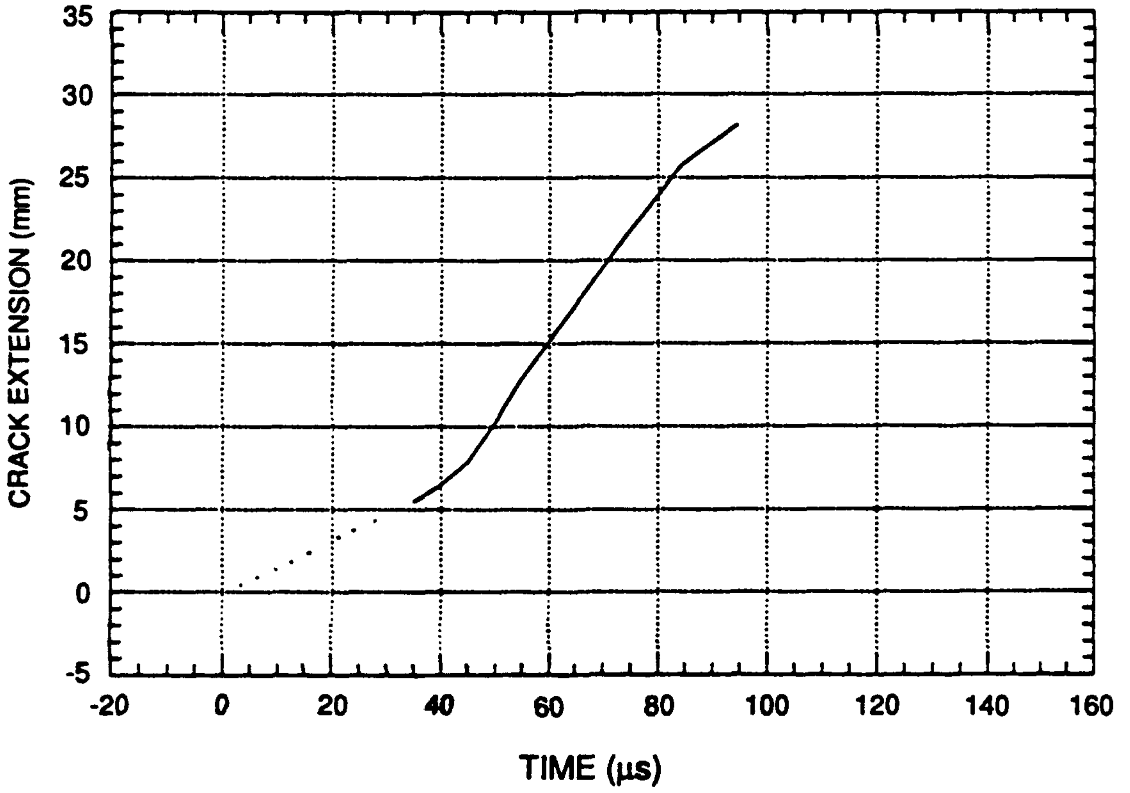

RA-7294-22

Figure 18. Crack extension history obtained from records in Figure 17.

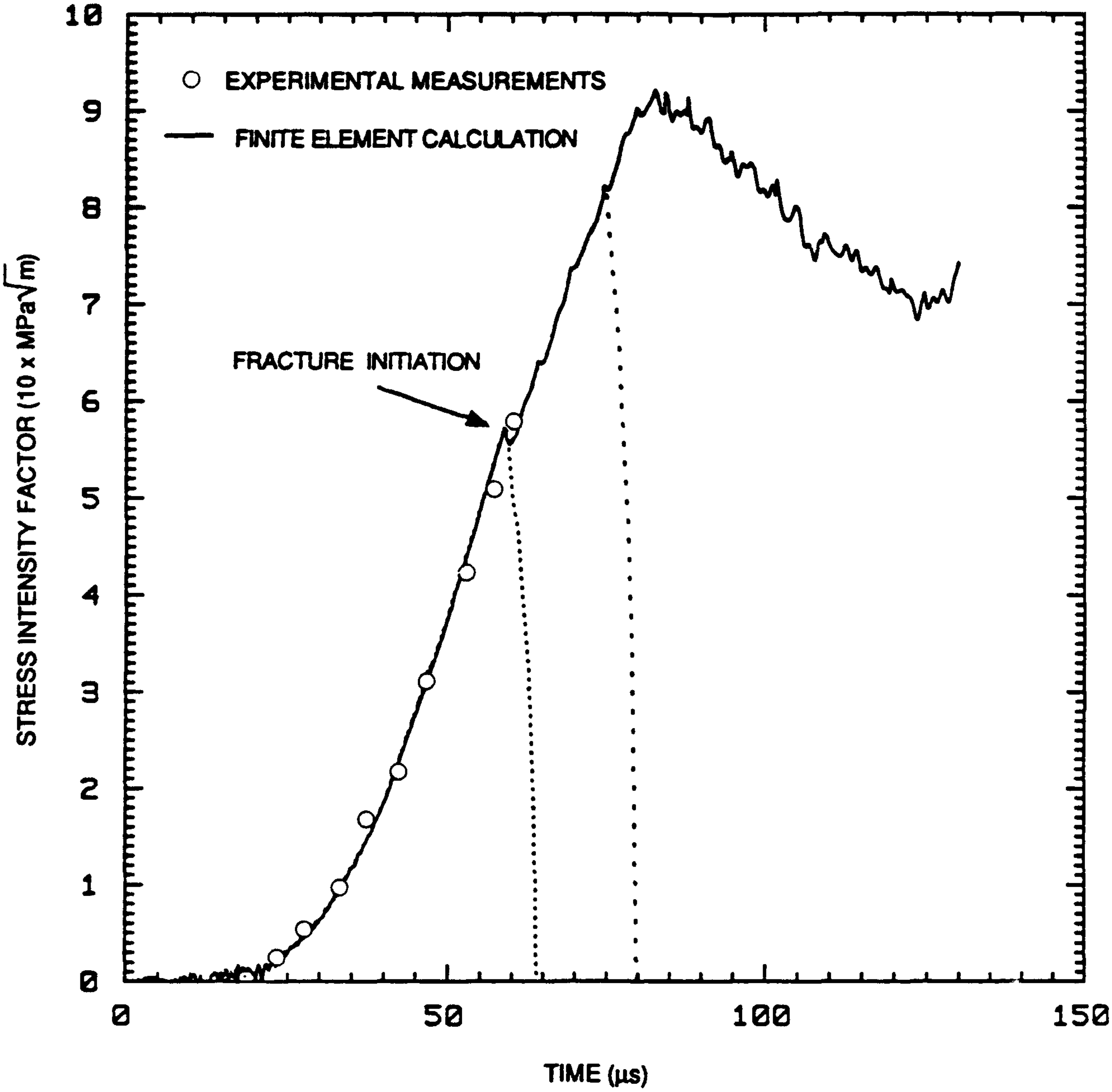

RA-7294-23

Figure 19. Stress intensity factor history calculated in the finite element simulation of experiment 300M steel Rectangular-1.

agreement is very good and inspires confidence in the simulation technique. After initiation, the stress intensity factor continues to rise up to 50% higher than the initiation value, then drops off more gradually. The peak in the stress intensity curve corresponds to the first change in crack velocity. Figure 20 plots the calculated strain histories at the positions of the strain gages in the experiments. Comparison with Figure 16 again shows good agreement between experiment and calculations: The strain histories for corresponding locations are very similar, the amplitudes are comparable,* and the times (relative to initiation) at which the strains are maximum are also in reasonable agreement, except that the peak in strain at position 4 appears too late in the calculation (68.5 μs after initiation) compared with the experiment (57.4 μs). In general, we do not consider the last 10 mm or so of the propagation, because the combination of small remaining ligament and compression applied by the hammer may invalidate the analysis method. Comparing the measured and calculated strain history at the initial crack or notch tip, we observe that after crack initiation, the strain drops much more rapidly in the calculation. This drop may be due to three-dimensional effects, but it may also indicate that the crack accelerates gradually in the experiment rather than instantaneously, as assumed in the calculation.

We obtained similar experimental and numerical results for experiment Rectangular-2 in which the crack arrested, leaving an unbroken ligament 8 mm-long.

Before we present and discuss the propagation toughness data, we must qualify the results of the numerical simulations. The calculated stress intensity history is sensitive to the details of the crack extension history input to the calculation. On the other hand, there is a considerable uncertainty about the history of the measured crack extension, which is due to (1) the relatively low framing rate (5 μs/frame), (2) the possibility that the crack front is curved in the interior of the specimen, and (3) the resolution limits in the analysis of the high-speed photographs. For instance, we cannot exclude the possibility that the crack may have arrested and reinitiated between two frames and that the crack extension process is discontinuous and consists of a series of small crack jumps. We have not yet established quantitative limits on the accuracy of our crack extension measurements, but we have made rough estimates of the range of possible variations and have used these ranges to evaluate the influence of crack extension histories on the stress intensity histories during crack extension. From this study, we conclude that the crack extension history has a significant influence on the results but that the general conclusions we draw below are still valid even with the range of uncertainty about the crack extension histories.

---

*We cannot expect the strain amplitudes to be exactly the same because the simulation assumes plane strain conditions, whereas the measurements were performed at the specimen surface (i.e., under plane stress conditions).

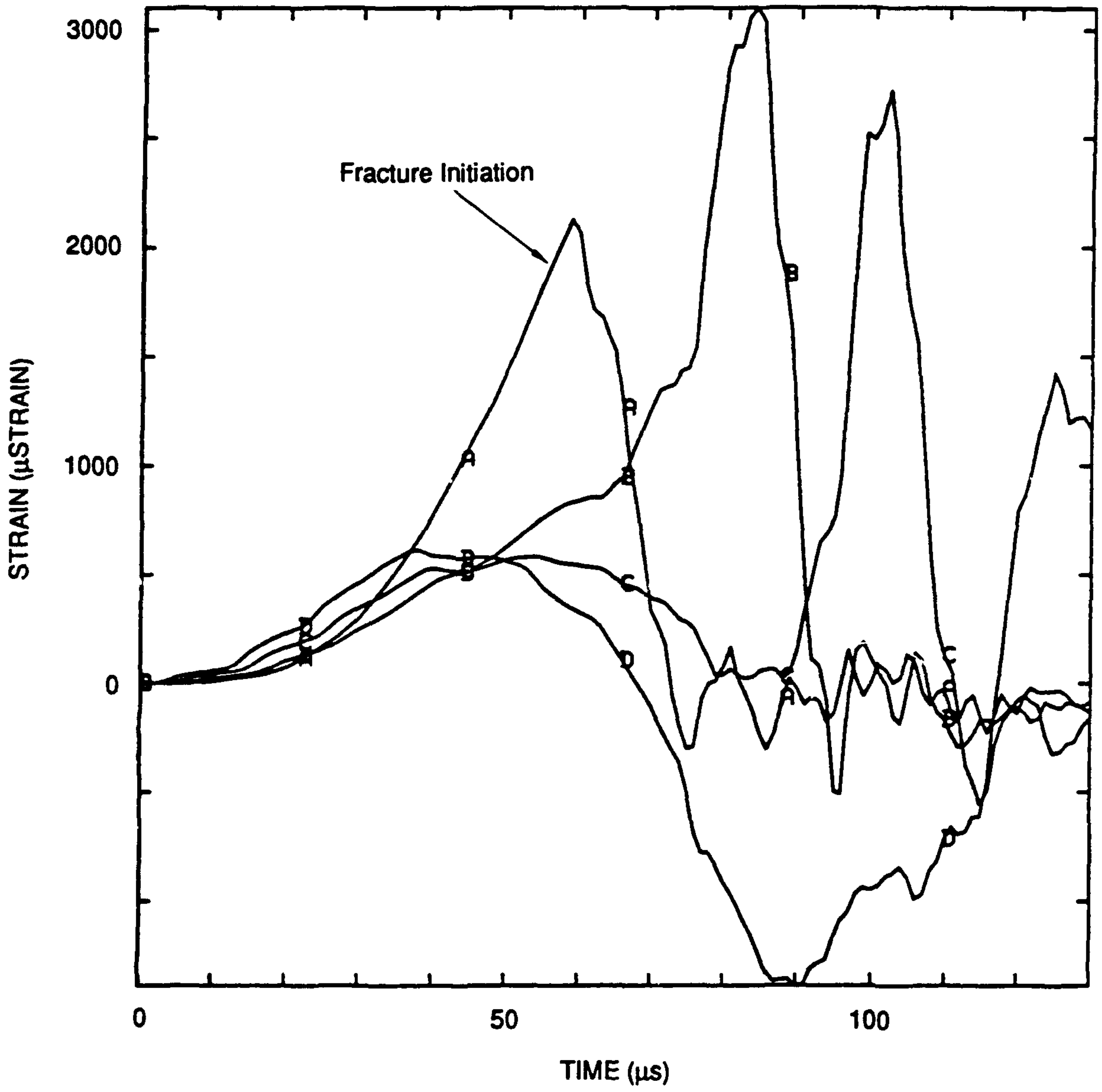

Figure 20. Calculated strain histories at the positions of the strain gages in experiment 300M steel Rectangular-1.

In analyzing the crack propagation results from the two 300M Steel Rectangular experiments, we assume that the crack propagates under instantaneous equilibrium conditions. In other words, we assume that the stress intensity applied to the crack tip by the bending specimen is equal to the toughness of the material at every instant during the propagation.

Our preliminary analysis of the results shows that within the range of crack velocities reached during the experiments (250-450 m/s), the propagation toughness does not vary systematically with crack velocity but rather in a more or less consistent way with the amount of crack extension Δa. For this reason, we present the propagation toughness results as a function of crack extension in Figure 21 (resistance curve). For the two fatigue precracked specimens, the toughness rises to values higher than 90 $\mathrm{MPa}\sqrt{\mathrm{m}}$ as the crack extends, then gradually decreases to values on the order of 75 to 80 $\mathrm{MPa}\sqrt{\mathrm{m}}$. The maximum toughness and the crack length at which it is reached depend on the accuracy of the crack extension history input for simulating the experiment. Calculations for the third experiment with a blunt notch, which assume an estimated load history, show that for this test the toughness continuously decreases from the high value applied at initiation (because of the blunt notch, we can apply about three times the initiation toughness value) until toward the end of crack extension, it reaches values on the order of 70 to 90 $\mathrm{MPa}\sqrt{\mathrm{m}}$. Because of the uncertainty about the load history, the results of the Rectangular-3 experiment are not discussed further here.

From these results, we conclude that the propagation toughness of 300M steel rises during crack extension to a value of approximately 75 $\mathrm{MPa}\sqrt{\mathrm{m}}$, which represents a 25% increase over the initiation toughness. This rise seems to occur over several millimeters of crack extension. The value of the arrest toughness estimated from the results of experiment Rectangular-2 is also about 75 $\mathrm{MPa}\sqrt{\mathrm{m}}$. Our earlier work[7] with 4340 steel (HRC 50) also suggested an increase in propagation toughness over initiation toughness similar to that reported here. The causes of the apparent rise in toughness are not clear, and further work is required to elucidate this point and to separate possible extrinsic structural effects from intrinsic microstructural effects.

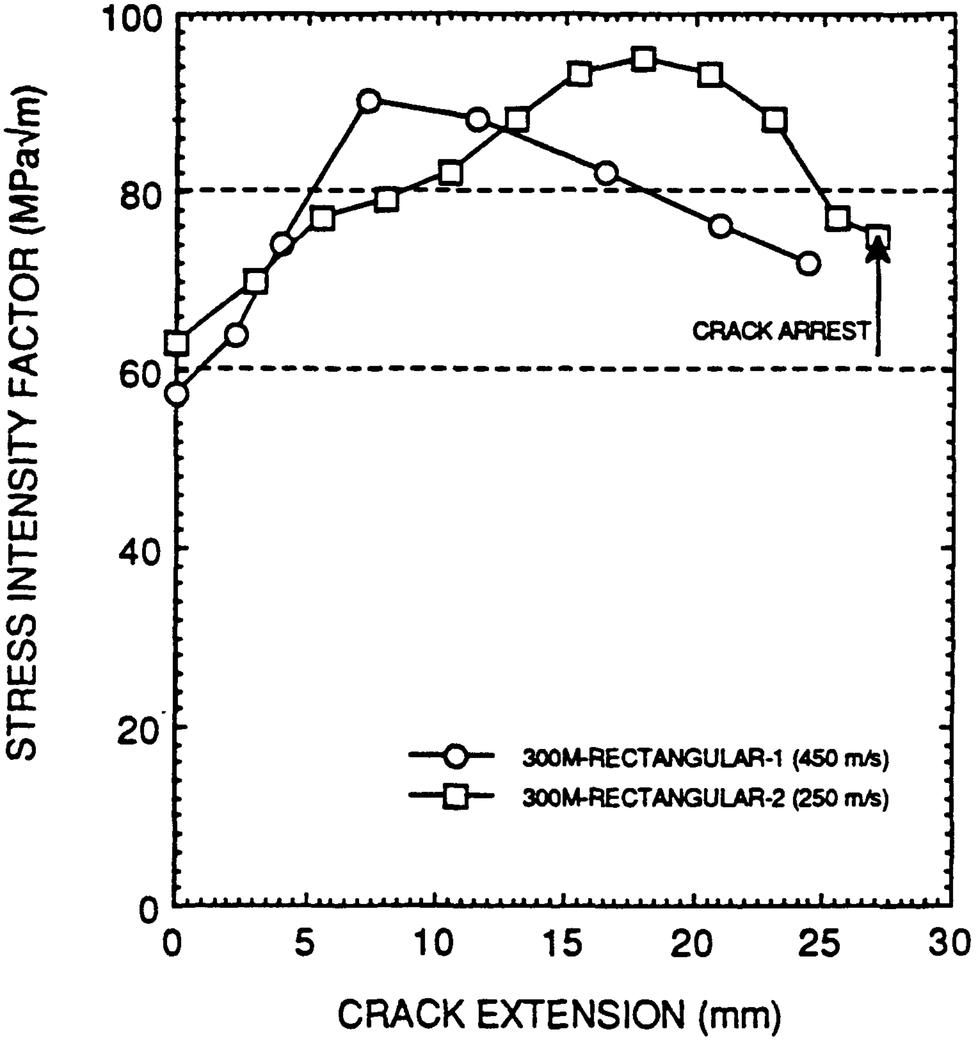

RA-7294-25

Figure 21. Stress intensity factor as a function of crack extension calculated for two crack propagation experiments with 300M steel.

FRASTA OF D6ac AND 300M STEELS

FRASTA CONCEPT AND PROCEDURES

Simply stated, the FRASTA technique compares quantitative three-dimensional topographies of conjugate fracture surfaces, reconstructs the details of the fracture process, and graphically presents the results as a series of plots. FRASTA was conceived from a kinetic interpretation of microfracture processes in materials, as discussed below.

Consider the development of a microcrack in a material under application of a load. Initially, the material undergoes local plastic flow before failure begins, at some weak spot or stress concentrator, in the form of a microvoid or microcrack. The newly formed microfracture surfaces are free surfaces, so the stresses on those surfaces fall to zero. Thus, the material immediately beneath the surfaces undergoes no further plastic deformation. The applied load is redistributed to unfractured material in front of the crack tip, which continues to deform plastically until it, too, fractures.

Microfracture extension results from the sequential process of deformation, microfracture, and redistribution of stresses. This sequential deformation and microfracture process produces differences in the amount of plastic deformation experienced locally by the material as a function of distance from the microfracture nucleation site and as a function of time after microfracture nucleation. Thus, this difference in the amount of plastic deformation experienced by local material is a record of the history of the microfracture events.

The difference in local plastic deformation, however, cannot be determined by examining simply one fracture surface. When a crack front moves through the plastic zone at the crack tip, it interacts with local microstructural features, so that the total amount of plastic deformation developed at the crack tip is divided unevenly between the two fracture surfaces. This interaction of the crack tip with the local microstructure and the uneven division of plastic deformation results in irregularities on the fracture surface. The total amount of plastic deformation occurring during fracture can be determined only by assessing the deformation on mating surfaces. Indeed, only by matching the topography of conjugate surfaces can we establish the nucleation sites and sequence of microcracking.

The FRASTA technique accesses information on microfracture evolution by obtaining precise, quantitative, three-dimensional topographic profiles of conjugate fracture surfaces and matching them, with the aid of a computer, to determine the development of local plastic deformation accompanying fracture. The information on differences in local plastic deformation is used to reconstruct the microfracture sequence from beginning to end.

The results of FRASTA are presented in two ways: (1) a series of fractured-area projection plots (FAPPs) and (2) a series of cross-sectional plots (XSPs) as a function of map separation. The FAPP is equivalent to a radiograph of the microcracks taken in a direction perpendicular to the fracture plane at one instant during crack extension. This plot provides information on the location(s) of the microcrack initiation site(s) and the projected area(s) of the microcrack(s) or crack(s). By examining a series of fractured-area projection plots produced as a function of map separation, we obtain a detailed picture of crack propagation.

The percentage of the fractured area in FAPP can also be computed and converted into the actual area or the average crack length if the examining window is rectangular. By plotting the area or crack length as a function of map displacement in micrometers, we can assess the crack growth rate.

The XSP shows a cross section perpendicular to the fracture surface, displaying how two surfaces match each other, the amount of overlap (plastic deformation necessary before fracture), and the amount of crack face opening displacement. The crack tip opening displacement determined from the plot can be related to the J-integral or stress intensity factor to assess the fracture toughness of the material or the loading conditions.

THREE-DIMENSIONAL FRASTA OF FRACTURE SPECIMENS

We performed three-dimensional FRASTA analysis of three fracture specimens: specimen 300M steel Rectangular-2, a D6ac specimen with deep side grooves that we had tested in a preliminary experiment to establish whether we could apply the usual (elastic) 1PB test procedure to D6ac steel, and specimen D6ac steel Curved-3.

Results for Specimen 300M Steel Rectangular-2

The fracture surface of 300M steel produced in the 1PB experiment is very flat and smooth and similar to the fracture surface of the thumbnail crack in Figure 6. The similarity in macroscopic appearance of the fracture surfaces of the penetrator case and the fracture specimen suggest that the data generated in the 1PB test and the associated fractographic observations are relevant to the forward failure of the case. On the other hand, we identify significant differences in the fracture surface morphology of the case tail section and the fracture specimen. As we pointed out earlier, we believe that these differences are due to differences in thickness, in loading mode, and possibly in microstructural conditions.

Figure 22a shows a SEM photograph of the fracture surface in the initial fatigue crack tip region; a magnified view of this region is shown in Figure 22b and indicates that fracture occurs by nucleation and growth of microvoids. The microscopic fracture process is thus similar to that observed in the tail fragment (compare Figure 8 and Figure 22).

Figure 23 shows scanning electron and scanning laser microscope (SLM) micrographs as well as topographic images of conjugate fracture surfaces of 300M steel Rectangular-2 specimen. The topographic data in the bottom two images of the figure served as input for the FRASTA analysis. Figure 24 presents a sequence of FAPPs showing the last stage of fatigue crack growth and the onset of rapid crack extension over the first 100 μm or so. The number at the bottom left of each plot is a measure of the separation of the crack surfaces (a value of 1 corresponds to a separation of 358 μm). Fatigue crack extension stops at (approximately) a separation of 0.606 and initiation of rapid crack extension at a separation of 0.616. The stage between these two values corresponds to blunting of the fatigue crack tip. The FAPPs reveal that, microscopically, crack extension is more or less uniform across the length of the observed crack front with a small fracture process zone. No isolated microcracks develop ahead of the main crack front.

Figure 25 plots the percentage of fractured area as a function of map separation. A small inflection in the otherwise essentially linear plot indicates the end of fatigue crack growth and the onset of monotonic rapid crack growth. The slope of the plot in the rapid crack growth region is related to the crack propagation resistance of the material. We are therefore working on an analysis of the fractured area plot that may allow us to extract crack propagation toughness data, which could be used in a local fracture model in numerical simulations.

Figure 26 illustrates the blunting process in more detail; it compares the XSP of the closed fatigue crack to the XSP of the fatigue crack at the onset of rapid crack growth. The crack tip opening displacement (CTOD) at this latter stage was about 9.7 μm. If we use the following approximate relationship between stress intensity factor K and CTOD,

$$K^2(1-\nu^2)/E = \mathrm{CTOD} * \sigma_{\mathrm{yield}} \qquad (1)$$

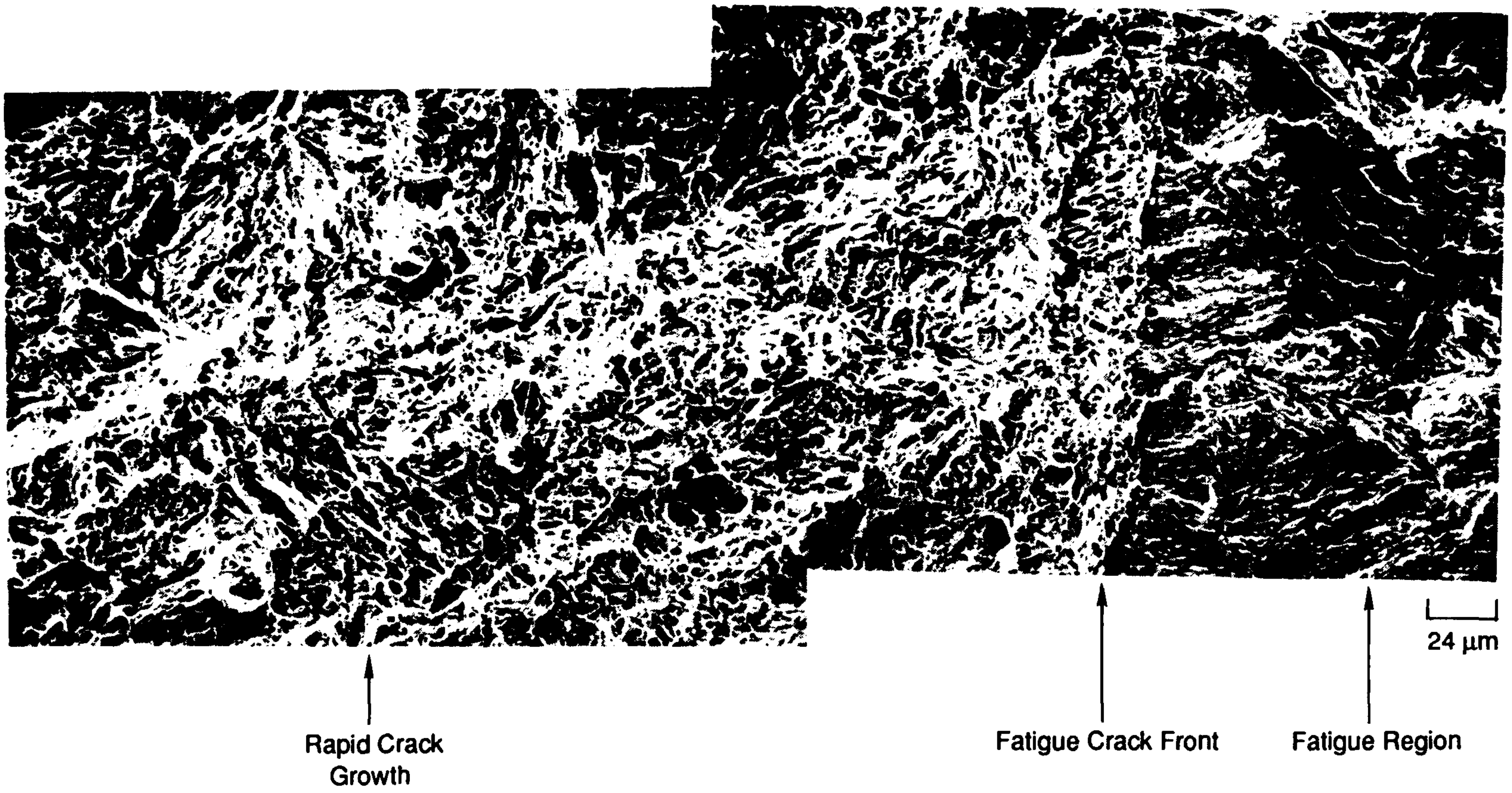

RP-7294-26

Figure 22. Scanning electron photograph of fatigue crack tip region in specimen 300M steel Rectangular-1.

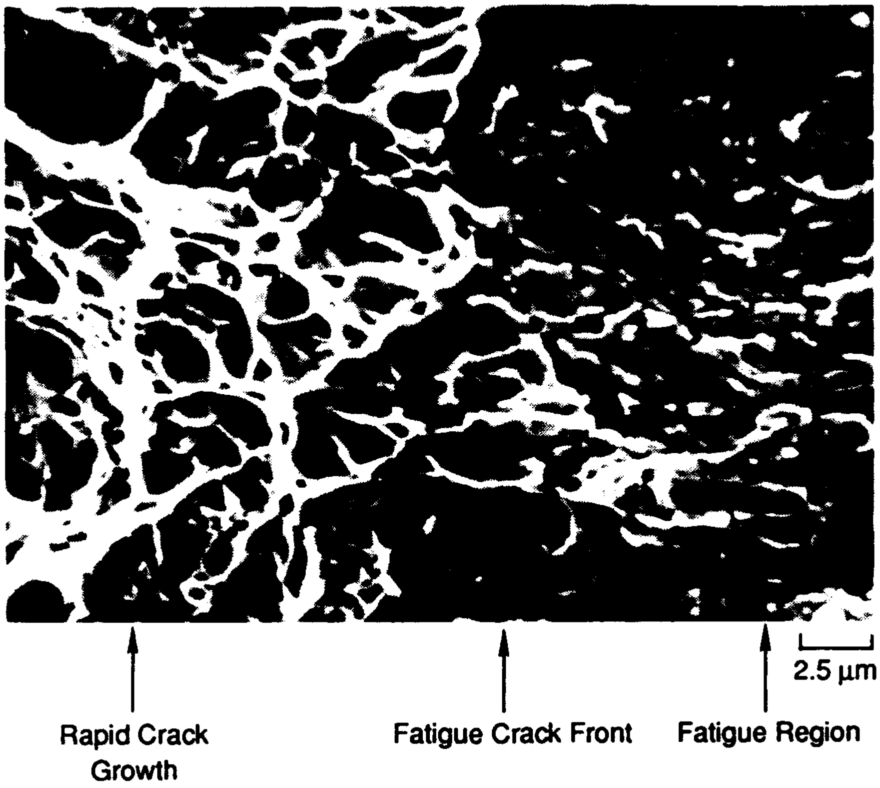

RP-7294-27

Figure 22. Scanning electron photograph of fatigue crack tip region in specimen 300M steel Rectangular-1 (concluded).

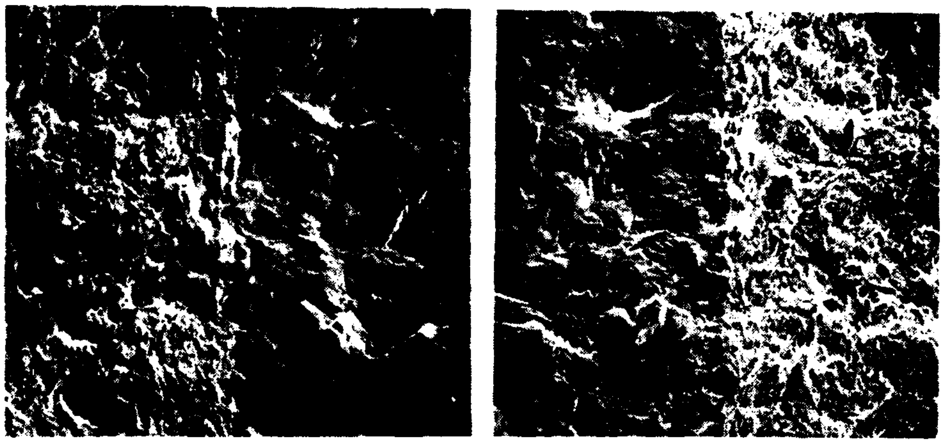

(a) SEM micrograph of surface A

(b) SEM micrograph of surface B

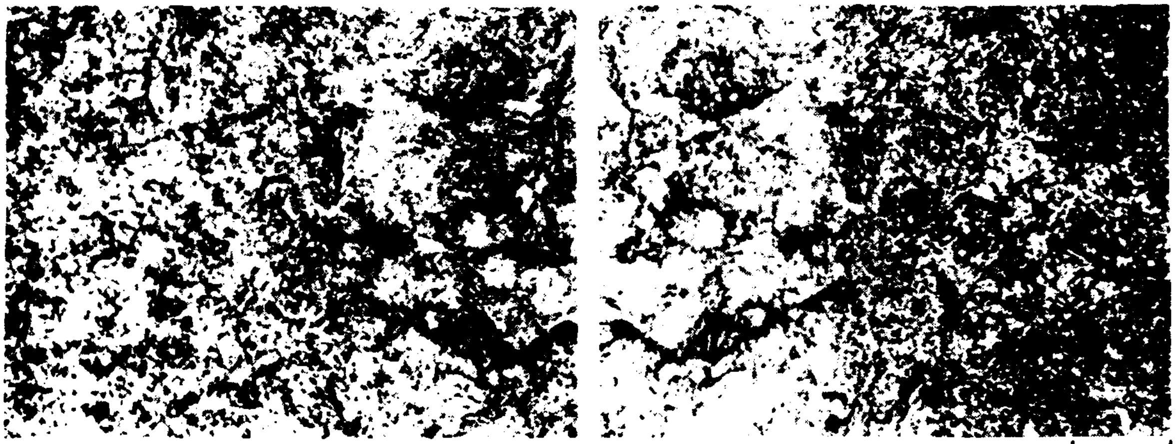

(c) Confocal-optics SLM micrograph of surface A

(d) Confocal-optics SLM micrograph of surface B

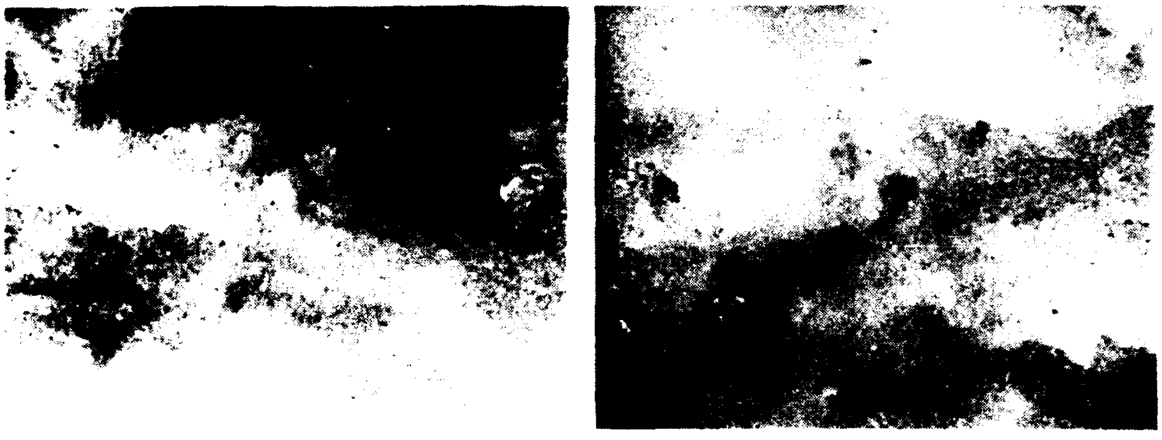

(e) Topography image of surface A made by SLM

(f) Topography image of surface B made by SLM

RP-7294-28

Figure 23. SEM and SLM micrographs and topographic images of conjugate fracture surfaces of 300M steel Rectangular-2 specimen.

(The area represents the end of fatigue-precrack and the beginning of rapid crack growth under impact loading.)

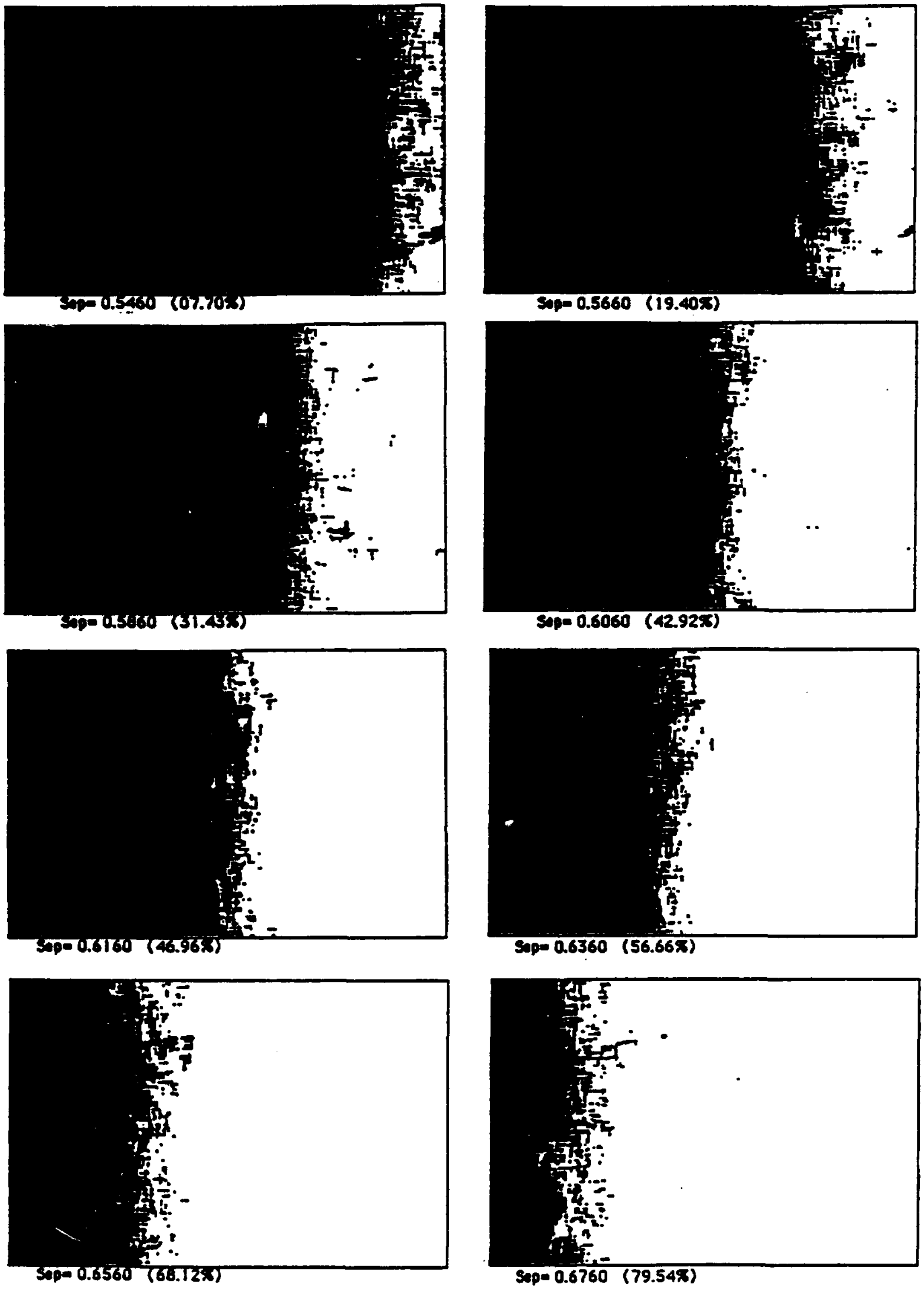

RA-7294-29

Figure 24. A series of fractured area projection plots for 300M steel Rectangular-2 specimen.

(The plot at separation = 0.606 corresponds to the end of fatigue precrack state and the plot at separation = 0.616 to the onset of rapid crack growth.)

Separation 1 = 358.0 μm

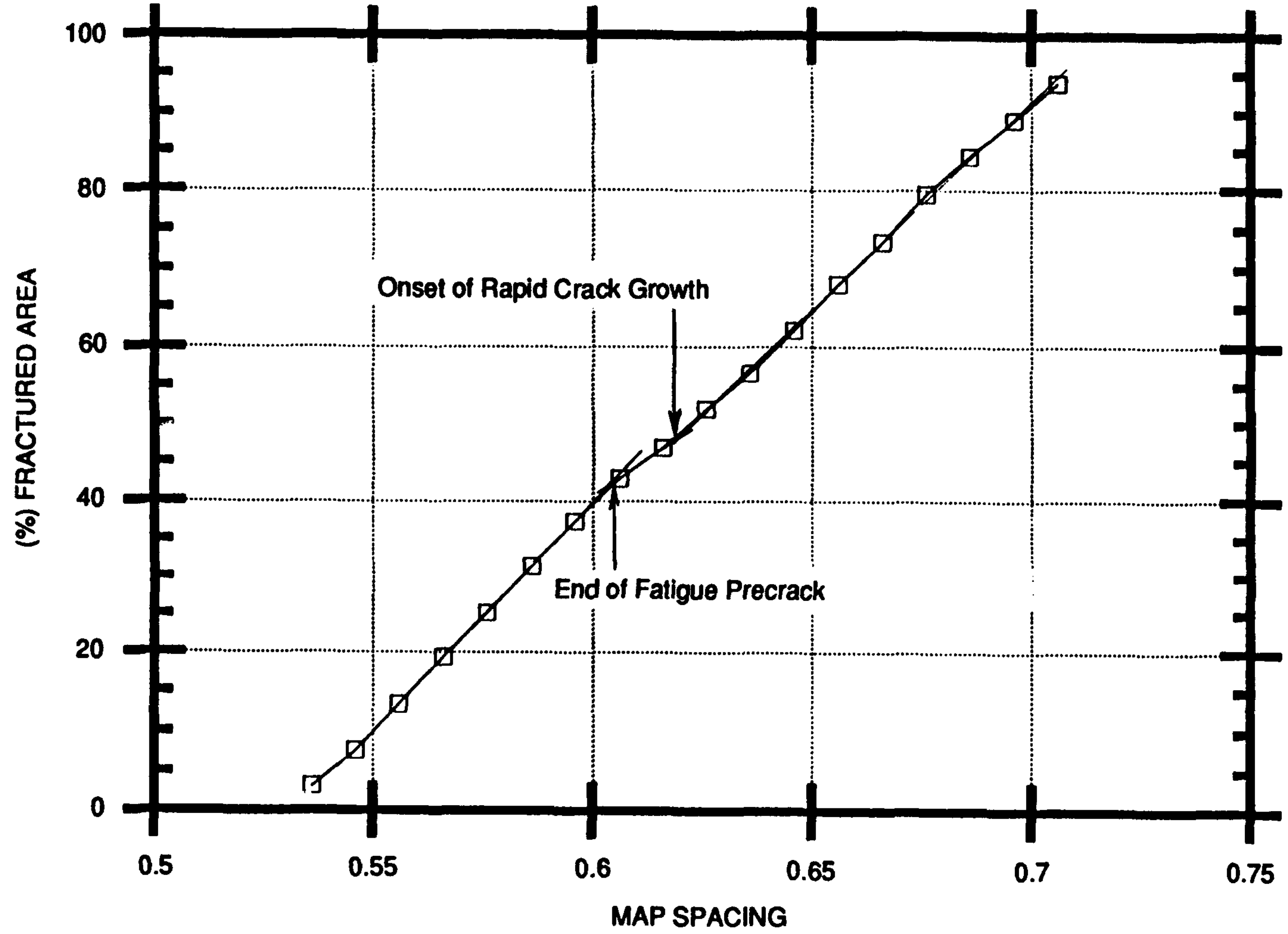

RAM-7294-30

Figure 25. Percentage of fractured area as a function of map separation for specimen 300M steel Rectangular-2.

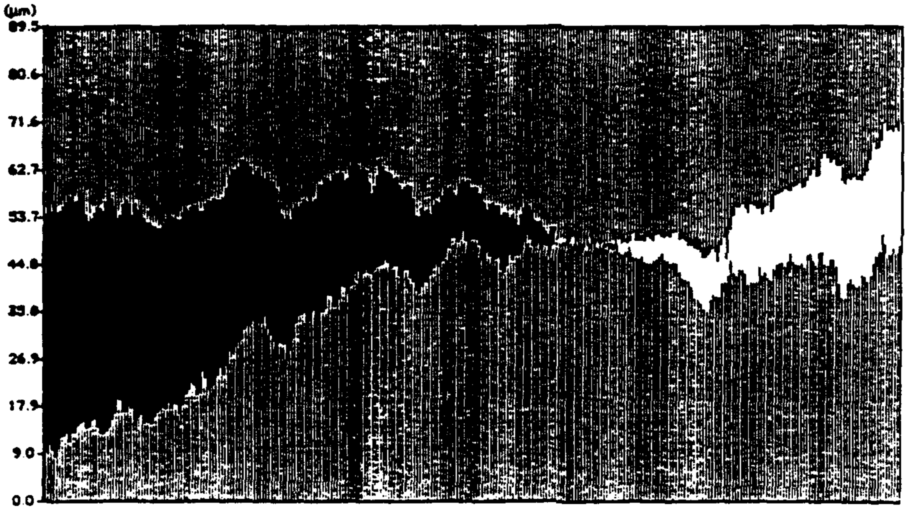

(a) Fatigue precrack surface closed state

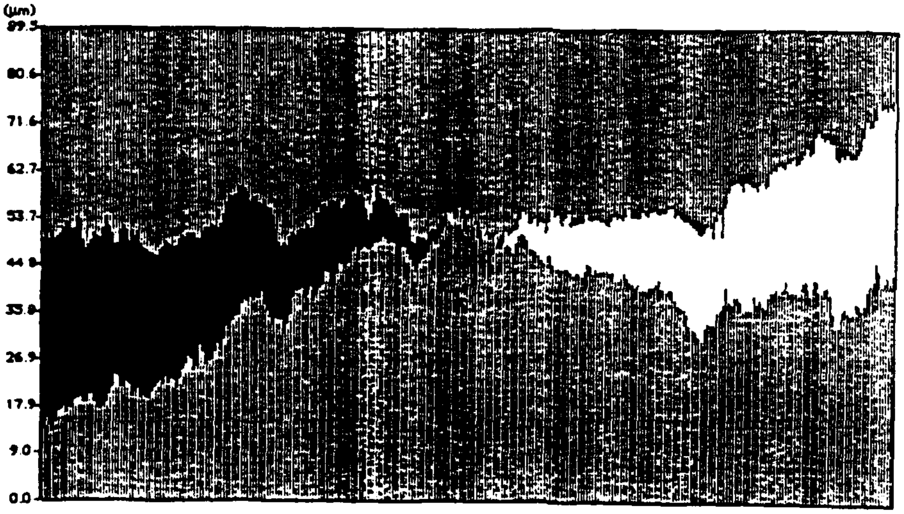

(b) Onset of rapid crack growth from the blunted fatigue crack tip

RP-7294-31

Figure 26. Cross-sectional plots for specimen 300M steel Rectangular-1 showing (a) a state at which the fatigue precrack surface was closed and (b) a state at which the onset of rapid crack growth from the blunted fatigue crack tip occurred. (Crack tip opening displacement at the onset of crack growth was about 9.7 μm.)

where E, ν, and σ_{yield} are Young's modulus, Poisson's ratio, and the yield stress, respectively, we estimate an initiation toughness K_{Id} of 69 MPa$\sqrt{m}$, based on the FRASTA CTOD measurement. As indicated in Table 3, this value is in surprisingly good agreement with the "continuum" measurement of K_{Id}.

Results for Side-Grooved D6ac Specimen

We performed an identical analysis on the side-grooved D6ac specimen, and the results are summarized in Figures 27 through 30. The fracture surface of the D6ac sample has a rougher appearance than that of the 300M specimen (compare Figures 23 and 27, bearing in mind the difference in magnification). The FAPPs in Figure 28 demonstrate that the microscopic crack extension process in D6ac steel involves the formation of microcracked regions ahead of the main crack, which gradually link up with the main crack by fracture of the remaining ligament. The advanced cracks appear somewhat elongated in a direction parallel to the main crack front (which corresponds to the axial direction of the case), suggesting a possible processing effect. Metallographic polished and etched cross sections would help to clarify this point. Clearly, the microscopic crack growth process in D6ac steel is significantly different from the uniform extension observed in 300M steel (compare Figures 24 and 28). This difference in fracture process can in no way be evaluated by simply examining fracture surfaces: only FRASTA analysis can reveal it. The difference is consistent with the difference in toughness established in the dynamic fracture experiments and provides an additional element to explain the difference in penetration performance of cases made from the two steels.

Figure 29, which plots the percentage of fractured area as a function of map displacement, reveals additional differences between the two steels. For D6ac steel, the percentage of fractured area plot has several marked slope inflections after the end of fatigue crack extension, which define regimes of crack growth. The regime between map spacings of 0.02 and 0.1 corresponds to blunting of the fatigue crack, with little increase in fractured area except for the breakage of a few isolated ligaments (see Figure 28). The regime between map spacings 0.1 and 0.2 corresponds to a slow crack growth rate, during which advanced microcracking occurs ahead of the blunted crack tip. This slow crack growth regime would be consistent with our previous observations on the crack tip strain records for D6ac steel. Beyond a map displacement of 0.2, the regime of rapid crack growth sets in.

Table 3
COD RESULTS OBTAINED WITH FRASTA

	300M	D6AC (SG)	D6AC (No SG)
First Crack Extension			
COD (μm)	9.7	9.0	11.2
Equivalent fracture toughness ($MPa\sqrt{m}$)	69	59	66
Onset of "rapid" crack extension			
COD (μm)	9.7	18.7	50.0
Equivalent fracture toughness ($MPa\sqrt{m}$)	69	86	140
Measured fracture toughness ($MPa\sqrt{m}$)	62	-	135

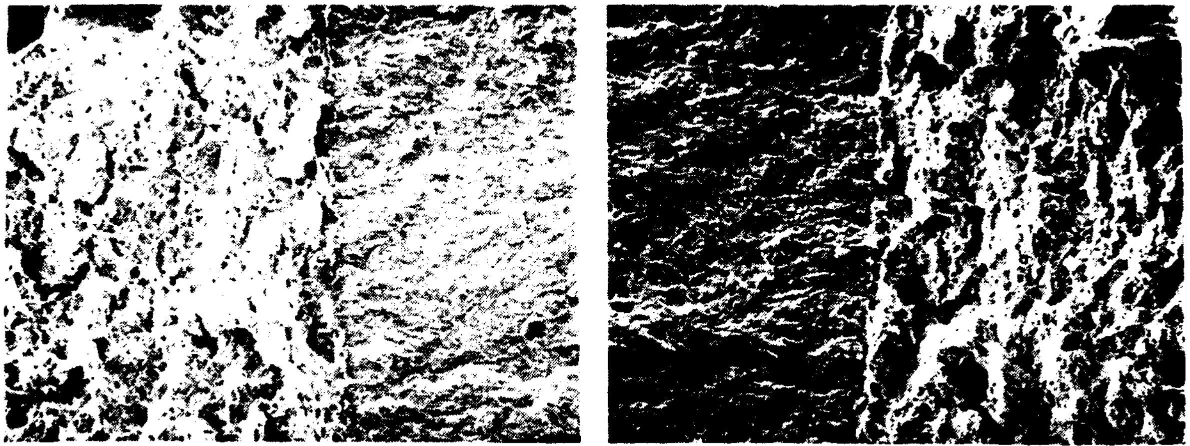

(a) SEM micrograph of surface A

(b) SEM micrograph of surface B

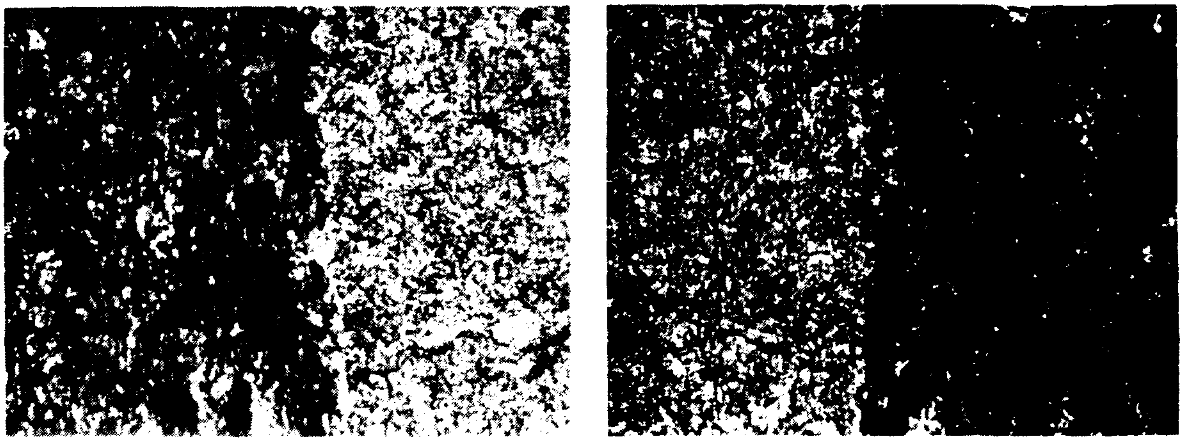

(c) Confocal-optics SLM micrograph of surface A

(d) Confocal-optics SLM micrograph of surface B

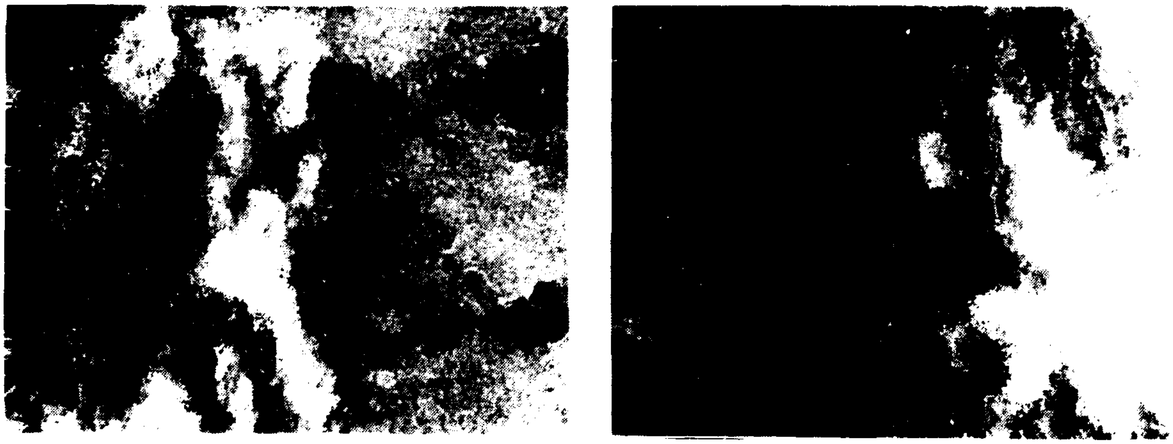

(e) Topography image of surface A made by SLM

(f) Topography image of surface B made by SLM

Figure 27. SEM and SLM micrographs and topographic images of conjugate fracture surfaces of D6ac steel specimen.

(The area represents the end of fatigue-precrack and the beginning of rapid crack growth impact loading.)

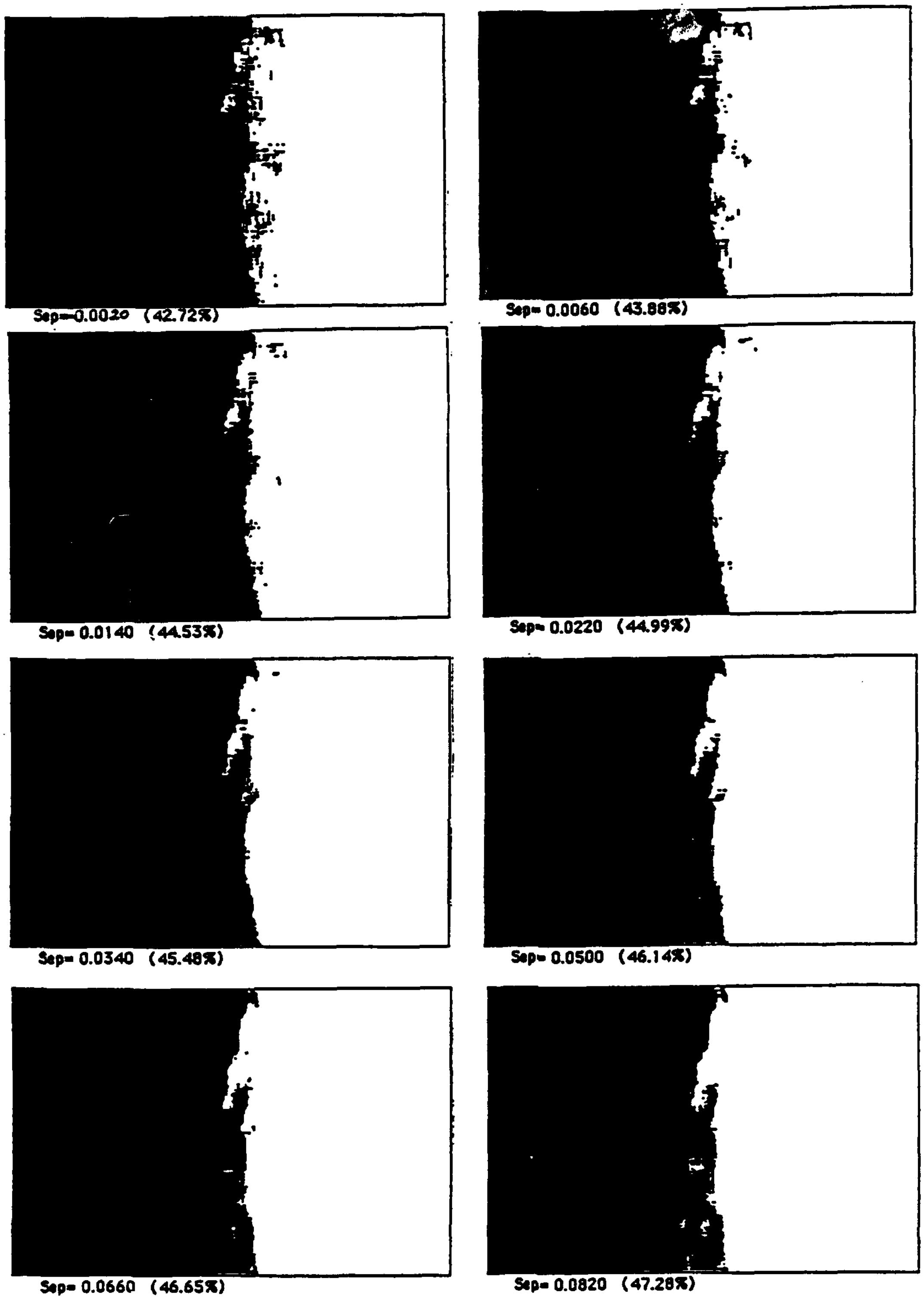

Figure 28. A series of fractured area projection plots for D6ac steel specimen.

(The plot at separation = 0.014 corresponds to the end of fatigue precrack state, the plot at separation = 0.098 to the onset of crack initiation, and the plot at separation = 0.210 to the onset of rapid crack growth.)

Separation 1 = 89.8 μm

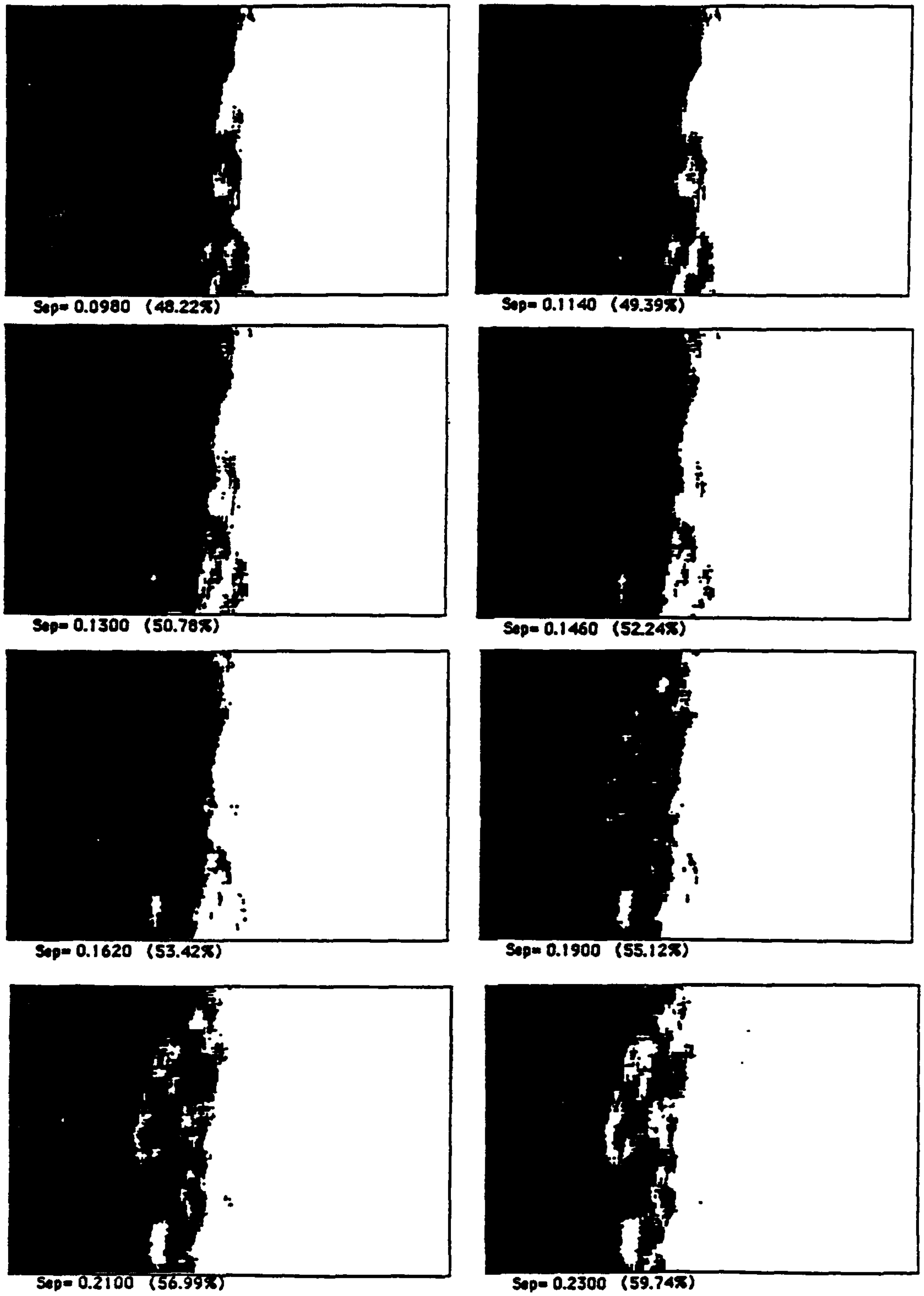

Sep= 0.0980 (48.22%)

Sep= 0.1140 (49.39%)

Sep= 0.1300 (50.78%)

Sep= 0.1460 (52.24%)

Sep= 0.1620 (53.42%)

Sep= 0.1900 (55.12%)

Sep= 0.2100 (56.99%)

Sep= 0.2300 (59.74%)

RA-7294-34

Figure 28. A series of fractured area projection plots for D6ac steel specimen. (continued)

(The plot at separation = 0.014 corresponds to the end of fatigue precrack state, the plot at separation = 0.098 to the onset of crack initiation, and the plot at separation = 0.210 to the onset of rapid growth)

Separation 1 = 89.8 μm

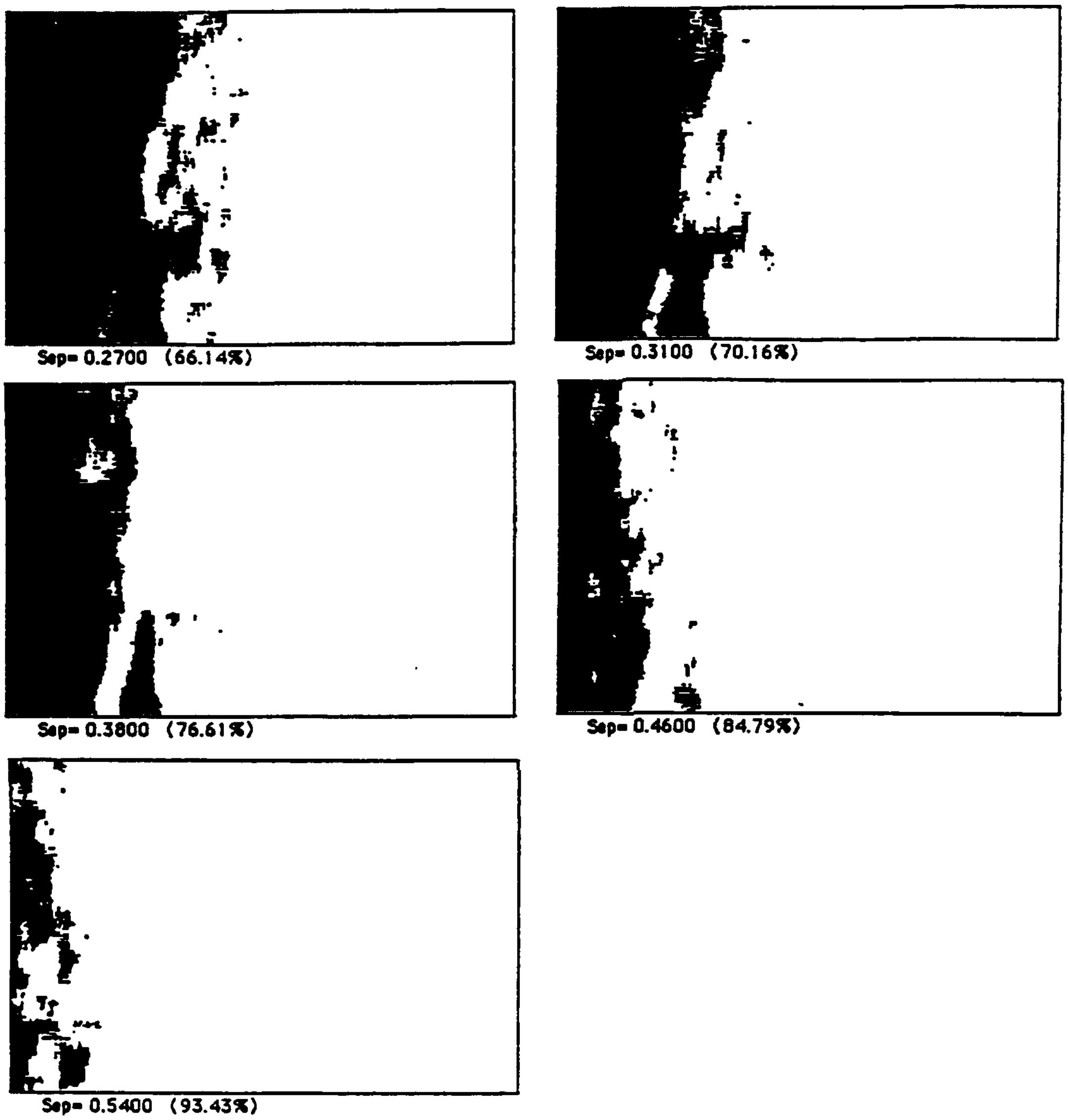

Sep= 0.2700 (66.14%)

Sep= 0.3100 (70.16%)

Sep= 0.3800 (76.61%)

Sep= 0.4600 (84.79%)

Sep= 0.5400 (93.43%)

RA-7294-35

Figure 28. A series of fractured area projection plots for D6ac steel specimen. (concluded)

(The plot at separation = 0.014 corresponds to the end of fatigue precrack state, the plot at separation = 0.098 to the onset of crackinitiation, and the plot at separation = 0.210 to the onset of rapid crack growth)

Separation 1 = 89.8 μm

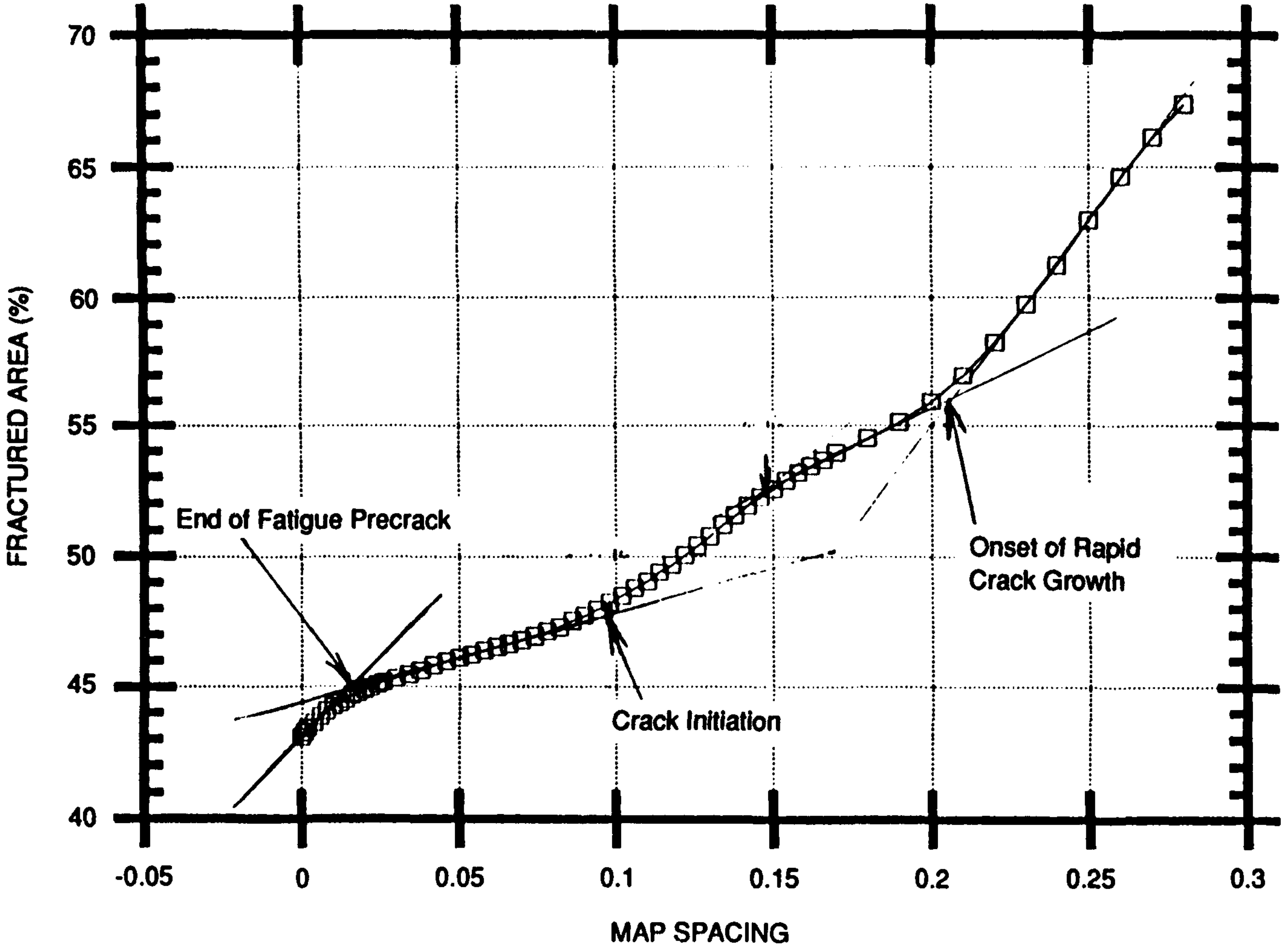

RAM-7294-36

Figure 29. Percentage of fractured area as a function of map separation for D6ac specimen.

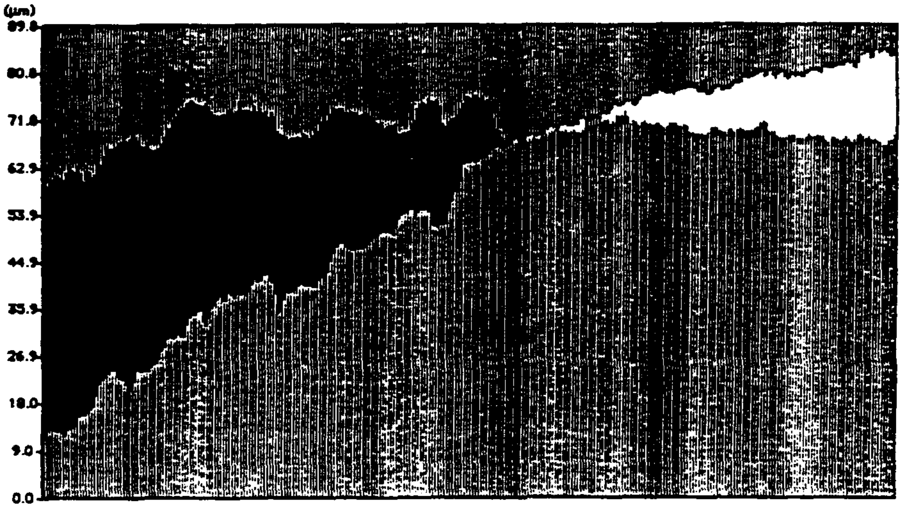

(a) Fatigue precrack surface closed state

(b) End of fatigue precracking state

RP-7294-37

Figure 30. A series of cross-sectional plots for D6ac steel specimen.

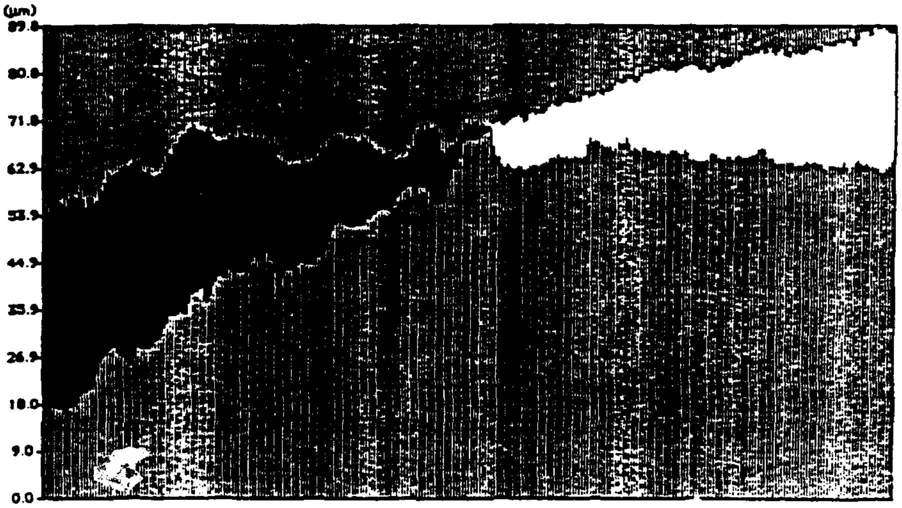

(c) Crack initiation at the blunted crack tip

(d) Onset of rapid crack growth from the blunted fatigue crack tip

RP-7294-38

Figure 30. A series of cross-sectional plots for D6ac steel specimen (concluded).

Figure 30 illustrates the crack opening profile for the various regimes of crack growth. In particular, Figure 30c and d shows that the CTOD at the onset of slow and rapid crack growth was 8.98 and 18.7 μm, respectively. This doubling of the CTOD over a crack extension of a few tens of micrometers indicates a strong resistance curve effect. Using equation 1 and of the yield strength measured in the Hopkinson bar experiments, we calculate approximate toughness values of 58 and 86 MPa$\sqrt{m}$, respectively, for the two regimes of crack growth.

Results for D6ac Steel Curved-3 Specimen

The FRASTA analysis of specimen D6ac steel Curved-3 gave essentially the same results as that of the side-grooved D6ac specimen. In particular, we observed the same advanced crack mechanism in the FAPPs and the same two stages of crack growth—slow and rapid growth—in the percent of fractured area versus map spacing plots. The values of the COD at the point of first crack extension measured in the XSPs are also very similar as indicated in Table 3 (9.0 μm versus 11.2 μm, which corresponds to toughness values of 59 MPa$\sqrt{m}$ versus 66 MPa$\sqrt{m}$). However, Table 3 reveals that at the onset of rapid crack extension the COD for the side-grooved and not side-grooved specimens are quite different (18.7 μm versus 50 μm, which corresponds to toughness values of 86 versus 140 MPa$\sqrt{m}$).

Although several details need additional characterization, the three-dimensional FRASTA analysis has highlighted significant differences in the fracture behavior of 300M and D6ac steels. Metallographic cross sections normal to the crack plane and parallel to the crack propagation direction provide more evidence of the differences and additional verification of the FRASTA results. Figure 31 shows photographs of the metallurgical cross sections of the 300M and side-grooved D6ac specimens analyzed by FRASTA. The edge of the 300M fracture plane is very smooth; the fatigue region and the rapid crack growth region are difficult to distinguish. In contrast, the crack growth region in the D6ac is very rough and jagged (as inferred from the SEM photograph and the FRASTA reconstruction) and can clearly be distinguished from the fatigue region. Therefore, the higher crack resistance of D6ac steel is associated with a much rougher fracture surface.

The COD data obtained with FRASTA for D6ac steel and presented in Table 3 suggest that the degree of constraint (side-grooved specimen or not side-grooved specimen) (1) does not significantly affect the material resistance to crack initiation but (2) has a large effect on the resistance to crack extension after only a few tens of microns of crack growth. Therefore, the

(a) Cross-sectional profile of 300M fracture surface

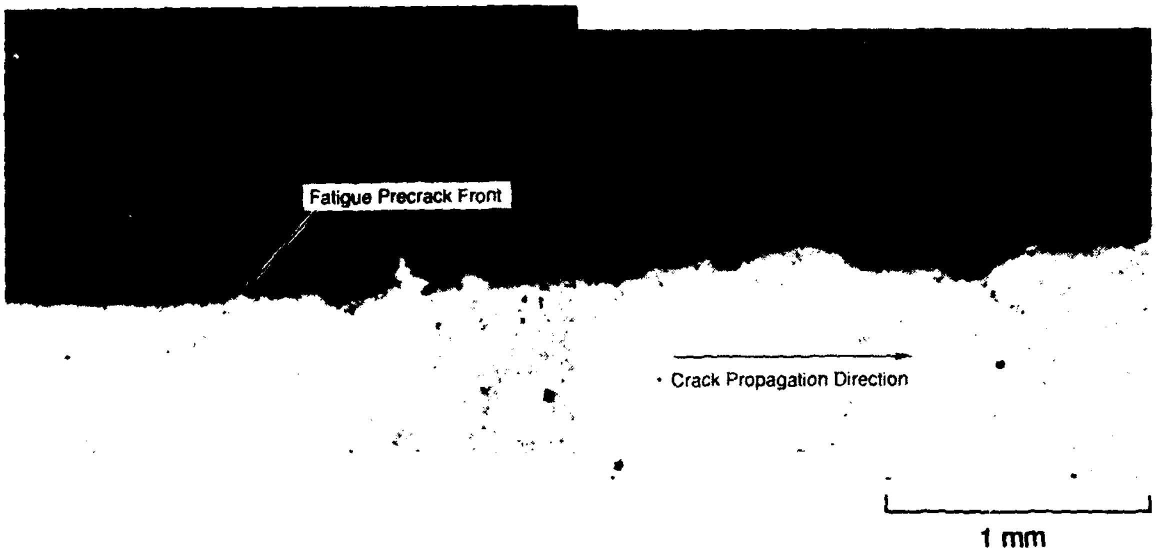

(b) Cross-sectional profile of D6AC fracture surface

RP-7294-39

Figure 31. Metallographic cross sections normal to the fracture plane and parallel to the crack propgation direction of 300 M and D6ac steel specimens.

crack has to extend a small amount and the plastic zone around the freshly initiated crack tip has to enlarge to allow relaxation of the triaxial state of stress.

Table 3 also shows a good agreement between the COD-derived toughness at the onset of rapid crack extension and the fracture toughness measured in the one-point-bend test. This agreement suggests that the toughness measured in the one-point-bend experiment represents the toughness after a small amount of crack extension.

TWO-DIMENSIONAL FRASTA OF 300M CASE FRAGMENTS

In the early stage of our investigation, we performed a two-dimensional analysis of the fracture of two tail fragments (region B of Figure 4a). We produced two matching metallographic cross sections normal to both the fracture plane and the crack propagation direction, photographed them to obtain contours of the edge of the fracture surface, then overlapped the contours in a process analogous to that shown in Figures 26 and 30, except that the cross section orientation is different. Figure 32 shows the reconstruction we obtained with this process and illustrates how a crack extends sideward through the case wall in a region with both flat tensile fracture and shear fracture. The main direction of crack extension is normal to the figure along the case circumference.

We integrated the fracture edge overlap δ for a relative position of the two cross sections corresponding to the appearance of the first microcrack in the tensile region and calculated the fracture energy per unit area (essentially the plastic work) and the fracture toughness. The procedure is illustrated in Figure 33 and can be performed over part or all of the cross section to estimate the fracture resistance of each individual region (tensile, shear, mixed). This analysis yielded values of the toughness of 170 $\mathrm{MPa}\sqrt{\mathrm{m}}$ in the tensile region, 290 $\mathrm{MPa}\sqrt{\mathrm{m}}$ in the shear and mixed region, and 190 $\mathrm{MPa}\sqrt{\mathrm{m}}$ averaging over the whole cross section. These values are significantly higher than those measured in the fracture experiments or with the three-dimensional FRASTA analysis of the fracture specimens. However, because fracture surface appearance and roughness of the tail fragment are significantly different from those of the rest of the case and of the fracture specimens, much higher toughness values may not be unreasonable.

The two-dimensional FRASTA analysis indicates another method—analogous to, but not identical with that based on the percentage of fractured area plots—of estimating local toughness values that could be used in computer simulations. We will continue developing and verifying these approaches in future work.

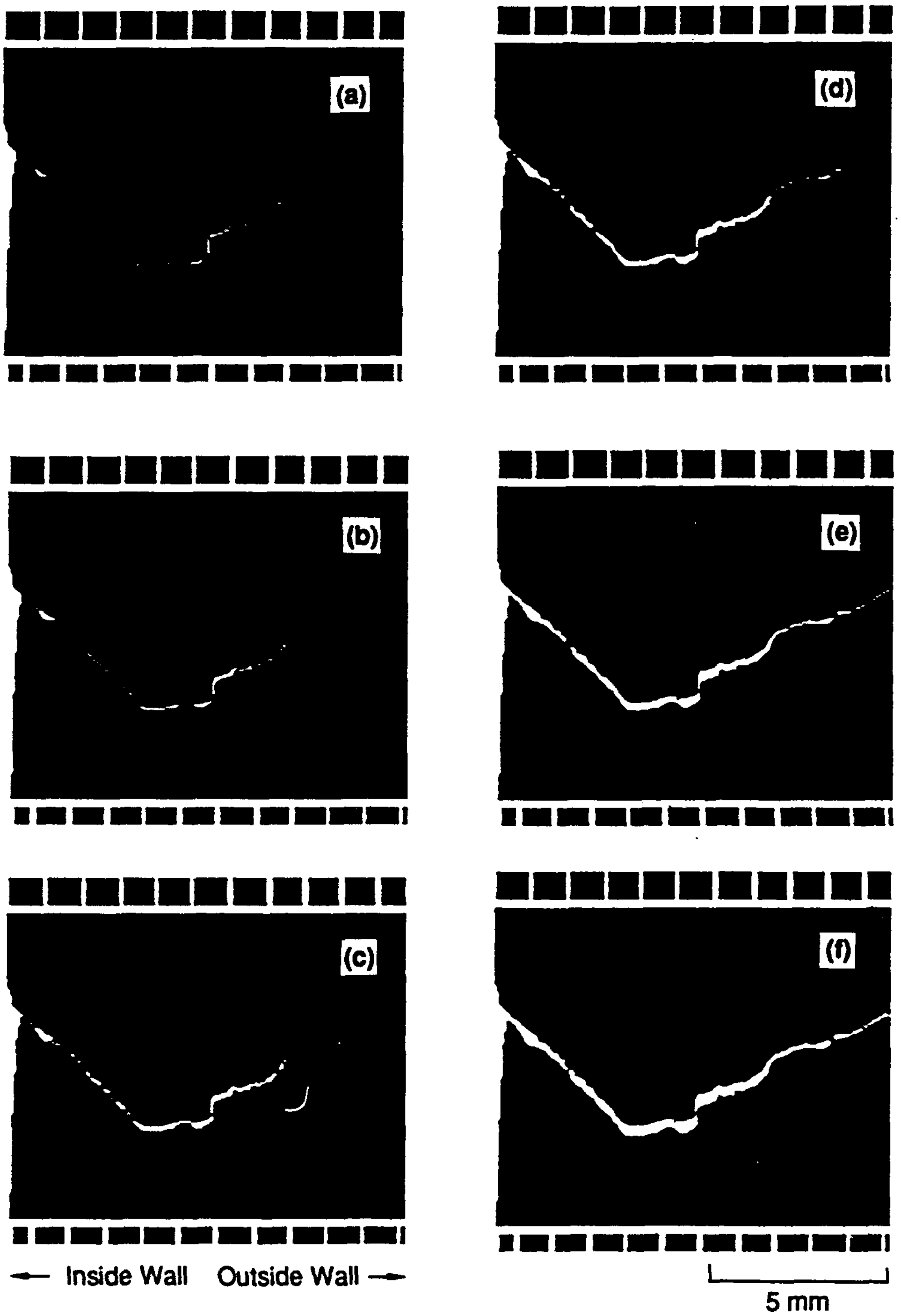

CP-314582-2

Figure 32. Two-dimensional FRASTA reconstruction of crack extension through the wall of the case in the tail region.

(See Figure 4 for location of fragment.)

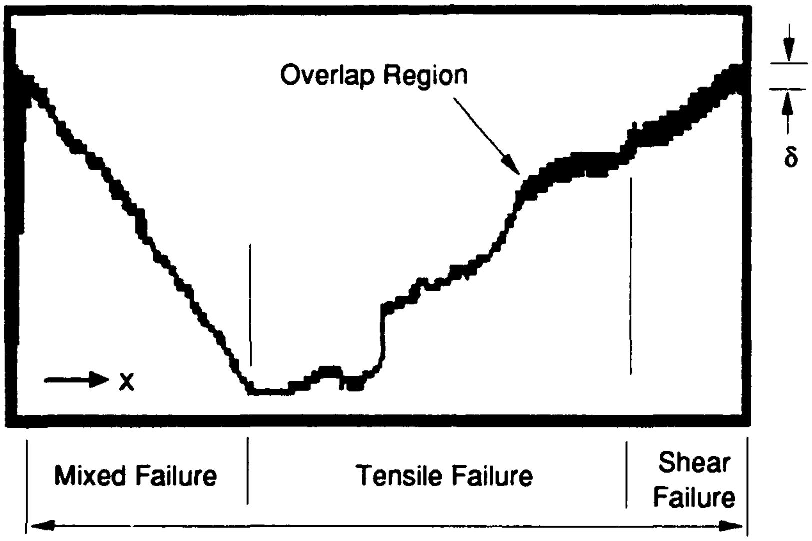

- $G \approx \frac{\sigma_o}{L} \int_o^L \delta(x)\,dx$

G = fracture energy per unit crack area
σ_o = flow stress ($\approx$ 2165 MPa)
$\delta(x)$ = overlap thickness as a function of distance

- $K = \sqrt{GE}$ = propagation toughness

E = Young's modulus

RAM-7294-40

Figure 33. Estimation of fracture energy per unit area and of the fracture toughness with two-dimensional FRASTA analysis.

TORSION HOPKINSON BAR EXPERIMENTS

The objective of the Hopkinson torsion bar experiments was to measure the stress-strain curve for the 300M and D6ac steels at loading rates comparable to those the bomb casings may experience during penetration events and to evaluate the tendency for adiabatic shear banding.

TEST PROCEDURE

The torsion Hopkinson bar experiment is a well-known dynamic material testing technique, so it will not be described here; for further details, the reader should consult Hartley et al.[8]

We prepared four torsion specimens each from the 300M and D6ac bomb casing materials and tested three specimens each. The geometry and dimensions of the specimens are shown in Figure 34. We first electrodischarge machined the specimens from the case with their axis perpendicular to the wall, then machined the central grooves with a cutting tool to achieve the desired specimen wall thickness. Before the experiments, axial lines were scribed on the inside wall of the specimen to provide a record of the final strain distribution in the specimen gage length.

We conducted all the torsion Hopkinson bar experiments at room temperature and at an engineering shear strain rate of 3000 s^{-1}.

RESULTS

Figures 35 and 36 show the three measured shear stress-shear strain curves for 300M and D6ac steel, respectively. The stress-strain curves for each material are quite reproducible, except the failure strain, which varies significantly from test to test.

Both steels display very little strain hardening. However, 300M steel has a much higher shear flow strength (the "plateau" value of the stress over most of the deformation) than D6ac (1300 MPa versus 947 MPa, a 37% difference). Correspondingly, the average shear strain at failure (i.e., at the point where the shear strength decreases rapidly with deformation) is about 33% smaller in 300M steel than in D6ac steel (0.1 versus 0.13). In view of the large difference in flow strength and fracture toughness, this difference in the failure shear strain appears rather modest.

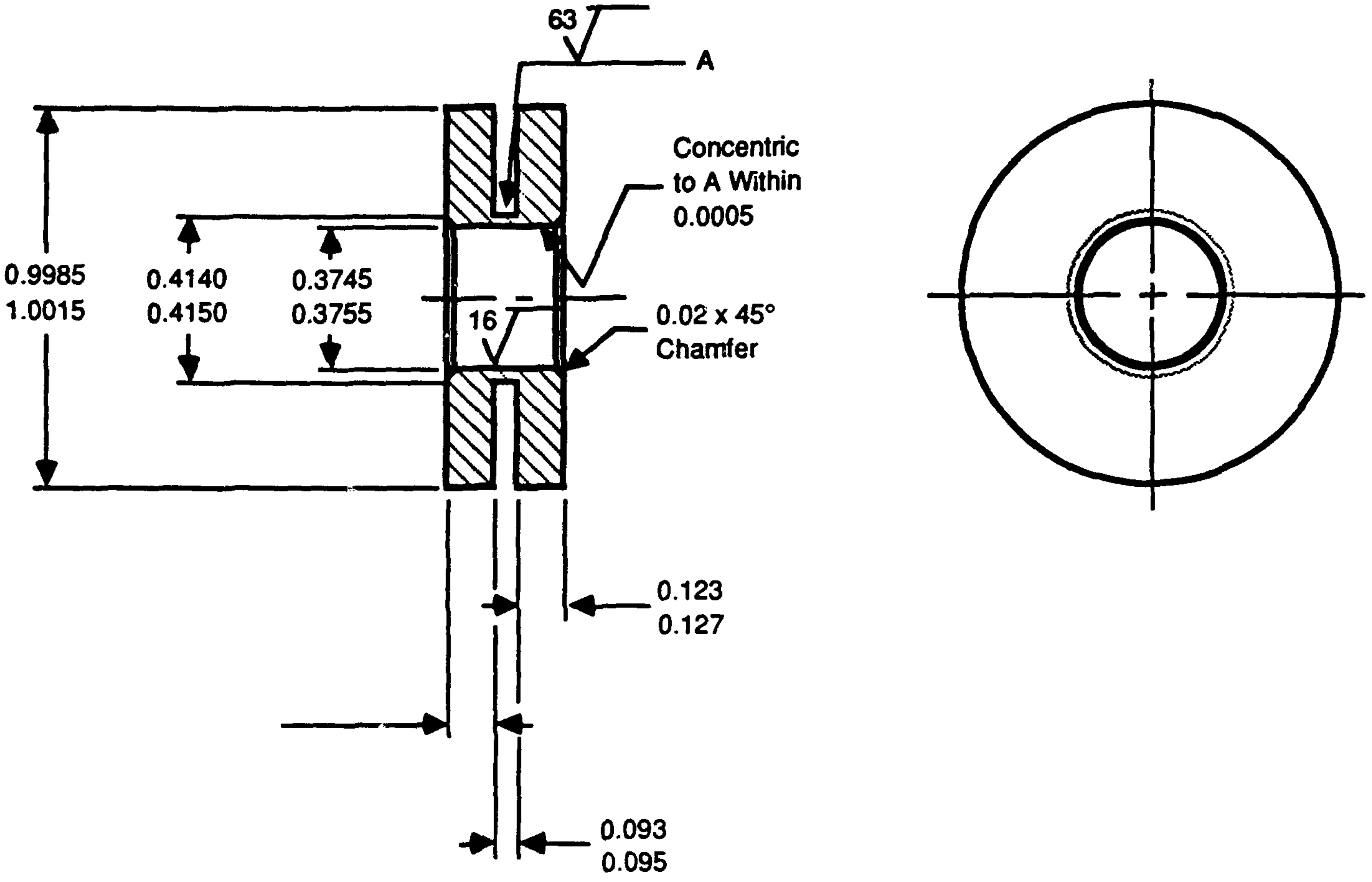

Note: Corner radii at
bottom of notch to
be less than 0.004
or as sharp as tool
will allow

RA-3606-1A

Figure 34. Specimen for torsion Hopkinson bar experiments.

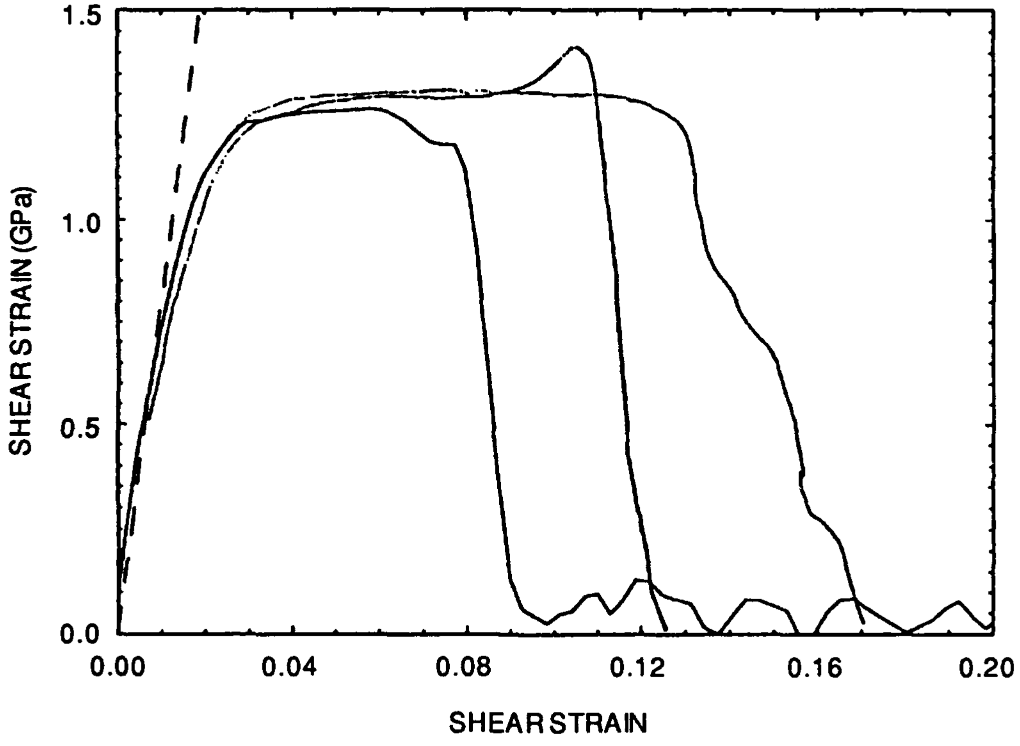

Figure 35. Dynamic shear stress-shear strain curve for 300 M steel.

(Result of 3 experiments)

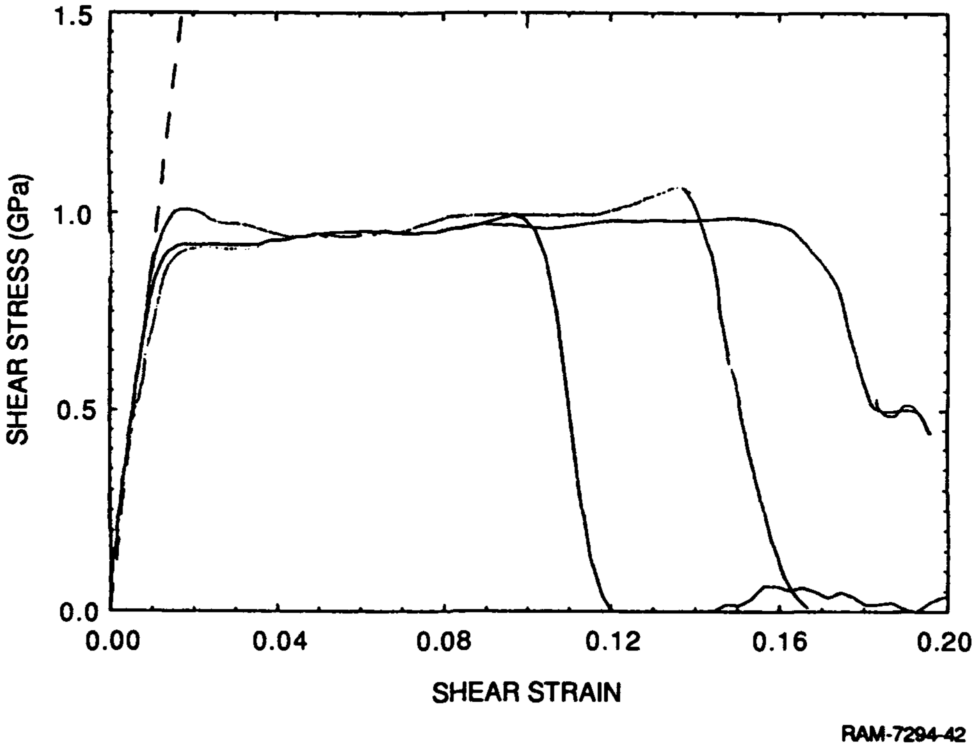

Figure 36. Dynamic shear stress-shear strain curve for D6ac steel. (Result of 3 experiments)

Figures 37 and 38 show the deformed axial scribed lines in the 2.38-mm gage length region of the 300M and D6ac specimens, respectively. We obtained these figures by photographing the two broken halves of each specimen, then assembling the photographs to reconstruct the complete deformed lines. The vertical dashed lines in the figures indicate the position of the shear failure plane. Figures 37 and 38 demonstrate that deformation was not uniform over the whole gage length. In the 300M specimen, deformation was limited to the central portion of the specimen gage length, whereas the edges remained undeformed. This nonuniformity is due to differences in wall thickness over the gage length because of blunted edges of the cutting tool used to machine the central groove of the specimen. (Maintaining sharp tool edges when machining steel with a Rockwell C hardness of 50 is difficult.) Because we assume, in reducing the torsion Hopkinson bar test data, that the strain in the specimen is homogeneous, we underestimate the actual strain experienced by the center portion of the specimen.

Comparison of the failure strain deduced by the conventional Hopkinson bar data analysis method with the strain measured from the photograph in Figure 37 reveals a difference of less than 10% between the two values (0.11 versus 0.12 for the specimen under consideration). In the vicinity of the failure plane, we observe no significant inflection in the scribe line that would indicate the formation of an adiabatic shear band (deformation band). Therefore, Figure 37 suggests that 300M steel fails in pure torsion by a shear fracture mechanism (nucleation and growth of elongated voids) or by nucleation and growth of a very narrow transformation band. Optical microscope observations of the failure surfaces indicate that the former mechanism is more likely and would be consistent with earlier observation in 4340 steel.[9,10]

In contrast to 300M steel, the shear deformation in D6ac is more or less uniform over the whole gage length, as indicated in Figure 38. The only exception is the immediate vicinity of the failure plane where we observe evidence of localization in a deformation band about 60 μm wide. Again, optical microscopy observations suggest that the final failure occurred by nucleation and growth of elongated voids. If we consider the strain localization that led to the final shear fracture, the failure strain for D6ac is much larger than that for 300M (>0.5)

In summary, 300M and D6ac steels have significantly different flow curves but rather similar average shear strains at failure. In 300M, final failure by what we believe is nucleation and growth of elongated voids is not preceded by any noticeable strain localization, whereas a thermomechanical instability (deformation adiabatic shear band) appears to form first in D6ac steel with fracture by nucleation, and growth of voids occurring later within that deformation band at a significantly larger (local) strain than in 300M steel.

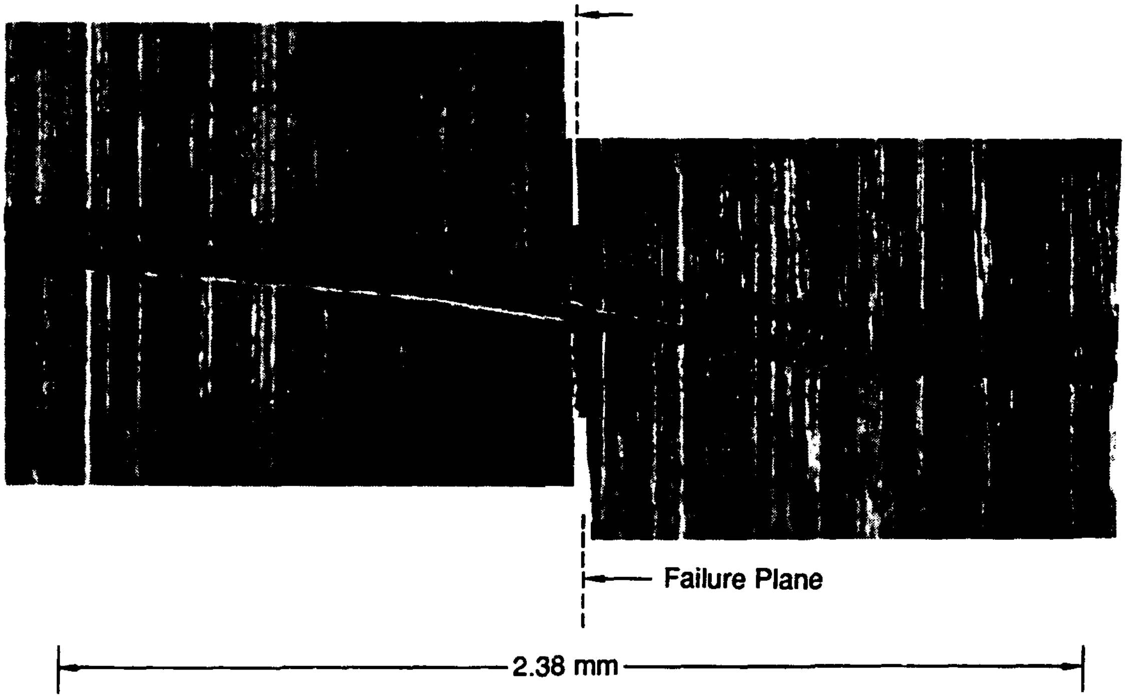

RP-7294-43

Figure 37. Deformed scribe line in 300 M steel torsion specimen showing nonuniform deformation along the gage length.

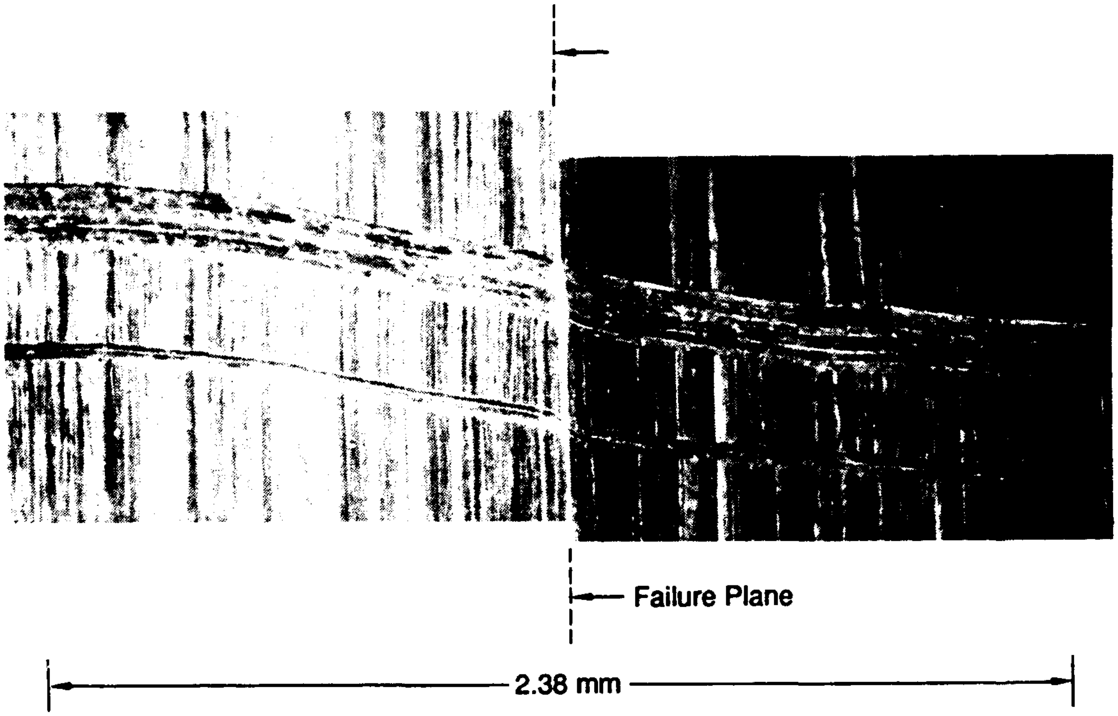

RP-7294-44

Figure 38. Deformed scribe line D6ac steel torsion specimen showing nonuniform deformation in the vicinity of the failure plane.

CONCLUSIONS

Although significantly more work is needed to develop a full understanding of how processing and microstructural conditions control the behavior of hard-target penetrators and their fracture properties, the results of this preliminary investigation lead to several important conclusions, which we summarize below.

- 300M and D6ac steels have significantly different dynamic flow properties (37% difference in flow stress) and dynamic (mode I) fracture toughnesses (100% at initiation) but rather similar average shear strains at failure. The local failure strains, however, are very different (0.1-0.12 for 300M compared with greater than 0.5 for D6ac).

- Both materials appear to show an increase in fracture resistance with small amounts of crack extension. This behavior is suggested by the analysis of the crack propagation experiments for 300M steel and by the FRASTA reconstruction and the crack initiation experiments for D6ac steel. The absolute increase and the rate of increase in fracture resistance with crack extension appear much more significant in D6ac steel.

- FRASTA reveals an important difference in the microprocesses of fracture in 300M and D6ac. Whereas crack growth is more or less uniform and continuous along the main crack front in 300M steel, the process is discontinuous and involves advanced microcracks in D6ac steel. This observation explains, at least partly, the differences in fracture resistance.

- Our preliminary failure analysis of the torsion specimens indicates that 300M and D6ac steels also have different failure mechanisms in dynamic torsion experiments. 300M appears to fail by nucleation and growth of elongated voids (shear fracture), whereas D6ac first undergoes a thermomechanical shear localization (deformation adiabatic shear band) before finally failing by propagation of a shear fracture within the shear band. These failure mechanisms should be confirmed by additional fractographic observations with a scanning electron microscope.

- The fracture surface appearance of 300M steel (flat tensile or mixed flat tensile and slant shear) varies dramatically depending on the location in the case. We believe that this difference is induced by the loading conditions, by differences in case wall thickness, and possibly by microstructural differences at various positions in the case. Preliminary estimates using FRASTA suggest that the different fracture modes are also associated with very different toughnesses.

- A rapid inspection of the failed 300M case reveals that it underwent ovalization, suggests a possible correlation between the deformation and cracking pattern, and leads to a plausible failure scenario involving transverse bending, ovalization, and circumferential bending.
- On the basis of the present preliminary results, we conclude that the difference in penetration behavior between 300M and D6ac steels, is due mostly to their difference in microscopic fracture properties.

From the point of view of fracture analysis and testing, our work has produced two additional results. First, we have identified and partially validated methods to extract local toughness information from fractographic measurements. After further development, these methods could contribute to the definition and calibration of local fracture models for use in numerical simulations of penetration events. Second, we have developed and validated a simple dynamic fracture test, the curved specimen one-point-bend test, that can be used to evaluate candidate penetrator materials or for quality control purposes in producing penetrators. The advantages of the test are its economy in preparing the specimen and its ability to test the case material in the proper processing condition and with the proper crack orientation.

REFERENCES

1. M. F. Kanninen, P. C. Gehlen, C. R. Barnes, R. G. Hoagland, G. T. Hahn, and C. H. Popelar, "Dynamic Crack Propagation Under Impact Loading," *Nonlinear and Dynamic Fracture Mechanics*, N. Perrone and S. N. Atluri, Eds. (American Society of Mechanical Engineers, New York, 1979), pp. 185-200.

2. J. F. Kalthoff, S. Winkler, W. Böhme, and D. A. Shockey, "Mechanical Response of Cracks to Impact Loading," in *Proceedings of the International Conference on Dynamical Properties and Fracture Dynamics of Engineering Materials* (Czechoslovak Academy of Sciences, Institute of Physical Metallurgy, Brno, Czechoslovakia, June 1983).

3. J. H. Giovanola, "Investigation and Application of the One-Point-Bend Impact Test," in *Fracture Mechanics: Seventeenth Volume, ASTM STP 905*, J. G. Underwood, R. Chait, C. W. Smith, D. P. Wilhelm, W. A. Andrews, and J. Newman, Eds. (American Society for Testing and Materials, Philadelphia, 1986), pp. 307-328.

4 T. Nakamura, C. F. Shih, and L. B. Freund, "Analysis of a Dynamically Loaded Three-Point-Bend Ductile Fracture Specimen," Brown University Report ONR0365/1 (1985).

5. J. O. Hallquist, "User's Manual for DYNA2D—An Explicit Two-Dimensional Hydrodynamic Finite Element Code with Interactive Rezoning," Lawrence Livermore National Laboratory Report UCID-18756 (1980).

6. J. O. Hallquist, "NIKE2D: A Vectorized, Implicit, Finite Deformation, Finite Element Code for Analyzing the Static and Dynamic Response of 2-D Solids," Lawrence Livermore National Laboratory Report UCID-1967 (1983).

7. J. H. Giovanola, "Crack Initiation and Extension in Steel for Short Loading Times, " in *Proceedings of DYMAT, International Conference on Mechanical and Physical Behavior of Materials Under Dynamic Loading*, Paris, September 2-5, 1985, Les Editions de Physique, Les Ulis, France, (1985), p. C5-171.

8. K. A. Hartley, J. Duffy, and R. H. Hawley, "The Torsional Kolsky (Split-Hopkinson) Bar," in *Metal Handbook® Ninth Edition, Volume 8, Mechanical Testing*, American Society for Metals, Metals Park, Ohio, pp. 218-228

9. J. H. Giovanola, "Adiabatic Shear Banding Under Pure Shear Loading. Part I: Direct Observation of Strain Localization and Energy Dissipation Measurements, " Mechanics of Materials, 7, 59, (1988).

10. J. H. Giovanola, "Adiabatic Shear Banding under Pure Shear Loading. Part II: Fractographic and Metallographic Observations, " Mechanics of Materials, 7, 73, (1988).

11 K. A. Hartley, "Temperature Profile Measurement During Shear Band Formation in Steels at High Strain Rates," *PhD Dissertation*, Division of Engineering, Brown University, Providence, May 1986.